CFD Methodologies for Compressible Atomising and Cavitating Multi-phase Flows

Hongjiang Yu
B.Eng (Hons), Dip.Eng (Merit)

Thesis submitted for the Degree of Doctor of Philosophy in Engineering

At the

National Centre for Maritime Engineering and Hydrodynamics

Australian Maritime College

University of Tasmania

April 2018

Abstract

Understanding the complex physics involved in compressible multi-phase flows has been a challenging topic in modern Computational Fluid Dynamics. This is particularly true when investigating the unsteady dynamics of flow in high pressure fuel injectors. The high pressure and impulsive nature of these flows lead to transient complex phenomena including flow separation, cavitation, interfacial instabilities and turbulence. These phenomena contribute to evolution of the spray atomisation in a nonlinear sense. Although useful information on injector flows has been obtained experimentally, the extremely small geometry of injector holes (10^{-4}-10^{-3} m) and the highly transient nature of nozzle flows still impose spatial and temporal limitations on experimental investigations. High fidelity numerical simulations serve as a promising tool to provide more insights into spray atomisation processes.

The injection of fuel sprays can be divided into three stages. In the first stage, turbulence is generated due to flow separation and cavitation in the injector. Subsequently, in-nozzle turbulence together with high flow inertia and wall shear lead to the development of surface instabilities incurring primary disintegration of the liquid jet into large structures such as ligaments and irregular droplets. In the final stage, large liquid structures further breakup into fine spherical droplets due to turbulent interaction with the gas in the combustion chamber.

In this thesis, three new numerical approaches to analysing different stages of the diesel spray evolution are developed. First, an efficiently parallelised Eulerian (Volume of Fluid) - Lagrangian (Lagrangian Parcel Tracking) coupling procedure is implemented. This procedure couples a high-resolution Eulerian description of primary spray breakup to an efficient Lagrangian tracking of droplet parcels for simulating secondary spray atomisation. Secondly, detailed investigation of the onset of cavitation and hydraulic flip in the injector is performed with a new compressible multi-phase Volume of Fluid cavitation code. Modelling of cavitation and air ingestion induced complete flow detachment in the injector is enabled by the use of multi-phase volume fraction transport equations. A modified multi-phase mixture energy equation integrating non-linear equations of state and cavitation source terms is then developed and employed to enable simulation of the high pressure injection process with improved fidelity, including thermal effects. Finally, the efficiency and resolution of the cavitation code is improved through the implementation of a compressible fractional step pressure-velocity coupling method for all Mach number flows. Particularly, low dissipation and high resolution are achieved using the Kurganov-Noelle-Petrova central-upwind flux scheme.

The performance of the developed numerical methods is demonstrated using a range of geometries from a cavitating square channel to injectors with sharp and rounded nozzle entrances at various injection conditions. In addition, the superiority of the all Mach number multi-phase cavitation code in numerical resolution and computing speed is demonstrated by comparing it with the traditional Pressure-Implicit-with-Splitting-of-Operators (PISO) algorithm.

Declaration and Statements

Declaration of Originality

I declare that this is my own work and has not been submitted in any form for another degree or diploma at any university or other institution of tertiary education. Information derived from the published or unpublished work of others has been duly acknowledged in the text and a list of references if given.

Authority of Access

This thesis may be made available for loan and limited copying in accordance with the Copyright Act 1968.

Statement Regarding Published Work Contained in the Thesis

The publishers of the papers comprising Chapters 2 to 4, inclusive, hold the copyright for that content, and access to the material should be sought from the respective journals. The remaining non published content of the thesis may be made available for loan and limited copying and communication in accordance with the above Statement of Access and the Copyright Act 1968.

Signature:_____ Date: 15/04/2018

Thesis by Journal Articles

The following four journal articles constitute four chapters of this thesis. The third article is currently under review in Fuel. Contents in chapter five will be submitted for publication after the submission of this thesis.

- Chapter 2: Yu, H., Goldsworthy, L., Ghiji, M., Brandner, P. A., & Garaniya, V. (2017). A parallel volume of fluid-Lagrangian Parcel Tracking coupling procedure for diesel spray modelling. Computers & Fluids, 150, 46-65. doi: 10.1016/j.compfluid.2017.03.027.

- Chapter 3: Yu, H., Goldsworthy, L., Brandner, P. A., & Garaniya, V. (2017). Development of a compressible multi-phase cavitation approach for diesel spray modelling. Applied Mathematical Modelling, 45, 705-727. doi: 10.1016/j.apm.2017.01.035.

- Chapter 4: Yu, H., Goldsworthy, L., Brandner, P. A., Li, J., & Garaniya, V. (2017). Modelling thermal effects in cavitating high-pressure diesel sprays using an improved compressible multi-phase approach, Fuel, 222, 125-145. doi: 10.1016/j.fuel.2018.02.104.

- Chapter 5: Yu, H., Goldsworthy, L., Brandner, P. A., & Garaniya, V. (2017). Adaption of fractional step method and central-up wind flux scheme for compressible multi-phase flows: Application to cavitating high-pressure diesel sprays, Manuscript in preparation.

Conference papers not included in this thesis, but can be accessed as supplementary material.

- Yu, H., Goldsworthy, L., Brandner, P. A., & Garaniya, V. Modelling of In-Nozzle Cavitation and Early Spray Breakup Using a Multi-phase Volume of Fluid Method, in: 20th Australasian Fluid Mechanics Conference, Perth, 2016.

- Yu, H., Garaniya, V., Pennings, P., & Vogt, J. Numerical analysis of cavitation about marine propellers using a compressible multi-phase VOF fractional step method, in: 9th Australasian Congress on Applied Mechanics, Sydney, 2017.

Statement of Co-Authorship

The following people and institutes contributed to the publication of work undertaken as part of this thesis.

Mr. Hongjiang Yu

National Centre for Maritime Engineering and Hydrodynamics
Australian Maritime College
University of Tasmania

Dr. Laurie Goldsworthy

Adjunct Senior Researcher
National Centre for Maritime Engineering and Hydrodynamics
Australian Maritime College
University of Tasmania

Professor Paul Brandner

Research leader
National Centre for Maritime Engineering and Hydrodynamics
AMC Cavitation research laboratory
Australian Maritime College
University of Tasmania

Dr. Vikram Garaniya

Senior Lecturer - Thermal and Process Engineering
National Centre for Maritime Engineering and Hydrodynamics
Australian Maritime College
University of Tasmania

Dr. Mohammadmahdi Ghiji
Postdoctoral research fellow
Centre for Environmental Safety and Risk Engineering
Victoria University

Mr. Jianzhi Li
CFD Software Engineer
Envision Energy (Nanjing) Software Technology Co., Ltd.

Paper 1-Chapter 2

Conceived idea and designed the Case Studies: Yu, Goldsworthy, Ghiji, Brandner and Garaniya
Performed the Case Studies: Yu (65%) and Ghiji
Analysed the data: Yu
Wrote the chapter/manuscript: Yu

Manuscript evaluation and submission: Yu, Goldsworthy, Brandner and Garaniya

Paper2-Chapter 3

Conceived idea and designed the Case Studies: Yu, Goldsworthy, Brandner and Garaniya
Performed the Case Studies: Yu (70%)
Analysed the data: Yu
Wrote the chapter/manuscript: Yu
Manuscript evaluation and submission: Yu, Goldsworthy, Brandner and Garaniya

Paper3-Chapter 4

Conceived idea and designed the Case Studies: Yu, Goldsworthy, Brandner, Li and Garaniya
Performed the Case Studies: Yu (70%)
Analysed the data: Yu
Wrote the chapter/manuscript: Yu
Manuscript evaluation and submission: Yu, Goldsworthy, Brandner and Garaniya

Chapter 5

Conceived idea and designed the Case Studies: Yu, Goldsworthy, Brandner and Garaniya
Performed the Case Studies: Yu (75%)
Analysed the data: Yu
Wrote the chapter/manuscript: Yu
Manuscript evaluation: Yu, Goldsworthy, Brandner and Garaniya

Dr. Laurie Goldsworthy (Primary Supervisor)

Adjunct Senior Researcher
National Centre for Maritime Engineering and Hydrodynamics
Australian Maritime College
University of Tasmania

Signature:_____ Date: 16/04/2018

Associate Professor Shuhong Chai

Acting Principal
National Centre for Maritime Engineering and Hydrodynamics
Australian Maritime College
University of Tasmania

Signature:_____ Date: 16/04/2018

Acknowledgement

I would like to express my deepest gratitude to the following people who helped develop this thesis:

- Dr. Goldsworthy, Dr. Garaniya and Professor Brandner for your guidance, encouragement and support throughout my PhD candidature.

- Ping Yu and Yuanchun Hong for being the most supportive, comforting and understanding parents.

- Luojia Zhang for taking care of me and always standing by my side through many difficult times.

- Hongyang Yu for being an encouraging and supportive brother.

- And finally, all my friends for their companionship.

To Ping Yu, Yuanchun Hong and Luojia Zhang

List of Abbreviations

AMG	Algebraic Multi-grid Methods
ASOI	After Start of Injection
ASOP	After Start of Penetration
CAD	Computer Aided Design
CFD	Computational Fluid Dynamics
CFL	Courant-Friedrichs-Lewy number
cFSM	Compressible Fractional Step Method
cFSMCavitatingInterFoam	All Mach number multi-phase VOF cavitation solver
CICSAM	Compressive Interface Capturing Scheme for Arbitrary Meshes
CN	Cavitation Number
CPU	Central Processing Unit
DCA	Direct Coupling Approach
DEP	Droplet Extraction Procedure
DIP	Droplet Identification Procedure
DNS	Direct Numerical Simulation
EOS	Equation Of State
FOAM	Field Operation And Manipulation
FSM	Fractional Step Method
KH	Kelvin Helmholtz
KNP	Kurganov-Noelle-Petrova scheme
LES	Large Eddy simulation
LPT	Lagrangian Parcel Tracking
LSM	Level Set Method
MULES	Multi- Dimensional Universal Limiter with Explicit Solution
NV	Normalised Variable
OpenFOAM	An open source finite volume CFD package
PDF	Probability Density Function
PISO	Pressure Implicit with Splitting of Operator
PISOCavitatingInterFoam	PISO based Compressible multi-phase VOF solver
PR	Peng-Robinson
RCM	Region Coupling Method
RHS	Right Hand Side
RKE	Resolved turbulent Kinetic Energy
RKDG	Runge Kutta Discontinuous Galerkin method
RT	Rayleigh Taylor
SCA	Statistical Coupling Approach
SGS	Sub Grid Scale
SIMPLE	Semi-Implicit Method for Pressure Linked Equations
VOF	Volume of Fluid
VOF-LPT	Volume of Fluid coupled with Lagrangian parcel tracking

List of Mathematical Operators

∂	Partial Derivative
∇	Gradient
$\nabla\cdot$	Divergence
∇^2	Laplacian
$\int_S$	Surface integration
$\int_A$	Integration over area
$\lvert\ \rvert$	Absolute value
X^T	Transpose of matrix X
$\sqrt[3]{\ }$	Cubic root
$\overline{\phi(x,t)}$	Favre filter
$\frac{d}{dt}$	Local derivative with respect to time
$\frac{D}{Dt}$	Material derivative with respect to time
$\sum_V$	Summation over a finite volume
$\max(\ )$	Find max value
$\min(\ )$	Find minimum value

List of Symbols

Characters

ρ	Density	$\left[kg/m^3\right]$
t	Time	$\left[s\right]$
Δt	Time step size	$\left[s\right]$
U	Velocity	$\left[m/s\right]$
p	Static pressure	$\left[Pa\right]$
τ	Shear stress tensor	
σ	Surface tension	$\left[N/m\right]$
κ	Surface curvature	
$\vec{n}$	Unit vector normal to liquid-gas interface	
δ	Dirac function	
α	Phase volume fraction	
ψ	Compressibility	
μ	Dynamic viscosity	$\left[Pa\ s\right]$
k	Sub-grid-scale kinetic energy	$\left[m^2/s^2\right]$
I	Identity tensor	
ε	Sub-grid-scale turbulent dissipation	
υ	Kinematic viscosity	$\left[m^2/s\right]$
Δ	Sub-grid length scale	$\left[m\right]$
V	Volume of the computational cell	$\left[m^3\right]$
h	Sensible specific enthalpy	$\left[J/kg\right]$
λ	Thermal conductivity	$\left[W/(m.K)\right]$
Φ	Species mass flux	
Pr	Prandtl number	
S_U^s	Parcel momentum source term	
X	Position vector	
C_D	Drag coefficient	
Re	Reynolds number	
m	Mass	$\left[kg\right]$
d	Diameter	$\left[m\right]$
$G(\ )$	Gaussian distribution	
r	Radius	$\left[m\right]$
D	Nozzle diameter	$\left[m\right]$
K_s	Nozzle index factor	
$\dot{m}$	Mass transfer rate	$\left[kg/s\right]$

$\dot{m}^{+}$	Condensation rate	$[kg/s]$
$\dot{m}^{-}$	Vaporisation rate	$[kg/s]$
C_a	Interface compression factor	
C_v	Coefficient for vaporisation	
C_c	Coefficient for condensation	
t_∞	Mean flow time scale	$[s]$
rR_b	Inverse of average nuclei diameter	$[1/m]$
n	Cavitation nuclei/bubble density	$[1/m^3]$
η	Kolmogorov length scale	$[m]$
W	Characteristic length	$[m]$
Δp	Pressure difference	$[MPa]$
Q	Q criterion	
ΔH	Enthalpy of phase change	$[J/kg]$
C_p	Constant pressure heat capacity	
K	Kinematic energy	$[J/kg]$
H'	Pressure dependent specific enthalpy	$[J/kg]$
R	Gas constant	
v_m	Molar volume	$[m^3/mol]$
Z	Compressibility factor	
ω	Acentric factor	
$\dot{m}_f$	Mass flow rate	$[kg/s]$
$\dot{M}_f$	Momentum flux	$[kg \cdot m/s^2]$
u_{eff}	Effective injection velocity	$[m/s]$
C_d	Discharge coefficient	
A_o	Nozzle cross-sectional area	$[m^2]$
ρ_0	Reference density	$[kg/m^3]$
l	Unit vector connecting cell centres	
a	Coefficient for KNP numerical scheme	
c	Speed of sound	
$\vec{S}$	Surface normal unit vector	
γ	Adiabatic index	
$\tilde{\rho}\tilde{U}$	Modified mass flow rate	$[kg/s]$
$\tilde{U}$	Modified velocity	
Δs	Distance between centres of two adjacent cells	

Subscripts

l	Liquid phase
v	Vapour phase
g	Gas phase
i	Incondensable gas phase
sgs	Sub-grid-scale
P	Parcel
rel	Relative
$cell$	Mesh element
nuc	Nuclei
inj	Injection
out	Back/outlet pressure
$i-j$	Phase pairs
r	Reduced
c	Critical
$left$	Upstream side of a mesh face
$right$	Downstream side of a mesh face
f	Variable on mesh faces

Superscripts

$n-1$	Previous time step level
n	Present time step level
$n+1$	Next time step level
*	Predicted time step level
$ideal$	Ideal fluid
$real$	Real fluid
P	Upstream direction
N	Downstream direction
min	Minimum value
Max	Maximum value

Table of Contents

1 Introduction

1.1 Aim of the Research

The study of the complex physics involved in compressible multi-phase flows is of paramount importance in applications across many industries. In particular, characterisation of multi-phase flow dynamics in various combustion systems has attracted substantial attention for performance optimisation and emission reduction. The complexity of these analyses is increased significantly when phenomena such as turbulence, phase change and large density variations are mandatorily considered. Conditions inducing these complex flow phenomena often include, but are not limited to, geometry change, high pressure gradients and interfacial interactions. They match well with the typical operating conditions of most gasoline, diesel and gas turbine engines. Therefore, manipulation of flow dynamics as a result of proper control of geometry and operating conditions in these engines can be employed to realise better efficiency and power gain with a reduced level of emission. This is largely based on achieving an in-depth understanding of how multi-phase flows (air-fuel mixtures) evolve in combustion chambers.

The evolution of air-fuel mixtures resulting from fuel injection into a combustion chamber can be divided into four stages. The first stage concerns the breakup of the liquid fuel jet from fuel injectors. The disintegration of the jet into liquid ligaments of various scales can be attributed to the combined effects of surface tension, inner-injector flow separation, liquid-wall shear, cavitation and turbulence. This is followed by secondary atomisation (owing to Kelvin-Helmholtz and Rayleigh Taylor instabilities) that breaks up large liquid structures into small scale spherical droplets (secondary droplets). In the third stage, turbulent droplet-gas interactions result in increasingly fragmented and dispersed secondary droplets in the combustion chamber. Finally, ignition of this air-fuel mixture by compression (diesel engines) or the use of spark plugs (gasoline engines) causes combustion that converts chemical energy of the fuel to useful mechanical power. Therefore, the atomisation of fuels in the combustion chamber has a direct effect on the quality of air-fuel mixing which governs the efficiency of combustion and the composition of the combustion products.

There are three major difficulties associated with experimental investigation of the atomisation processes in combustion chambers. First, the evolution of the flow from liquid fuel jets to dispersed secondary droplets involves significant change in flow scales. Typically, the scale of the liquid phase (fuel) can vary from millimetre level to sub-micron level in the process of atomisation. This imposes scale limitations on experimental analysis of such multi-scale problems due to the difficulty in simultaneously imaging internal and external injector flows. The second major difficult comes from the fact that it is extremely difficult to distinguish liquid droplets and liquid core in the dense spray region using optical measurements. This limits the experimental investigation to characterisation of macroscopic properties of fuel sprays such as penetration length, spray angle and penetration velocity. Although X ray analyses can reveal time averaged information on the spray core, limited information is obtained on the transient physics of secondary droplets. Further, statistics on the size and distribution of fuel droplets (which is an important indication of air-fuel mixing quality) in the combustion chamber are limited to the optically less dense regions of the spray.

The third major difficulty is related to the small time scale at which cavitation initiates and collapses inside the injector nozzle. The study of injector nozzle cavitation is important because it could potentially improve spray atomisation but is detrimental to the structural integrity of nozzle injectors due to its erosive nature. However, since cavitation and collapse of vapour cavities often occur at microsecond or even nanosecond level in real size non-transparent fuel injectors, experimental characterisation of such phenomenon with a high temporal and spatial resolution is challenging. The scale limitations and optical barrier encountered in experimental investigations of fuel sprays flow physics can potentially be overcome using high resolution numerical models.

The main focus of this research work is to conduct detailed analyses on how in-nozzle phenomena affect the fragmentation of liquid fuel jets using advanced numerical models, with the view of obtaining more insights into atomisation processes of fuels in high pressure combustion chambers.

1.2 Research Milestones and Research Questions

The development of advanced numerical approaches for the modelling of spray evolution from in-nozzle phenomena to secondary atomisation involves accomplishing the following milestones:

- Development of a high fidelity Eulerian (VOF) - Lagrangian (LPT) parallel coupling procedure for diesel spray modelling - To solve the multi-scale problem and overcome the optical barrier.
- Integration of a mass conservative cavitation model into a new compressible multi-phase VOF code - To improve modelling of in-nozzle cavitation and cavitation induced hydraulic flip.
- Implementation of a modified multi-phase mixture energy equation based on specific sensible enthalpy - To take into account enthalpy of phase change, thermal effects of cavitation and pressure dependent fluid properties.
- Adaption of an all Mach number fractional step method integrating a low dissipative central-upwind flux scheme - To improve the numerical resolution and efficiency of all developed models.

In addition, each milestone is completed by answering a relevant research question. These questions are listed below:

- The run-time coupling of VOF-LES and LPT-LES is computationally intensive. How can this coupling be implemented with least simulation effort and time?
- Which cavitation model requires least interference from the use of empirical constants? Is it justifiable to only validate the multi-phase cavitation code at low injection pressure conditions?
- Are linear Equations of State, internal energy based energy equation and constant fluid properties still valid for modelling fuel injection and atomisation at engine-like conditions?
- Is the PISO algorithm suitable and efficient for modelling compressible multi-phase flows over a wide range of Mach numbers?

1.3 Research Scope and Contributions

In this work, advanced numerical methods addressing the three major difficulties encountered in experimental investigations of fuel atomisation have been developed using a finite volume library OpenFOAM 2.4.0 as the platform for the development of new solvers. To deal with the multi-scale problem, an efficiently parallelised VOF-LPT coupling procedure is developed in Chapter 2. This procedure couples a high-resolution VOF-LES for the capturing of sharp liquid-gas interfaces in the region where major disintegration of the liquid jet occurs to an efficient LPT-LES for the description of secondary spray atomisation. A parallel-computing droplet identification and extraction procedure is implemented to transform insufficiently resolved liquid structures in the VOF simulation into spherical parcels that are then tracked in the LPT simulation. These simulations employ two grids that are partially overlapping. The overlapping region is placed to encompass the maximum extent of primary jet breakup and liquid core penetration. Two-way coupling of pressure and velocity fields between these simulations is performed by interpolating the corresponding field data at runtime between their grids in the overlapping region. Minimised computational intensity is achieved by only deploying the droplet identification and extraction procedure in the coupling region. Also, numerical dissipation as the result of interpolating field data between inconsistent grids is eliminated by employing identical grid topology and resolution in the coupling region for both simulations. In addition, a KH-RT secondary breakup model is integrated into the LPT simulation to allow modelling of secondary atomisation and sampling of secondary droplets statistics. The implementation of the region coupling VOF-LPT-LES method solves the multi-scale problem by enabling simultaneous high-fidelity simulation of primary and secondary fuel atomisation coupled with in-nozzle phenomena.

In addition to solving the multi-scale problem, an improved compressible multi-phase code is developed for the modelling of in-nozzle cavitation as described in Chapter 3. The improvements, as compared to two-phase VOF based cavitation approaches, include the added ability to simulate hydraulic flip induced air ingestion and improved mass conservation. The former is achieved with the addition of volume fraction transport equations for incondensable gases and the latter is accomplished by adding mass transfer source terms due to cavitation to the volume fraction transport equation of all phases. Investigation of in-nozzle cavitation and its effects on the subsequent spray evolution with a high temporal and spatial resolution is enabled by performing high quality LES resolving at least 80% of the turbulent kinetic energy in the flow. This forms the mathematical basis that allows the extension of the new compressible multi-phase cavitation code to account for cavitation and pressure related thermal effects, as described in Chapter 4. The extension of the code involves two major modifications. The first modification is associated with the implementation of a modified multi-phase mixture energy equation formulated based on specific sensible enthalpy. Enthalpy of phase change is added as an energy source term to allow for temperature variation due to cavitation. The second modification features the integration of realistic equations of state and pressure dependent fluid properties, which enables non-linear correlation between density, pressure and temperature for all phases. Therefore, the change of the liquid-gas mixtures thermal states due to cavitation and significant pressure variation at various scales can be analysed in a non-intrusive manner, which is extremely difficult with experimental measurements.

Finally, this thesis proposes novel techniques extending all developed codes to all Mach number flows with improved efficiency and reduced numerical dissipation, as described in Chapter 5. The process starts with the adaption of a low dissipative non-oscillating central upwind flux scheme to an all Mach number fractional step method for single-phase compressible flows. Validations considering single-phase compressible flows with a wide range of Mach numbers (0-3) are performed to demonstrate the feasibility and merits of such adaption by comparing it with a PISO based all Mach number solver. This provides directions for mathematical manipulations that incorporate the all Mach number fractional step method integrated with the KNP scheme into the compressible multi-phase cavitation code. The superiority of the all Mach number multi-phase code in resolving small scale turbulences and computing speed is demonstrated by comparing it with the PISO based multi-phase cavitation code developed in early stages of this research.

The development of advanced CFD methodologies for compressible multi-phase flows in this thesis could offer substantial benefits to numerical investigations of spray atomisation processes. High pressure fuel sprays can be simulated at conditions that match well with those of real injection processes with high fidelity. This servers a promising tool for engine designers and manufacturers to determine optimum operating conditions that contribute to maximum air-fuel mixing, leading to improved combustion efficiency and reduced pollution.

1.4 Thesis Structure

A summary of the thesis outline is provided in below section. These chapters are, to a large extent, self-contained and can be read independently.

Chapter 2: A parallel Volume of Fluid-Lagrangian Parcel Tracking coupling procedure for diesel spray modelling

This chapter describes a parallel VOF-LPT coupling procedure for the modelling of diesel spray atomisation from in-nozzle phenomena to primary and secondary atomisation. A parallel droplet identification and extraction procedure is developed to convert insufficiently resolved VOF liquid structures to Lagrangian Parcels. High fidelity and efficient field coupling between two simulations is achieved with the implementation of a region coupling method (RCM) that is executed at runtime.

Chapter 3: Development of a compressible multi-phase cavitation approach for diesel spray modelling

Chapter 3 extends the two-phase VOF based cavitation approaches to multi-phase flows by solving additional volume fraction transport equations for incondensable gas phases. Improved mass conservation in cavitation modelling is ensured by adding mass transfer source terms due to cavitation to the volume fraction transport equation of all phases.

Chapter 4: Modelling thermal effects in cavitating high-pressure diesel sprays using an improved compressible multi-phase approach

Chapter 4 incorporates non-linear Equations of State and pressure dependent fluid properties for all phases into the compressible multi-phase cavitation code described in chapter 3. Coupling of non-linear Equations of State and thermal-physical properties of the fluids is performed with the use of a modified multi-phase mixture energy equation formulated based on specific sensible enthalpy. Enthalpy of phase change is added as an energy source term to the energy equation, allowing for temperature variation due to cavitation.

Chapter 5: Adaption of fractional step method and central-upwind flux scheme for compressible multi-phase flows: Application to cavitating high-pressure diesel sprays

Chapter 5 proposes a novel technique that adapts a low dissipative non-oscillating central upwind flux scheme to an all Mach number fractional step method. This chapter also outlines detailed mathematical derivations that integrate the improved all Mach number fractional step algorithm into the multi-phase cavitation code.

Chapter 6: Closure

This final chapter summarizes all the findings of this thesis and points out several new directions for future research

Appendix

The appendix contains detailed derivation of the specific enthalpy based mixture energy equation.

2 A parallel Volume of Fluid-Lagrangian Parcel Tracking coupling procedure for diesel spray modelling

Abstract

A parallel computing Eulerian/Lagrangian multi-scale coupling procedure for diesel spray simulation is presented. Early breakup of the diesel jet is captured by using a compressible Volume of Fluid (VOF) method. In regions where the phase interface can no longer be sufficiently resolved, separated and small scale liquid structures are described by a Lagrangian Parcel Tracking (LPT) approach, in conjunction with secondary breakup modelling and a turbulence stochastic dispersion model. The coupling of these two descriptions utilises a Region Coupling Method and an efficiently parallelised droplet identification and extraction procedure. This approach enables run-time VOF-LPT field coupling and filters small-scale liquid structures that are suitable candidates for Eulerian-liquid-structure/Lagrangian droplet conversion, preserving their position, mass and momentum. The coupling procedure is initially applied to model the atomisation of a simple liquid jet and the results are compared with that of a statistical coupling approach to demonstrate the performance of the developed coupling procedure. Its application is then extended to simulate a real diesel spray from a nozzle with a sharp entrance. Coupling in-nozzle phenomena such as flow separation, flow detachment and turbulence to the primary and secondary spray atomisation, provides a tool for the prediction of complex spray dynamics.

Keywords: Eulerian (Volume of Fluid); Lagrangian (Lagrangian Parcel Tracking); Parallel coupling; Two-phase flows; Compressible flow; Diesel spray atomisation.

2.1 Introduction

Achieving an efficient combustion process in diesel engines requires optimally combined effects of air and fuel mixing, turbulence generation and interaction of spray and engine geometry. This involves improving the atomisation of the diesel spray by taking into account various operating conditions such as different nozzle designs, operating temperatures as well as the injection and chamber pressures. Many studies have focused on these aspects in an effort to realise more efficient combustion and reduced emissions [1].

In diesel engines, the fuel is injected at a high pressure into the combustion chamber where it follows a series of disintegration processes. Initially, the interaction between the fuel and nozzle geometry results in a flow regime dominated by separation, cavitation and aerodynamic instabilities causing primary jet break-up in the vicinity of the nozzle exit [1, 2]. In this process, the fragmentation of the intact liquid core generates large liquid structures that will undergo secondary breakup and further disintegrate into small droplets. At the next stage, the spacing between droplets increases further downstream of the nozzle due to air entrainment and turbulent droplet-gas interaction, and the droplet size decreases owing to secondary breakup and evaporation.

The primary and secondary breakup mechanisms have been extensively studied experimentally, see for example [3-7]. The use of different measuring techniques especially X-ray analysis of diesel sprays has provided comprehensive information on the liquid penetration, cross-sectional projected density distribution. The measurement of these parameters can help gain a qualitative understanding about the diesel spray evolution. However, the shot to shot variation of sprays makes it difficult to quantitatively capture the detailed features of the spray at different stages [4]. Therefore, to obtain information on the spatial and temporal spray evolution with high resolution, computational simulations are essential.

Due to the complex behaviour of the diesel spray in the primary and secondary atomisation processes, various computational approaches have been proposed and developed to simulate these. For primary atomisation, interface capturing/tracking methods such as the Volume of Fluid (VOF) method [8-14], Level Set Method (LSM) [15, 16] and the combination of both[17, 18] are widely adopted. In the VOF method, the liquid and gas are treated as two immiscible phases that are both described in the Eulerian framework. A transport equation calculating the volume fraction of each phase in a cell is employed and the derived gradient of the volume fraction of the dense phase is used to construct the liquid interface. This intrinsically allows the simulation of jet breakup, liquid core disintegration and droplet coalescence in a volume conservative manner. However, sufficiently discretising all small scale liquid structures can lead to exponential increase in mesh elements, leading to excessive demand in computational time for complex two-phase flow cases. In the secondary atomisation, due to the increasingly dominant effect of surface tension on small scales, small liquid structures start to become either spherical or elliptical, and they fall in the framework of LPT. However, in order for these small structures to be valid for Lagrangian modelling, they need to be smaller than the grid size. To ensure numerical stability, the maximum size of particles is recommended to be smaller than 20% of the local grid size for Lagrangian particle tracking [19, 20]. This is one of the main limitations of the Lagrangian

modelling that grid size could be larger than what might be desirable for good resolution of small scale flow features. A wide range of Lagrangian models have been developed specifically for the modelling of spray atomisation. Most of these are based on the Lagrangian description of individual droplets or parcels with an additional level of modelling for the primary and secondary atomisation [21-30]. The comparison of four different atomisation models, namely the Wave model [31], the Huh and Gosman atomisation model [32] and the MPI-1 and MPI-2 atomisation models is detailed in [33]. One of the drawbacks of these models is the lack of detailed attention to the effects of in nozzle flow phenomena (e.g. flow separation, cavitation and turbulence), resulting in the inaccurate prediction of primary spray breakup. However, they possess the advantage that it is rather efficient to simulate the evolution of a cluster of small-scale liquid structures without a high demand in computational time. This is enabled by the use of many well-developed secondary breakup models. Typically, the KH model by Reitz [23] as one of the earliest developed droplet breakup models predicts the development of aerodynamically induced disturbances on the liquid surface employing the Kelvin-Helmholtz (KH) mechanism. This mechanism relates the radii of parent and child parcels with the fastest growing wave length on the liquid surface and its corresponding growth rate. The RT model by Amsden *et al.* [34], on the other hand, describes Rayleigh-Taylor instabilities growing on a liquid-gas interface due to the density jump between gas and liquid. A parameter known as the break up time is introduced in this model, and it acts as a trigger to initiate the breakup process when the growing time of RT waves on the droplet surface is greater than the break up time. A hybrid model combining the KH and RT models is then developed to account for both the primary and secondary breakup of jets using a switching threshold Weber Number We = 12 [35].

In the light of the development of various primary and secondary atomisation modelling approaches, many attempts have been made to combine the merits of interface tracking/capturing and Lagrangian particle tracking. One of the first Interface-Tracking/Point Particle Tracking coupling procedures for jet breakup simulation is reported by Hermann *et al.* [36]. A dual grid method in which Eulerian (Level Set) and Lagrangian (point particle tracking) descriptions of liquid spray are handled respectively on two individual grids with two-way momentum coupling was first introduced in spray modelling. A similar approach however with adaptive mesh refinement capability is demonstrated by Tomar *et al.* [37] where the liquid interface is captured by using a local mesh refinement algorithm and small droplets are tracked as Lagrangian spherical particles in the region where the mesh is sufficiently coarse. Both approaches identify liquid structures having a volume smaller than a predefined threshold value from the Eulerian simulation and transfer them into individual particles eligible for particle tracking. These methods are often referred to as the Direct Coupling Approach (DCA) and provide unique ways to deal with mesh inconsistency problems encountered in simultaneous modelling of primary and secondary spray atomisation. One of the main drawbacks of DCA is the limitation that droplets generated from Eulerian simulation can only be expensively tracked as individual particles due to the absence of secondary breakup modelling. This is either because the exclusive use of velocity field information in the Eulerian-Lagrangian coupling disables the use of a secondary breakup model [36] or the computational power is insufficient for the integration of an adaptive mesh refinement method with secondary breakup modelling [37]. Consequently, applications of these approaches are limited to capturing only a small segment of the liquid jet breakup process (e.g. only 30 μs after start of injection

in Hermann *et al.* [36] and five days for one unit time in Tomar *et al*. [37]). On the other hand, the secondary breakup models, typically the KH-RT model, can group fluid particles of similar properties in a limited number of parcels. The use of the parcel concept can ease the computational strain by reducing the number of individual particles tracked in the Lagrangian modelling of the spray. Without the parcel assumption, the application of the DCA methods to detailed study of complex multi-phase flows is computationally restricted. Alternatively, the development and implementation of a Eulerian-Lagrangian Spray Atomisation (ELSA) model attributed to Burluka *et al*. [38] and Desportes *et al.* [39] effectively integrated the Lagrangian parcel tracking with a single-phase Eulerian model. However, this model treats liquid and gas as a single-phase mixture, hence the surface tension effect is not accounted for. The evaluation of mean size of the liquid ligaments is determined only by solving a transport equation for liquid/gas interface density. More recent developments in spray modelling give rise to many mathematical approximations that statistically couple the primary and secondary atomisation processes. A representative study conducted by Grosshans *et al.* [40] presents the use of a coupling layer located within the region where the transition from primary to secondary atomisation occurs. The volume, velocity and position of liquid structures are sampled on the coupling layer in the Eulerian framework till statistical convergence is achieved. Sampled data are then implemented as initial conditions with the parcel assumption for the subsequent modelling of secondary atomisation in a Lagrangian reference. In contrast, the probability density functions of the droplet size were extracted from the entire Eulerian domain by Befrui *et al.* [41] and the sampled size distribution data were used to reinitialise the spray simulation using the Lagrangian parcel tracking method. The statistical coupling procedures are advantageous in terms of efficiency and have relatively higher accuracy as compared to the pure Lagrangian description of the liquid spray. However, the stochastic way in which data are sampled and initialized for the second stage of spray modelling inevitably compromises the flow information supplied by the more accurate Eulerian modelling of the in-nozzle and near-nozzle flow. Also, their applications are limited to modelling static sprays due to the fact that the primary and secondary sprays are not directly coupled.

The objective of this study is therefore to advance the recent work on Eulerian/Lagrangian coupling [10, 36, 40, 41], using an open source finite volume tool OpenFOAM, by (1) development of a parallel processing procedure for the identification and extraction of droplets from VOF simulation and injecting them in the LPT framework, (2) development of a conservative transient region coupling procedure that allows runtime exchange of fluid information between VOF and LPT in the region where Eulerian-Lagrangian transition occurs, (3) integration of a sub-grid stochastic turbulent droplet dispersion model to improve the capability of an existing Lagrangian solver in OpenFoam and (4) allowing the modelling of the secondary breakup of large droplets extracted from the VOF simulation and the generation and tracking of child parcels in the LPT simulation. The developed code enables simulation for the complete evolution of the transient diesel spray from in-nozzle flow to atomised droplets.

2.2 Numerical Method

2.2.1 Region Coupling Method

One of the most challenging problems in diesel spray simulation is the different scales with which the continuous phase and the dispersed phase are modelled. Specifically, the primary breakup of the liquid jet requires a refined grid to capture the surface instabilities which generate large ligaments. These ligaments further interact with surrounding gases to produce smaller liquid structures (droplets) which are rather expensive to be discretised by an even finer grid. They fall in the Lagrangian reference that entails a coarse grid typically 5 times the size of droplets [19, 20]. This mesh inconsistency problem has been tackled either by a dual grid approach [10, 36] or a statistical coupling [40, 41] with the former being more accurate and the latter being more computationally efficient. The dual grid approach uses two entirely overlapping grids of different resolution, between which the exchange of momentum is performed with a conservative interpolation scheme [16]. However, due to the discrepancy in resolution between the two grids, the loss of background flow information is inevitable in the interpolation process. This problem is more severe in most statistical coupling approaches, which utilise statistically converged data sampled from the Eulerian simulation to initialise the Lagrangian simulation. The Region Coupling Method (RCM) described in this section overcomes the problems of both approaches.

The RCM employs two grids that are only partially overlapping. It enables regional coupling of an Eulerian liquid-Eulerian gas (VOF) regime with an Eulerian gas-Lagrangian droplets (LPT) regime. The coupling is performed by interpolating field information between the liquid-gas mixture in the VOF simulation and the carrier phase (gas) in the LPT simulation. After receiving field information from the VOF simulation, the two-way interaction of the carrier phase and droplets is handled in the LPT simulation. The effects of the droplet dynamics on the carrier phase is then reflected on the VOF simulation through the two-way field interpolation process. The overlapping region is where the transition from primary to secondary spray atomisation occurs and it couples the VOF and LPT simulations with two identical overlapping grids. *Figure 2-1* shows the position of this region in relation to the spray. The developing spray is divided into three stages, namely the primary breakup stage when an intact liquid core is present, the transition stage (dense region) at which the liquid core starts to disintegrate into large ligaments and finally the diluted phase in which small liquid structures form and are dispersed by the carrier phase. It should be mentioned that the right end of the coupling region should be placed far away from the maximum liquid penetration to avoid potential boundary effects and to prevent unconverted VOF droplets from escaping the domain.

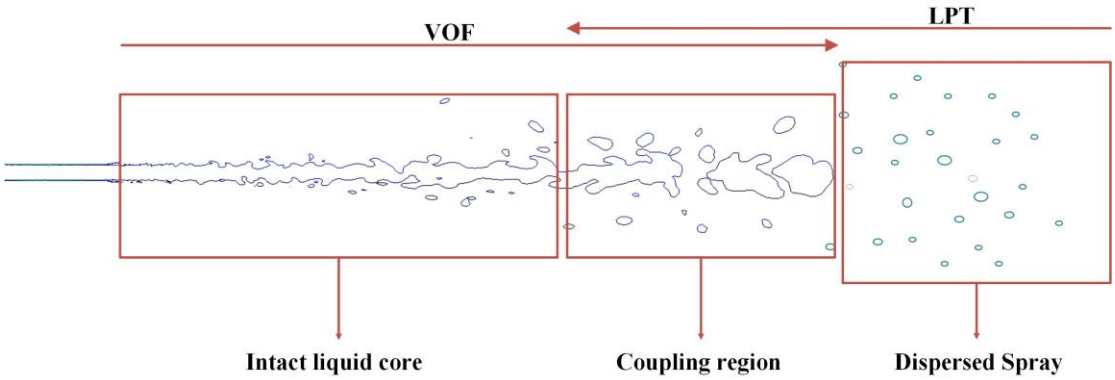

Figure 2-1: Region VOF-LPT coupling for a liquid diesel spray. The RCM is employed in the coupling region where VOF and LPT overlap.

One disadvantage of the RCM is that a decision has to be made as to where to place the overlap region, which requires that the Eulerian code needs to first be run till the liquid penetration reaches maximum within a predefined injection period. The maximum liquid penetration is defined at the furthest point (along the penetration) where a grid cell has a liquid volume fraction (α_l) greater than 0.05.

However, a relatively coarse mesh can be employed with the VOF method to estimate the maximum liquid penetration. Alternatively, the use of generic experimental data can also help determine the extent of a diesel spray by using the Musculus and Kattke model [42], for example. The present study utilises an incremental method where the VOF domain is gradually extended to accommodate the maximum liquid penetration. This is achieved through expanding the VOF computational domain incrementally along the penetration and reinitialising the simulation with the new domain by mapping the field data from the previous simulation. In this process, the time and location at which major breakup of the liquid core occurs are also determined. After the maximum liquid penetration has been estimated, the coupling region should be placed to encompass the entire dense (major breakup) region that encompasses most large ligaments. Also, the end of the VOF-LPT coupling region is placed far away from the maximum penetration to allow flow recirculation and avoid pressure reflection. The latter is achieved by employing a non-reflective boundary condition at the end of the VOF domain. The same grid generation strategy is also applied in the direction perpendicular to the penetration. This prevents all liquid structures from escaping the domain.

In the coupling region, it is computationally difficult to sufficiently describe all liquid structures of different scales using a refined grid with the VOF method. Therefore, the mesh resolution is progressively coarsened along the penetration of the liquid jet. The transition from a fine grid to a relatively coarse grid corresponds to the transition from VOF to LPT. The transition from VOF to LPT results in the decrease in the number of mesh elements that can be used to capture the interface of a liquid structure. At some points, the interface of the generated liquid structures can no longer be sufficiently resolved by the VOF method. These liquid structures are identified and converted to Lagrangian droplets if their volumes are sufficiently smaller than the local cells in which their centroids lie. Therefore, a Droplet Identification Procedure (DIP) and a Droplet Extraction Procedure (DEP) comparing the volume of a liquid structure with the volume of a local cell containing this structure's centroid are developed. The code

automatically adapts to the grid and frees users from defining a fixed threshold volume. It allows a greater variety of droplet diameters with a non-uniform grid than a uniform one. However, a threshold percentage determining the amount by which a liquid structure is smaller than its host cell needs to be defined. In this study, a liquid structure is recognised as a suitable Lagrangian droplet candidate if it has a volume smaller than 20% of the host cell's volume in the coupling region, as suggested in Arlov *et al.* [19].

The droplet conversion procedure enables the use of identical grids for both the VOF and LPT simulations in the coupling region. It solves the mesh inconsistency problem and allows high fidelity field coupling between VOF and LPT as the field mapping can be performed between two identical grids. Since interpolating field information between two identical grids produces negligible dissipation especially in mapping sub-scale kinetic energy, this method is independent of the turbulence model used. On the other hand, Large Eddy Simulation is chosen as the closure model for the governing equations in the present study. It is a less computationally intensive alternative to Direct Numerical Simulation and offers better ability to reflect the effects of local turbulence on the evolution of the bulk flow than the Reynolds averaged governing equations. However, it is only used to demonstrate the ability of the coupling procedure to model a transient diesel spray. The grid resolution is not necessarily fine enough for high resolution LES throughout the entire computational domain.

To reduce the computational intensity, the DIP and DEP as well as the two-way field mapping between VOF and LPT are deployed only in the coupling region. The two-way field mapping uses a volume conservative coupling algorithm taken from the parallel map-Fields utility of OpenFOAM [43], known as cellVolumeWeight. It is a volume averaging algorithm that allows cell to cell conservative mapping of vector and scalar fields between two grids.

2.2.2 VOF

The VOF employed in the present study is based on a mathematical model composed of governing equations for the conservation of mass and momentum of a two-phase system, accredited to E. De Villiers *et al.* [44]. This system comprises two immiscible, compressible fluids and accounts for the surface tension between the two-phases. The single set of mass and momentum transport equations are:

$$\frac{\partial \rho}{\partial t} + \nabla \cdot \left(\rho U \right) = 0 \tag{2-1}$$

$$\frac{\partial \rho U}{\partial t} + \nabla \cdot \left(\rho U \bullet U \right) = -\nabla p + \nabla \cdot \tau + \int_{S(t)} \sigma \kappa n \cdot \delta \left(x - x^{'} \right) ds \tag{2-2}$$

where U is the velocity and ρ is the mixture density. The mixture density is closely related to the local volume fraction α of each phase with $\alpha = 1$ representing a computational cell fully filled with liquid, while $\alpha = 0$ indicates a cell entirely occupied by gas. Any cell having $0 < \alpha < 1$ contains an interface segregating liquid and gas. For liquid-gas calculations, the mixture density in each computational unit is obtained from:

$$\rho = \alpha_l \rho_l + \left(1 - \alpha_l \right) \rho_g \tag{2-3}$$

where α_l is the volume fraction of liquid phase, ρ_l and ρ_g are the respective liquid and gas densities.

The integral term in Eqn (2-2) is a Dirac function that only produces a non-zero value when $x = x^{'}$ which is an indication of the existence of a liquid interface. This source term accounts for the effect of surface tension force on the liquid jet breakup process. The evaluation of this term is achieved following E. De Villiers *et al.* [44] through the continuum surface force model of Brackbill *et al.* [45] as:

$$\int_{S(t)} \sigma n\kappa \cdot \delta\left(x - x^{'}\right) ds \approx \sigma\kappa\nabla\alpha \tag{2-4}$$

where σ is the surface tension coefficient, α is the volume fraction of the liquid phase which is obtained from the solution of a transport equation:

$$\frac{\partial \rho\alpha}{\partial t} + \nabla \cdot \left(\rho U \alpha\right) = 0 \tag{2-5}$$

and n is a unit vector normal to the liquid surface, κ is the interface curvature calculated from the solution of liquid phase volume fraction α:

$$\kappa = \nabla \cdot \left(\frac{\nabla\alpha}{|\nabla\alpha|}\right) \tag{2-6}$$

The system of equations is closed by an equation of state:

$$\begin{cases} \rho_l = \rho_0 + p\psi_l \\ \rho_g = p\psi_g \end{cases} \tag{2-7}$$

with ψ_l and ψ_l being the compressibility for liquid and gas phases respectively. The dynamic viscosity of the mixture is obtained through:

$$\mu = \alpha_l \mu_l + \left(1 - \alpha_l\right)\mu_g \tag{2-8}$$

The VOF interface tracking method is a simple and flexible approach for the prediction of two-phase flows. A major limitation of this method is its limited ability to ensure boundedness of liquid volume fraction and preserve sharp interfaces without an interface reconstruction algorithm such as Piecewise Linear Interface Construction (PLIC) [46]. In the context of OpenFOAM, this problem is tackled with a 'Multi-Dimensional Universal Limiter with Explicit Solution" (MULES) accredited to Henry Weller together with the CICSAM interface compression scheme [47]. However, the numerical instabilities due to unboundedness of liquid volume fraction are not fully eliminated. Alternatively, high resolution prediction of flow with a free liquid surface can be achieved by local (Adaptive Mesh Refinement [37]) or global grid refinement [48]. The present study adopts a globally refined grid for the VOF simulation. Another limitation of the current compressible VOF method is that the generated gas at low pressure sites is given the properties of air due to the lack of a phase change model. The generation of gas is primarily due to the flow separation downstream of the sharp nozzle inlet. The flow separation causes detachment of liquid from the wall and gas has to be introduced to satisfy the unity volume fraction ($\alpha_l + \alpha_g = 1$) under a two phase flow regime. This gas does not condense back to liquid fuel when the local pressure recovers above the vapour pressure. The incondensable gas then accumulates along the wall, causing complete detachment of liquid from the nozzle wall (hydraulic flip).

The LES model is integrated in equations (2-1), (2-2) and (2-4) through a local volume averaging procedure that decomposes relevant phase-weighted hydrodynamic variables into resolvable and sub-grid scale components. The elimination of the sub-grid fluctuations from direct simulation is done through a filtering process together with the

non-linear convective terms in equation (2-2). This process generates additional terms comprising correlation of sub-scale variables that entail closure through additional modelling. Of these terms, the most crucial one is the Sub-Grid-Scale (SGS) stress that governs the effect of unresolved turbulence scales on momentum transport process and its dissipation. This term is defined as:

$$\tau_{sgs} = \overline{U \cdot U} - \overline{U} \cdot \overline{U} \tag{2-9}$$

The closure of the SGS stress is achieved through a sub-grid eddy viscosity model given as:

$$\tau_{sgs} + \frac{\mu_{sgs}}{\rho}\left(\nabla \overline{U} + \nabla \overline{U}^{T}\right) = \frac{2}{3} kI \tag{2-10}$$

in which k is the SGS turbulence kinetic energy and μ_{sgs} is the SGS turbulent viscosity. These SGS turbulence parameters are calculated by using a one-Equation eddy model for evaluating k attributed to Yoshizawa [49].

$$\frac{\partial k}{\partial t} + \nabla \cdot \left(k\overline{U}\right) - \nabla \cdot \left[\left(\upsilon + \upsilon_{sgs}\right)\nabla k\right] = -\frac{1}{2}\tau_{sgs} : \left(\nabla \overline{U} + \nabla \overline{U}^{T}\right) - \varepsilon \tag{2-11}$$

where $\varepsilon = C_{\varepsilon} k^{(3/2)} / \Delta$ is the turbulent dissipation, $\upsilon_{sgs} = C_k k^{(1/2)} \Delta$ is the SGS kinematic viscosity ($\Delta = \sqrt[3]{V}$ represents the SGS length scale in which V represents the volume of the computational cell under consideration). The turbulent coefficients found from statistical analyses are $C_k = 0.07$ and $C_{\varepsilon} = 1.05$ [49]. As the emphasis of this study is placed mainly on obtaining reasonable resolution of spray simulation and the current implementation of LES is sufficient for this purpose, other SGS terms pertaining to density, mass transfer, phase fraction and surface tension are neglected.

2.2.3 LPT

The LPT method is derived based on the consideration of momentum exchange between the gas phase and the dispersed liquid phase, which is primarily described in the work of Jangi *et al.* [26]. This is achieved through the inclusion of additional source terms for the exchange rate of mass ($S_{\rho}^{s} = S_{Z}^{s}$), momentum (S_{U}^{s}) and heat (S_{h}^{s}) between the two phases in the gas phase governing equations, while the dynamics of the liquid phase are handled by Newton's second law. The evaporation of fuel is not considered in the present study as the spray is modelled at room temperature, therefore S_{ρ}^{s} and S_{Z}^{s} are assumed to be zero. The Favre-filtered LES conservation equations for the gas phase can be expressed as:

$$\frac{\partial \overline{\rho}}{\partial t} + \nabla \cdot \left(\rho U\right) = \overline{S_{\rho}^{s}} = 0 \tag{2-12}$$

$$\frac{\partial \overline{\rho} U}{\partial t} + \nabla \cdot \left[\overline{\rho} U U - \overline{\tau} + \tau_{sgs}\right] = \overline{S_{U}^{s}} \tag{2-13}$$

$$\frac{\partial \overline{\rho} h}{\partial t} + \nabla \cdot \left(\overline{\rho} U h\right) - \nabla \cdot \left[\overline{\lambda} \nabla \cdot T + h_{sgs}\right] = \overline{S_{h}^{s}} \tag{2-14}$$

$$\frac{\partial \overline{\rho} Z}{\partial t} + \nabla \cdot \left(\overline{\rho} U Z\right) - \nabla \cdot \left[\overline{\rho D} \nabla \cdot Z + \Phi^{Z}{}_{sgs}\right] = \overline{S_{Z}^{s}} = 0 \tag{2-15}$$

The over-line signifies the general filtering:

$$\overline{\phi(x,t)} = \int G(r,x)\phi(x-r,t)dr \tag{2-16}$$

where the integration is applied to the entire field with the filtering function satisfying the normalization condition:

$$\int G(r,x)dr = 1 \tag{2-17}$$

The tilde represents the Favre filtering:

$$\overline{\rho\phi} = \overline{\rho}\cdot\phi \tag{2-18}$$

in which ϕ is a dependant fluid field variable.

Apart from general fluid parameters, enthalpy h , thermal diffusion coefficient λ , mass diffusion coefficient D , mixture fraction Z and SGS species mass fluxes $\Phi^{Z}{}_{sgs}$ can be introduced to account for energy exchange and to ensure conservation. While the one-equation eddy model can be utilised to estimate the SGS stress term τ_{sgs} , the additional terms h_{sgs} and $\Phi^{Z}{}_{sgs}$ entail closure in order to close equations (2-14)-(2-15). They are modelled using a gradient diffusion-closure:

$$h_{sgs} = -\overline{\rho C_p}\frac{\upsilon_{sgs}}{\mathrm{Pr}^{sgs}}\nabla\cdot T \tag{2-19}$$

$$\Phi^{Z}{}_{sgs} = -\rho\frac{\upsilon^{sgs}}{Sc^{sgs}}\nabla\cdot Z \tag{2-20}$$

In Lagrangian spray simulation, the spray is considered as a discrete phase comprising a large quantity of parcels that are transported using Newtown's second law. The LPT method then provides closure for the source terms $\overline{S_U^s}$ in equation (2-13). The dynamics equations of the dispersed liquid phase are expressed as:

$$\frac{d}{dt}X_P = U_P \tag{2-21}$$

$$\frac{d}{dt}U_P = \frac{C_D}{\tau_P}\frac{\mathrm{Re}_P}{24}\left(U_g - U_P\right) = \frac{C_D}{\tau_P}\frac{\mathrm{Re}_P}{24}U_{rel} \tag{2-22}$$

and the drag coefficient is estimated as:

$$\begin{cases} C_D = \dfrac{24}{\mathrm{Re}_P}\left(1+\dfrac{1}{6}\mathrm{Re}_P^{2/3}\right) & \mathrm{Re}_P < 1000 \\ C_D = 0.424 & \mathrm{Re}_P \geq 1000 \end{cases} \tag{2-23}$$

Here X_P is the parcel position vector and U_P is the parcel velocity vector. The relative velocity U_{rel} between the parcel and the surrounding gases is denoted as $U_g - U_P$. For simplicity, the interaction between liquid and gas phases is accounted for by considering only the gravity and drag forces experienced by each parcel. The calculation of this force is given in equations (2-23) where the parcel Reynolds number is expressed as $\mathrm{Re}_P = \rho_g\left|U_{rel}\right|d_P/\mu_g$ with ρ_g being the density of gas phase, d_P being the parcel diameter and μ_g being the gas phase dynamic viscosity. $\tau_P = \rho_P {d_P}^2/18\mu_g$ is the time taken for a parcel to respond to local disturbances, also known as the parcel characteristic time. The instantaneous local velocity difference U_{rel} cannot be directly evaluated and requires closure. The current study employs

O'Rourke's stochastic turbulence dispersion (STD) model [50] to estimate U_{rel} which, in LES formulation, can be written as:

$$U_{rel} = U + U_P^{'} - U_p \tag{2-24}$$

where U can be obtained by solving equation (2-13) and $U_P^{'}$ is the stochastic velocity vector accounting for the localised dispersion of parcels through the interaction with gases. $U_P^{'}$ is assumed to satisfy a Gaussian distribution with the variance $\sigma = \sqrt{2k_{sgs}/3}$ and the mean of zero. In this way, the Gaussian distribution $G(U_{P,i}^{'}) = 1/\sigma\sqrt{2\pi}\exp\left(-U_{P,i}^{'}/2\sigma\right)^2$ randomly assigns values to each component of $U_P^{'}$ at every integration step of the gas (Eulerian) phase. In each computational cell, the momentum source term in equation (14) can be then obtained from:

$$\overline{S_U^s} = \frac{1}{V_{cell}}\sum\frac{d}{dt}\left(m_p U_{P,i}\right) \tag{2-25}$$

in which m_p is the mass of parcels under consideration and the summation is over all parcels existing in a computational cell having a volume of V_{cell}.

2.2.4 Secondary breakup model

According to Solsjö *et al.* [51], it is reasonable to assume that Kelvin-Helmholtz (KH) and Rayleigh-Taylor (RT) instabilities can occur simultaneously in the secondary breakup regime due to the high injection velocity. The KH-RT breakup model is therefore utilised to predict the atomisation process of secondary droplets in the LPT-LES simulation. In the present study, the KH-RT model allows the generation of parcels from the breakup of the large Lagrangian droplets (parent droplets) converted from the VOF liquid structures. Specifically, the diameters of the generated parcels (which are also referred to as child parcels) are determined by the KH-RT model after the breakup of the parent droplets. The number of fluid particles a child parcel contains is then determined by ensuring mass conservation before and after the secondary breakup of a parent droplet. Further details of the implementation of the KH-RT breakup model as well as the model constants ($B_0 = 0.61, B_1 = 10, C_{RT} = 0.1, C_\tau = 1$) used in this study can be found in Kitaguchi *et al*. [52].

2.2.5 Collison model

The collision of parcels is handled by a Stochastic Trajectory Collision (STC) model [53]. Unlike the O'Rourke collision model [54] which initiates collision of two parcels when they occupy the same computational cell and their estimated probability of collision is higher than a threshold value, the STC model takes the trajectory of each participant into account. This model considers the onset of collision between two parcels when their trajectories intersect, and the intersection point is reached at the same time within one Eulerian integration step.

2.2.6 Droplet Identification Procedure (DIP)

In this section, the development of a parallel droplet identification procedure is described. This procedure is designed to identify liquid structures that are smaller than

20% of their host cell's volume. In addition, it is determined that these liquid structures should be discretised by less than 5 mesh cells in order to minimise the effect of droplet eccentricity. Specifically, in the case that a small liquid structure satisfies the maximum volume criterion for VOF-LPT conversion and is spread over 5 or more mesh elements, it can have rather high eccentricity as depicted in *Figure 2-2*. Extracting such a liquid ligament and representing it with a spherical droplet in the LPT simulation can be a significant source of error especially for sub-grid physics. Therefore, only liquid structures that satisfy the minimum volume requirement and are discretised by less than 5 elements are considered eligible candidates for VOF-LPT conversion. Further, only identifying and extracting liquid structures occupying less than 5 mesh elements is computationally advantageous that such a process is not implemented on all large scale liquid structures which are dominant in the VOF simulation.

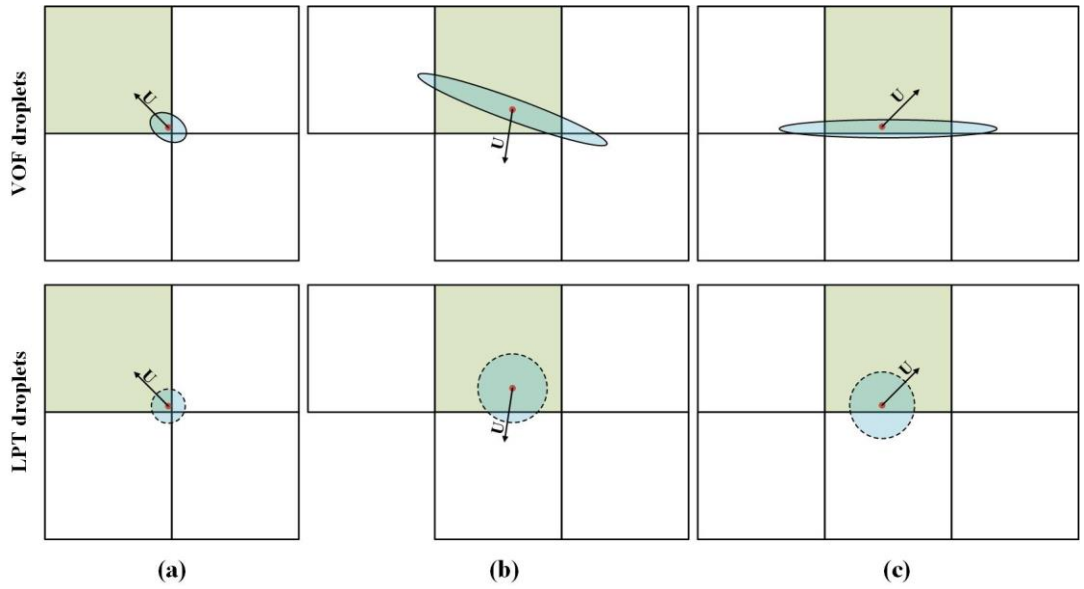

Figure 2-2: Three moving liquid structures having a velocity vector U and a volume smaller than 20% of their host cell (shaded in green) are captured by 4 mesh cells (a), 5 mesh cells (b) and 6 mesh cells (c) in the VOF domain. After a volume conservative conversion to LPT droplets, they are represented with spherical droplets at the same location in the LPT domain.

In the context of OpenFOAM, field values such as velocity, pressure, temperature and liquid volume fraction (α_l) are stored at the centre of the controlled volumes (mesh cells). The interpolation of the cell-centred values to the face centres based on the face flux (advection) and values in neighbouring cells is fundamental to the finite volume method. The interpolation methods and schemes are detailed in Rusche [55]. In the present study, the identification process involves grouping adjacent liquid-containing cells ($\alpha_l \geq 0.05$) sharing one cell face which has a liquid volume fraction $\alpha_l \geq 0.05$ to form contiguous liquid structures. The reason for the selection of $\alpha_l = 0.05$ is to minimise the numerical instabilities introduced by the unboundedness of liquid volume fraction in each computational cell. The unboundedness of liquid volume fraction means that a cell with $\alpha_l \approx 0$ could have a α_l fluctuating between 0 and 10^{-6} depending on the solver's precision. For mesh cells with relative poor orthogonal quality, the range of fluctuation can become larger (10^{-3}) depending on the temporal resolution and number of corrections in the MULES loop. The use of a smaller liquid volume threshold

can result in the generation of a large number of physically unrealistic small droplets mainly due to oscillation of liquid volume fraction. This does not ensure mass conservation in the VOF-LPT conversion process. On the other hand, using a larger threshold can lead to the negligence of a considerable amount of small liquid structures that have a volume fraction slightly higher than 0.05. Allowing these droplets to be continuously modelled by the VOF method constitutes a significant source of error for the modelling of sub-grid physics in the VOF simulation. Moreover, the identification method is slower with the use of a smaller threshold liquid volume fraction. Typically, using $\alpha_l = 0$ can result in the increase in computational time by an order of magnitude compared to that of $\alpha_l \geq 0.05$.

In the developed procedure, the identified contiguous structures' velocities (U_P), centroids (x_P) and equivalent spherical diameters (R_p) are evaluated as:

$$V_p = \sum_N \alpha_l V_{cell} \tag{2-26}$$

$$R_p = \frac{1}{2}\left(\frac{6V_P}{\pi}\right)^{\frac{1}{3}} \tag{2-27}$$

$$X_P = \frac{1}{V_P}\sum_N X_{cell}\alpha_l V_{cell} \tag{2-28}$$

$$U_P = \frac{1}{V_P}\sum_N U_l \alpha_l V_{cell} \tag{2-29}$$

Hereafter *N* is the total number of adjacent computational cells with a liquid volume fraction greater than 0.05. The summation is over all identified mesh cells that belong to a complete liquid structure. The identification process is shown in *Figure 2-3(a)*. To ensure the uniqueness of every liquid structure across the entire domain, the next step is to update the IDs of all liquid structures according to the rank of their host processor, as depicted in *Figure 2-3(b)*.

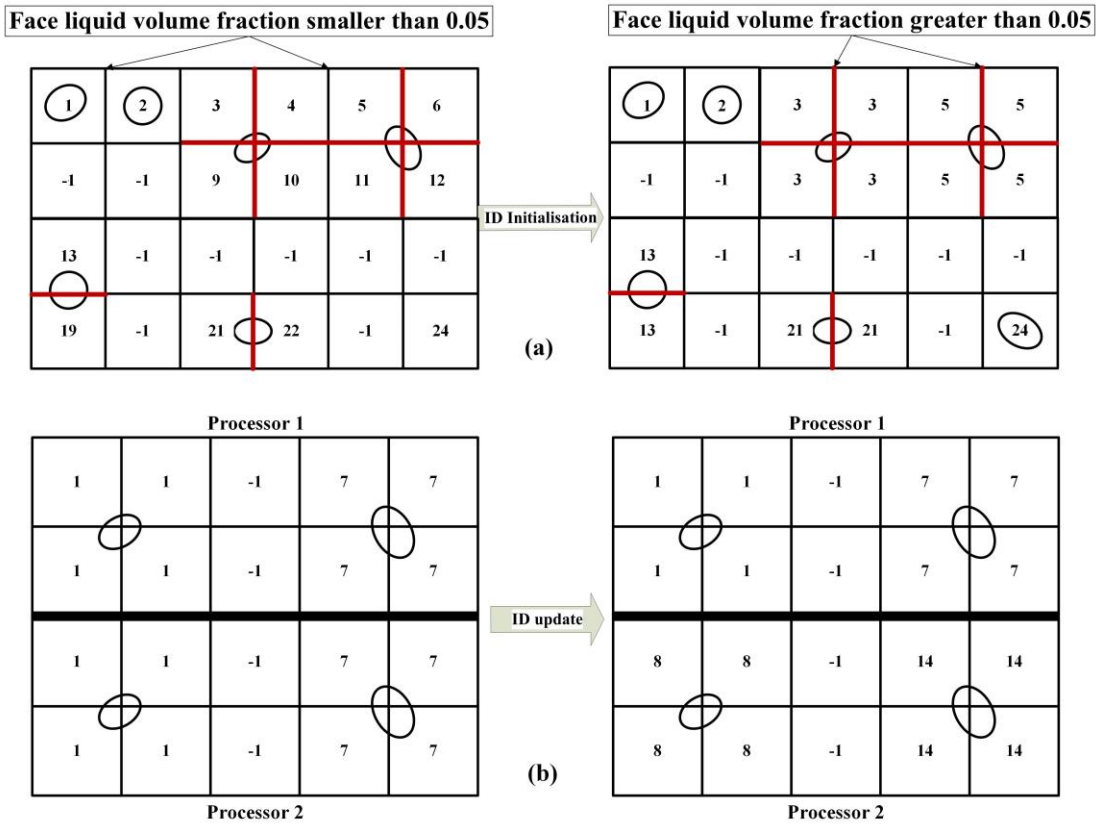

Figure 2-3: (a) ID initialisation of liquid structures. Adjacent liquid-containing cells sharing a cell face with $\alpha_l \geq 0.05$ (marked in red) are combined to form contiguous liquid structures. The ID of a combined liquid structure is changed to be the same as the associated cell bearing the smallest ID. An individual cell containing liquid but not having a liquid containing neighbour is also identified as an individual liquid structure. Cells of zero liquid volume fraction are tagged with -1. (b) Updating of the liquid structure IDs across the computational domain. Each processor adds the maximum ID received from its higher ranked neighbour to its local liquid structures to ensure the uniqueness of every liquid structure in the domain.

2.2.7 Droplet Extraction Procedure (DEP)

In parallel computing mode, another important point that should be considered is the preservation of liquid structures that are on or approaching processor patches. This is because when a liquid structure moves from one processor domain to another, it is possible for it to be broken into droplets that are then erroneously extracted from the domain by the DEP. This procedure identifies liquid structures smaller than a pre-defined volume threshold, extracts and converts them to spherical droplets (by assigning $\alpha_l = 0$ to corresponding cells in the VOF domain) that are injected into the Lagrangian domain. This situation is illustrated in *Figure 2-4*.

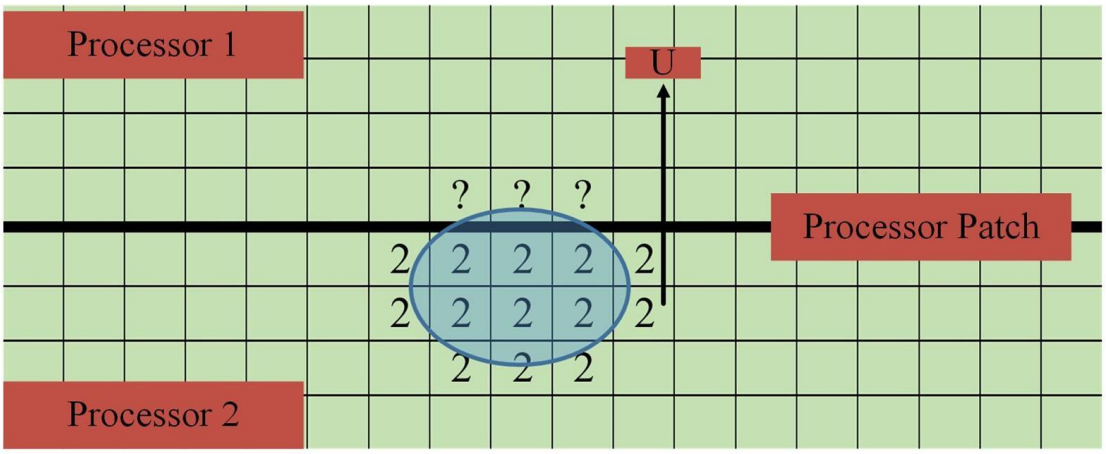

Figure 2-4: A liquid structure (ID=2) which is crossing the processor patch with a velocity vector U. The portion that could be erroneously extracted is tagged with question marks.

When a liquid structure crosses the processor patch, one cell in processor 1 will experience an increase in liquid volume fraction. Initially, as the liquid content might be too small to occupy this cell and there are no neighbours with $\alpha_l > 0.05$, the liquid contained would be recognised by the DEP as a suitable candidate for liquid structure-droplet conversion if a threshold of one cell volume was defined. Consequently, the entire liquid structure shown in *Figure 2-4* would be non-physically extracted and transferred into same size Lagrangian droplets. These droplets could have a volume smaller than or equal to the volume of the first host cell in processor 1, and the size of computational time step largely governs the rate at which volume fraction increases in this cell. The degree of this problem is increasingly noticeable when high temporal resolution is required, especially when running LES.

A protection procedure is thus developed and implemented to tackle this problem. It simply stores IDs of all cells that are on processor patches in a Hash-table as different keys. These "keys" are triggered to locally deactivate the DEP when a liquid structure is detected to infect processor patch cells. The DEP therefore only applies to extract small liquid structures that are not on or in close proximity to process patches. One disadvantage of such method is that it is dependent on the number and location of processor patches. Liquid structures suitable for VOF-LPT conversion which are in the vicinity of processor patches are not extracted such that this can be a source of error for the subsequent LPT simulation. However, contribution of this error can be negligible due to the small number of processor patch cells as compared to cells in the decomposed domain especially for high level parallel applications. Finally, properties of all the extracted liquid structures are sent to the master processor by its slaves and are stored in three Hash-tables (*Table 2-1*) designated to record liquid structures' (pre-LPT droplets) IDs and their corresponding x_P, U_P and R_p.

Table 2-1: Hash-tables storing properties of pre-LPT droplets.

Hash-table 1		*Hash-table 2*		*Hash-table 3*	
Droplet ID	R_p	*Droplet ID*	X_P	*Droplet ID*	U_p
1	R_1	*1*	(x_1, y_1, z_1)	*1*	(u_1, v_1, w_1)
2	R_2	*2*	(x_2, y_2, z_2)	*2*	(u_2, v_2, w_2)
3	R_3	*3*	(x_3, y_3, z_3)	*3*	(u_3, v_3, w_3)
….	….	….	….	….	….

The implementation of the identification and extraction procedure has a limited influence on the parallel efficiency of the original VOF code in OpenFOAM, simply because it does not increase the communications between processors as the assembly of liquid structures is strictly restricted within each processor domain. The use of the protection procedure eliminates the need to assemble liquid structures across processors, which would be computationally expensive. The complete droplet identification process is schematically shown in *Figure 2-5*.

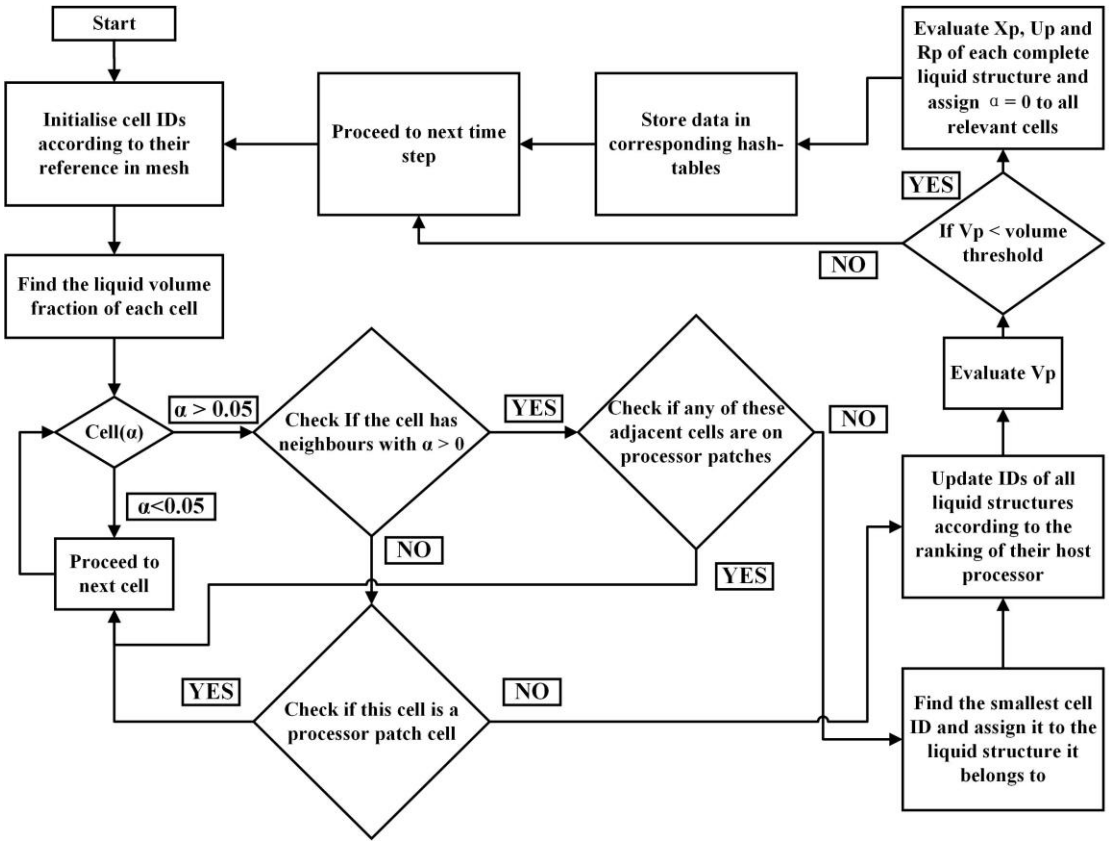

Figure 2-5: Flow process for parallel droplet identification algorithm.

In the present study, the LPT droplets are not converted back to VOF liquid structures when the mesh is sufficiently fine for VOF simulation. This decision is made based on considering the complexity and accuracy of the reversed VOF-LPT transition.

Specifically, it is difficult to determine which and how many cells to which liquid volume fraction would be assigned to represent one Lagrangian droplet. Also, converting Lagrangian droplets into VOF ligaments without taking into account how the liquid interface of the ligaments is distributed across various VOF cells could be a large source of error especially for the modelling of sub-grid physics. Implementing algorithms to accurately describe the LPT-VOF transition would require development of a new sub-grid Eulerian model which is beyond the scope of this study. In addition, executing such a complex algorithm in transient LES simulations could be impractical because only marginally higher accuracy would be gained at the expense of greatly increased computing time.

Before the publication of this work, the capabilities of the developed parallel droplet identification and extraction procedures have been demonstrated in Ghiji *et al.*'s work [56, 57] (up to 512 CPUs) to be able to quantify the effects of grid resolution on the number of secondary droplets generated due to the breakup of liquid jet.

2.2.8 Droplet injector

The next step in VOF-LPT coupling is the injection of droplets transferred by the DEP to the Lagrangian domain. The injection process must satisfy conservation laws in order to preserve the accuracy of coupling. This involves developing a utility able to read information from the three Hash-tables and transform them into Lagrangian droplets, preserving their mass, momentum and positions. A new automatic injector with such capabilities is developed as part of the coupling method. This injector scans every entry in the three Hash-tables at run-time and acquires the volume, position and velocity of the droplets to be injected. The process diagram shown in *Figure 2-6* schematically depicts how this injector works.

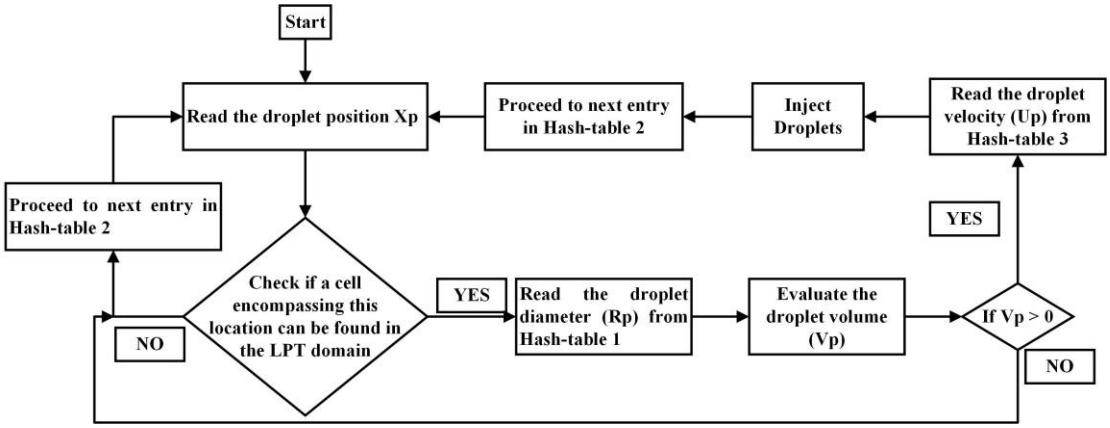

Figure 2-6: Process flow for the droplets injection. The customised droplet injector reads information from the Hash-tables and converts it into droplets that are injected into the LPT simulation.

Based on the recent work of Ghiji *et al*. [57], the governing equations are solved by OpenFOAM using a Pressure Implicit with Splitting of Operator (PISO) algorithm. In each Eulerian time-step, the intermediate velocity field (U^*) in the VOF simulation is first evaluated using a semi-discretised momentum equation which consists of a predicted velocity field, an explicit pressure correction term and a surface tension source term [58]:

$$U^* = \frac{H(U^{n-1})}{a} - \frac{1}{a}\nabla p^{n-1} + S_{surface} \tag{2-30}$$

where U^{n-1} and p^{n-1} are velocity and pressure fields mapped from the LPT solution obtained from the previous Eulerian time-step.

Divergence of the predicted velocity field is then substituted into the two-phase pressure equation of which the detailed derivation can be found in our previous work [59]:

$$\begin{cases} \dfrac{\alpha_l}{\rho_l}\left[\psi_l \dfrac{\partial p^{n-1}}{\partial t} + U^{n-1}\cdot\nabla\left(\rho_l\right)\right] + \dfrac{1-\alpha_l}{\rho_g}\left[\psi_g \dfrac{\partial p^{n-1}}{\partial t} + U^{n-1}\cdot\nabla\left(\rho_g\right)\right] \\ + \\ \nabla\cdot\left(U^*\right) \\ = 0 \end{cases} \tag{2-31}$$

Equation (2-30) is then recalculated to update the velocity field using the solution of equation (2-31). The evaluated pressure (p^n) and velocity (U^{n-1}) fields are then mapped to the LPT simulation to initiate a similar pressure-velocity coupling procedure (comprising the particle force source term $S_{particle}$) within the same Eulerian time-step:

$$U^* = \frac{H(U^n)}{a} - \frac{1}{a}\nabla p^n + S_{particle} \tag{2-32}$$

$$\frac{1}{\rho_g}\left[\psi \frac{\partial p^n}{\partial t} + U^n\cdot\nabla\left(\rho_g\right)\right] + \nabla\cdot\left(U^*\right) = 0 \tag{2-33}$$

Finally, the calculated pressure (p^{n+1}) and velocity (U^{n+1}) fields are mapped to the VOF simulation to initiate the next Eulerian time-step.

To solve the pressure-velocity coupling equations, a bounded Normalised Variable (NV) Gamma differencing scheme [60] with a blending factor of 0.2 is used for the convection terms and an interface compression scheme (CICSAM) [47] for high resolution interface capturing. A conservative, second order scheme (Gauss linear corrected) is employed for Laplacian derivatives and a second order backward discretisation scheme is adopted for temporal terms.

2.3 Test Case

A comparison of the RCM and a statistical coupling approach (SCA) is presented in this section. The test case, as outlined in the work of Grosshans *et al*.[40], concerns the atomisation of a simple diesel spray injected from a nozzle which has a diameter (d) of 100 µm. The liquid jet has an initial injection velocity of 500 m/s following a top hat profile at the nozzle exit, which corresponds to a Reynolds number of 15000 and a jet Weber number of 1.2×10^6. The ambient is filled with air of which the density is 14.8 kg/m3. The ambient pressure is 52 bar and the liquid and gas have a density ratio of 10 and a viscosity ratio of 46.

2.3.1 Comparison of VOF simulation

Similar to Grosshans *et al*.'s statistical coupling approach, a VOF simulation is first run to determine the position of the coupling region. In this case, the coupling region is placed where the averaged liquid volume fraction along the centre line of the jet is lower than 0.25 indicating the onset of major jet breakup. The liquid volume fraction is averaged at every time-step using OpenFOAM's runtime field-Averaging utility and the averaging time relates to the jet crossing the domain 15 times. A Cartesian equidistant grid duplicating the highest resolution case (cell size = 0.05d) considered in Grosshans *et al*.' work [40] is generated and employed for the VOF simulation..

Figure 2-7 shows that the averaged liquid volume fraction becomes lower than 0.25 at z=24d in the RCM-VOF simulation and at z=26d in the Grosshans-VOF simulation [40]. Although two cases depict similar trend along the penetration axis, the RCM-VOF method predicts a higher jet disintegration intensity after 5d from the tube exit since the averaged liquid volume fraction is slightly lower than Grosshans-VOF's prediction. The deviation between two simulations can be attributed to the different numerical approaches employed (RCM-VOF: Finite Volume Method, Grosshans-VOF: Finite Difference Method). Specifically, the FVM based VOF is able to capture shear layer instabilities most probably generated due to either the Kelvin-Helmholtz mechanism [61] (*Figure 2-8*) or 2D Tollmien-Schlichting instability [62] while the FDM based VOF only predicts a smooth exiting jet within several diameters downstream of the tube exit (readers can refer to Figure 15 in ref. [40]). Other factors include the use of different numerical and time integration schemes between the RCM-VOF simulation and the Grosshans-VOF simulation.

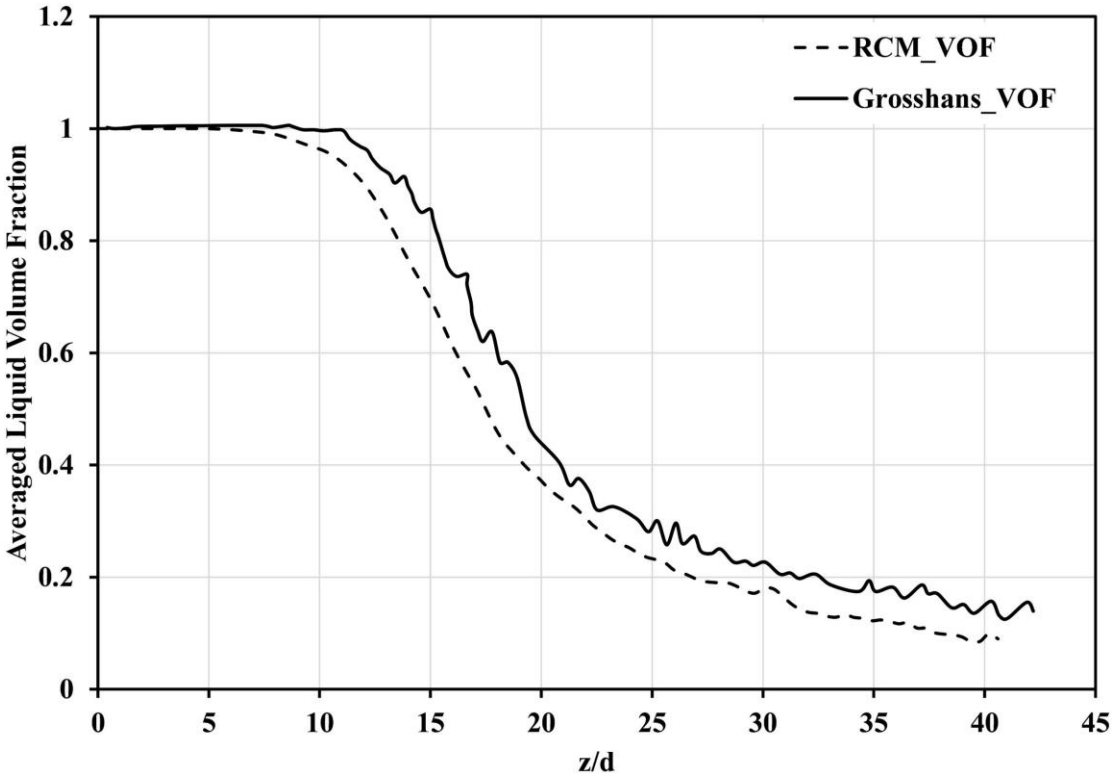

Figure 2-7: Plotted average liquid volume fraction along the jet centre line for the RCM-VOF simulation and the Grosshans-VOF simulation [40]. The distance from nozzle exit is non-dimensionalised by nozzle diameter d.

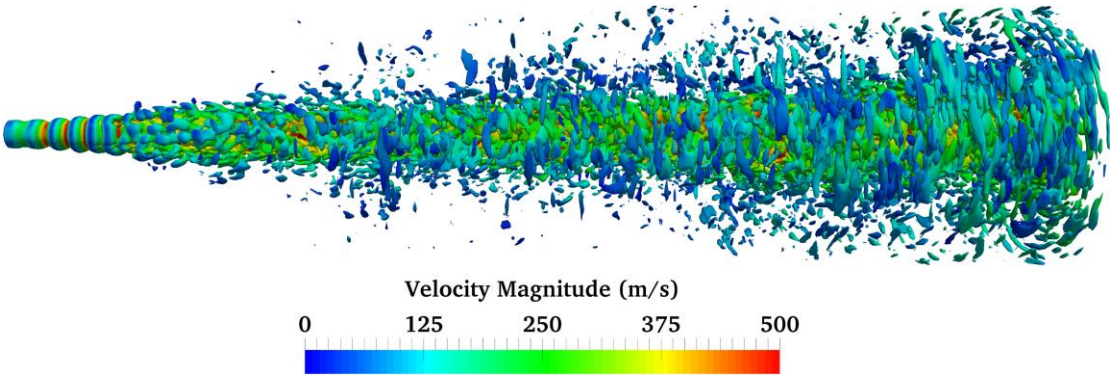

Figure 2-8: Contour plot of liquid volume fraction represented by an isosurface after the jet has penetrated the domain for 15 times. The liquid volume fraction is coloured by velocity magnitude.

2.3.2 Comparison of coupling simulation

In order to make a consistent comparison in terms of the droplet size distribution between the RCM and the SCA, the coupling region in the RCM simulation is placed after z=29.6d which is also the position of the coupling layer in the Grosshans-SCA simulation [40]. The coupling region extends the length of the computational domain to 41d which is kept the same as the computational domain used in [40]. Finally, the RCM is employed in the VOF-LPT coupling region to identify liquid structures suitable for VOF-LPT conversion and transfer them into the LPT simulation. The simulation is performed for an extended time equivalent to the jet crossing the entire VOF-LPT domain 10 times. The liquid jet isosurface together with the converted droplets are displayed in *Figure 2-9*. The droplet cloud visualisation and analysis of the size distribution reveal that most converted droplets have a diameter between 1 μm and 10 μm, which is consistent with the droplet size distribution obtained by Grosshans *et al*. [40] as shown in *Figure 2-10*. However, significantly larger quantity of small droplets (3-8 μm) are identified and extracted by the RCM while SCA produces a droplet size PDF which shifts more to larger droplet diameters. On the one hand, these differences can be attributed to the slightly higher breakup intensity predicted by the RCM-VOF method. On the other hand, indistinguishably converting all liquid structures sampled at the coupling layer without applying a volume threshold leads to the generation of more large Lagrangian droplets in the SCA simulation. Since the size of these droplets do not necessarily satisfy the requirement that a Lagrangian droplet must be smaller than the local grid size, it is more difficult to ensure numerical stability in the SCA than in the RCM.

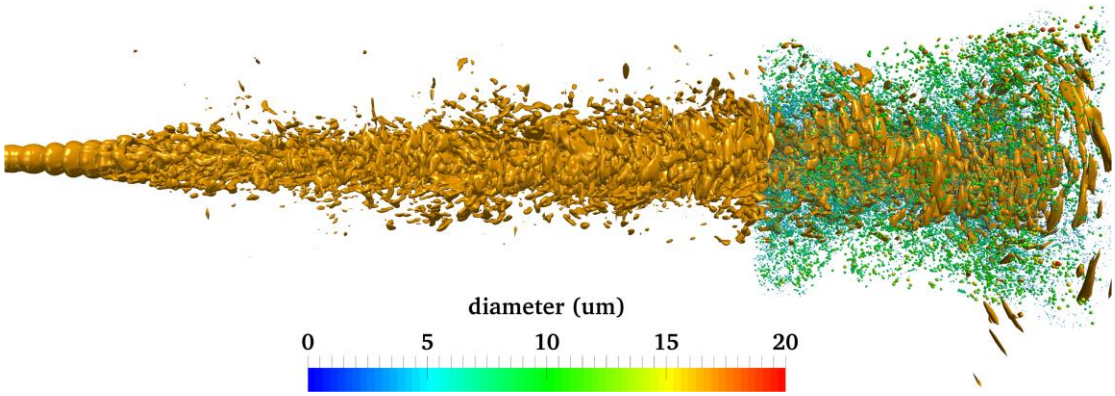

Figure 2-9: Atomisation of a simple liquid jet using the RCM method. The 0.1 liquid volume isosurface is coloured in brown while the converted Lagrangian droplets are scaled and coloured according to their diameters.

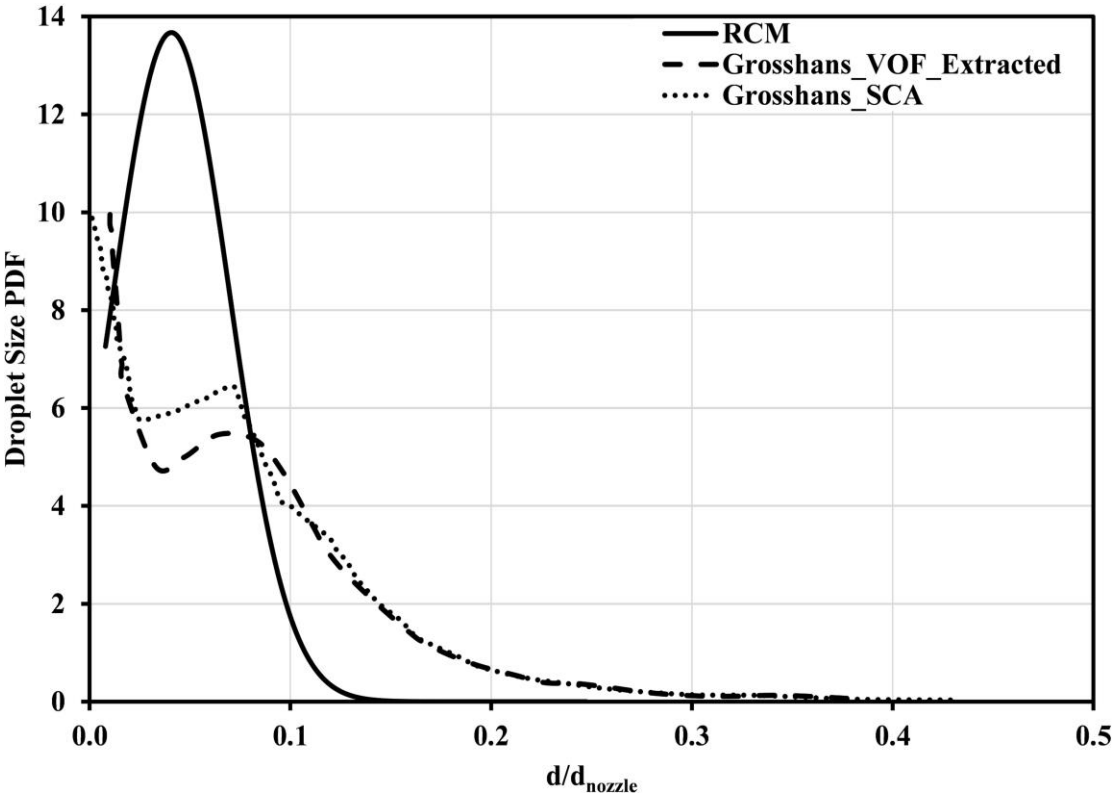

Figure 2-10: Comparison of predicted droplet size distributions between RCM and SCA. The size distribution calculated for the extracted VOF droplets from the Grosshans-VOF simulation is also added to demonstrate the difference between the RCM and SCA. The droplet diameter is non-dimensionalised by the nozzle diameter.

The effects of different decomposition strategies on the identification and extraction of droplets are demonstrated using 16, 32, 64, 96, 128 and 196 CPU processors. The simulation time is equivalent to the jet crossing the entire domain 10 times. A scotch method is employed to ensure that each processor domain is assigned with equal numbers of mesh elements. The numerical instability in time integration is eliminated by fixing the time step size at 1.4×10^{-9} s for all simulations. As shown in *Figure 2-11*(a), decomposing the computational domain with increasing number of CPUs has a diminishing effect on the droplet identification and conversion procedures. Moreover, the size distributions of converted droplets under different decomposing conditions

display negligible difference as depicted in *Figure 2-11(b)*. These comparisons demonstrates RCM's good adaptability to high level parallel simulations.

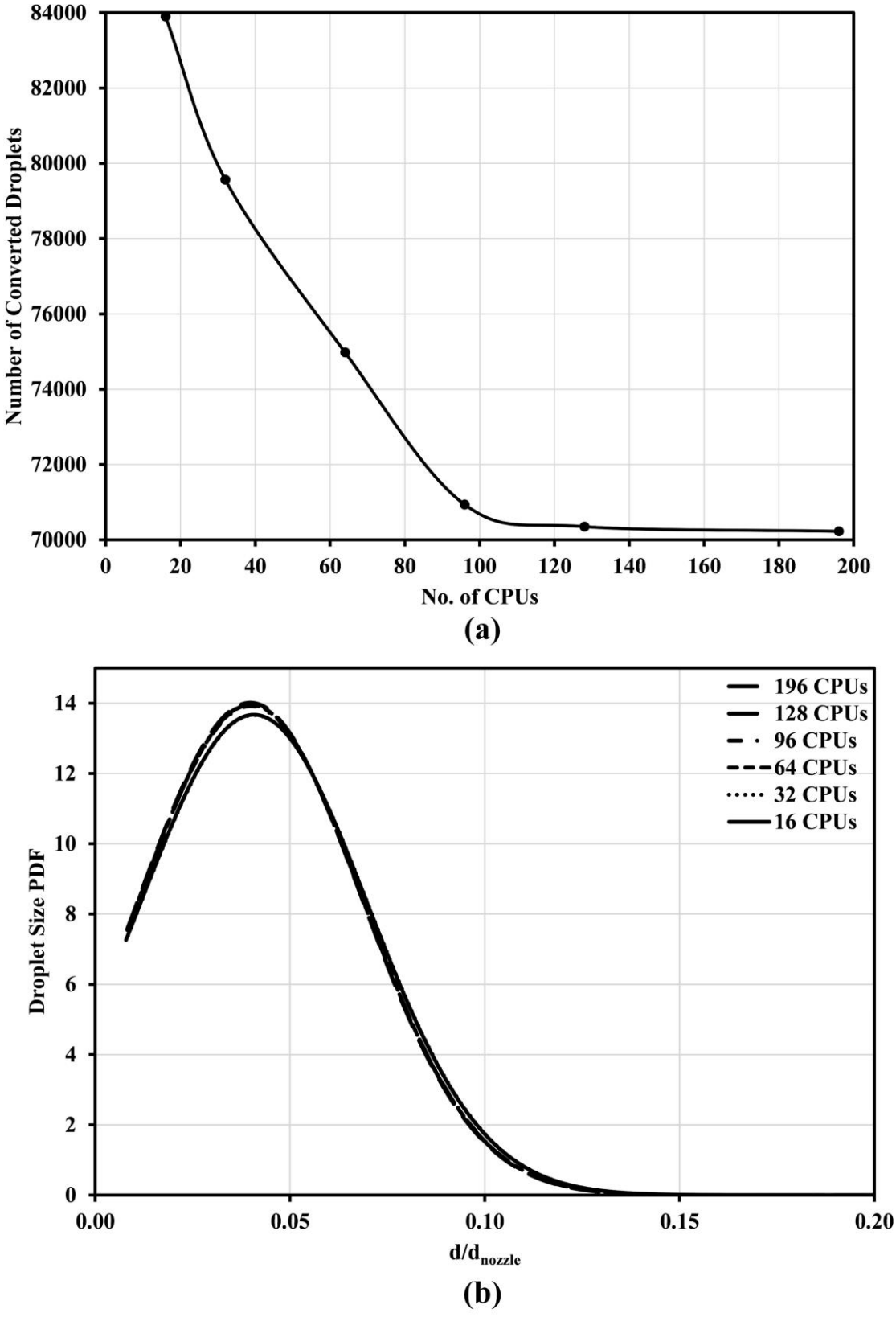

Figure 2-11: Comparison of the quantity of converted droplets (a) and their size distributions (b) using different number of CPUs.

2.4 Coupling of in-nozzle flow to spray atomisation

In this section, the application of the RCM is further extended to couple the in-nozzle flow with the primary and secondary spray atomisation. Firstly a pure VOF simulation is performed to determine the location and size of the VOF-LPT coupling region. Secondly the simulation of a real diesel spray from in-nozzle flow to secondary atomisation with transient VOF-LPT coupling is presented. The simulation is run until 200 μs after start of injection (ASOI).

2.4.1 Boundary conditions

Experimental conditions given in the work of Goldsworthy *et al.* [4], relevant for a non-evaporative spray from a sharp edged orifice are simulated. The ambient volume is non-reactive and initially filled with compressed air at 30 bar. Boundary conditions for the simulation cases are similar to the experimental conditions in Goldsworthy *et al.* [4] and Ghiji *et al.* [57] given in *Table 2-2*. However, in the absence of direct measurement, sac pressure is assumed to increase from chamber pressure (30 bar) to 850 bar after 50 μs then to 1200 bar after a further 25 μs then constant at 1200 bar to the end of simulation at 200 μs. This assumption is to some extent arbitrary but is made based on published data that the sac pressure increases rapidly during needle opening [63-65]. For instance, Moon *et al.* [63] found that the quasi-steady state jet velocity was reached when the needle was only elevated to 17% of the maximum lift. The ramp is chosen to give an approximate estimation of pressure variation due to needle dynamics. The reduced pressure rise rate in the second 25 μs is adopted to avoid numerical instabilities. This sac pressure ramp is same as that used by Ghiji *et al.* [57].

Table 2-2: Boundary conditions for spray injection corresponding to the 200 μs simulations. Nozzle diameter is used as the characteristic length.

Parameter	Value
Injection pressure	1200 bar
Nozzle diameter (D)	0.25mm
Nozzle length	1.6mm
Nozzle index factor (K_S)	0
Fuel	Diesel
Fuel density	832 kg/m^3
Gas	Compressed air
Density ratio	42
Fuel kinematic viscosity	2.5226×10^{-6} m^2/s
Surface tension	0.03 N/m
Temperature (Fuel and Ambient)	298 K
Chamber pressure	30 bar
Cavitation number	1.025
Fuel Reynolds number	7000≤Re≤47000

The cavitation number CN is calculated from:

$$CN = \frac{P_{injection} - P_{vapour}}{P_{injection} - P_{ambient}} \tag{2-34}$$

$$\mathrm{Re}_l = \frac{\rho_l U_l D}{\mu_l} \tag{2-35}$$

2.4.2 Computational grid

The simulations comprise an injector and a fixed volume chamber. The injector grid is designed to include an inlet, a sac and a nozzle while the chamber mesh is shaped as a conical cylinder allowing a smooth transition of a fine grid in the nozzle to a relatively coarse grid at the end of the chamber. The geometry configuration of the computational domain is shown in *Figure 2-12*.

To achieve high resolution, mesh elements of 0.15 μm (1.5 times of the gas phase Kolmogorov scale and one-fifth of the liquid phase Kolmogorov scale [57]) are distributed in the nozzle where the in-nozzle flow separation, flow detachment and turbulent fluctuations are captured. The grid quality and resolution in the primary atomisation region (within 12D from the nozzle exit) are kept consistent with the finest grid employed in Ghiji *et al.*'s study [57]. To solve the problem that overly refined mesh can lead to the generation of excessive quantity of sub-micron droplets, the cell size is proportionally increased from 0.15 μm at the nozzle exit to $\Delta x = \Delta y = \Delta z = 210$ μm at the end of the chamber, with a growth rate of 1.02 along penetration axis. The maximum cell size of 210 μm is related to the finest grid used for a LPT-LES simulation of a diesel spray in Jangi *et al.* [26]. In total, 25 million hexahedral cells are used to discretise the computational domain.

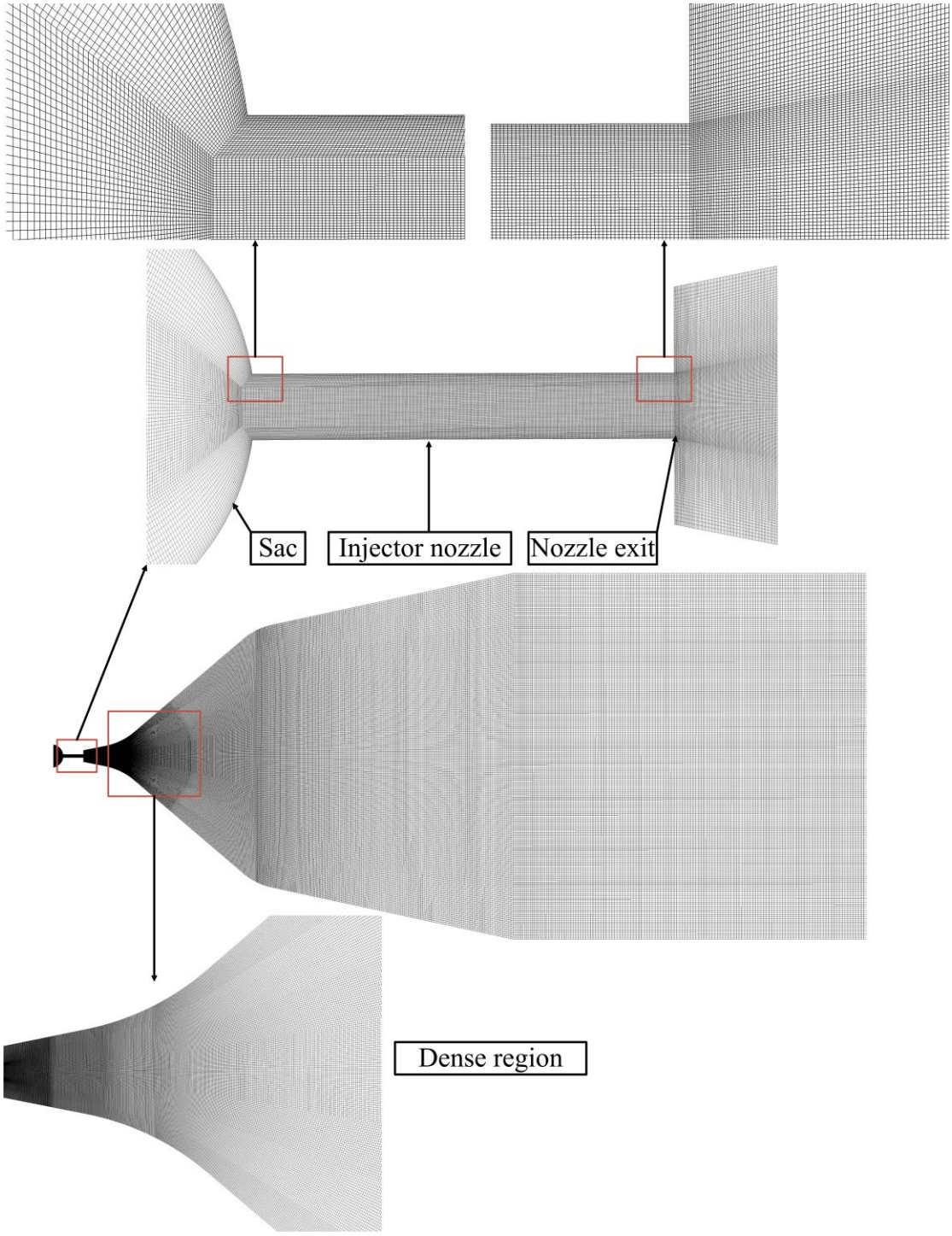

Figure 2-12: Computational grid design. Enlarged views are shown for the grid design at the nozzle entrance, in the nozzle hole, at the nozzle exit and in the dense region where the transition from fine grid to coarse grid starts. The total number of cells are 25 million and smallest cell size is 0.15 µm.

The injector is initially filled with fuel up to the nozzle exit such that air is not present in the region near the nozzle entrance and the start of injection occurs shortly after the start of simulation. The VOF simulation is initiated with the boundary configurations provided in *Table 2-3*, corresponding to *Figure 2-13*. The maximum Courant-Friedrichs-Lewy (CFL) number is set to 0.2, which gives an average time step size of 1.2×10^{-9} s.

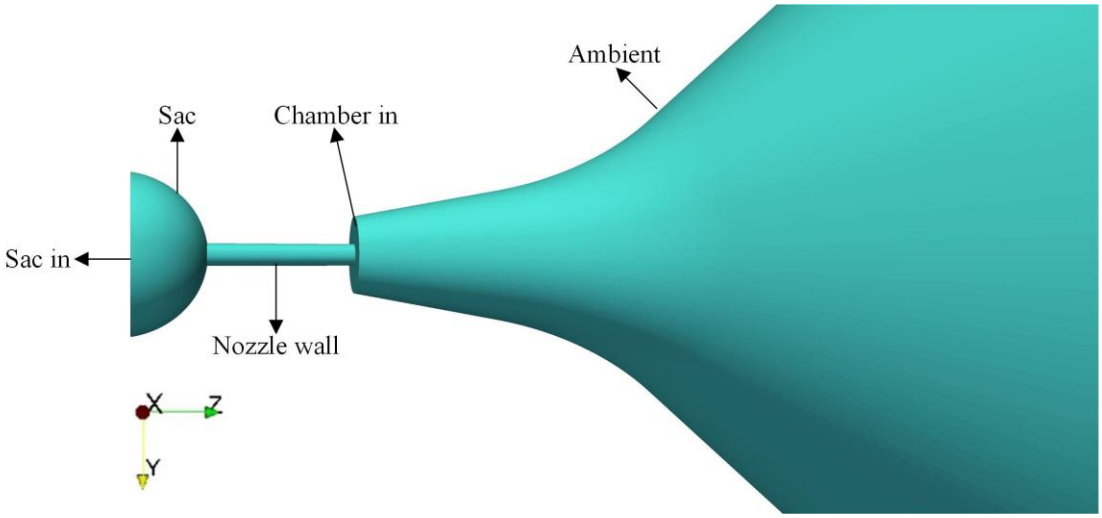

Figure 2-13: Boundary names and locations of the computational grid.

Table 2-3: Boundary configurations for the computational grid.

Boundary	Value
Sac in	Pressure inlet 30-1200 bar in 200 µs
Sac	No-slip and zero gradient (adiabatic)
Nozzle wall	No-slip and zero gradient (adiabatic)
Chamber in	No-slip and zero gradient (adiabatic)
Ambient	Non-reflective pressure boundary with a reference 30 bar

The simulation is performed on a computer cluster only using 96 core i7 (3.4GHz) processors which are granted a total of 96GB physical memory.

Prior to the generation of the LPT grid, a pure VOF simulation is run to 200 µs ASOI. The volume fraction plots for the VOF simulation at onset of major jet breakup (90 µs ASOI) and at end of simulation (200 µs ASOI) are shown in *Figure 2-14(a)*. Major jet breakup is designated to occur from 90 µs ASOI when the liquid core starts to disintegrate. The smearing of the liquid-gas interface along the penetration axis can be attributed to the gradually coarsened mesh in the direction of penetration and the deviation of liquid structures from the central cut plan due to turbulence induced spray atomisation. The coupling region is then placed after 52D from the injector inlet to encompass the entire region where an intact liquid core ($\alpha_l < 0.5$) does not exist at 90 µs and 200 µs ASOI, as shown in *Figure 2-14(a)*.

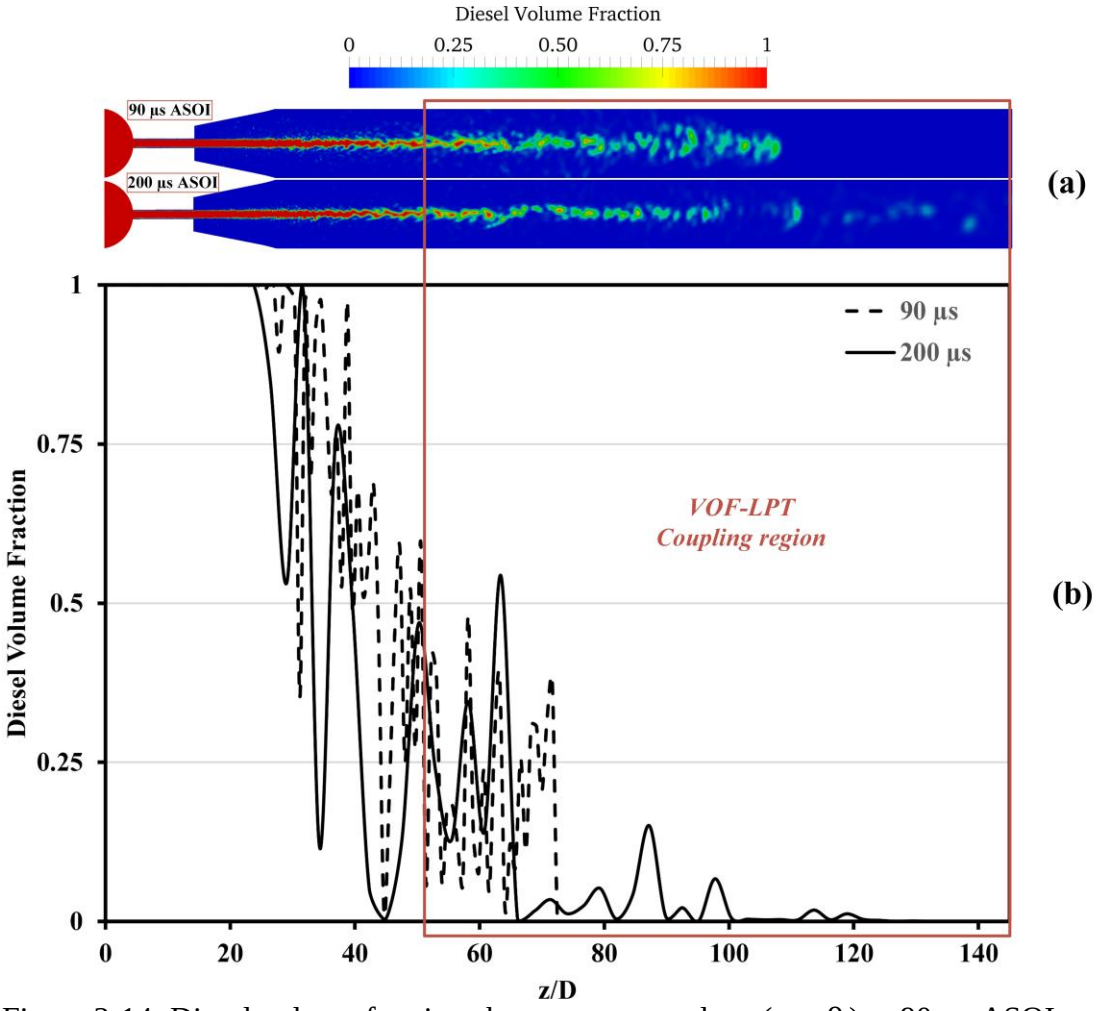

Figure 2-14: Diesel volume fraction shown at centre plane ($x = 0$) at 90 µs ASOI and 200 µs ASOI (a), and the instantaneous variation of diesel volume fraction along the penetration axis at 90 µs ASOI and 200 µs ASOI (b). The VOF-LPT coupling region is placed after 52D from the injector inlet.

Based on the pure VOF simulation, the computational domain is separated into two regions respectively for the VOF and LPT simulations. These two simulations are connected by the coupling region where the two-way mapping of velocity and pressure fields is deployed. It should be pointed out that the overlapping VOF-LPT regions have identical mesh design and elements distribution in order to ensure high fidelity field mapping between two simulations. After the grid separation, the minimum and maximum cell sizes in the coupling region are Δz_{min} = 58 µm (start of coupling region) and Δz_{max} = 140 µm (end of coupling region). As shown in *Figure 2-15*, the length and the maximum diameter of the conical section of the mesh in the chamber are based on the spray angle and spray penetrating length reported in Bong [33]. The coupling region is extend further 55 nozzle diameters from the point of maximum liquid penetration to avoid potential boundary effects imposed by the right end of the coupling region. All dimensions are non-dimensionalised by the nozzle diameter.

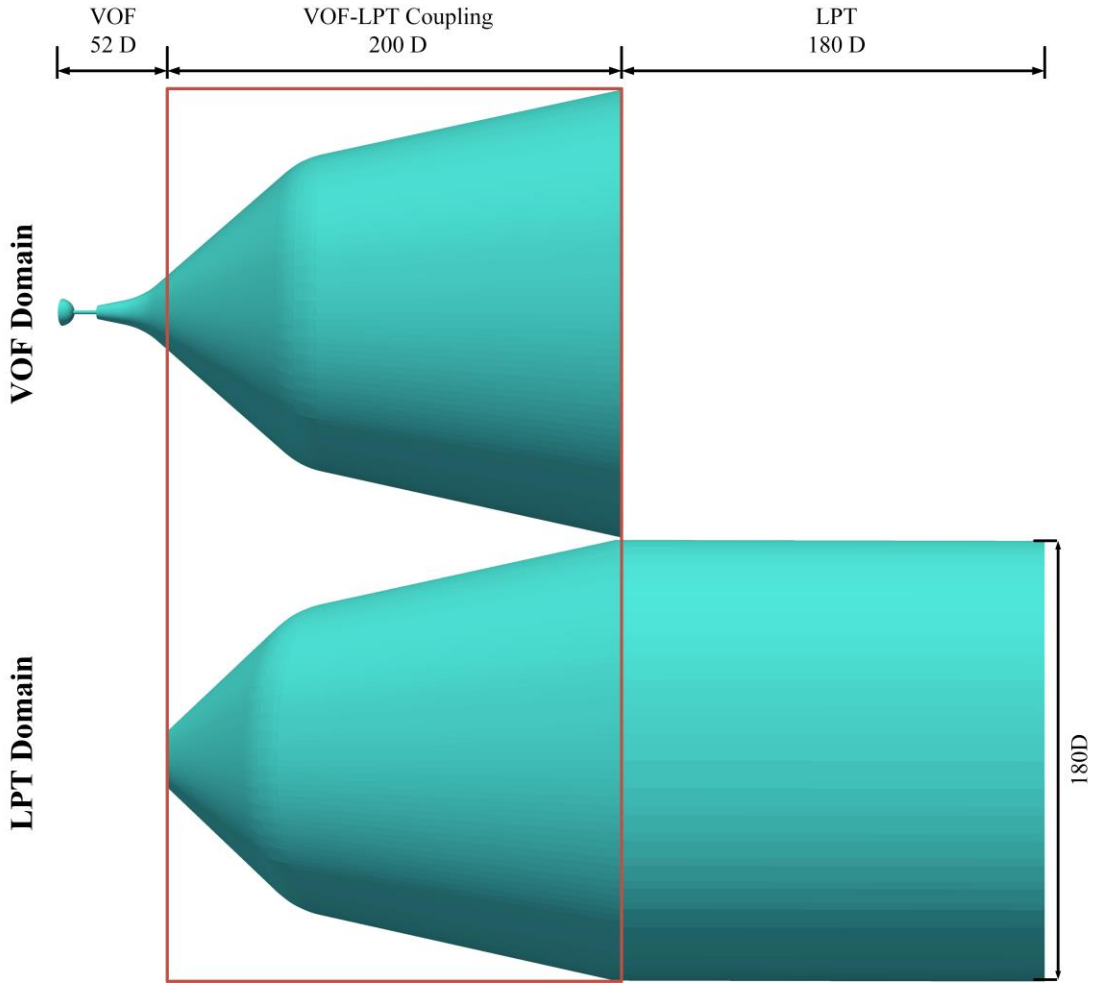

Figure 2-15: The geometry information for the VOF and LPT domains. The coupling region is enclosed in red box. The size of the LPT domain is determined from the results reported in Bong [33]. All dimensions are normalised by the nozzle diameter (D).

2.4.3 Pure VOF simulation

In *Figure 2-16(a-d)*, the emerging spray is represented by a 0.5 diesel volume fraction isosurface coloured by turbulent kinetic energy while the fluid in the sac is coloured by diesel volume fraction displayed at the $x = 0$ plane. The 'mushroom' like leading edge is formed due to aerodynamic forces exerted by the compressed air ahead of the spray tip. The disintegration of this mushroom-like structure at the periphery due to aerodynamic shear provides an initial mechanism for droplet formation. At 25 ASOI, toroidal transverse waves start to develop on the liquid-gas interface upstream of the mushroom structure. These spanwise waves could be potentially generated due to either Kelvin-Helmholtz instability or 2D Tollmien-Schlichting instability as recently reported by Shinjo and Umemura from DNS for a low Reynolds number [62]. In-nozzle cavitation is observed to initiate from the sharp nozzle inlet and the growth of cavitation pockets all the way up to the nozzle exit together with liquid-wall shear contribute to the development of surface disturbances. This is evident after 35 µs ASOI with the appearance of 3D surface instabilities (breakup) increasing in quantity and magnitude with time. It is also noticed that once the flow has separated from the nozzle wall due to cavitation induced hydraulic flip, the quantity and magnitude of surface instabilities are diminished. This can be attributed to the minimised effects of wall shear on the

liquid surface. Nevertheless, the absence of wall shear and the decrease in effective flow area lead to increased injection velocity, which is reflected by apparent increase in interfacial turbulent kinetic energy at 45 µs ASOI.

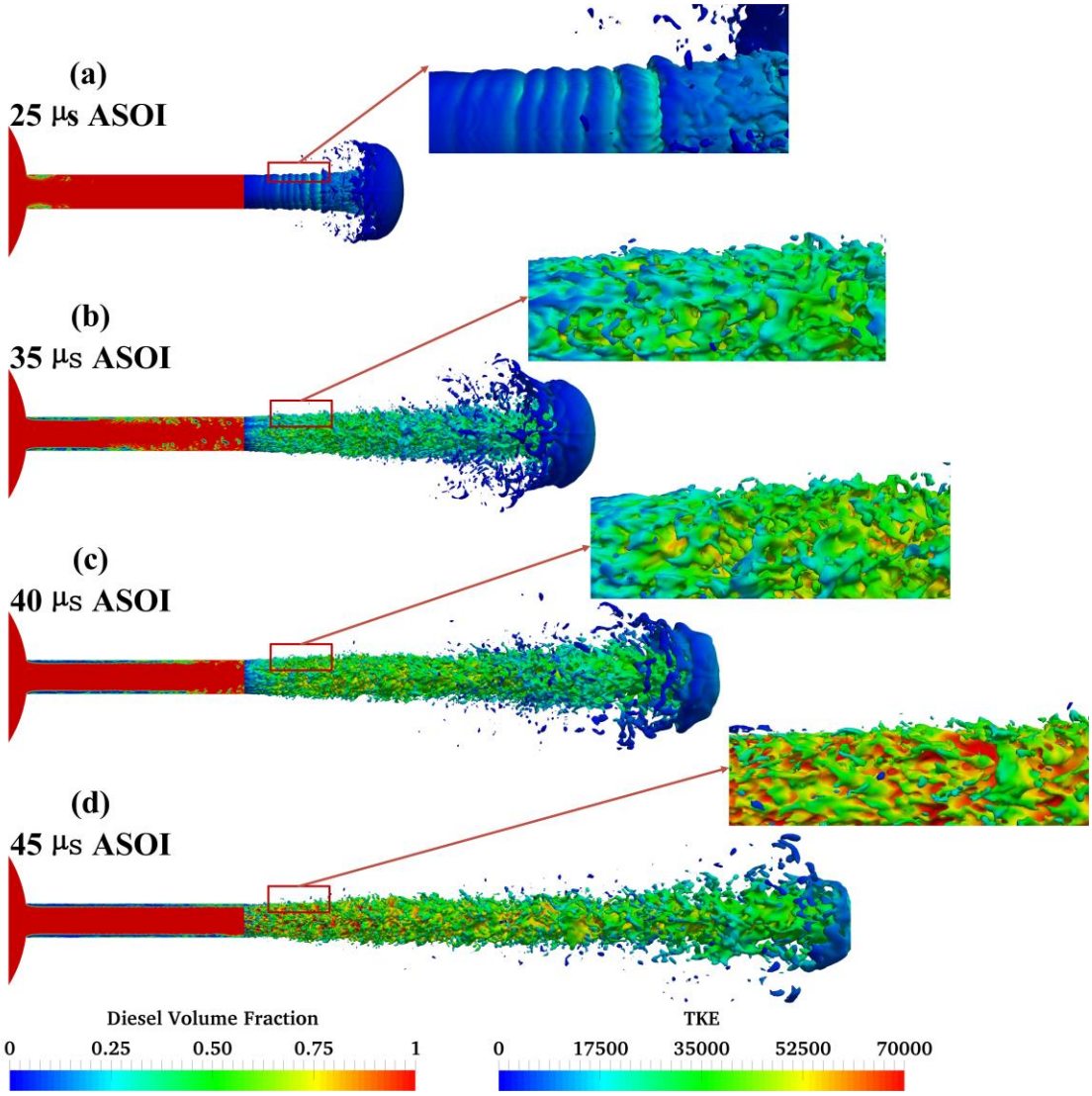

Figure 2-16: Evolution of in-nozzle and liquid jet turbulent structures at 25, 35, 40 and 45 µs ASOI. In images a-d, in nozzle flow is coloured by diesel volume fraction displayed at $x = 0$ plane; liquid-gas isosurface of 0.5 is used to represent the emerging spray coloured by turbulent kinetic energy. Detailed evolution of surface instabilities are shown in the enlarged images. Animation showing the simulated primary atomisation of the diesel spray using pure VOF can be found in [66] (https://www.youtube.com/watch?v=pZlppXNau-g&ab_channel=HongjiangYu).

In this study, a mesh sensitivity analysis has not been done because for VOF-LES methods, increasing mesh refinement always leads to an increasingly high resolution of interphase capturing. Unlike the Reynolds averaged models, such a trend persists until the mesh is fine enough for a DNS simulation. On the other hand, the quality of the LES simulation is assessed by evaluating the resolved kinetic energy as a fraction of the estimated total kinetic energy in the computational domain, as reported by Yu *et al.*[59]. The resolved kinetic energy is obtained from the Root Mean Square of the velocity components and consecutively time averaged over the simulation. It is then divided by the estimated total kinetic energy (resolved kinetic energy + contribution of

the sub-grid kinetic energy) to quantify how much kinetic energy is resolved by the grid. As shown in *Figure 2-17*, the chamber flow around and at the liquid-gas interface is very well resolved since the resolved kinetic energy is more than 90% of the total kinetic energy [67]. This indicates that turbulent disturbances causing spray breakup in the chamber are sufficiently captured by the grid. However, a decrease in the measured simulation resolution (only 50%-75% of kinetic energy is resolved) is observed in the nozzle wall boundary layer and in the liquid core region within 10 diameters upstream and downstream of the nozzle exit. In these regions, acceleration of liquid spray and the presence of liquid-gas velocity shear in the nozzle generate significant small scale turbulences that cannot be sufficiently resolved by the grid. The smallest turbulent length scale in these regions can become equivalent to the gas phase Kolmogorov scale which was evaluated to be 0.1 µm by Ghiji *et al.* [57]. To resolve all turbulences at this scale, the grid size must be less than half of the gas phase Kolmogorov scale [58] and only DNS can be employed to obtained a fully resolved flow. Nevertheless, performing a DNS of the entire spray breakup is computationally impractical at such a high Reynolds number and therefore is not considered in this study.

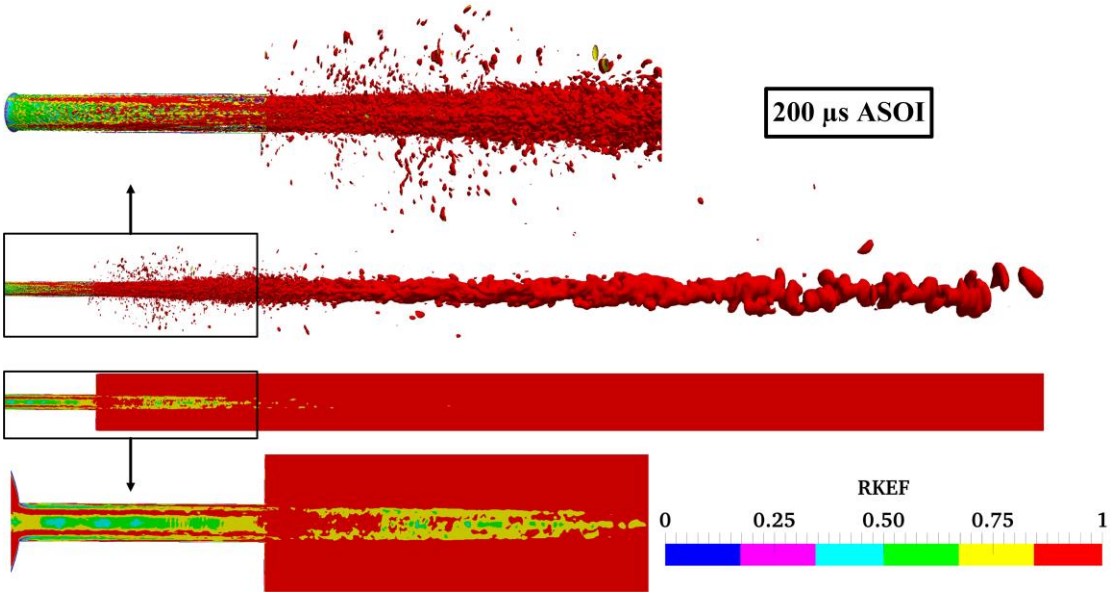

Figure 2-17: Resolved kinetic energy as a fraction of total kinetic energy plotted at the liquid isosurface ($\alpha_l = 0.05$) and at the $x = 0$ plane. Detailed distribution of this fraction in the injector nozzle is also shown in the enlarged views. The fraction of resolved kinetic energy and its contour plot are time averaged over the simulation.

2.4.4 VOF-LPT coupling

2.4.4.1 Droplet identification and extraction

The demonstration of the droplet identification and extraction procedure is performed in the first time step of the VOF-LPT coupling simulation, 0.4 nanosecond after 90 µs ASOI. During this period, 1913 liquid structures discretised by less than 5 cells and smaller than 20% of their host cells are identified. The physics of these liquid structures can no longer be accurately predicted by the VOF-LES method and therefore they are extracted from the VOF domain, inserted and modelled in the LPT domain as depicted in the 0.05 liquid volume isosurface plots of *Figure 2-18(a-b)*. As shown in the histograms of *Figure 2-18(a-b)*, the number of VOF droplets that are discretised by less

than 5 cells decreases significantly (more than 90%) after droplets identification and extraction.

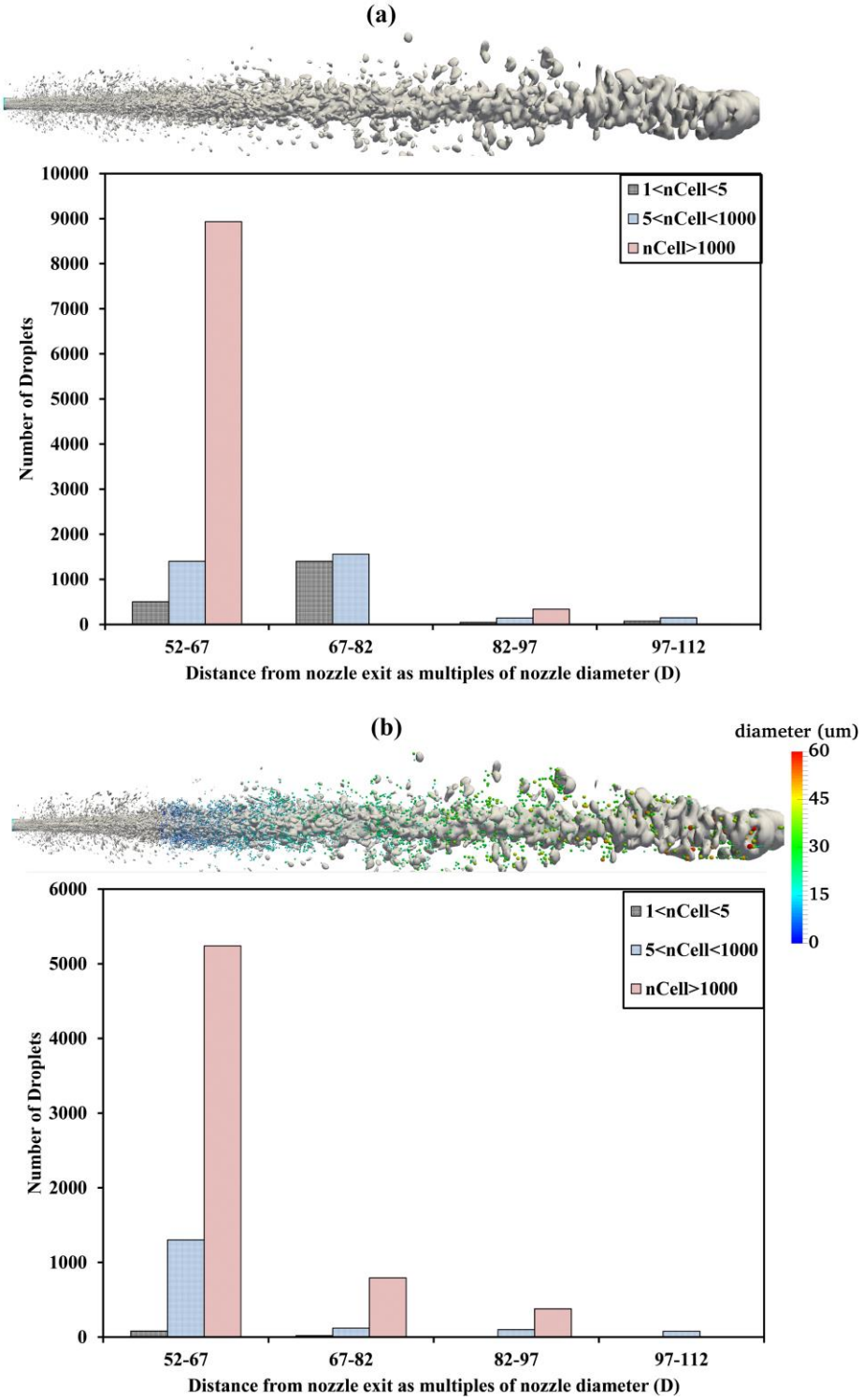

Figure 2-18: Contour plots of 0.05 liquid volume isosurface before (a) and after (b) the first time-step of the VOF-LPT coupling simulation. In image (b), the converted Lagrangian droplets are scaled and coloured according to their diameters. Also, numbers of VOF droplets captured by 1 to 5 cells and by greater than 5 cells before (a) and after (b) the first time-step are statistically represented using histograms. More than 90% of the droplets captured by less than 5 mesh cells have been extracted and converted to Lagrangian droplets.

2.4.4.2 Secondary atomisation

Major spray breakup is simulated to occur from 90 µs ASOI, hence the simulation of the secondary atomisation is initiated from 90 µs ASOI. It is linked to the primary atomisation through the RCM. The two-way field coupling of pressure and velocity fields allows the effects of in-nozzle flow separation, flow detachment and turbulence to be conveyed to the LPT simulation and the effects of LPT droplet-gas interaction to be reflected on the VOF simulation. The field coupling is performed at every Eulerian time-step during the VOF-LPT simulation. The field mapping results between two simulations in the overlap region at 200 µs ASOI can be seen in *Figure 2-19* to be indistinguishable. It preserves the field information in the mapping process and the high-fidelity exchange of field data between two simulations enables high resolution coupling of VOF-LPT.

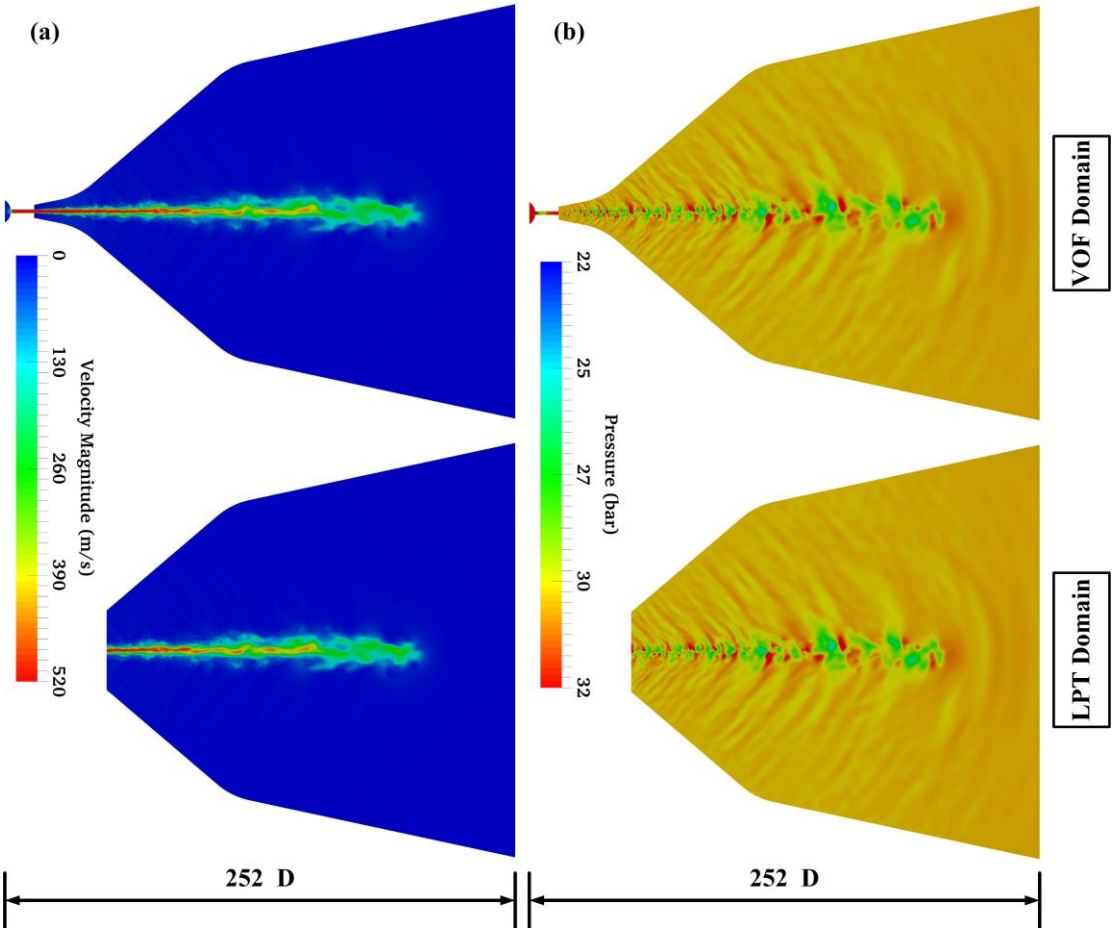

Figure 2-19: Mapping of velocity and pressure fields between the VOF and LPT simulations at 200 µs ASOI. The pictures on the left (a) show contour plots of velocity magnitude at the centre plane ($x = 0$), while the pictures on the right (b) display the pressure at the centre plane.

The atomised diesel jet, the transferred Lagrangian droplets, and the remaining VOF phase interface geometry at 100 and 200 µs ASOI are shown in *Figure 2-20*. At 100 µs ASOI, stripped off liquid structures from the liquid core start to be converted into Lagrangian droplets in the major breakup region. These large parent droplets undergo secondary breakup that generates child parcels which have a diameter smaller than 30 µm. At 200 µs ASOI, approximately 0.9 million droplets have been transferred into the Lagrangian simulation while the unconverted liquid structures (Blobs) are still

modelled in the VOF domain. The diameters of these fine droplets range from 0.8 µm up to 74 µm, which indicates a wide spectrum of droplet diameters attributed to the RCM. With the intensifying droplet-gas interaction, the turbulent effects of the flow on the droplets at the sub-grid level increases the spacing between droplets and produces a more dispersed spray cloud. At the spray tip, interaction of the turbulent air and the secondary droplets leads to the formation of a mushroom like penetrating spray. Also, recirculation of the droplet clouds (circled in red) is observed to occur in the middle section of spray. This is mainly attributed to droplets entrainment of which the modelling is enabled by the implementation of the LES stochastic droplet dispersion model. The breakup of secondary droplets is statistically represented by the droplet-size distribution in *Figure 2-21*. The size distribution at four instants continuously shifts to the left due to the atomisation of secondary droplets which is governed by the KH-RT model. In order to further demonstrate the effectiveness of the implemented dispersion and secondary breakup models, spray morphology and size distribution of secondary droplets are compared between 200 µs ASOI and 300 µs ASOI in *Figure 2-22*. During this 100 µs, large visible liquid structures in the spray cloud have disappeared due to atomisation and the spray has penetrated for a further 16 D with an 11% increase in maximum spray width. Moreover, in this period the size distribution of the secondary droplets (depicted in *Figure 2-23*) shifts slightly more to a spectrum of smaller diameter and displays a higher possibility for the occurrence of droplets smaller than 5 µm. This indicates further breakup of child parcels into smaller liquid droplets. More detailed and comprehensive analysis of the effects of the implementation of these two models will be considered in future work.

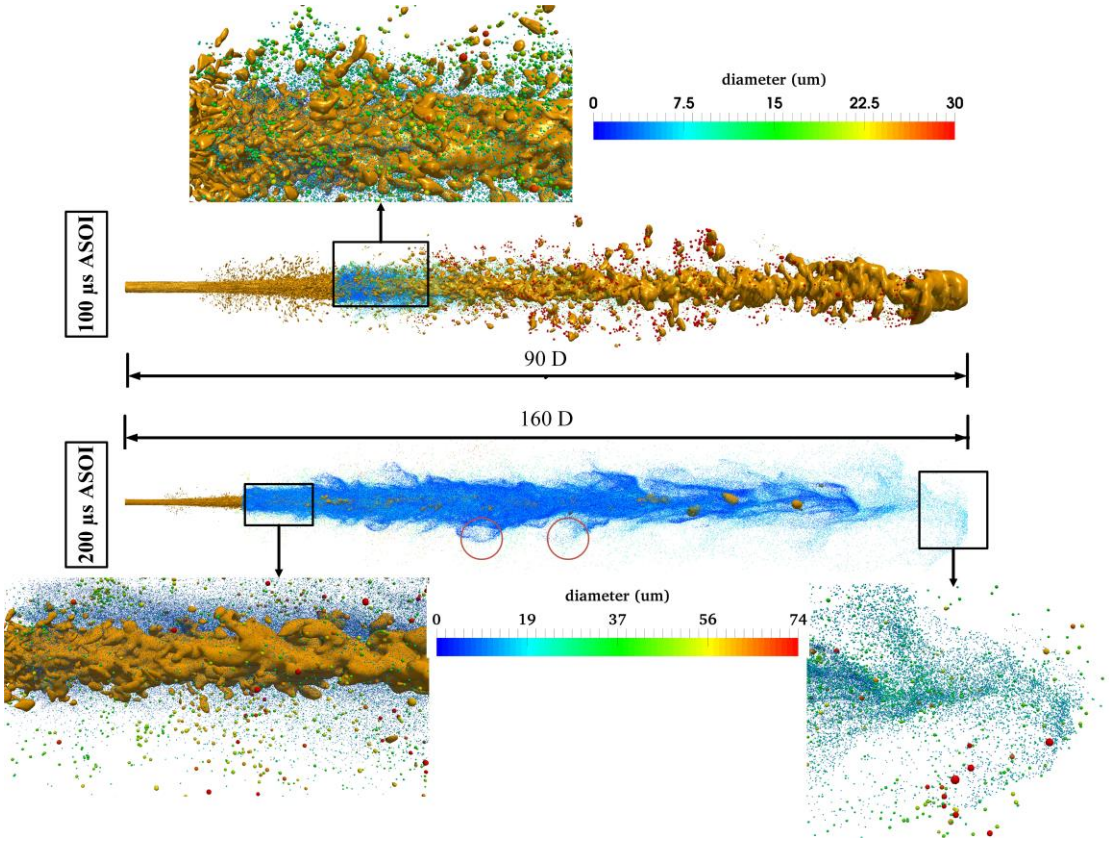

Figure 2-20: Secondary atomisation of the diesel fuel jet at 100 µs and 200 µs ASOI. The iso-surface ($\alpha_l = 0.05$) of the liquid jet is coloured brown and the Lagrangian droplets are scaled and coloured according to their diameters. The squared areas are

enlarged for better clarity and the circled areas are where entrainment of spray clouds occurs. Animation showing the simultaneous simulation of primary and secondary spray atomisation using the parallel VOF-LPT coupling procedure can be found in [68] (https://www.youtube.com/watch?v=hajIFoEr4D4&ab_channel=HongjiangYu).

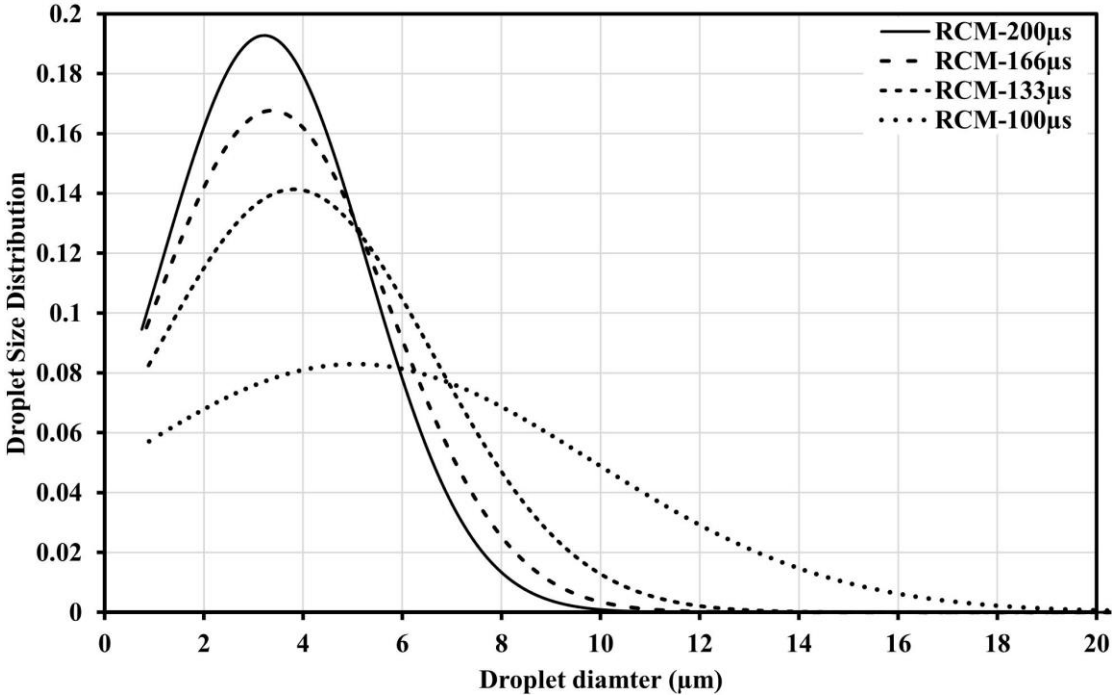

Figure 2-21: Comparison of Lagrangian-droplet-size distribution at four instants (t =100, 133, 166 and 200 μs after start of injection).

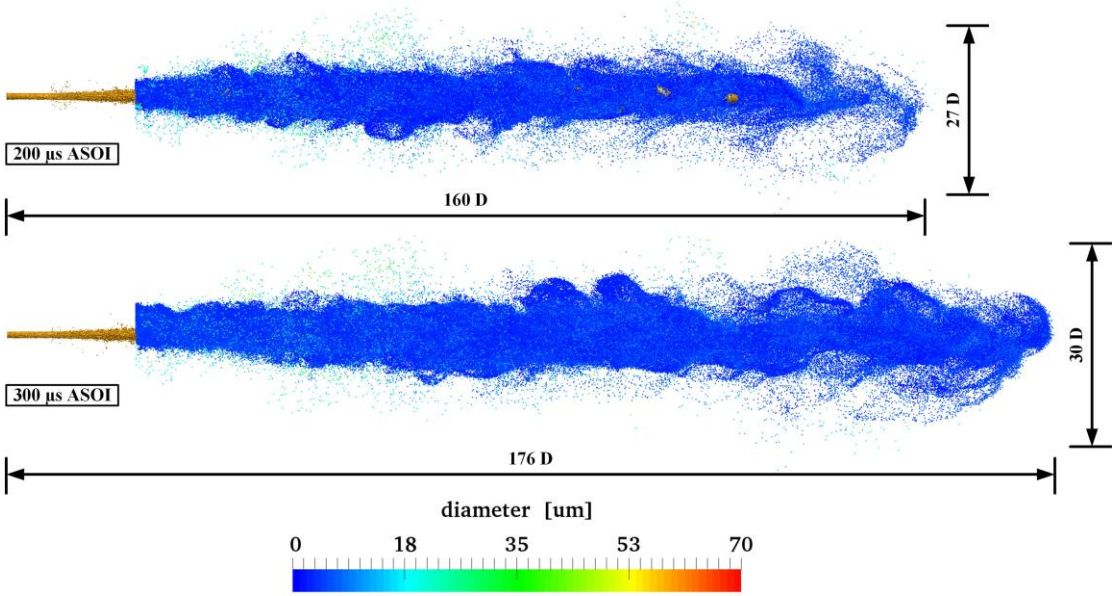

Figure 2-22: Comparison of spray morphology, in terms of spray penetration and width, between 200 μs ASOI and 300 μs ASOI.

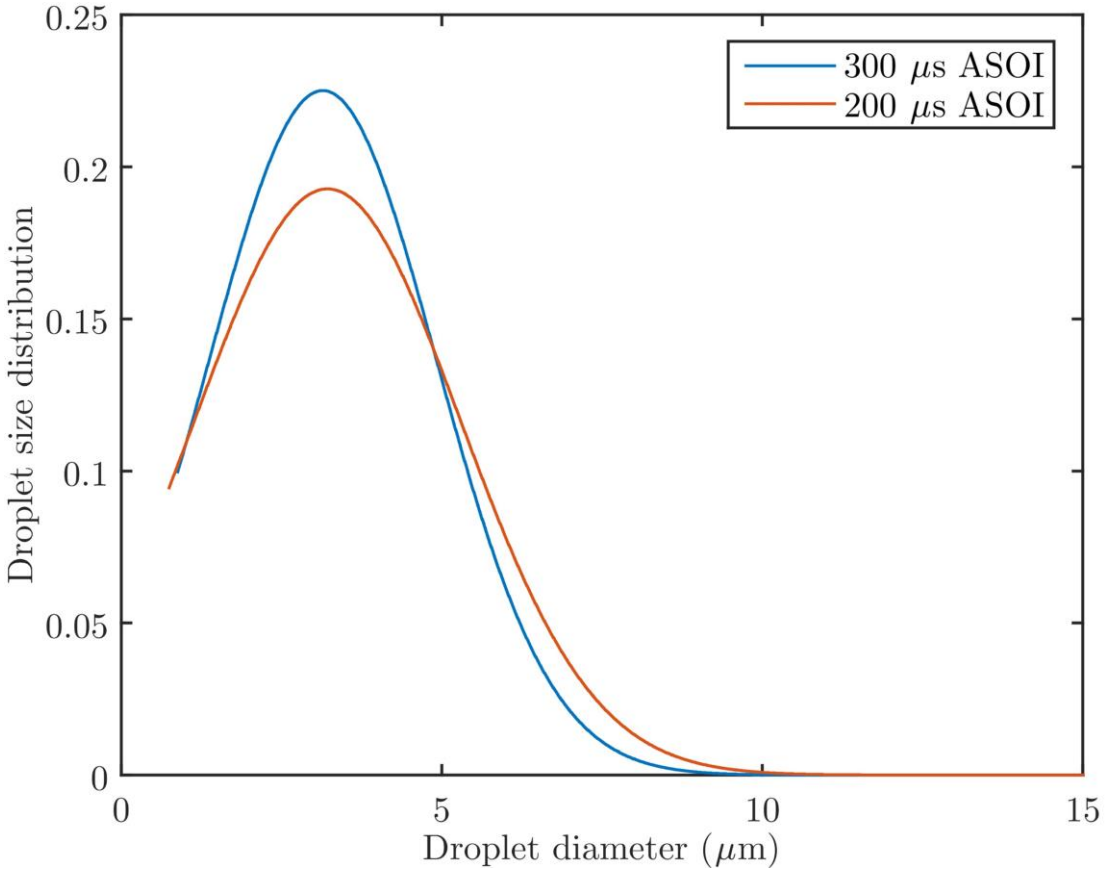

Figure 2-23: Comparison of Lagrangian-droplet-size distribution between t = 200 µs ASOI and t = 300 µs ASOI.

2.5 Conclusions

In this paper a parallel VOF-LPT coupling procedure between an Eulerian-Eulerian Volume of Fluid and an Eulerian-Lagrangian Lagrangian Parcel Tracking is presented. The coupling procedure links the VOF and LPT simulations with parallelised droplet identification, extraction and insertion procedures and a region coupling method that are deployed in a VOF-LPT transition region. The use of two identical grids in the transition region enables high-resolution coupling of velocity and pressure fields between VOF-LES and LPT-LES, which is independent of the turbulence model. The implementation of KH-RT secondary breakup, LES Stochastic Turbulence Dispersion and Stochastic Trajectory Collision models allows the use in the LPT simulation of the parcel assumption as a better replacement for the point particle tracking approach. The coupling procedure is first compared with a statistical coupling approach of which the applications are strictly restricted to the modelling of static sprays. The comparison demonstrates that:

- The parallel processing procedure for the identification and extraction of droplets from VOF simulation has negligible effects on the droplet statistics with different domain decomposition strategies
- The region coupling method is able to predict the transient spray evolution from a liquid jet to dispersed secondary droplets with high fidelity, which is attributed to the implementation of a conservative transient region coupling procedure.

The capability of the coupling approach is further demonstrated by application to the modelling of a real diesel spray from a nozzle with a sharp entrance, from which it was shown that:

- The sub-gird LES dispersion model and the trajectory collision model enable the modelling of droplets entrainment in the middle section of the spray, as well as the formation of a mushroom droplet cloud at the spray tip.
- The KH-RT secondary breakup model allows the simulation of secondary atomisation of the droplets, which produces a penetrating spray with a decreasing average droplet diameter.

Overall, the parallel droplet identification, extraction and insertion procedures together with the region coupling method are shown to be applicable to the simulation of complex diesel injection processes. Further validation of the proposed coupling procedure will be considered in future work.

3 Development of a compressible multi-phase cavitation approach for diesel spray modelling

Abstract

The influence of in-nozzle phenomena including cavitation on the morphology of the spray from a diesel injector with a sharp nozzle inlet is investigated numerically. A compressible, multi-phase Volume of Fluid Large Eddy Simulation is implemented in the OpenFOAM environment. The volume fraction transport equations for liquid and gas phases are reformulated to include mass transfer source terms. These source terms are modelled with two cavitation models by Schnerr and Kunz, which are extended to eliminate non-physical mass transfer rates. Validation is carried out only for the Schnerr cavitation model due to its independence of empirical parameters. The numerical method is validated by comparing the simulated mass flow rates, pressure and velocity profiles at different cavitation conditions against published experimental data obtained using a slightly converging square channel. Favourable comparison between simulations and experiments is achieved with minor discrepancies attributable to uncertainties in fuel properties, experimental artefacts and assumptions made in numerical models. Application of the method to calculation of in-nozzle phenomena and primary breakup of a diesel spray reveals that in-nozzle flow separation, wall shear and cavitation contribute greatly to the fragmentation of the jet. Comparison of the two cavitation models shows that after the onset of complete flow detachment, the Kunz implementation predicts higher air inflow at the nozzle outlet than the Schnerr model.

Keywords: Multi-phase flow; Volume of Fluid; Large eddy simulation; Cavitation; Primary atomisation

3.1 Introduction

In order to understand the whole atomisation process of a diesel spray, it is necessary to identify flow phenomena that lead to primary and secondary spray breakups. The atomisation of a diesel spray injected at high pressure can be induced by interaction with ambient gas and in-nozzle flow characteristics such as turbulence, flow separation and cavitation. The knowledge of spray formation is essential to allow prediction of spray behaviour during the injection process. In this study, characteristics of in-nozzle flow, particularly the onset of flow separation and cavitation as well as the production of turbulence, which are often considered to be the main reason for primary breakup [69-72] are numerically investigated.

The onset of cavitation in many types of diesel injectors has been reported to enhance the atomisation process of the emerging diesel spray and increase the dispersion angle in numerous studies [73-79]. For a nozzle with a sharp inlet the high pressure gradient and fluid inertia cause the flow to separate and form a region of contracted flow. Flow separation reduces the effective area and creates a recirculation zone in which pressure can reduce to or below fluid vapour pressure [70, 72]. Formation of the contracted area and adverse pressure gradients often occur around a sharp nozzle entrance after which cavities generated can build up along the nozzle wall and may extend beyond the nozzle exit. The term supercavitation is often used to describe collapse of cavities several diameters downstream of the nozzle entrance such that they do not influence the flow at inlet. Depending on relative length of the cavities and nozzle, vapour bubbles may collapse outside the nozzle exit [70, 80]. Moreover, there are situations where flow separation and cavitation can result in complete detachment of fluid flow from the nozzle wall. In those cases, air can be drawn into low pressure regions of the nozzle, resulting in a phenomenon known as hydraulic flip. When hydraulic flip occurs, the flow does not experience wall shear. As a result, production of turbulence near the wall decreases significantly and spray atomisation may be suppressed, which leads to a narrower spray [81]. However, complete hydraulic flip has only been observed in some scaled injector models at relatively low injection pressures [72, 82, 83]. Schmidt *et al.* [80] reported that it is unlikely for complete hydraulic flip to occur in real-scale nozzles operating at realistic conditions, as conditions causing hydraulic flip are somewhat abnormal.

Despite considerable efforts into experimental investigation of internal nozzle flow and early spray breakup, simultaneous imaging of the internal nozzle flow and the spray is difficult and more recent work has focused mainly on enlarged replicas or real-size nozzles with simplified designs [74, 84-86]. On the other hand, validated computational models have shown advantages in providing greater insight into the internal nozzle flow as a supplement to existing experimental observations and measurements.

Many different models [81, 87-91] have been developed with each of them having different assumptions. These models are either based on an Eulerian description of the liquid and vapour phases, or on an Eulerian-Lagrangian coupled regime where the continuous and dispersed phases are handled within Eulerian and Lagrangian frameworks respectively with the exchange of mass and momentum. The single fluid Eulerian approaches for cavitation modelling can be categorised as homogenous models in which liquid and vapour bubbles are treated as a continuous mixture. An additional transport equation is added to account for the phase change [92, 93]. An

alternative to single fluid Eulerian models is the two-fluid Eulerian approach to cavitation modelling. In this approach, instead of treating the liquid and vapour as one homogenous mixture, two sets of conservation equations are solved for each phase with total mass fraction as unity in each computational cell always being satisfied [94-96]. The vapour bubble dynamics are handled by the Rayleigh equation [91, 97] which also acts as the basis for the formulation of interfacial mass transfer between the two phases. In the Eulerian-Lagrangian framework, the liquid phase is handled in the Eulerian description while the vapour phase is treated as Lagrangian bubbles and tracked according to Newton's second law. The exchange of momentum between the phases is accounted for using a source term in the momentum equation of the continuous phase [98-100]. Additionally, such models require random insertion of cavitation nuclei which subsequently grow into vapour bubbles. The initial properties of the bubbles are expressed in terms of diameter and density which are user defined parameters [101].

Recently, implementation of the two-phase Volume of Fluid (VOF) method for prediction of primary spray breakup with the effects of in-nozzle flow has been reported by De Villiers *et al.* and Ghiji *et al.* [56, 102]. The VOF method is advantageous because it intrinsically allows the modelling of liquid breakup in a volume conservative manner. Capturing a sharp interface can help elucidate the behaviour of the diesel spray under various nozzle design and operating conditions. Moreover, it enables the modelling of primary atomisation with fewer assumptions as compared with the widely adopted Eulerian-Lagrangian approaches. Further, the implementation of a sharp interface capturing scheme reported by Ubbink [47] gives VOF an extra advantage in atomisation modelling. The incompressible VOF method has also been integrated with cavitation models to study internal nozzle cavitation and its effects on the emerging spray by Marcer *et al.* [103, 104]. The traditional two-phase VOF method only allows the interaction of the liquid phase and one gas phase to be modelled. However, in diesel engines, liquid fuel, fuel vapour and air can often co-exist in the chamber and phase change due to either cavitation or evaporation occurs exclusively between fuel and its vapour. In addition, the injection of fuel may exceed the speed of sound in the gas phase within the chamber due to high injection pressure in modern diesel engines. Modelling the spray atomisation under diesel engine operating conditions therefore falls into the framework of compressible multi-phase flow with phase change. There are, however, few implementations of compressible cavitation models with interface tracking capability in a multi-phase regime reported in the literature. Thus, the main objective of the present study is to develop a compressible multi-phase VOF method with cavitation modelling capability for improved diesel spray simulations.

3.2 Description of the VOF approach

The VOF method adds phase transport equations accounting for the volume fraction of each phase to the governing equations. It is a volume conservative approach in which the unity volume fraction must be satisfied regardless of the quantity of phase considered. For a two-phase flow, only one transport equation is needed for the dense phase while the volume fraction of the other phase can be derived from conservation laws:

$$\frac{\partial(\rho_l \alpha_l)}{\partial t} + \nabla \cdot (\rho_l \alpha_l U) = \dot{m} \tag{3-1}$$

$$\alpha_v = 1 - \alpha_l \tag{3-2}$$

where $\dot{m}$ is the phase change mass transfer rate, α_l and α_v are volume fractions of the liquid and vapour phases respectively. For a multi-phase flow with phase change, transport equations for all phases must be used.

$$\frac{\partial(\rho_l\alpha_l)}{\partial t}+\nabla\cdot(\rho_l\alpha_l U)=\dot{m} \tag{3-3}$$

$$\frac{\partial(\rho_v\alpha_v)}{\partial t}+\nabla\cdot(\rho_v\alpha_v U)=-\dot{m} \tag{3-4}$$

$$\frac{\partial(\rho_i\alpha_i)}{\partial t}+\nabla\cdot(\rho_i\alpha_i U)=0 \tag{3-5}$$

$$\alpha_l+\alpha_v+\alpha_i=1 \tag{3-6}$$

where the subscripts l and v are for the liquid and vapour phases respectively, while i represents phases that do not take part in the phase change process. Note, the velocity vector U in the above formulations should be expressed as $U=\alpha_l U_l+\alpha_v U_v+\alpha_i U_i$ only for those cells where α has intermediate values (e.g. across the interface). The source term on the RHS is the rate of mass transfer expressed as:

$$\dot{m}=\dot{m}^{+}+\dot{m}^{-} \tag{3-7}$$

The rate of condensation $\dot{m}^{+}$ and vaporisation $\dot{m}^{-}$ of the liquid phase on the phase interface can be modelled by phase change models such as those by Kunz [105] and Schnerr [106]. The detailed implementation of these models is discussed in the next section.

In Eqn (3-5), the convection term can be expanded as:

$$\nabla\cdot(\rho_i\alpha_i U)=\rho_i\left(\nabla\cdot(\alpha_i U)\right)+\alpha_i(U\cdot\nabla\rho_i) \tag{3-8}$$

Applying this procedure to Eqn (3-3), (3-4) and (3-5) with further mathematical manipulations we obtain:

$$\begin{cases}\dfrac{\partial\alpha_l}{\partial t}+\nabla\cdot(\alpha_l U)=-\dfrac{\alpha_l}{\rho_l}\left[\dfrac{\partial\rho_l}{\partial t}+U\cdot\nabla\rho_l\right]+\dfrac{\dot{m}}{\rho_l}\\ \dfrac{\partial\alpha_v}{\partial t}+\nabla\cdot(\alpha_v U)=-\dfrac{\alpha_v}{\rho_v}\left[\dfrac{\partial\rho_v}{\partial t}+U\cdot\nabla\rho_v\right]-\dfrac{\dot{m}}{\rho_v}\\ \dfrac{\partial\alpha_i}{\partial t}+\nabla\cdot(\alpha_i U)=-\dfrac{\alpha_i}{\rho_i}\left[\dfrac{\partial\rho_i}{\partial t}+U\cdot\nabla\rho_i\right]\end{cases} \tag{3-9}$$

For conciseness, the total derivative terms in the above equation can be simplified to obtain:

$$\begin{cases}\dfrac{\partial\alpha_l}{\partial t}+\nabla\cdot(\alpha_l U)=-\dfrac{\alpha_l}{\rho_l}\left[\dfrac{D\rho_l}{Dt}\right]+\dfrac{\dot{m}}{\rho_l}\\ \dfrac{\partial\alpha_v}{\partial t}+\nabla\cdot(\alpha_v U)=-\dfrac{\alpha_v}{\rho_v}\left[\dfrac{D\rho_v}{Dt}\right]-\dfrac{\dot{m}}{\rho_v}\\ \dfrac{\partial\alpha_i}{\partial t}+\nabla\cdot(\alpha_i U)=-\dfrac{\alpha_i}{\rho_i}\left[\dfrac{D\rho_i}{Dt}\right]\end{cases} \tag{3-10}$$

Addition of all equations in Eqn (3-10) leads to:

$$\nabla \cdot U = -\left(\frac{\alpha_l}{\rho_l}\left[\frac{D\rho_l}{Dt}\right] + \frac{\alpha_v}{\rho_v}\left[\frac{D\rho_v}{Dt}\right] + \frac{\alpha_i}{\rho_i}\left[\frac{D\rho_i}{Dt}\right]\right) + \dot{m}\left(\frac{1}{\rho_l} - \frac{1}{\rho_v}\right) \quad (3\text{-}11)$$

Adding and subtracting $\alpha(\nabla \cdot U)$ to the RHS of Eqn (3-10) for each phase and utilising Eqn (3-11), the multi-phase transport equations can be expressed as:

$$\begin{cases} \dfrac{\partial \alpha_l}{\partial t} + \nabla \cdot (\alpha_l U) = -\dfrac{\alpha_l}{\rho_l}\left[\dfrac{D\rho_l}{Dt}\right](1-\alpha_l) + \alpha_l(\nabla \cdot U) + \alpha_l\left[\dfrac{\alpha_v}{\rho_v}\dfrac{D\rho_v}{Dt} + \dfrac{\alpha_i}{\rho_i}\dfrac{D\rho_i}{Dt}\right] \\ +\dot{m}\left(\dfrac{1}{\rho_l} - \alpha_l\left(\dfrac{1}{\rho_l} - \dfrac{1}{\rho_v}\right)\right) \\ \dfrac{\partial \alpha_v}{\partial t} + \nabla \cdot (\alpha_v U) = -\dfrac{\alpha_v}{\rho_v}\left[\dfrac{D\rho_v}{Dt}\right](1-\alpha_v) + \alpha_v(\nabla \cdot U) + \alpha_v\left[\dfrac{\alpha_l}{\rho_l}\dfrac{D\rho_l}{Dt} + \dfrac{\alpha_i}{\rho_i}\dfrac{D\rho_i}{Dt}\right] \\ -\dot{m}\left(\dfrac{1}{\rho_v} + \alpha_v\left(\dfrac{1}{\rho_l} - \dfrac{1}{\rho_v}\right)\right) \\ \dfrac{\partial \alpha_i}{\partial t} + \nabla \cdot (\alpha_i U) = -\dfrac{\alpha_i}{\rho_i}\left[\dfrac{D\rho_i}{Dt}\right](1-\alpha_i) + \alpha_i(\nabla \cdot U) + \alpha_i\left[\dfrac{\alpha_l}{\rho_l}\dfrac{D\rho_l}{Dt} + \dfrac{\alpha_v}{\rho_v}\dfrac{D\rho_v}{Dt}\right] \\ -\alpha_i\dot{m}\left(\dfrac{1}{\rho_l} - \dfrac{1}{\rho_v}\right) \end{cases} \quad (3\text{-}12)$$

An artificial compression term $\nabla \cdot \left(\alpha_l\alpha_v(U_l - U_v) + \alpha_l\alpha_i(U_l - U_i)\right)$ has to be added to the above transport equations for each phase to preserve the sharpness of the liquid-gas interface. The final form of the multi-phase transport equations comprising phase change source terms can then be expressed as:

$$\begin{cases} \dfrac{\partial \alpha_l}{\partial t} + \nabla \cdot (\alpha_l U) + \nabla \cdot \left(\alpha_l\alpha_v(U_l - U_v) + \alpha_l\alpha_i(U_l - U_i)\right) = -\dfrac{\alpha_l}{\rho_l}\left[\dfrac{D\rho_l}{Dt}\right](1-\alpha_l) + \alpha_l(\nabla \cdot U) \\ +\alpha_l\left[\dfrac{\alpha_v}{\rho_v}\dfrac{D\rho_v}{Dt} + \dfrac{\alpha_i}{\rho_i}\dfrac{D\rho_i}{Dt}\right] + \dot{m}\left(\dfrac{1}{\rho_l} - \alpha_l\left(\dfrac{1}{\rho_l} - \dfrac{1}{\rho_v}\right)\right) \\ \dfrac{\partial \alpha_v}{\partial t} + \nabla \cdot (\alpha_v U) + \nabla \cdot \left(\alpha_v\alpha_l(U_v - U_l) + \alpha_v\alpha_i(U_v - U_i)\right) = -\dfrac{\alpha_v}{\rho_v}\left[\dfrac{D\rho_v}{Dt}\right](1-\alpha_v) + \alpha_v(\nabla \cdot U) \\ +\alpha_v\left[\dfrac{\alpha_l}{\rho_l}\dfrac{D\rho_l}{Dt} + \dfrac{\alpha_i}{\rho_i}\dfrac{D\rho_i}{Dt}\right] - \dot{m}\left(\dfrac{1}{\rho_v} + \alpha_v\left(\dfrac{1}{\rho_l} - \dfrac{1}{\rho_v}\right)\right) \\ \dfrac{\partial \alpha_i}{\partial t} + \nabla \cdot (\alpha_i U) + \nabla \cdot \left(\alpha_i\alpha_l(U_i - U_l) + \alpha_i\alpha_v(U_i - U_v)\right) = -\dfrac{\alpha_i}{\rho_i}\left[\dfrac{D\rho_i}{Dt}\right](1-\alpha_i) + \alpha_i(\nabla \cdot U) \\ +\alpha_i\left[\dfrac{\alpha_l}{\rho_l}\dfrac{D\rho_l}{Dt} + \dfrac{\alpha_v}{\rho_v}\dfrac{D\rho_v}{Dt}\right] - \alpha_i\dot{m}\left(\dfrac{1}{\rho_l} - \dfrac{1}{\rho_v}\right) \end{cases} \quad (3\text{-}13)$$

The artificial compression terms are also referred as "counter gradient" transport by Henry Weller [107] and enable interface compression with a numerical compression scheme. They are only active in the interface region due to the presence of $\alpha_l\alpha_i$, $\alpha_v\alpha_i$

and $\alpha_l\alpha_v$. In order to ensure that the compression term does not bias the solution in any way, it should only introduce flow of α (dense phase) normal to the interface, i.e. in the direction $\frac{\nabla\alpha}{|\nabla\alpha|}$. This condition suggests a model for the relative velocity $U_c = U_l - U_v$ between any two phases of the form:

$$U_c = c_a |U| \frac{\nabla\alpha}{|\nabla\alpha|} \tag{3-14}$$

where *cAlpha* (c_a) is used to regulate the rate of compression. The compression rate should be set to preserve interface sharpness, but more than that, might introduce unnecessary numerical difficulties or expense. Generally, a value of 1 is recommended for c_a to ensure conservative compression. The resolution of the interface can be further enhanced by using a value greater than one. However, it may lead to physically unrealistic high velocities on the interface commonly known as parasitic currents [108]. In addition, diffusive liquid-vapour and vapour-gas interfaces due to phase change and gas mixing processes are allowed by setting the compression factor in the CICSAM scheme to 0 at these interfaces. To ensure boundedness of phase volume fractions (volume fraction does not go below zero or beyond unity), the phase transport equations are solved using the 'Multi- Dimensional Universal Limiter with Explicit Solution' (MULES) accredited to Henry Weller. This method is coded in OpenFOAM but not documented in the open literature.

The present study employs VOF with LES turbulence modelling. The VOF-LES approach is based on a mathematical model composed of governing equations for the conservation of mass and momentum of a multi-phase system, according to De Villiers *et al.* [102]. This system comprises three immiscible, compressible fluids and accounts for the surface tension between them. The single set of mass and momentum transport equations for the mixtures is:

$$\frac{\partial\rho}{\partial t} + \nabla\cdot(\rho U) = 0 \tag{3-15}$$

$$\frac{\partial\rho U}{\partial t} + \nabla\cdot(\rho U \otimes U) = -\nabla p + \nabla\cdot\tau + \int_{S(t)} \sigma\kappa n\cdot\delta(x-x')\,ds \tag{3-16}$$

where the density of the mixture ρ is related to the volume fractions and densities of all phases as:

$$\rho = \alpha_l\rho_l + \alpha_v\rho_v + \alpha_i\rho_i \tag{3-17}$$

In the above equations, the subscript *i* represents the incondensable phase (air). The last term in Eqn (3-16) accounts for the effect of surface tension force. It is non-zero only at the interface due to the presence of a Dirac function δ which gives a non-zero value when $x = x'$. However, zero interfacial tension is assumed between liquid and vapour. The evaluation of the surface tension force between liquid and air is achieved following the approach by De Villiers *et al.* [102] through the continuum surface force model of Brackbill *et al*. [45].

$$\int_{S(t)} \sigma n\kappa\cdot\delta(x-x')\,ds \approx \sigma\kappa\nabla\alpha \tag{3-18}$$

The phase volume fraction α in the above equation can be obtained by solving the phase transport equations Eqn (3-13), while the surface curvature is calculated from:

$$\kappa = \nabla \cdot \left(\frac{\nabla \alpha}{|\nabla \alpha|} \right) \tag{3-19}$$

According to Jasak [109] and Demirdžić *et al.* [110], the momentum equation needs to be discretised to have a semi-discretised form before it can be solved in OpenFOAM. The semi-discretised form of the momentum equation is given as:

$$U_p = \frac{H(U)}{a_p} - \frac{1}{a_p} \nabla p \tag{3-20}$$

The above formulation relates velocity only to pressure and therefore can be applied to general flows. For multi-phase flows, the $H(U)$ terms consist of two parts: the "transport part", including matrix coefficients for all neighbours multiplied by corresponding velocities and the "source part" (apart from the pressure gradient) comprising the source part of transient terms and the effects of surface tension force on velocities. Divergence of the velocity field can then be expressed as divergence of a predicted velocity field (momentum predictor) and a pressure correction term (explicit velocity correction). Readers can refer to an implicit pressure-velocity coupling numerical algorithm [109] for more details.

$$\nabla \cdot U = \nabla \left(\frac{H(U)}{a_p} \right) - \nabla \left(\frac{1}{a_p} \nabla p \right) \tag{3-21}$$

To include the contribution of compressibility to the pressure equation, the mass conservation (transport) equation for each phase needs to be split into the following two parts as:

$$\frac{\partial \alpha_l \rho_l}{\partial t} + \nabla \cdot \left(\alpha_l \rho_l U \right) = \dot{m} \rightarrow \begin{cases} \dfrac{\alpha_l}{\rho_l} \left[\dfrac{\partial \rho_l}{\partial t} + U \cdot \nabla \rho_l \right] \\ + \\ \nabla \cdot \left(\alpha_l U \right) + \dfrac{\partial \alpha_l}{\partial t} \\ = \dfrac{\dot{m}}{\rho_l} \end{cases} \tag{3-22}$$

$$\frac{\partial \alpha_v \rho_v}{\partial t} + \nabla \cdot \left(\alpha_v \rho_v U \right) = -\dot{m} \rightarrow \begin{cases} \dfrac{\alpha_v}{\rho_v} \left[\dfrac{\partial \rho_v}{\partial t} + U \cdot \nabla \rho_v \right] \\ + \\ \nabla \cdot \left(\alpha_v U \right) + \dfrac{\partial \alpha_v}{\partial t} \\ = -\dfrac{\dot{m}}{\rho_v} \end{cases} \tag{3-23}$$

$$\frac{\partial \alpha_i \rho_i}{\partial t} + \nabla \cdot \left(\alpha_i \rho_i U \right) = 0 \rightarrow \begin{cases} \dfrac{\alpha_i}{\rho_i} \left[\dfrac{\partial \rho_i}{\partial t} + U \cdot \nabla \rho_i \right] \\ + \\ \nabla \cdot \left(\alpha_i U \right) + \dfrac{\partial \alpha_i}{\partial t} \\ = 0 \end{cases} \tag{3-24}$$

Assuming the flow satisfies the perfect fluid assumption, the ideal fluid equation of state can be used to relate pressure and density:

$$\rho = \psi p \tag{3-25}$$

Substituting Eqn (3-25) into Eqn (3-22), (3-23) and (3-24) and assuming constant compressibility, we obtain:

$$\begin{cases} \dfrac{\alpha_l}{\rho_l} \left[\dfrac{\partial p \psi_l}{\partial t} + U \cdot \nabla \left(\rho_l \right) \right] \\ \dfrac{\alpha_v}{\rho_v} \left[\psi_v \dfrac{\partial p}{\partial t} + U \cdot \nabla \left(\rho_v \right) \right] \\ \dfrac{\alpha_i}{\rho_i} \left[\psi_i \dfrac{\partial p}{\partial t} + U \cdot \nabla \left(\rho_i \right) \right] \end{cases} \tag{3-26}$$

By substituting Eqn (3-26) into Eqn (3-22), (3-23) and (3-24) accordingly, the continuity equation for each phase can be reformulated as:

$$\begin{cases} \dfrac{\alpha_l}{\rho_l} \left[\psi_l \dfrac{\partial p}{\partial t} + U \cdot \nabla \left(\rho_l \right) \right] \\ + \\ \nabla \cdot \left(\alpha_l U \right) + \dfrac{\partial \alpha_l}{\partial t} \\ = \dfrac{\dot{m}}{\rho_l} \end{cases} \tag{3-27}$$

$$\begin{cases} \dfrac{\alpha_v}{\rho_v} \left[\psi_v \dfrac{\partial p}{\partial t} + U \cdot \nabla \left(\rho_v \right) \right] \\ + \\ \nabla \cdot \left(\alpha_v U \right) + \dfrac{\partial \alpha_v}{\partial t} \\ = -\dfrac{\dot{m}}{\rho_v} \end{cases} \tag{3-28}$$

$$\begin{cases} \dfrac{\alpha_i}{\rho_i} \left[\psi_i \dfrac{\partial p}{\partial t} + U \cdot \nabla \left(\rho_i \right) \right] \\ + \\ \nabla \cdot \left(\alpha_i U \right) + \dfrac{\partial \alpha_i}{\partial t} \\ = 0 \end{cases} \tag{3-29}$$

Addition of Eqn (3-27), (3-28) and (3-29) leads to the formulation of pressure equation which consists of a *pEgnComp* (compressible) term and a *pEqnIncomp* (incompressible) term.

$$\begin{cases} \dfrac{\alpha_l}{\rho_l}\left[\psi_l \dfrac{\partial p}{\partial t} + U\cdot\nabla\left(\rho_l\right)\right] + \dfrac{\alpha_v}{\rho_v}\left[\psi_v \dfrac{\partial p}{\partial t} + U\cdot\nabla\left(\rho_v\right)\right] + \dfrac{\alpha_i}{\rho_i}\left[\psi_i \dfrac{\partial p}{\partial t} + U\cdot\nabla\left(\rho_i\right)\right] : pEqnComp \\ + \\ \nabla\cdot U - \dot{m}\left(\dfrac{1}{\rho_l} - \dfrac{1}{\rho_v}\right) : pEgnIncomp \\ = 0 \end{cases} \tag{3-30}$$

To link the pressure equation with the semi-discretised momentum equation, divergence of the velocity field is replaced with Eqn (3-21) to give the complete pressure equation implemented in OpenFOAM:

$$\begin{cases} \dfrac{\alpha_l}{\rho_l}\left[\psi_l \dfrac{\partial p}{\partial t} + U\cdot\nabla\left(\rho_l\right)\right] + \dfrac{\alpha_v}{\rho_v}\left[\psi_v \dfrac{\partial p}{\partial t} + U\cdot\nabla\left(\rho_v\right)\right] + \dfrac{\alpha_i}{\rho_i}\left[\psi_i \dfrac{\partial p}{\partial t} + U\cdot\nabla\left(\rho_i\right)\right] : pEqnComp \\ + \\ \nabla\left(\dfrac{H}{a_p}\right) - \nabla\left(\dfrac{1}{a_p}\nabla p\right) - \dot{m}\left(\dfrac{1}{\rho_l} - \dfrac{1}{\rho_v}\right) : pEgnIncomp \\ = 0 \end{cases} \tag{3-31}$$

The source term due to cavitation is added to the incompressible part of the pressure equation. Once the pressure is solved, it is applied to evaluate velocity field following Eqn (20) through a pressure-velocity coupling algorithm.

The LES model is integrated in Eqn (3-15), (3-16) and (3-18) through a local volume averaging procedure that decomposes relevant phase-weighted hydrodynamic variables into resolvable and sub-grid scale components. Elimination of the sub-grid fluctuations from direct simulation is done through a filtering process together with the non-linear convective terms in Eqn (3-16). This process generates additional terms comprising correlation of sub-scale variables that entail closure through additional modelling. Amongst these terms, the most crucial one is the Sub-Grid-Scale (SGS) stress that governs the effect of unresolved turbulence scales on momentum transport process and its dissipation. This term is defined as:

$$\tau_{sgs} = \overline{UU} - \overline{U}\,\overline{U} \tag{3-32}$$

The closure of the SGS stress is achieved through a sub-grid eddy viscosity model given as:

$$\tau_{sgs} + \frac{\mu_{sgs}}{\rho}\left(\nabla\overline{U} + \nabla\overline{U}^{T}\right) = \frac{2}{3}kI \tag{3-33}$$

in which k is the SGS turbulence kinetic energy and μ_{sgs} is the SGS turbulent viscosity. These SGS turbulence parameters are calculated using a one-Equation eddy model for evaluating k attributed to Yoshizawa [49].

$$\frac{\partial k}{\partial t}+\nabla\cdot\left(k\overline{U}\right)-\nabla\cdot\left[\left(\upsilon+\upsilon_{sgs}\right)\nabla k\right]=-\frac{1}{2}\tau_{sgs}:\left(\nabla\overline{U}+\nabla\overline{U}^{T}\right)-\varepsilon \quad (3\text{-}34)$$

where $\varepsilon=C_{\varepsilon}k^{(3/2)}/\Delta$ is the turbulent dissipation, $\upsilon_{sgs}=C_{k}k^{(1/2)}\Delta$ is the SGS kinematic viscosity ($\Delta=\sqrt[3]{V}$ represents the SGS length scale in which V represents the volume of the computational cell under consideration). The turbulent coefficients found from statistical analyses are $C_k=0.07$ and $C_{\varepsilon}=1.05$ [49].

3.3 Mass transfer models

3.3.1 Kunz model

The Kunz mass transfer model [105] treats the vaporisation rate $\dot{m}^{-}$ of the liquid phase at the interface as being proportional to the liquid volume fraction and the amount by which the local pressure p is below vapour pressure p_v. Therefore, the model does not take into account the nucleation of bubbles within the bulk liquid phase. Cavitation inception simply occurs when the static pressure at a point(s) in the fluid domain reduces to vapour pressure. The condensation rate $\dot{m}^{+}$, on the other hand, is only active when vapour is present in a computational unit (or mesh cell) ($1-\alpha_l-\alpha_i>0$) and the local pressure is higher than the vapour pressure. The term $\max\left(p-p_v,0.001p_v\right)$ is used to avoid division by zero. The modified Kunz equations are:

$$\begin{cases}\dot{m}^{-}=\dfrac{C_v\rho_v\alpha_l\min\left(p-p_v,0\right)}{\left(\frac{1}{2}\rho_l U_{\infty}^{\ 2}\right)t_{\infty}}\\ \dot{m}^{+}=\dfrac{C_c\rho_v\left(\alpha_l-\alpha_i\right)^2\max\left(1-\alpha_l-\alpha_i,0\right)\max\left(p-p_v,0\right)}{t_{\infty}\max\left(p-p_v,0.001p_v\right)}\end{cases} \quad (3\text{-}35)$$

C_v and C_c appearing in Eqn (3-35) are two empirical constants (here C_v=1, C_c=1). Values for empirical constants C_v and C_c are chosen to ensure conservative modelling of vaporisation and condensation (rate of mass gain in vapour is equal to rate of mass loss in liquid). This choice also allows direct comparison of the two cavitation models since there are no empirical constants used in the Schnerr cavitation model discussed below. Thus, tuning of these constants is not performed in the present study. Both rates are non-dimensionalised by a mean flow time scale t_{∞}.

$$t_{\infty}=\frac{L_c}{U_{\infty}} \quad (3\text{-}36)$$

where U_{∞} is the free stream velocity and L_c the characteristic length (nozzle diameter).

3.3.2 Schnerr and Sauer model

The Schnerr and Sauer model [106] is based on bubble dynamics from the generalised Rayleigh-Plesset equation. In the present study, a phase change limiter $\max\left(1-\alpha_l-\alpha_i,0\right)$ is added to eliminate numerical instabilities (unbounded volume

fraction) introduced by physically unrealistic condensation and vaporisation rates. The modified vaporisation and condensation rates are defined as:

$$\begin{cases} \dot{m}^{-} = \dfrac{3\rho_l\rho_v}{\rho}\alpha_l \max\left(1-\alpha_l-\alpha_i,0\right)\left(rR_b\right)\sqrt{\dfrac{2}{3\rho_l\left(\left|p-p_v\right|+0.001p_v\right)}}\min\left(p-p_v,0\right) \\ \dot{m}^{+} = \dfrac{3\rho_l\rho_v}{\rho}\alpha_l \max\left(1-\alpha_l-\alpha_i,0\right)\left(rR_b\right)\sqrt{\dfrac{2}{3\rho_l\left(\left|p-p_v\right|+0.001p_v\right)}}\max\left(p-p_v,0\right) \end{cases} \tag{3-37}$$

The inverse of the cavitation nuclei radius rR_b is related to α_l, α_i and bubble density n by:

$$rR_b = \left(\frac{4\pi n\alpha_l}{3\left(\max\left(1-\alpha_l-\alpha_i,0\right)+alpha_{Nuc}\right)}\right)^{1/3} \tag{3-38}$$

where the nucleation site volume fraction $alpha_{Nuc}$ is used to avoid division by zero.

$$alpha_{Nuc} = \frac{n\pi\left(d_{Nuc}\right)^3}{6+n\pi\left(d_{Nuc}\right)^3} \tag{3-39}$$

Therefore, the implementation of the modified Schnerr and Sauer model requires only the specification of the bubble diameter at the nucleation site d_{Nuc} and the bubble density $n(cm^{-3})$. In the present study, bubble diameter is set as 0.1 μm (20% of the smallest mesh size 0.47 μm) and bubble density is set to 2.0×10 cm^{-3} based on the suggestion of Schnerr *et al*. [106] and the criterion that the average total volume of bubbles in each mesh cell does not exceed 20% of smallest mesh cell in order to make $alpha_{Nuc}$ reasonably small.

The choice of these two mass transfer models is based on the consideration that they are formulated based on phase volume fractions and can be readily integrated into the VOF method. Since they are both derivatives of the generalised Rayleigh-Plesset equation, a direct comparison between them is possible.

3.3.3 Numerical configuration

The governing equations are solved by employing a Pressure Implicit with Splitting of Operator (PISO) algorithm. Based on the recent work of Ghiji *et al.* [56], a bounded Normalised Variable (NV) Gamma differencing scheme proposed by Jasak *et al.* [60] with a blending factor of 0.5 is applied to the convection terms and an interface compression scheme (CICSAM) by Ubbink [47] is used for interface compression. A conservative, second order scheme (Gauss linear) is employed for Laplacian derivatives and a second order backward discretisation scheme is adopted for temporal terms.

3.4 Validation of the numerical model

The experimental data from Winklhofer *et.al.* [111] is used for a comprehensive model validation. Measurements are taken for diesel fuel passing through a 300 μm thick

square channel where the injection pressure is fixed at 10 MPa and the back pressure is varied to change the extent of cavitation from inception through to choked flow. Although the injection pressure is lower than modern diesel injection systems which typically produce up to 200 MPa, the data are still used for validation due to lack of available experimental data at high injection pressures. The channel has an inlet width of 301 µm and is slightly converging through a length of 1000 µm to give an outlet width of 284 µm. In order to achieve a range of flow conditions from sub-cavitating to choked flow, the inlet is rounded to give a radius of 20 µm. The computational domain used in the present study for the square channel is shown in *Figure 3-1*. Fuel inlet is set at the left end of the geometry, while a simplified non-reflective pressure outlet is applied to the right end. The remaining face patches of the computational domain are configured to be no-slip and adiabatic walls with a zero-gradient boundary condition for all hydrodynamic variables. The cavitation is normally characterised by a global cavitation number (CN) commonly defined as:

$$CN = \frac{p_{inj} - p_{out}}{p_{out} - p_v} \tag{3-40}$$

Fuel is set to fill the geometry up to the channel exit at 304 K and 10 MPa. Detailed properties of the fuel and operating conditions are given in *Table 3-1*.

Table 3-1: Fuel properties and boundary conditions based on experimental setup [111, 112].

Parameter	Value
Injection pressure	10 MPa
Fuel	Diesel fuel
Fuel density	832 kg/m^3
Gas	Compressed air
Fuel dynamic viscosity	0.0065 N s/m^2
Surface tension	0.03 N/m
Vapour density	0.1361 kg/m^3
Vapour pressure	2000 Pa
Vapour dynamic viscosity	5.953×10^{-6} N s/m^2
Temperature	304 K
Ambient pressure	3-8 MPa
Cavitation number	0.25-2.33
Max velocity	150 m/s
Fuel Reynolds number	1817−5452

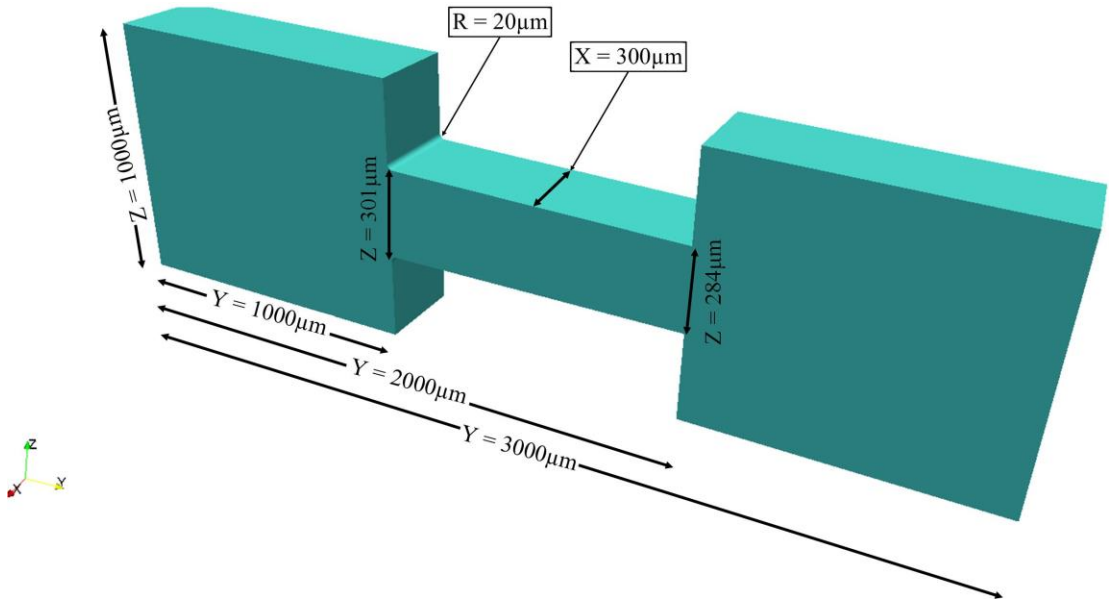

Figure 3-1: Mesh geometry for modelling of the experimental flow by Winklhofer et.al. [111] within a nominally square channel of thickness 300 µm, an inlet width of 301 µm, inlet radius of 20 µm, outlet width of 284 µm and a channel length of 1000 µm.

As shown in *Figure 3-2*, hexahedral mesh cells with a minimum size of 0.5 µm are distributed along the channel wall with a growth rate of 1.02 towards the channel centre and outside channel, resulting in the use of 6 million elements for the whole computational domain. The Kolmogorov scale η representing the smallest hydrodynamic turbulent scale can be obtained from:

$$\eta = \frac{W}{(\mathrm{Re})^{3/4}} \tag{3-41}$$

$$\mathrm{Re} = \frac{\rho u W}{\mu} \tag{3-42}$$

The characteristic length W is the outlet width (284 µm) of the channel and Re is the flow Reynolds number defined by density (ρ), flow velocity (u) and dynamic viscosity (μ) in Eqn (3-42). Due to density variation in compressible flow, a single Kolmogorov scale cannot be determined for gas phases which are highly compressible. However, as the density of the liquid fuel stays relatively constant at 832 kg/m^3 due to low compressibility, its Kolmogorov scale η_l can be estimated to be 0.47 µm. The minimum mesh size in the boundary layer is comparable with the liquid fuel Kolmogorov scale in the square channel.

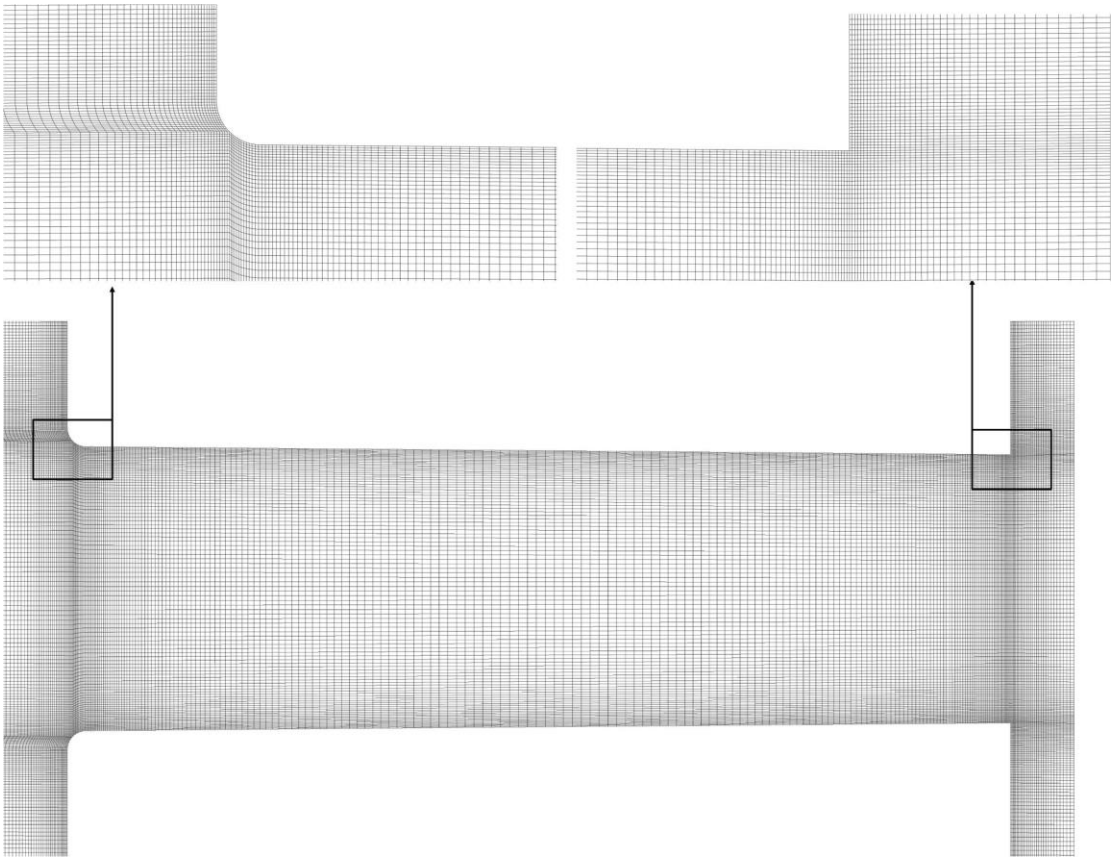

Figure 3-2: Computational domain for the square channel. Minimum mesh size of 0.5 μm is used to form the boundary layer near the channel wall. The mesh distribution is shown at the centre plane ($x = 0$) of the square channel. Detailed meshing topology around the channel inlet and exit is depicted in the enlarged views. Layers of mesh elements are constructed from the boundary layer with a growth rate of 1.02. In total 6 million mesh elements are used to discretise the computational domain.

To validate the cavitation model for different conditions, the back pressure is varied from 7.5 to 2 MPa, corresponding to a pressure difference (Δp) from 2 to 7.5 MPa. The Schnerr mass transfer model described in section 3 is used to model cavitation phenomenon due to its independence of empirical constants. In total 10 simulations with different Δp values were run to quasi-steady state where the velocity at the channel exit stabilises, as shown in *Figure 3-3*. All simulations were performed on a high performance cluster with 48 CPUs and 60GB of physical memory. The average temporal step size was around 1.5 ns with a fixed Courant number of 0.3. The wall clock time for each simulation was around 150 hours.

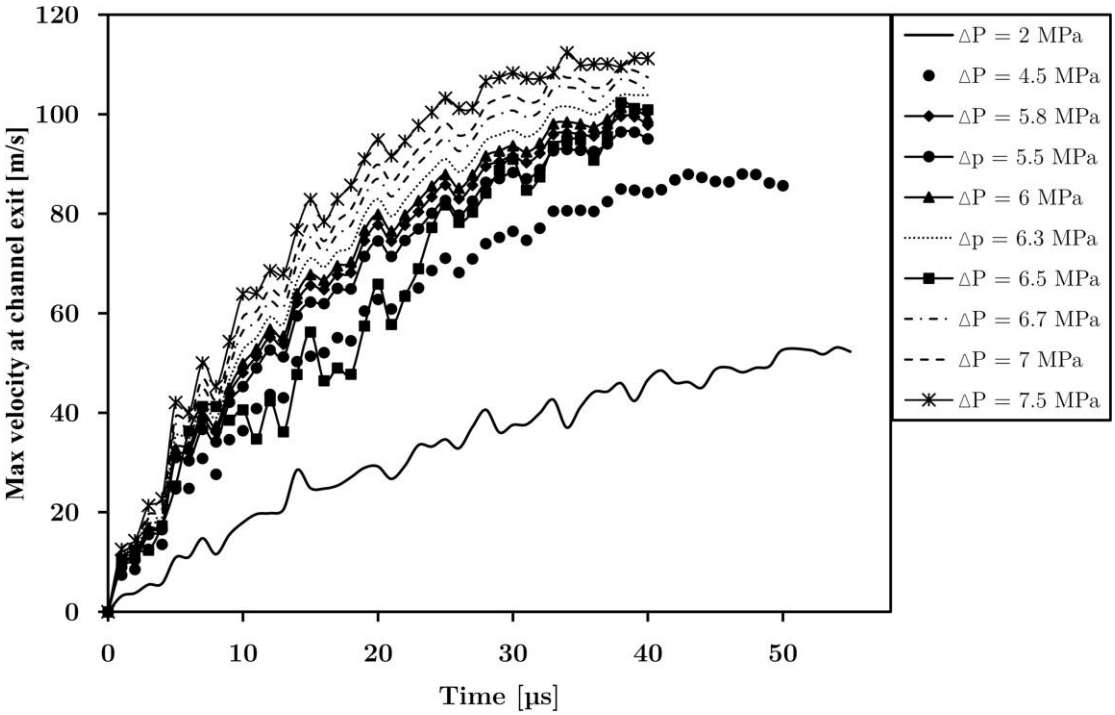

Figure 3-3: Time dependent maximum velocity at the channel exit for 10 different pressure conditions. The flow reaches quasi-steady state at around 40 μs for Δp = 2 MPa cases and 55 μs for Δp = 2 MPa.

Comparison of simulated and measured mass flow rates and pressure data at different flow conditions are presented in *Figure 3-4*. The developed numerical model captures the effect of pressure on mass flow rates with favourable accuracy. The trend that mass flow rate increases almost linearly with increasing difference between injection and back pressures is also well captured. When the difference between injection and back pressures has exceeded 7 MPa (Δp > 7 MPa), both experiment and simulation show that further reducing the back pressure has only a minor effect on the rate of injection. This is because, at Δp = 7 MPa, the flow has become choked (e.g. mass flow rate does not increase with decrease in back pressure). The collapse of the mass flow rate after the flow has become choked is also reported by Payri *et al*. [113]. When the flow becomes choked, flow separation and cavitation induced pressure reduction in the first half of the channel and the pressure rise with recovery of flow area in the second half are accurately simulated, as shown in *Figure 3-4(b).* However, pressure values at the outlet could be affected by some experimental artefacts since the measurement is approximately one-third lower than the specified outlet pressure. Numerical prediction is therefore not expected to match experimental measurements at the outlet.

In *Figure 3-5*, comparison of averaged velocity profiles at the contracted core (53 μm from the channel inlet) shows that the predicted values are comparable with the measured data. The velocity profiles are symmetric due to nozzle symmetry. The flow velocity reaches to a maximum in the shear layer due to flow separation (40 μm from the wall) and decreases towards the channel centre. With higher pressure differences, an increase in flow velocity is observed. However, the simulations over-predict the velocity especially near the channel wall. This could be partly attributed to underestimation of fluid viscosity. Moreover, values such as surface tension and viscosity in Table 1 could have large margins of error [112]. Also, the compressibility of diesel vapour is an estimation based on the ideal gas law. Another reason could be

the assumption that the channel wall is perfectly smooth, which results in the omission of the effects of wall roughness on the fluid flow. Further, the accuracy of the experimental data is uncertain.

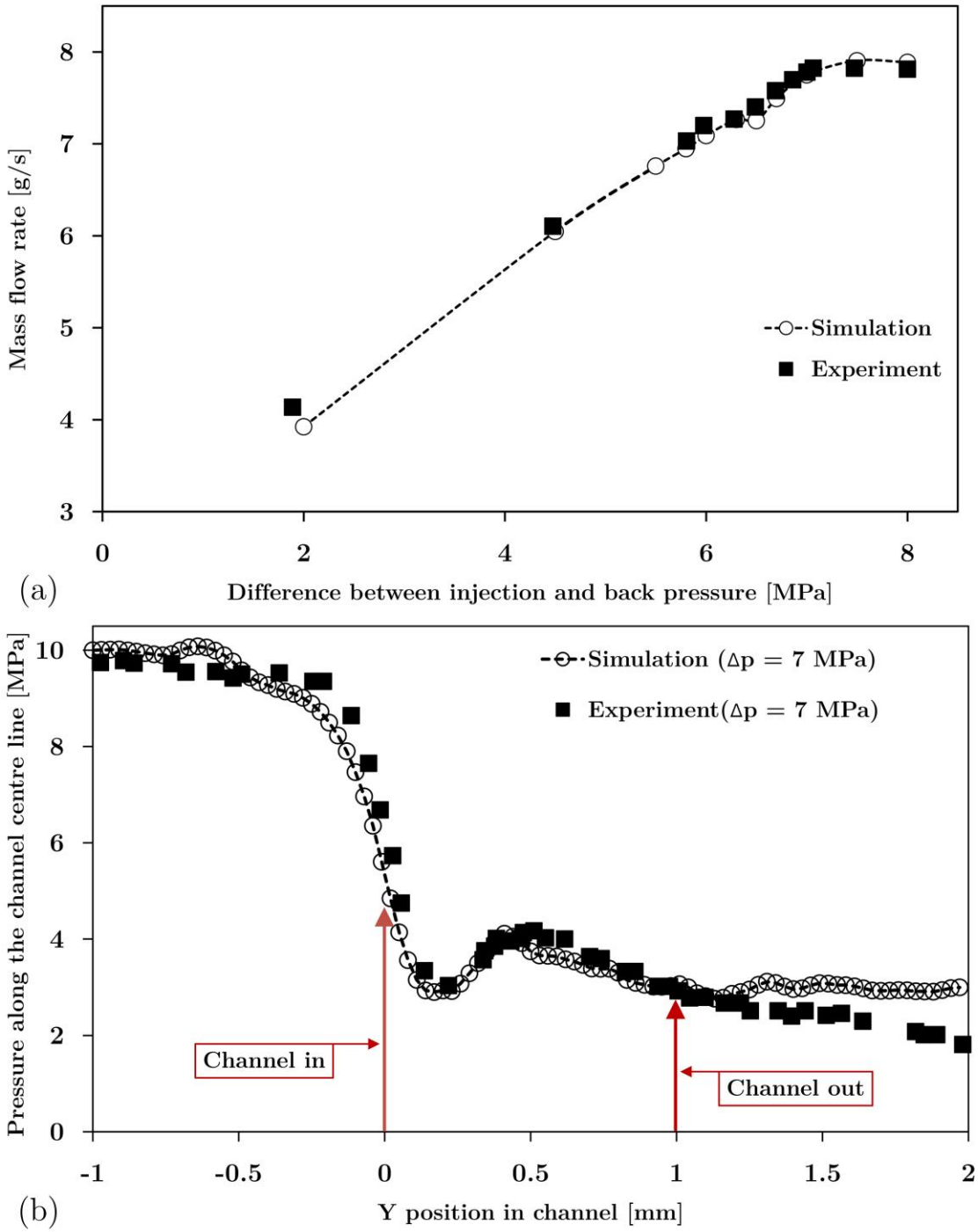

Figure 3-4: Comparison of the measured and simulated mass flow rates at different pressure conditions (a), and pressure along the channel centre line when the flow becomes choked (b). Simulation results are averaged over 10 µs after the quasi-steady condition has been achieved.

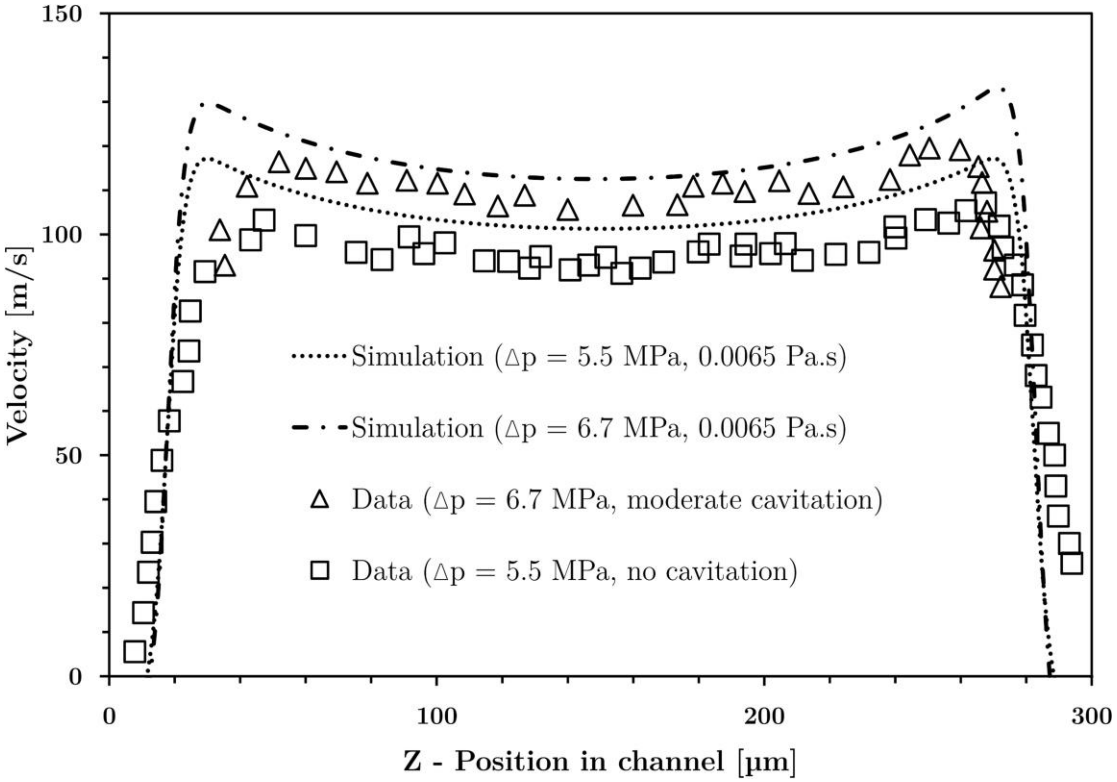

Figure 3-5: Simulated and measured velocity profiles at 53 µm from channel inlet. Data are collected for 100 bar injection pressure and two different back pressures (no cavitation: 4.5 MPa and developed cavitation: 3.3 MPa). Both simulated velocity profiles are time averaged over 10 µs after the quasi-steady condition has been achieved.

Reduction of pressure downstream of the channel entrance before cavitation inception is demonstrated by both simulation and experiment as shown in *Figure 3-6(a)*. The extent of the low pressure region simulated is consistent with the experimental measurements. Cavitation inception occurs when the back pressure is set to 40 bar (Δp = 6 MPa *Figure 3-6(b)*). As the back pressure decreases, vapour cavities start to form in the recirculation zone and build up along the channel wall. At 30 bar back pressure (Δp = 7 MPa) the flow is choked and complete separation of flow from the channel entrance occurs (*Figure 3-6(c)*). When the pressure difference increases to 8 MPa (*Figure 3-6(d)*), a contracted liquid core can be observed in the channel, indicating that the flow has become fully choked. The observed deviation between simulations and experiments, in terms of extent and morphology of the cavitation, can be attributed to the reasons given above. Specifically, apart from uncertainties in fluid properties, omission of surface imperfections on the round entrance and channel wall in the numerical model leads to less cavitation formation in the channel compared with the experiments. These uncertainties, however, are difficult to eliminate in numerical simulations due to limited computing power. Further, the experimental data shown in *Figure 3-6(c-d)* represent the ensemble average of 20 instantaneous images taken under the same operating conditions, while the simulations are time averaged for 10 µs immediately after quasi-steady flow conditions have developed for a single realisation. In general, the developed numerical model is able to capture in-nozzle cavitation phenomena well and therefore is used to investigate the inner and near nozzle flow of a real size diesel injector.

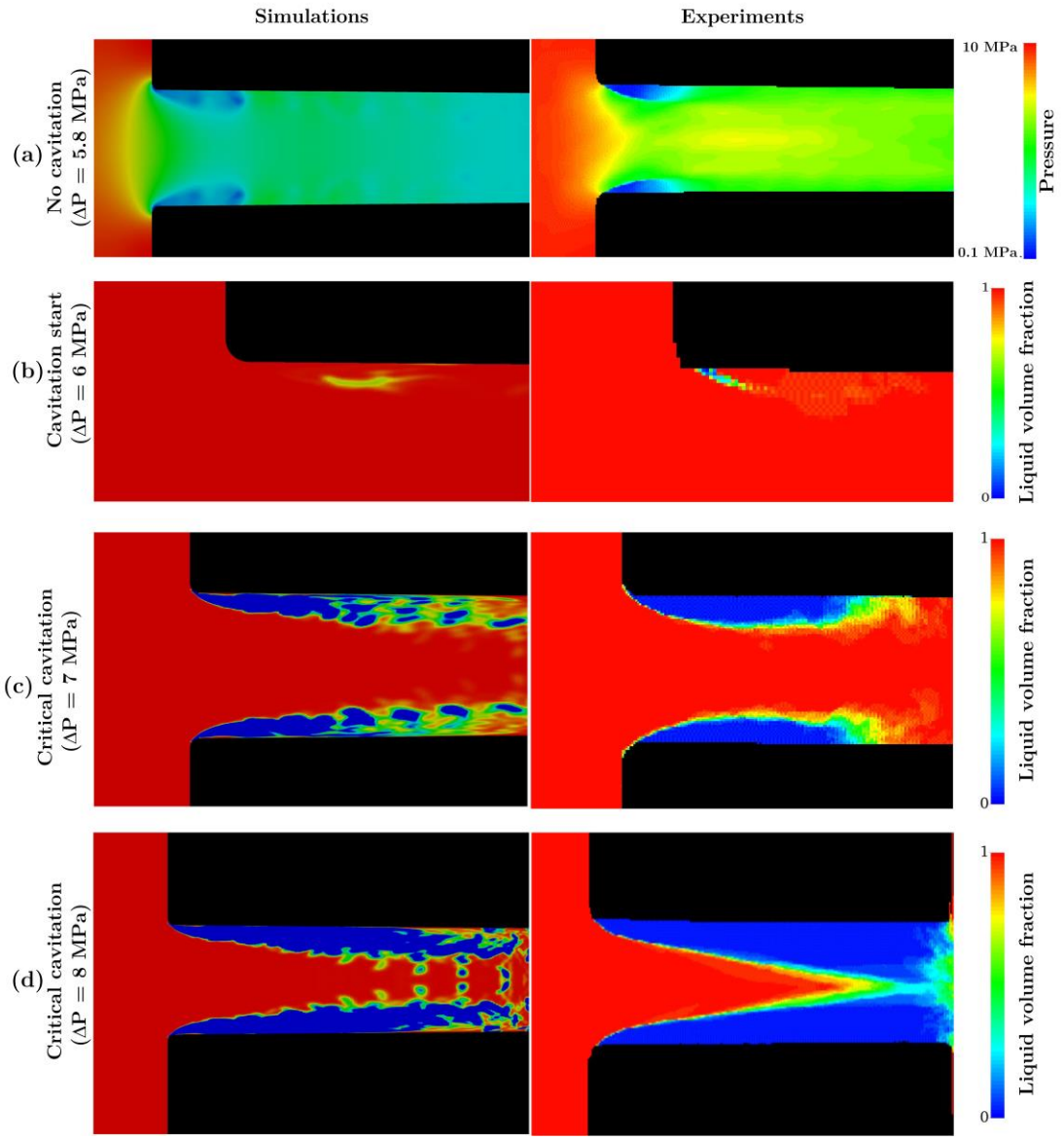

Figure 3-6: Averaged pressure contour plots (a) at the nozzle centre plane ($x = 0$) for Δp = 5.8 MPa; Averaged contour plots (b) of liquid volume fraction for Δp = 6 MPa (start of cavitation); and averaged contour plots (c) and (d) of liquid volume fraction Δp = 7&8 MPa (fully choked flow). The simulation images are obtained by time averaging the pressure and liquid volume fraction fields over 10 µs immediately after the quasi-steady flow conditions have developed for a single realisation, while the experimental results are based on ensemble averaging for a set of 20 images taken under the same operating conditions.

3.5 Characterisation of nozzle flow and primary spray breakup

The effects of the Kunz and Schnerr cavitation models on the predicted internal nozzle flow and primary breakup of a diesel spray are presented in this section. To demonstrate the capability of the developed compressible multi-phase cavitation model and the effects of cavitation, simulated inner flow phenomena and near nozzle flow structures are compared with predictions from the same method without a phase change model using multi-phaseCompressibleInterFoam (referred to as non-cavitating).

3.5.1 Case setup

Experimental conditions summarised in Ghiji *et al.* [56], relevant for a non-evaporating spray injected into a constant volume chamber from a sharp edged orifice are simulated. The properties of the diesel fuel and vapour, except for the temperature and Reynolds number, are given in *Table 3-1*. The ambient region (chamber) is non-reactive and initially filled with compressed air at 3 MPa. The computational domain representing a diesel injector includes the sac, nozzle and a portion of the chamber is shown in *Figure 3-7*. Boundary conditions are similar to the experimental setup of Ghiji *et al.* [56] given in *Table 3-2*. The experimental installation is capable of 120 MPa injection pressure but only the first 100 µs of injection is presented in this study because transition from onset of cavitation to complete flow detachment is simulated to occur within this period. For simplicity, the pressure at the sac inlet is increased linearly from 3 MPa to 60 MPa in 100 µs due to the lack of detailed knowledge of the time varying pressure profile in the injector sac.

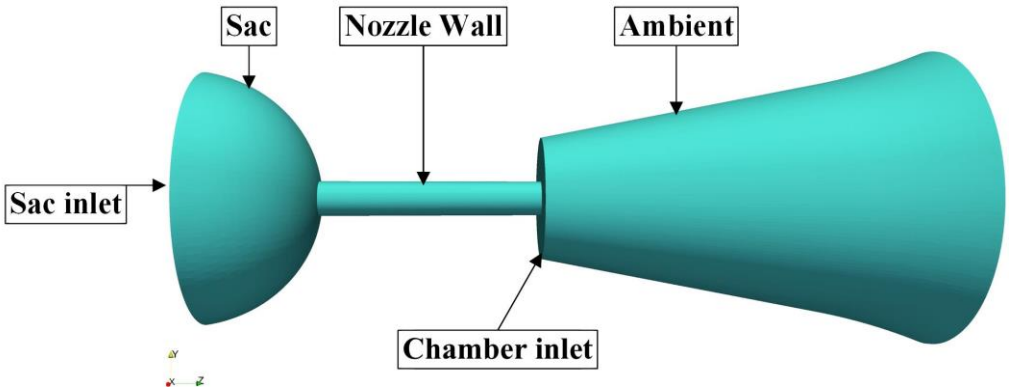

Figure 3-7: Boundary definitions and the computational domain.

Table 3-2: Initial and boundary configurations for the diesel spray simulation. The nozzle diameter is used as the characteristic length for relevant parameters. The indicated injection velocity and range of fuel Reynolds number are estimated at quasi-steady conditions [56] when the pressure in the injector sac reaches 120 MPa.

Parameter	Value
Nozzle diameter	0.25 mm
Nozzle length	1.6 mm
Chamber pressure	3 MPa
Temperature	298 K
Cavitation number	0-19.01
Indicated injection velocity (U_∞)	367 m/s
Fuel Reynolds number	7000−37000
Fuel turbulence intensity	4.4%
Fuel Kolmogorov scale	0.1 µm
Gas turbulence intensity	10%
Maximum sac inlet pressure	60 MPa
Sac	No-slip and zero gradient (adiabatic)
Nozzle wall	No-slip and zero gradient (adiabatic)
Chamber in	No-slip and zero gradient (adiabatic)
Ambient	Non-reflective pressure boundary (adiabatic)

When the sac pressure reaches 60 MPa at the end of simulation, the indicated injection velocity and fuel Reynolds number would be much smaller than those estimated at quasi-steady state where the sac pressure increases to 120 MPa in the experiment. According to Eqn (3-41), the fuel Kolmogorov scale at the end of simulation is thus expected to be larger than 0.1 µm which is estimated at 120 MPa sac pressure. Based on this consideration and the computing capacity, the smallest mesh size of 0.7 µm is used for the boundary layer in the nozzle. A growth rate of 1.02 is applied from the boundary layer to the remaining parts of the computational domain, which results in the use of a total 12 million hexahedral mesh elements. Detailed meshing topology and dimensions for the computational domain are shown in *Figure 3-8*.

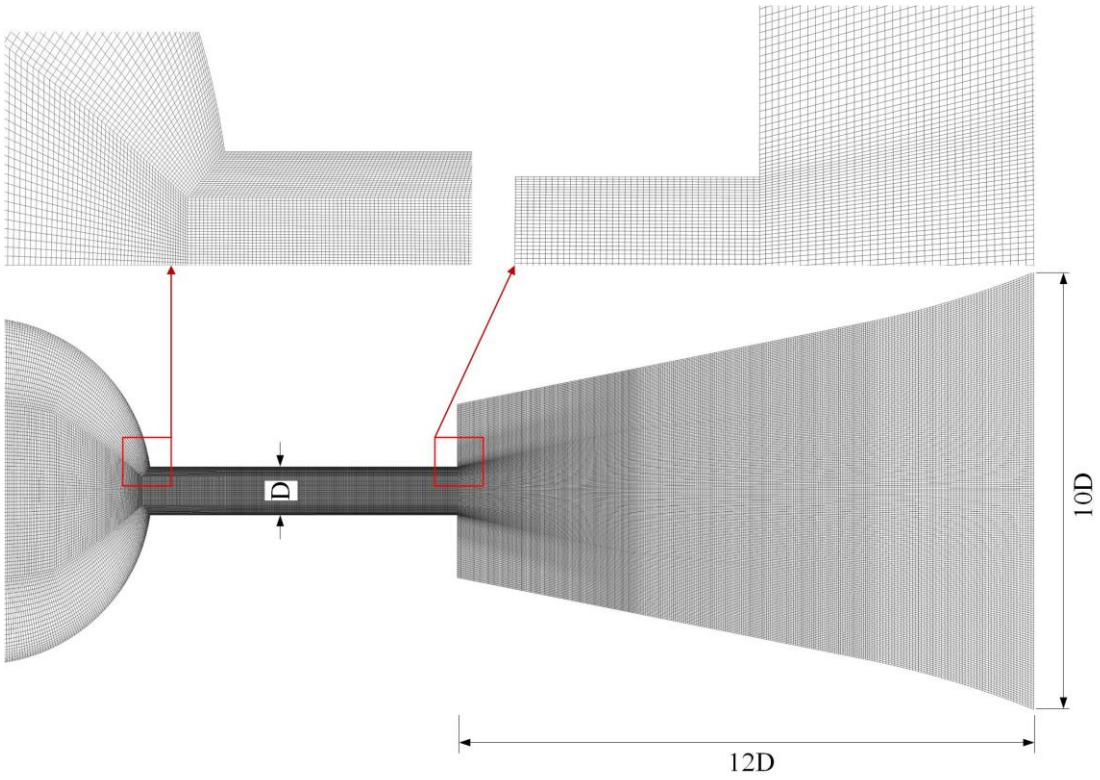

Figure 3-8: Dimensions and mesh topology for the computational domain. Refined hexahedral elements of 0.7 µm are distributed in the nozzle at the wall. The mesh size increases gradually from the nozzle with a grow rate of 1.02. In total, 12 million hexahedral elements are used.

Simulations with the Kunz model, the Schnerr model and the non-cavitating method were performed using 64CPUs and 80GB of physical memory. The max Courant number was set to 0.2 ensuring high resolution temporal integration with an average step size of 1 ns. The wall clock time for each simulation was around 200 hours. All contour plots presented below are shown for the centre plane ($x = 0$) unless otherwise specified.

3.5.2 Internal flow phenomena

At the sharp nozzle inlet, flow separation creates a recirculation zone in which pressure can decrease to vapour pressure as shown in *Figure 3-9(a)* at 25 µs after start of injection (ASOI). This triggers phase change and fuel starts to vaporise as depicted in

Figure 3-9(b). Both implemented cavitation models are able to capture this phenomenon, while the non-cavitating method does not allow cavities to form.

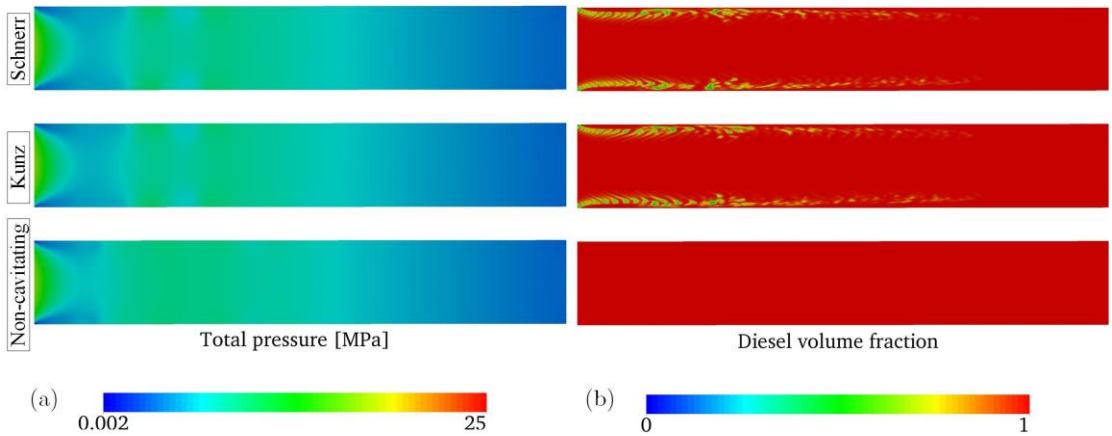

Figure 3-9: Contour plots of pressure (a) and diesel volume fraction (b) at 25 µs ASOI. Cavities form in the recirculation region after the sharp nozzle inlet where local pressure reduces to vapour pressure. Cavities are not present in the non-cavitating simulation due to the absence of a phase change model.

When cavitation occurs, the effective flow area of the nozzle is decreased. To compensate for the reduced flow area, the flow velocity in the cavitation region increases as can be seen in *Figure 3-10(a)*. This complies with the observation of Payri *et al*. [79] that cavitation is accompanied by an increase in velocity coefficient. Further downstream where the local pressure increases, the effective area recovers due to collapse of cavities and therefore the axial flow velocity is reduced. This explains why the cavitation models predict a more extended high velocity region in the nozzle (500 µm from the inlet) than that (250 µm from the inlet) predicted by the non-cavitating simulation where the recovery of flow area occurs earlier. In *Figure 3-10(b)*, the turbulent eddies are depicted using a Q [114, 115] isosurface of 5×10^5 [s^{-2}] which is coloured by total pressure. Small and large turbulent eddies generated and developed within the boundary layers are captured by each cavitation model, while the non-cavitating method predicts mainly the production of large scale eddies. Formation and collapse of cavities together with wall shear lead to a relatively unstable flow in the nozzle as compared to the non-cavitating case in which the flow only experiences wall shear. This indicates that initially cavitation is a significant source for internal nozzle flow irregularities.

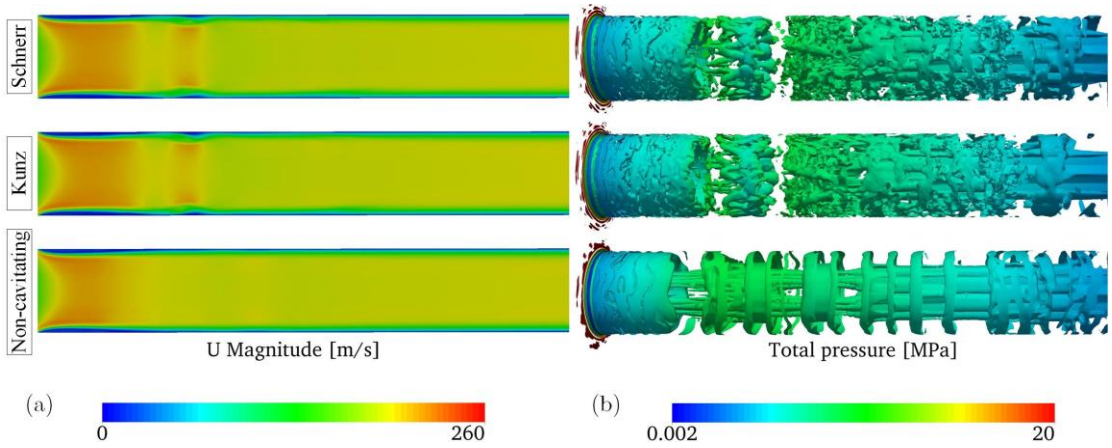

Figure 3-10: Contour plots of velocity magnitude (a) and turbulent eddies (b) in the nozzle for three simulation cases at 25 µs ASOI. The high velocity region extends about 500 µm and 250 µm into the orifice in the cavitation and non-cavitating simulations respectively. Turbulent eddies are represented by a Q [114, 115] isosurface of 5×10^5 [s^{-2}], coloured by total pressure. The absence of cavitation induced turbulence in the non-cavitating simulation leads to a more stable boundary layer flow than the cavitating simulations where flow is disturbed by both wall shear and cavitation.

At a later stage (30 µs ASOI), as depicted in *Figure 3-11(a)*, the growth of cavities along the nozzle wall all the way to the nozzle exit signifies that generated cavities now have a collapse time comparable to their transit time in the nozzle [70]. This can be further escalated to supercavitation when vapour cavities extend and collapse outside the nozzle exit, which is discussed in the next section. Increase in the quantity of eddies generated in the boundary layer is observed to be concurrent with the growth of cavities from 25 µs (*Figure 3-10(b)*) to 30 µs ASOI (*Figure 3-11(b)*). In comparison with the flow at 25 µs ASOI, the low pressure region (pressure ≤ 2 MPa) at 30 µs ASOI extends further, about one-quarter of the nozzle length into the orifice. Apart from pressure variation in the boundary layer, flow structures simulated by the non-cavitating method do not exhibit significant difference between 25 µs and 30 µs due to unchanging wall shear.

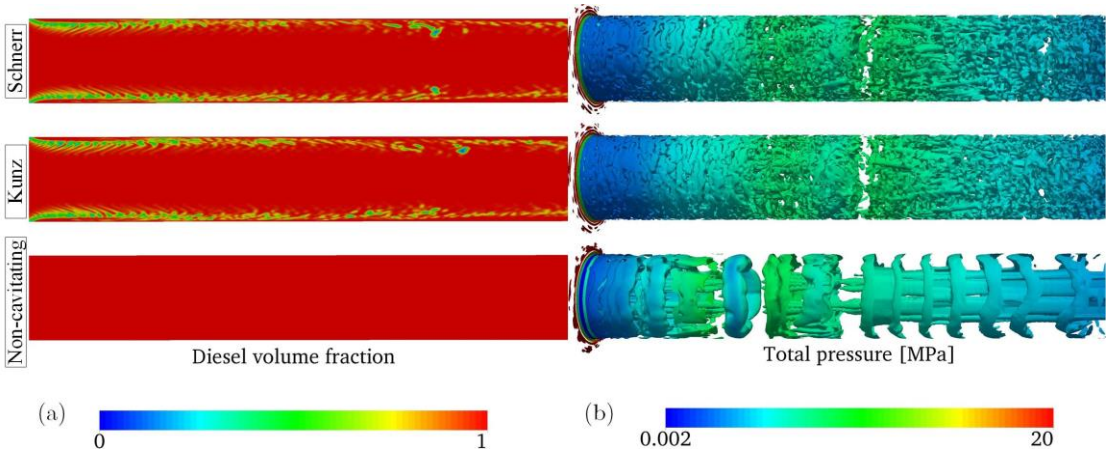

Figure 3-11: Contour plots of diesel volume fraction (a) and turbulent structure (b) for three simulation cases at 30 µs ASOI. Turbulent eddies are represented by a Q [114, 115] isosurface of 5×10^5 [s^{-2}], coloured by total pressure. More small scale turbulent eddies are generated in the cavitation simulations, while the turbulence predicted by the non-cavitating simulation exhibits negligible difference with that predicted at 25 µs ASOI. The low pressure region (pressure ≤ 2MPa) in the cavitation simulations extends about one-quarter nozzle length into the orifice.

After the jet has completely detached from the nozzle wall (56 µs ASOI), air starts to be drawn into the nozzle. This is triggered by the pressure difference between the vapour phase in the nozzle and the gas phase in the chamber, which creates a pressure gradient that drives air into the orifice. Air entrainment only extends around 200 µm into the orifice, not all the way to the contracted core. The end result is that the wall boundary layer consists of three different mixtures: vapour and liquid; vapour, liquid and ambient gas; then liquid and ambient gas, moving from inlet to exit. The composition of the mixture in the boundary layer at onset of complete flow detachment agrees with the predictions for a cavitating nozzle reported by Westlye *et al.* [81].

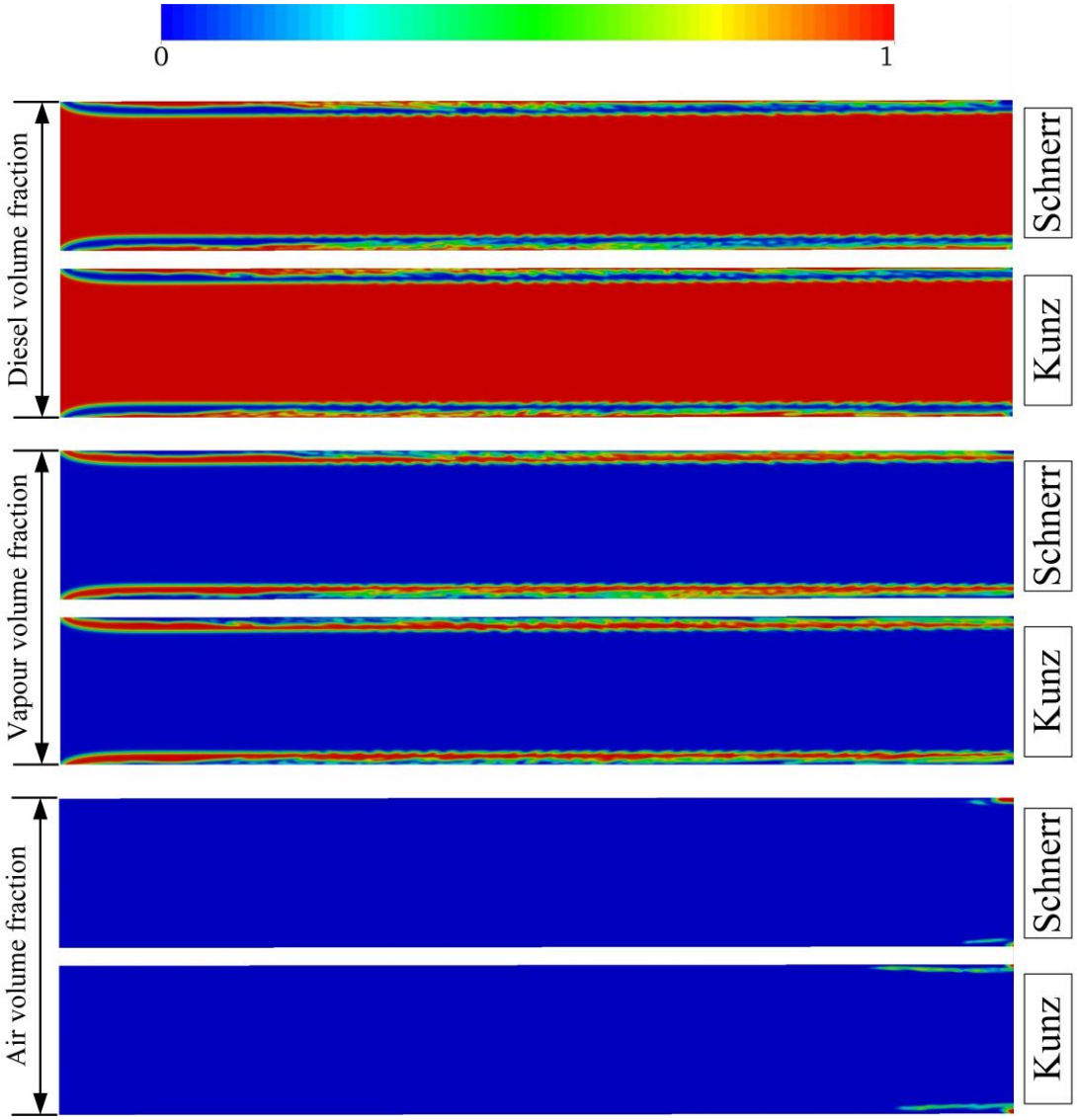

Figure 3-12: Sectional contour plots of diesel, vapour and air volume fractions in the nozzle at 56 µs ASOI when complete flow detachment occurs. Moving from left (nozzle entrance) to right (nozzle exit), the boundary layer consists of three types of mixture: vapour and liquid; vapour, liquid and ambient gas; then liquid and ambient gas. Model comparison shows that more air is drawn in the nozzle exit in the Kunz simulation.

The main difference between the Schnerr and Kunz simulations from the results shown in *Figure 3-12* is the ingestion of air into the orifice. In the Kunz model, the rate of vaporisation is inversely proportional to the in-nozzle free stream velocity (indicated injection velocity in *Table 3-2*), as can be interpreted from Eqn (3-35). In the present study, the indicated injection velocity is estimated at quasi-steady conditions, which could be much higher than the maximum injection velocity at the end of simulation. This results in underestimation of diesel vaporisation rate in the Kunz model compared with the Schnerr model. At the end of the nozzle, pressure rise enhances vapour condensation on the liquid-vapour interface. Since the Kunz model predicts less vapour production throughout the simulation compared to the Schnerr model, it allows more air into the orifice in order to compensate for the reduced vaporisation rate.

In *Figure 3-13*, comparing the velocity profiles at the nozzle exit at 56 µs ASOI reveals that injection velocity from the non-cavitating method is lower than the cavitating

models. The reason for the prediction of higher injection velocity by the cavitation models is the complete detachment of the jet from the wall, eliminating the effects of wall shear on the jet. Also, the reduction in viscosity in the vapour occupied zone results in a more squared velocity profile captured by the two cavitation models than that by the non-cavitating code. Such a top hat velocity profile has also been demonstrated by Payri *et al.* [116] for a one-hole cavitating nozzle. In the boundary layer within 15 µm of the wall, however, the pressure gradient triggers air inflow at the nozzle exit. The negative velocity gradient caused by air inflow results in the prediction of a lower velocity boundary layer flow by the cavitation models compared to the non-cavitating case. Also, the Kunz model gives a slightly lower flow velocity in the boundary layer compared to the Schnerr model. This can be attributed to the reduced vaporisation rate in the Kunz model, leading to a larger pressure gradient at the nozzle outlet.

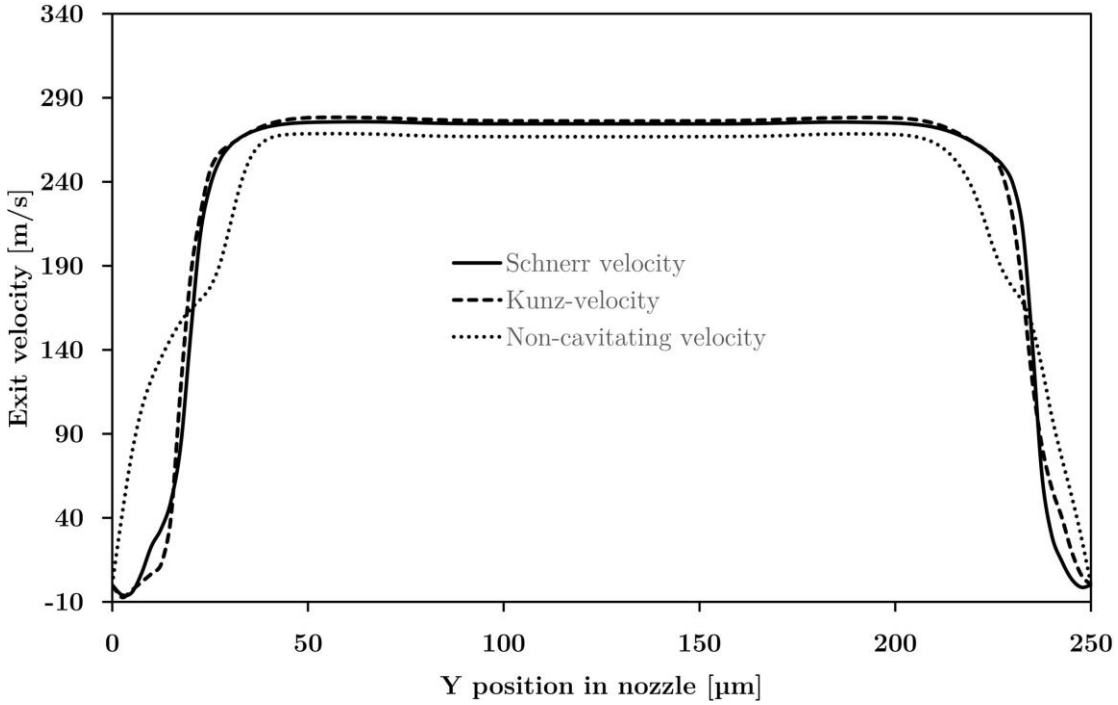

Figure 3-13: Comparison of velocity profiles simulated using Kunz, Schnerr and non-cavitating models at the nozzle exit after complete flow detachment in the nozzle (56 µs ASOI).

In *Figure 3-14* sectional contour plots of vorticity magnitudes at the start, middle and end sections of the nozzle tube for the three different models at 56 µs ASOI are presented. At 5 µm from the nozzle inlet, wall shear and liquid acceleration enhance the production of turbulence in the boundary layer for all cases. The extent of boundary layer turbulence is observed in the non-cavitating simulation to be slightly less (thinner) than the other two cases owing to the absence of cavities. Moving from the inlet to the end section, it is observed in the cavitation simulations that there is minimum production of turbulence due to wall shear because of the presence of vapour between the jet and the nozzle wall [81]. However, high level of turbulence (vorticity > 3.7×10^7 [s^{-1}]) is observed at the liquid-vapour interface. The reason for this could be the difference in viscosity and velocity between the liquid and vapour phases, resulting in shear stresses that enhance turbulence production on the interface. On the other hand, the persistent liquid-wall interaction in the non-cavitating simulation leads to increased turbulence towards the nozzle wall primarily due to wall shear. However, the level of

turbulence from liquid-wall interaction is much smaller than that from liquid-vapour interaction.

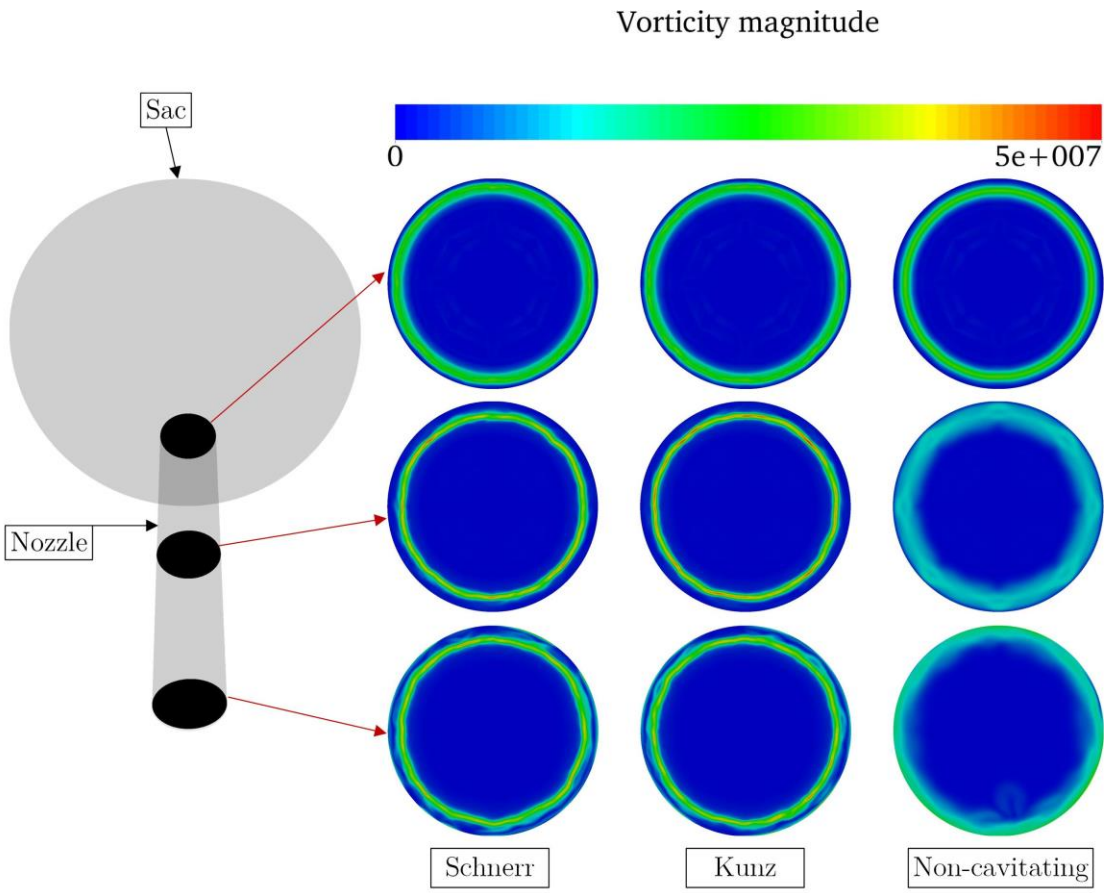

Figure 3-14: Sectional contour plots of vorticity magnitudes taken at the start (5 µm from the inlet) middle and end sections of the nozzle length for three simulations. All plots are taken at 56 µs ASOI (after complete flow detachment).

3.5.3 Primary spray breakup

The penetrating spray and the nozzle flow are represented in *Figure 3-15* by a liquid volume fraction isosurface ($\alpha = 0.9$) coloured by velocity magnitude. The temporal evolution of the spray is displayed at 19, 20, 37 and 56 µs ASOI. At 1 µs before internal flow separation, the emerging spray predicted by the three models is of similar shape. The mushroom like structure at the leading edge is the result of interaction of the compressed air ahead of the penetrating tip and the liquid jet. Surface instabilities start to develop at the edge of the mushroom structure and only minor disturbances are observed on the liquid surface. At 20 µs ASOI, a ring of cavitation bubbles is predicted by the cavitation models in the separation region near the nozzle entrance. By 37 µs ASOI aerodynamic forces start to strip small scale structures such as liquid ligaments and droplets from the liquid surface in the wake and at the edge of the 'mushroom'. In-nozzle turbulence and cavities have grown in the boundary layer, which enhance surface instabilities on the jet. The flow structures simulated by the Schnerr and Kunz models exhibit negligible difference, while the non-cavitating code predicts a much less disturbed exiting jet. However, the opposite trend is observed after the occurrence of complete flow detachment when wall shear disappears in the cavitation simulations at 56 µs ASOI. After this transition to complete flow detachment, the cavitation models

predict that the spray dispersion is narrowed and there is an intact liquid core leaving the nozzle exit. The near wall region is completely filled with mixtures composed of liquid, vapour and ambient gas connected to the chamber (also seen in *Figure 3-12*). At this stage the non-cavitating code captures a more turbulent exiting jet than the cavitation models. This is attributed to the persistent presence of wall shear (refer to comparison in *Figure 3-13* and *Figure 3-14*) which introduces turbulent disturbances on the surface of the jet. Note however that there is still a layer of high vorticity generation for the cavitating cases at the junction of the liquid core and the vaporous cavity, as shown in *Figure 3-14*.

Sectional contour plots of diesel volume fraction before (30 μs ASOI) and after onset of supercavitation (37 μs ASOI) are shown in *Figure 3-16*. The internal nozzle flow is displayed as well as the emerging spray. In the cavitation simulations at 37 μs ASOI, development of long cavities occurs in the first half of the nozzle while residual cavitation bubbles from early stages (30 μs) detach from the nozzle wall forming cavitation clouds and continue to travel downstream until they collapse outside the nozzle exit. Flow reattachment is observed just downstream as recovery of flow area. At the leading edge of the jet, in comparison with the Schnerr model, the Kunz model predicts a mushroom structure with a slightly smaller span and a deeper necking just behind the mushroom. The reason could be underestimation of vaporisation rate on the liquid-vapour interface in the Kunz model. The effects of the reduced vaporisation, however, are not significant from visual comparison of the two cavitation simulations and more comprehensive parametric analyses would be required to fully quantify this. Surface irregularities observed in the non-cavitating case are considerably smaller. This indicates that, as well as wall shear and in nozzle flow separation, cavitation is a significant factor contributing to early breakup of the spray. In the non-cavitating simulation, primary breakup of the spray is observed despite the elimination of the effects of in-nozzle cavitation. The in-nozzle flow separation and wall shear, in this case, are the main sources of surface instabilities, which contribute to primary spray breakup. To quantify the effect of in-nozzle cavitation on the emerging spray, a liquid core analysis technique of Leboissetier *et al*. [117] is employed. In *Figure 3-17*, the spray is divided into three different zones that have been exclusively occupied by liquid (grey), gas (black) or liquid-gas interface (white). The width of the spray is measured at the first protrusion of the liquid-gas interface along the penetration axis for all cases. Visual and measurement comparison reveal that in-nozzle cavitation contributes significantly to the increase in spray dispersion width and the generation of irregularities on the jet surface. This is consistent with experimental measurements and observations by Payri *et al*. [79, 113].

Details in the vapour collapse region of the jet are resolved in *Figure 3-18* which shows sectional contour plots of diesel volume fraction, total pressure and rate of condensation at 37 μs ASOI. Once cavities extend outside the nozzle exit, they collapse within the liquid jet with pressure recovery. However, low pressure regions appear where cavities collapse. This may be attributable to liquid inertia and cavity oscillations. Localised low pressure regions and convex surface protrusions are observed to correlate spatially with regions of high vapour condensation rate. The presence and collapse of cavities within the liquid jet creates pressure gradients , as observed by Schnerr *et al*. [118]. The exclusion of the surface tension force between liquid and vapour also adds diffusion to the interface where the condensation rate is high. The results shown in *Figure 3-16* and *Figure 3-17* show the amplitudes of surface instabilities in the cavitating cases to be much greater than those in the non-cavitating case. The presence of collapsing

cavitation bubbles within the emerging jet suggests they play a role in the greater development of surface instabilities and breakup in the cavitating cases compared with the non-cavitating despite the presence of turbulence.

3.5.4 Quality of the LES simulation

A mesh sensitivity study has not been done because for VOF-LES methods, increasing mesh refinement always leads to an increasingly high resolution of interphase capturing. Unlike the Reynolds averaged models, such a trend persists until the mesh is fine enough for a DNS simulation. However, the quality of the LES can be assessed by evaluating the resolved kinetic energy as a fraction of the total kinetic energy in the computational domain for the simulation with the Schnerr Model. The resolved kinetic energy is obtained from the Root Mean Square of the velocity components and time averaged over the simulation. It is then divided by the time averaged total kinetic energy (resolved kinetic energy + contribution of the sub-grid kinetic energy) to quantify how much kinetic energy is resolved by the grid. As shown in *Figure 3-19*, the spikes are where fluctuation in velocity occurs e.g. at the nozzle inlet, outlet and the liquid-gas interface. The fluctuation of velocity can lead to less kinetic energy captured by the grid. Therefore the decrease in the percentage of the resolved kinetic energy. However, the flow is very well resolved by the grid from the inlet up to the end of the chamber since the resolved kinetic energy is more than 85% of the total kinetic energy [67]. This indicates that the in-nozzle phenomena and their effects on the early spray breakup are sufficiently captured and LES is valid for the entire domain and simulation.

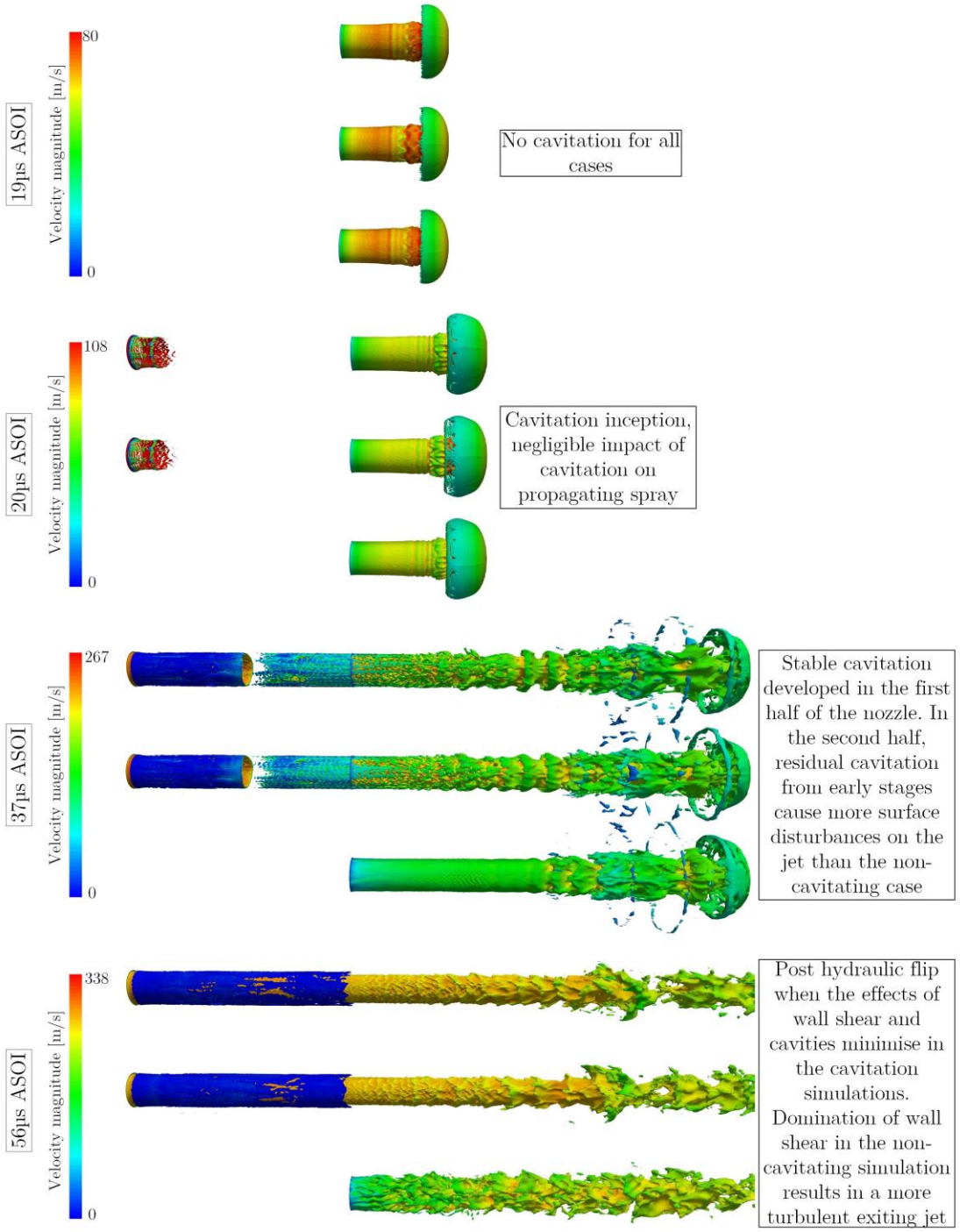

Figure 3-15: Penetrating spray represented by a liquid volume isosurface ($\alpha = 0.9$) coloured by velocity magnitude. The temporal evolution of the spray is displayed at 19, 20, 37 and 56 μs ASOI (Top: Schnerr, Middle: Kunz, Bottom: non-cavitating).

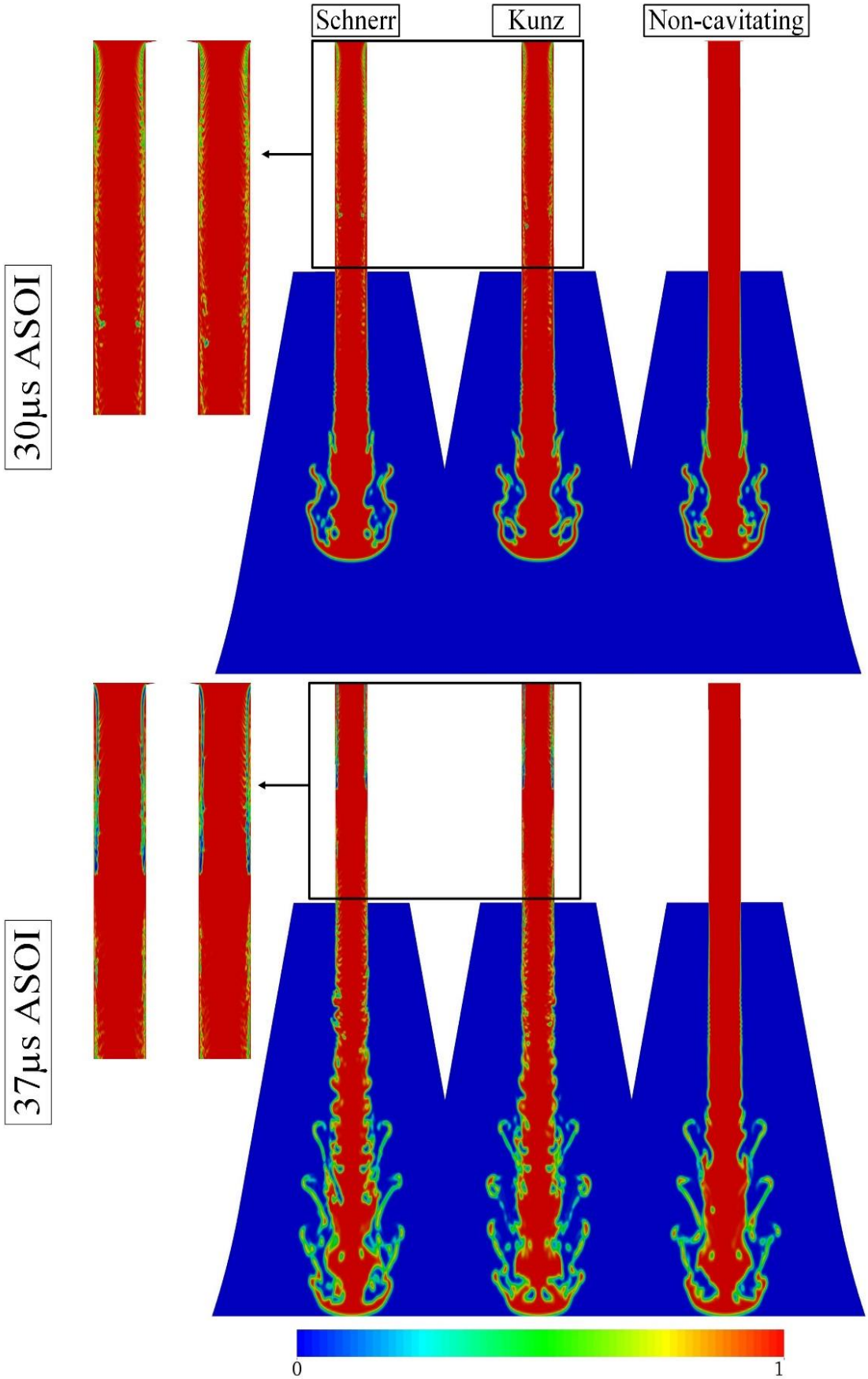

Figure 3-16: Sectional contour plots of diesel volume fraction before (30 µs) and after onset of supercavitation (37 µs ASOI). The process illustrating the connection between

the in-nozzle flow and the morphology of the emerging spray is shown for all models considered in the present study. The development of long cavities at 37 μs in the first half of the nozzle, reattachment of flow just downstream and residual bubbles from early stage (30 μs) appearing in the second half are shown in the enlarged views for the cavitation simulations. In both cavitation simulations, the combined effects of cavitation and liquid/vapour shear result in a more irregular jet entering the chamber as compared to the non-cavitating simulation.

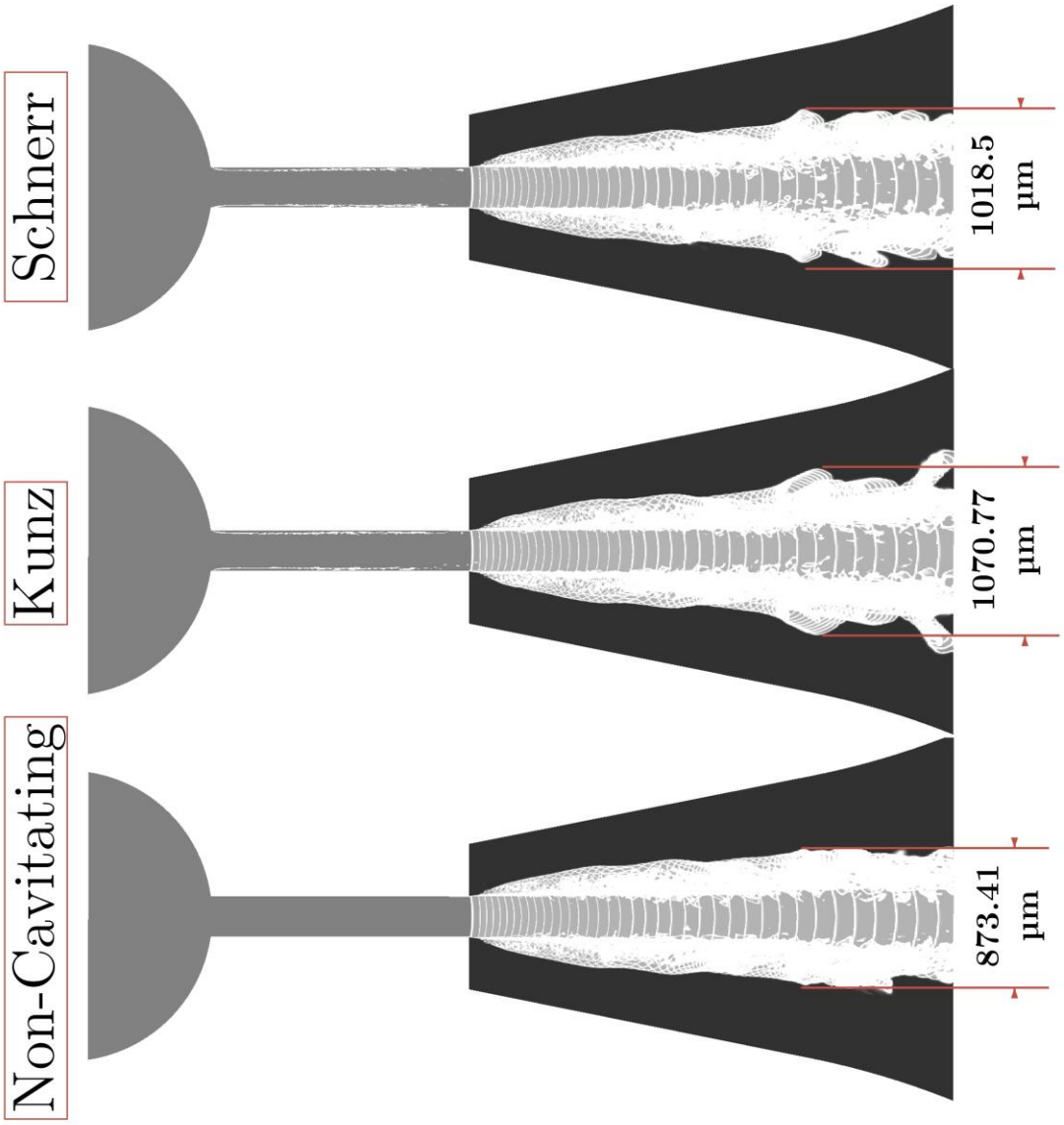

Figure 3-17: Time-average liquid core analysis: grey indicates liquid core, white represents the two-phase (spray) region and black represents the gas. The simulation is averaged from the start of injection to the onset of complete flow detachment. Width of the spray is measured at the first protrusion of liquid-gas interface along the penetration axis.

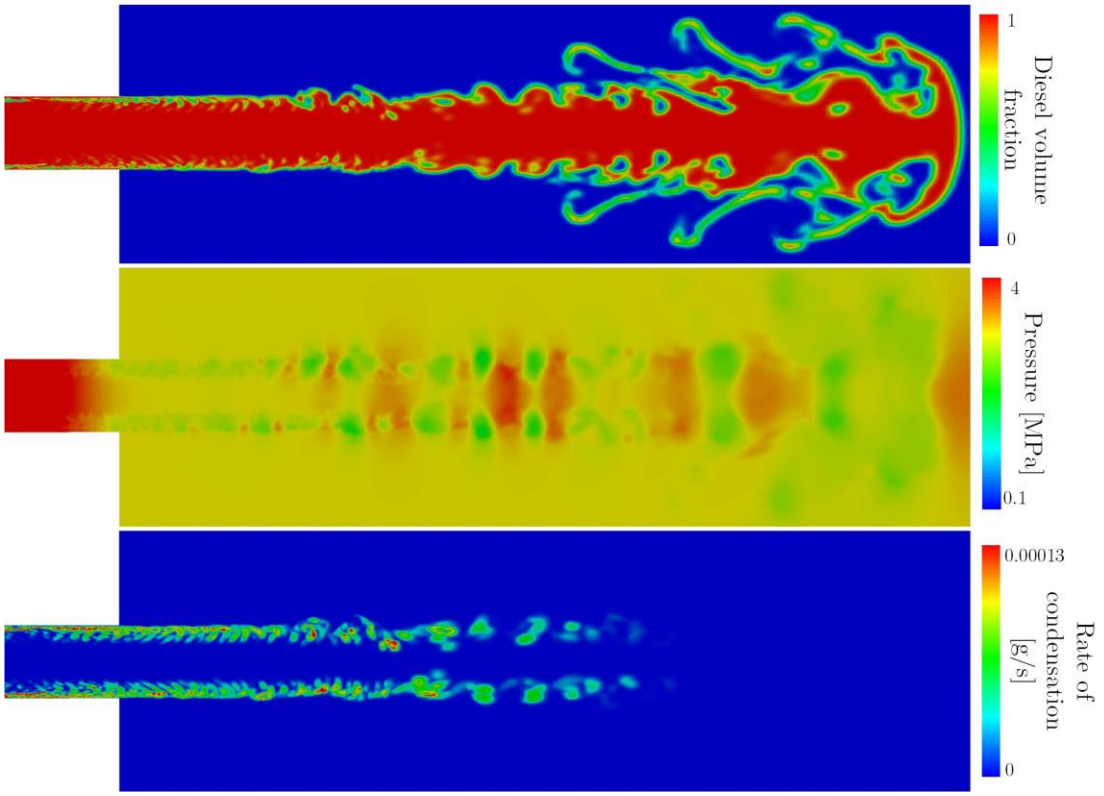

Figure 3-18: Sectional contour plots of diesel volume fraction, total pressure and rate of condensation at 37 µs ASOI. Localised low pressure regions and convex surface protrusions are observed to correlate spatially with regions of high vapour condensation rate.

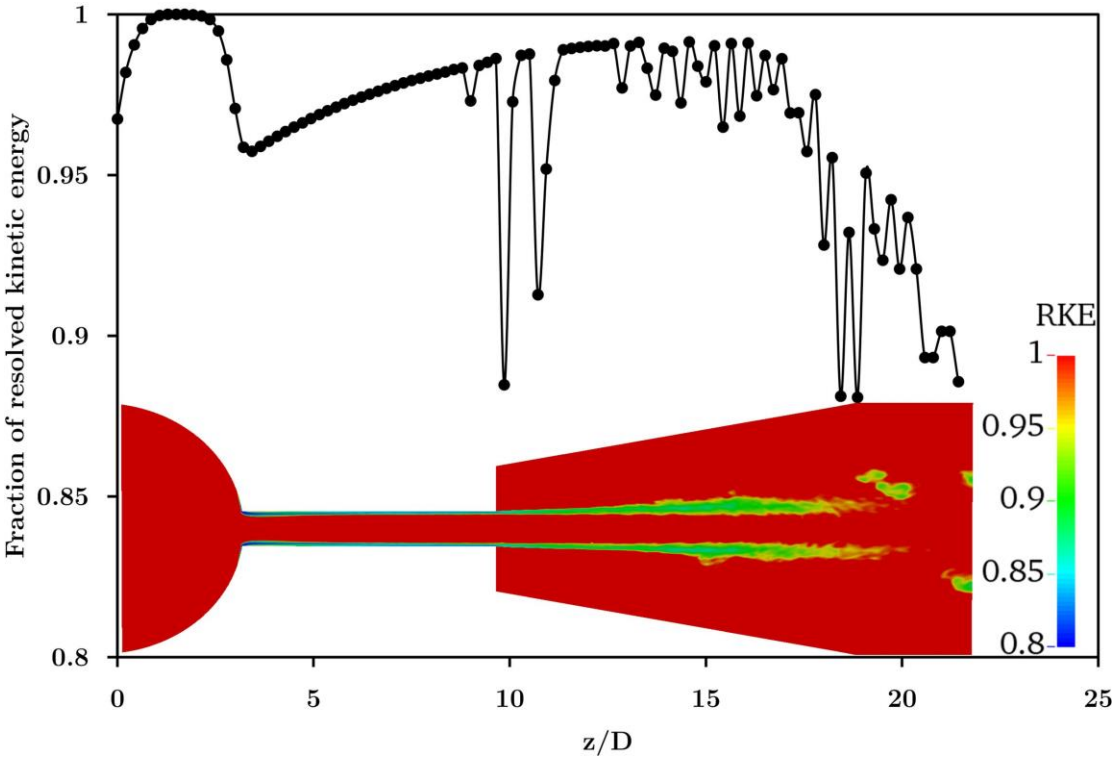

Figure 3-19: Resolved kinetic energy as a fraction of total kinetic energy plotted along the axis of penetration. Distribution of this fraction is shown in the contour plot at the

$x = 0$ plane. The fraction of resolved kinetic energy and its contour plot are time averaged from start of injection to onset of complete flow detachment.

3.6 Conclusions

A new compressible multi-phase VOF LES is developed for modelling the flow from a diesel injector with a sharp nozzle inlet. The method together with the implementation of the Schnerr cavitation model is partially validated against data and observations obtained from published experiments with a slightly converging square channel. It has been demonstrated that the developed model can predict the effects of pressure on the formation and propagation of cavitation in the nozzle. There is, however, a slight over-prediction of flow velocities in the near wall region compared with experimental data, which could be attributed to uncertainties in fluid properties, assumptions made in the numerical approach and/or experimental error. Further numerical analysis is needed to validate the model, preferably at higher injection pressures since modern diesel engines often operate with injection pressure up to 200 MPa. Implementation of this method using two alternative cavitation models to predict in-nozzle flows and primary breakup has revealed:

- Flow separation occurs just after the sharp nozzle inlet where inertia causes increase in flow velocity downstream.
- The pressure in the contraction region can reduce to vapour pressure, leading to vaporisation of fuel and formation of vapour cavities.
- The appearance of cavities along the wall initially corresponds to an increase in the quantity of eddies generated in the boundary layer.
- Vapour cavities forming at the nozzle inlet can grow to an extent that detaching bubbles collapse within the liquid jet after exiting the nozzle, enhancing jet breakup.
- The combined effects of wall shear and in-nozzle cavitation in the cavitation simulations lead to a jet with a higher breakup intensity and wider spray than that in the non-cavitating simulation in which the jet experiences only wall shear.
- The onset of complete flow detachment minimises turbulence production in the nozzle due to elimination of wall shear.
- Air starts to be drawn into the nozzle orifice (about 200 μm into the nozzle), after complete flow detachment has occurred, because of the pressure difference between the chamber and nozzle orifice.
- By comparing non-cavitating and cavitating simulations after the onset of complete flow detachment, it is apparent that apart from in-nozzle flow separation and cavitation, another important factor contributing to the primary breakup of the spray is the wall shear experienced by the jet in the nozzle.

This work forms the basis of phase change modelling for diesel spray at higher injection pressure conditions. Its application can be further extended by integrating a more advanced formulation for energy conservation to better model the thermodynamics of phase change due to cavitation. This will be considered in future work.

4 Modelling thermal effects in cavitating high-pressure diesel sprays using an improved compressible multi-phase approach

Abstract

In this study, the influence of in-nozzle phenomena including flow separation, cavitation, turbulence and hydraulic flip on the morphology of the spray emerging from a convergent-divergent-convergent diesel injector is investigated numerically. Non-linear equations of state for the liquid diesel, diesel vapour and chamber gas are employed for the simulation of high pressure diesel injection and atomisation processes. A modified multi-phase mixture energy equation which takes into account enthalpy of phase change due to cavitation is integrated into a previously developed compressible, multi-phase Volume of Fluid Large Eddy Simulation. The mass transfer source terms are modelled using a modified Schnerr and Sauer cavitation model. The new multiphase cavitation solver is developed and implemented in the OpenFOAM environment and is termed as PISOCavitatingInterFoam. This solver is validated by comparing simulated mass flow rates, momentum fluxes, effective injection velocities and discharge coefficients at different injection conditions against published experimental data obtained using the same injector. Favourable comparison between simulations and experimental measurements is achieved with minor discrepancies attributable to unknown experimental uncertainties and assumptions made in numerical modelling. Calculation of in-nozzle flow and primary spray breakup reveals that interfacial instabilities generated due to in-nozzle flow separation, cavitation and liquid-wall shear contribute greatly to the jet fragmentation. The increase in sensible enthalpy due to wall shear induced viscous heating together with enthalpy of condensation increase the surface temperature of the exiting jet. Comparison of the flow physics before and after the onset of hydraulic flip indicates that wall shear is one of the main mechanisms inducing most of the energy for jet breakup. This modelling shows that vapour production at nozzle entrance remains after the onset of hydraulic flip, limiting the extent of ambient air influx. In addition, the onset of hydraulic flip causes production of near nozzle shockwaves as a result of significantly increased injection velocity attributable to minimised wall shear. This aspect needs more experimental evidence and simulations to confirm and validate.

Key words: Multi-phase flow; Volume of Fluid; Large Eddy Simulation; Cavitation; Shockwaves; Primary atomisation

4.1 Introduction

It is well understood that the atomisation characteristics of diesel sprays have a profound impact on the air-fuel mixing process and thus the combustion efficiency and pollutant formation. The preliminary factors governing the quality of atomisation include in-nozzle flow separation, cavitation, turbulence and liquid-gas interaction when the spray enters the combustion chamber. At high injection pressures, atomisation of the diesel spray is found to be enhanced especially when cavitation occurs in injector nozzles [72, 74, 75].

In fuel injector nozzles, high pressure gradients caused by flow contraction and acceleration at the nozzle inlet can initiate flow separation. This reduces the effective flow area and creates a recirculation zone in which static pressure can decrease to, or below, fuel vapour pressure [70, 72]. The onset of cavitation then generates vapour in the flow just downstream of the nozzle inlet, which in turn decreases wall shear on the flow. Consequently, wall shear reduction leads to increase in maximum flow velocity in the nozzle. Further downstream where local pressure recovers, condensation and collapse of cavities restore the flow effective area and wall shear, which then decrease axial flow velocity [116]. Depending on the relative length of the cavities and nozzle, vapour bubbles may persist and collapse in the jet outside of the nozzle exit [80]. Collapse of cavities within the jet enhances jet breakup intensity, further increasing the spray dispersion angle [79, 113]. Moreover, there are situations where flow separation and accumulation of cavities can result in complete detachment of fluid flow from the nozzle wall [119]. In those cases, ambient gases are drawn into low pressure regions of the nozzle, causing formation of mixtures composed of liquid, vapour and ambient gas near the nozzle wall [81]. In addition, the occurrence of complete flow detachment in the nozzle eliminates wall shear on the liquid jet. Thus, production of interfacial instabilities is minimised and spray atomisation is supressed, which decrease the spray dispersion width [81]. Despite the advantage that cavitation can potentially enhance atomisation, conditions triggering the generation of in-nozzle cavities such as high injection pressure and the use of sharp nozzle inlets are often achieved at the cost of reduced longevity of fuel injectors. At high injection pressures, cavitation caused by high flow inertia and flow separation were found to erode the sharp nozzle entrance of a square throttle in time of the order of 200 µs in Greif *et al.*'s work [120]. This promotes the use of a rounded nozzle inlet which not only maintains a desired discharge coefficient but also improves the durability of fuel injectors by suppressing cavitation. However, suppression of cavitation due to the decrease in the extent of the recirculation zone eliminates the benefit that allowing cavitation could potentially improve atomisation and air/fuel mixing. Alternatively, cavitation can be initiated at several nozzle diameters downstream of the rounded entrance by adding a convergent-divergent section to the nozzle [89, 121]. The resultant venturi effect can lead to sufficiently low pressure for cavitation to occur.

Due to the extremely small size of injector holes which have an average length of 1 mm and a diameter varying from 100 µm to 300 µm for most automotive diesel engines, experimental investigations of the in-nozzle phenomena and their effects on the subsequent jet breakup are challenging. Although useful information has been obtained from large scale replicas of fuel injector nozzles, the scale effects have been recognised to contribute significantly to the deviation in cavitation morphology between enlarged and real-scale injector nozzles [80, 122]. For instance, cavitation structures differ from

enlarged-scale nozzles (clouds of bubbles) to real-scale nozzles (cavitation pockets). On the other hand, the scale limitation encountered in experimental investigations of flow physics in a real-scale cavitating fuel injectors can potentially be overcome using numerical models.

As far as two-phase models are concerned, attempts have been made by Ghiji *et al.* [48, 56] and De Villiers *et al*. [102] to link in-nozzle turbulence with early breakup of the diesel spray using an incompressible Volume of Fluid (VOF) approach. However, the absence of a phase change model results in the omission of the effects of cavitation on the spray evolution. Inclusion of compressibility effects and phase change through the implementation of a Tait equation of state and a cavitation model has enabled the capturing of extreme pressure peaks triggered by collapse of cavities in Koukouvinis *et al.*'s work [123]. A more advanced compressible approach adopting an energy equation based on sensible internal energy was employed by Ghiji *et al.* [57] and Yu *et al*. [124] to investigate the breakup of a cavitating diesel spray. Nevertheless, omission of the shear stress and phase change source terms in the energy equation makes it difficult for these models to ensure energy conservation. Furthermore, two-phase approaches have demonstrated their ability to only capture the generation and collapse of cavities in the fuel injector nozzles [89, 101, 121, 125]. Extending such methods to model near nozzle flow requires incondensable chamber gases to be specified as vapour, which can lead to physically unrealistic vapour condensation as mostly the chamber pressure is well above the vapour pressure. This is mainly attributed to the exclusion of the dynamics of a third phase (ambient gas).

Most recently, Cailloux *et al*. [126] and Yu *et al*. [59, 127] extended the compressible VOF method to incorporate multi-phase dynamics and mass conservative cavitation. The validation of this work, however, was only carried out for diesel injection at low injection pressures (up to 10 MPa). Application of this method to higher injection pressures (up to 200 MPa) as required for modern automotive diesel engines is still not reported in the open literature. Thus, the main objective of the present study is to advance the previously developed compressible multi-phase VOF cavitation method [59] with the capability to, (1) simulate high pressure diesel injection process and, (2) account for the thermal effects of pressure variation and cavitation on fluid properties. The former is achieved through the implementation of non-linear equations of states for liquid diesel, diesel vapour and ambient gas (air). Inclusion of pressure and cavitation related thermal effects is accomplished by adding phase change sources terms to a standard total energy equation formulated based on sensible specific enthalpy and extending it to multi-phase flows. The models described in this chapter have been implemented as an application in the finite volume library OpenFOAM 2.4.0 and given the name PISOCavitatingInterFoam.

The present chapter is divided into six sections. In section 4.2, a description of the compressible multi-phase VOF governing equations is provided together with the implementation of a modified Schnerr and Sauer cavitation model. The detailed formulation and implementation of the modified energy equation is presented in section 4.3. This is followed by detailed descriptions on the non-linear equations of state employed for the liquid and gas phases in section 4.4. Validation of the code for high injection pressures is then detailed in section 4.5 along with analyses on the in-nozzle and near nozzle flow physics. Finally, the main conclusions of the investigation are drawn in section 4.6.

4.2 Description of the VOF approach

The multi-phase VOF method adds transport equations accounting for the volume fraction of each phase. The VOF method is intrinsically volume conservative in that the unity volume fraction is always satisfied regardless of the number of phases considered. For a multi-phase flow with phase change, a separate transport equation must be used for each individual phase in order to strictly ensure mass conservation. A detailed derivation of the phase transport equations can be found in our previous work [59].

$$\left.\begin{aligned} &\frac{\partial\left(\rho_l\alpha_l\right)}{\partial t}+\nabla\cdot\left(\rho_l\alpha_l U\right)=\dot{m}\\ &\frac{\partial\left(\rho_v\alpha_v\right)}{\partial t}+\nabla\cdot\left(\rho_v\alpha_v U\right)=-\dot{m}\\ &\frac{\partial\left(\rho_i\alpha_i\right)}{\partial t}+\nabla\cdot\left(\rho_i\alpha_i U\right)=0\\ &\alpha_l+\alpha_v+\alpha_i=1 \end{aligned}\right\} \tag{4-1}$$

where $\dot{m}$ is the phase change mass transfer rate, α_l , α_v and α_i are volume fractions of the liquid, vapour and ambient gas (air) phases respectively. The mass transfer source term on the RHS can be expressed as:

$$\dot{m}=\dot{m}^{+}+\dot{m}^{-} \tag{4-2}$$

The rate of condensation $\dot{m}^{+}$ and vaporisation $\dot{m}^{-}$ on the liquid-vapour interface are modelled using the Schnerr and Sauer cavitation model [128, 129] with the following modifications:

$$\dot{m}=\frac{3\rho_l\rho_v}{\rho}\alpha_l\alpha_v\left(rR_b\right)\sqrt{\frac{2\left|p-p_v\right|}{3\rho_l}}\begin{cases}\dot{m}^{+}=\dfrac{3\rho_l\rho_v}{\rho}\alpha_l\alpha_v\left(rR_b\right)\cdot\\ \sqrt{\dfrac{2}{3\rho_l\left(\left|p-p_v\right|+0.001p_v\right)}}\max\left(p-p_v,0\right)\\ \dot{m}^{-}=\dfrac{3\rho_l\rho_v}{\rho}\alpha_l\alpha_v\left(rR_b\right)\cdot\\ \sqrt{\dfrac{2}{3\rho_l\left(\left|p-p_v\right|+0.001p_v\right)}}\min\left(p-p_v,0\right)\end{cases} \tag{4-3}$$

The above modifications ensure that condensation and vaporisation do not occur simultaneously when both vapour and liquid are present in a computational cell. This is based on the consideration that it is physically impossible for local static pressure p to be greater and smaller than the vapour pressure p_v at the same time. Also, the $0.001p_v$ term is added to avoid division by zero when local static pressure approaches the vapour pressure. The inverse of the cavitation nuclei radius rR_b is related to α_l , α_v and bubble density n by:

$$\left.\begin{aligned} rR_b &= \left(\frac{4\pi n\alpha_l}{3\left(\alpha_v+\alpha_{nuc}\right)}\right)^{1/3} \\ \alpha_{nuc} &= \frac{n\pi\left(d_{nuc}\right)^3}{6+n\pi\left(d_{nuc}\right)^3} \end{aligned}\right\} \tag{4-4}$$

where α_{nuc} is cavitation nuclei's volume fraction which is expressed in terms of the average nuclei diameter $d_{nuc}\left(m\right)$ and the nuclei concentration $n\left(m^{-3}\right)$. According to Schnerr and Sauer [128], they are defined as 10^{-6} m and 10^{13} m^{-3} respectively. This high bubble density results in vaporisation at the vapour pressure. It is assumed that there are sufficient nucleation sites for the cavitation process to follow equilibrium, with the rate of vaporisation and condensation determined by the difference between the local pressure and the vapour pressure.

To ensure boundedness of phase volume fractions (volume fraction does not go below zero or beyond unity), the phase transport equations with phase change source terms are solved using the 'Multi- Dimensional Universal Limiter with Explicit Solution' (MULES) accredited to Henry Weller and the detailed formulation is provided in Damián's work [130]. Volume fractions of each phase obtained from the solution of the phase transport equations are then related to the mixture density ρ and velocity U to form the mixture continuity and momentum equations.

$$\left.\begin{aligned} &\rho = \alpha_l\rho_l + \alpha_v\rho_v + \alpha_i\rho_i \\ &U = \alpha_l U + \alpha_v U + \alpha_i U \\ &\frac{\partial\rho}{\partial t} + \nabla\cdot\left(\rho U\right) = 0 \\ &\frac{\partial\rho U}{\partial t} + \nabla\cdot\left(\rho UU\right) = -\nabla p + \nabla\cdot\tau + \sum\int_{S(t)}\sigma_{i-j}\kappa n\cdot\delta\left(x-x'\right)ds \end{aligned}\right\} \tag{4-5}$$

In the mixture momentum equation, the last term accounts for the combined effects of surface tension between phase pairs (e.g. liquid-vapour, liquid-gas and vapour-gas). It is non-zero only at the interface due to the presence of a Dirac function δ (non-zero when $x = x'$). However, zero surface tension is assumed at the liquid-vapour and vapour-gas interfaces by setting $\sigma_{liquid-vapour} = 0 \,\&\, \sigma_{vapour-gas} = 0$. This leads to diffusive liquid-vapour and gas-vapour interfaces due to the phase change and gas mixing processes. The evaluation of the surface tension ($\sigma_{liquid-gas}$) term is achieved following the approach provided by De Villiers *et al*. [102] through the continuum surface force model of Brackbill *et al*. [45].

$$\left.\begin{aligned} &\sum\int_{S(t)}\sigma_{i-j}n\kappa\cdot\delta\left(x-x'\right)ds \approx \sum\sigma_{i-j}\kappa\nabla\alpha \\ &\kappa = \nabla\left(\frac{\nabla\alpha}{\left|\nabla\alpha\right|}\right): surface-curvature \end{aligned}\right\} \tag{4-6}$$

To find numerical solutions for pressure and velocity, the mixture momentum equation needs to be semi-discretised. According to Jasak [109] and Demirdžić *et al*. [110] , the semi-discretised form of the momentum equation is given as:

$$U_p = \frac{H(U)}{a_p} - \frac{1}{a_p}\nabla p \tag{4-7}$$

For multi-phase flows, the $H(U)$ terms consist of two parts: the "transport part", including matrix coefficients for all neighbours multiplied by corresponding velocities and the "source part" (apart from the pressure gradient) comprising the source part of transient terms and the effects of surface tension force on velocities. Divergence of the velocity field can then be expressed as divergence of a predicted velocity field (momentum predictor) and a pressure correction term (explicit velocity correction). A detailed description of the implicit pressure-velocity coupling numerical algorithm can be found in Jasak's PhD thesis [109].

$$\nabla \cdot U = \nabla\left(\frac{H(U)}{a_p}\right) - \nabla\left(\frac{1}{a_p}\nabla p\right) \tag{4-8}$$

Based on Eqn (4-1), (4-5), (4-8) and the pressure-density relation ($\rho = p\psi$), the formulation of the mixture pressure equation which comprises a compressible $\langle 1 \rangle$ and an incompressible $\langle 2 \rangle$ terms can be obtained by following the derivation in our previous work [59]:

$$\left.\begin{aligned} &\frac{\alpha_l}{\rho_l}\left[\psi_l \frac{\partial p}{\partial t} + U \cdot \nabla(\rho_l)\right] + \frac{\alpha_v}{\rho_v}\left[\psi_v \frac{\partial p}{\partial t} + U \cdot \nabla(\rho_v)\right] + \frac{\alpha_i}{\rho_i}\left[\psi_i \frac{\partial p}{\partial t} + U \cdot \nabla(\rho_i)\right] : \langle 1 \rangle \\ &+ \\ &\nabla\left(\frac{H}{a_p}\right) - \nabla\left(\frac{1}{a_p}\nabla p\right) - \dot{m}\left(\frac{1}{\rho_l} - \frac{1}{\rho_v}\right) : \langle 2 \rangle \\ &= 0 \end{aligned}\right\} \tag{4-9}$$

The source term due to cavitation is added to the incompressible part of the pressure equation. Once the pressure is solved, it is applied to evaluate the velocity field following Eqn (4-7) through the Pressure-Implicit-with-Splitting of Operators (PISO) algorithm.

In the present study, the Large Eddy Simulation (LES) model is integrated in Eqn (4-5) through a local volume averaging procedure that decomposes relevant phase-weighted hydrodynamic variables into resolvable and sub-grid scale components. Elimination of the sub-grid fluctuations from direct simulation is done through a filtering process together with the non-linear convective terms in Eqn (4-5). This process generates additional terms comprising correlation of sub-scale variables that entail closure through additional modelling. Amongst these terms, the most crucial one is the Sub-Grid-Scale (SGS) stress that governs the effect of unresolved turbulence scales on momentum transport process and its dissipation. This term is defined as:

$$\tau_{sgs} = \overline{UU} - \overline{U} \cdot \overline{U} \tag{4-10}$$

The closure of the SGS stress is achieved through a sub-grid eddy viscosity model given as:

$$\tau_{sgs} + \frac{\mu_{sgs}}{\rho}\left(\nabla\overline{U} + \nabla\overline{U}^{T}\right) = \frac{2}{3}kI \tag{4-11}$$

in which I is the identity tensor, k is the SGS turbulence kinetic energy and μ_{sgs} is the SGS turbulent viscosity. These SGS turbulence parameters are calculated using a one-Equation eddy model for evaluating k attributed to Yoshizawa [49].

$$\frac{\partial k}{\partial t} + \nabla\cdot\left(k\overline{U}\right) - \nabla\cdot\left[\left(\upsilon + \upsilon_{sgs}\right)\nabla k\right] = -\frac{1}{2}\tau_{sgs} : \left(\nabla\overline{U} + \nabla\overline{U}^{T}\right) - \varepsilon \tag{4-12}$$

where $\varepsilon = C_{\varepsilon}k^{(3/2)}/\Delta$ is the turbulent dissipation, $\upsilon_{sgs} = C_{k}k^{(1/2)}\Delta$ is the SGS kinematic viscosity ($\Delta = \sqrt[3]{V}$ represents the SGS length scale in which V represents the volume of the computational cell under consideration). The turbulent coefficients found from statistical analyses are $C_{k} = 0.07$ and $C_{\varepsilon} = 1.05$ [49].

4.3 Energy equation

For compressible VOF methods, specific total energy of the mixture can be expressed as the sum of specific sensible enthalpy and kinetic energy.

$$\frac{\partial\left(\rho h\right)}{\partial t} + \nabla\cdot\left(\rho U h\right) + \frac{\partial\left(\rho K\right)}{\partial t} + \nabla\cdot\left(\rho U K\right) - \frac{\partial p}{\partial t} = \nabla\cdot\left(\tau\cdot U\right) - \nabla\cdot q \tag{4-13}$$

in which $\frac{\partial p}{\partial t}$ and $\nabla\cdot\left(\tau\cdot U\right)$ are included to account for the thermal effects of pressure variation and shear stress on the flow. Replacing $-\nabla\cdot q$ with $\lambda\left(\nabla^{2}T\right)$ according to Fourier's law of heat conduction [109] leads to:

$$\frac{\partial\left(\rho h\right)}{\partial t} + \nabla\cdot\left(\rho U h\right) + \frac{\partial\left(\rho K\right)}{\partial t} + \nabla\cdot\left(\rho U K\right) - \frac{\partial p}{\partial t} = \nabla\cdot\left(\tau\cdot U\right) + \lambda\left(\nabla^{2}T\right) \tag{4-14}$$

It is generally considered that thermal equilibrium prevails over phase interfaces, which gives rise to a continuous temperature field. A thermal non-equilibrium can only exist for cases that involve chemical reaction or flux of energy to and from other systems. Since heat transfer across system boundaries and chemical reaction are not considered in this study, it is therefore practical to assume a continuous temperature distribution across phase interfaces [131]. Thus, the energy equations for liquid, vapour and gas phases can be expressed in terms of energy densities as:

$$\left.\begin{aligned}
&\frac{\partial\left(\alpha_l\rho_l h_l\right)}{\partial t}+\nabla\cdot\left(\alpha_l\rho_l h_l U\right)+\frac{\partial\left(\alpha_l\rho_l K\right)}{\partial t}+\nabla\cdot\left(\alpha_l\rho_l UK\right)-\frac{\alpha_l\rho_l}{\rho}\left[\frac{\partial p}{\partial t}+\nabla\cdot\left(\tau\cdot\mathrm{U}\right)\right]\\
&=\frac{\alpha_l\rho_l\lambda_l}{\rho}\left(\nabla^2 T\right)\\
&\frac{\partial\left(\alpha_v\rho_v h_v\right)}{\partial t}+\nabla\cdot\left(\alpha_v\rho_v h_v U\right)+\frac{\partial\left(\alpha_v\rho_v K\right)}{\partial t}+\nabla\cdot\left(\alpha_v\rho_v KU\right)-\frac{\alpha_v\rho_v}{\rho}\left[\frac{\partial p}{\partial t}+\nabla\cdot\left(\tau\cdot\mathrm{U}\right)\right]\\
&=\frac{\alpha_v\rho_v\lambda_v}{\rho}\left(\nabla^2 T\right)\\
&\frac{\partial\left(\alpha_g\rho_g h_g\right)}{\partial t}+\nabla\cdot\left(\alpha_g\rho_g h_g U\right)+\frac{\partial\left(\alpha_g\rho_g K\right)}{\partial t}+\nabla\cdot\left(\alpha_g\rho_g KU\right)-\frac{\alpha_g\rho_g}{\rho}\left[\frac{\partial p}{\partial t}+\nabla\cdot\left(\tau\cdot\mathrm{U}\right)\right]\\
&=\frac{\alpha_g\rho_g\lambda_g}{\rho}\left(\nabla^2 T\right)
\end{aligned}\right\} \tag{4-15}$$

Following Haider's derivation [132] of a mixture energy equation for a two-phase VOF model, energy source term due to cavitation $\dot{m}\left(h_i+\Delta H\right)$ is added to the RHS of the energy equations for the liquid and vapour phases in Eqn (4-15). This source term comprises interfacial mass transfer rate $\dot{m}$, specific enthalpy h_i of the liquid/vapour mass that takes part in the phase change process and enthalpy of phase change ΔH .With the addition of these source terms, the mixture energy equation can be rewritten as:

$$\left.\begin{aligned}
&\frac{\partial\left(\alpha_l\rho_l h_l\right)}{\partial t}+\nabla\cdot\left(\alpha_l\rho_l h_l U\right)+\frac{\partial\left(\alpha_l\rho_l K\right)}{\partial t}+\nabla\cdot\left(\alpha_l\rho_l KU\right)-\frac{\alpha_l\rho_l}{\rho}\left[\frac{\partial p}{\partial t}+\nabla\cdot\left(\tau\cdot\mathrm{U}\right)\right]\\
&=\frac{\alpha_l\rho_l\lambda_l}{\rho}\left(\nabla^2 T\right)+\dot{m}\left(h_l+\Delta H\right)\\
&\frac{\partial\left(\alpha_v\rho_v h_v\right)}{\partial t}+\nabla\cdot\left(\alpha_v\rho_v h_v U\right)+\frac{\partial\left(\alpha_v\rho_v K\right)}{\partial t}+\nabla\cdot\left(\alpha_v\rho_v UK\right)-\frac{\alpha_v\rho_v}{\rho}\left[\frac{\partial p}{\partial t}+\nabla\cdot\left(\tau\cdot\mathrm{U}\right)\right]\\
&=\frac{\alpha_v\rho_v\lambda_v}{\rho}\left(\nabla^2 T\right)-\dot{m}\left(h_v+\Delta H\right)\\
&\frac{\partial\left(\alpha_g\rho_g h_g\right)}{\partial t}+\nabla\cdot\left(\alpha_g\rho_g h_g U\right)+\frac{\partial\left(\alpha_g\rho_g K\right)}{\partial t}+\nabla\cdot\left(\alpha_g\rho_g UK\right)-\frac{\alpha_g\rho_g}{\rho}\left[\frac{\partial p}{\partial t}+\nabla\cdot\left(\tau\cdot\mathrm{U}\right)\right]\\
&=\frac{\alpha_g\rho_g\lambda_g}{\rho}\left(\nabla^2 T\right)
\end{aligned}\right\} \tag{4-16}$$

In Eqn (4-16), partial differentiation of the specific enthalpy of each phase can be expressed as the addition of a temperature dependent term and a pressure dependent term:

$$\partial h_i = C_{pi}\partial T+\left(\frac{\partial h_i}{\partial p}\right)_T\partial p \tag{4-17}$$

The second term on the RHS of Eqn (4-17) is replaced with $\partial H_i'$ for simplicity. Applying Eqn (4-17), multiplying $\frac{1}{\rho_i C_{pi}}$ to the corresponding phase enthalpy equations in Eqn (4-16), utilising the volume fraction transport equations (Eqn (4-1)) and with further mathematical manipulation, the mixture energy equation comprising source terms due to vaporisation and condensation can be obtained and implemented in OpenFOAM as (A detailed derivation of the mixture energy equation can be found in Appendix A):

$$\begin{aligned}
&\left[\frac{\partial \rho T}{\partial t}+\nabla\cdot\left(\rho T U\right)\right]-\left(\frac{\alpha_l\lambda_l}{C_{pl}}+\frac{\alpha_v\lambda_v}{C_{pv}}+\frac{\alpha_g\lambda_g}{C_{pg}}\right)\left(\nabla^2 T\right)\\
&+\left(\frac{\alpha_l}{C_{pl}}+\frac{\alpha_v}{C_{pv}}+\frac{\alpha_g}{C_{pg}}\right)\left[\frac{\partial \rho K}{\partial t}+\nabla\cdot\left(\rho K U\right)-\frac{\partial p}{\partial t}-\nabla\cdot\left(\tau\cdot \mathrm{U}\right)\right]\\
&+\left(\frac{\alpha_l}{C_{pl}}\right)\left[\frac{\partial \rho H_l'}{\partial t}+\nabla\cdot\left(\rho H_l' U\right)\right]+\left(\frac{\alpha_v}{C_{pv}}\right)\left[\frac{\partial \rho H_v'}{\partial t}+\nabla\cdot\left(\rho H_v' U\right)\right] \qquad (4\text{-}18)\\
&+\left(\frac{\alpha_g}{C_{pg}}\right)\left[\frac{\partial \rho H_g'}{\partial t}+\nabla\cdot\left(\rho H_g' U\right)\right]\\
&=\dot{m}\rho\left[\left(\Delta H-K\right)\left(\frac{1}{\rho_l C_{pl}}-\frac{1}{\rho_v C_{pv}}\right)\right]
\end{aligned}$$

The implementation of the modified multi-phase mixture energy formulation ensures energy conservation by taking into account enthalpy of phase change. This together with the inclusion of pressure and shear stress related terms enable prediction of temperature variation as a combined effect of cavitation, flow compressibility and interfacial shear. However, phase change source terms due to evaporation are not considered since the spray is injected at room temperature and therefore considered as non-evaporating.

4.4 Equation of State

In this study, different forms of equation of state calculating phase densities based on temperature and pressure variations are adopted for the liquid and gas phases. Using a single cubic equation of state with mixing rules for immiscible phases in the VOF framework is invalid because VOF requires that each individual phase is treated as a pure substance and given an independent equation of state. This limitation of VOF can be overcome by using a homogeneous model described by Matheis *et al*. [133] with the cost that surface tension is neglected. Since this study concerns spray atomisation attributed to the development of interfacial instabilities, surface tension is mandatorily considered, which is easily achieved with the VOF approach. Therefore, for the vapour and air phases, independent Peng-Robinson (PR) gas equations of state [134] with different sets of model constants are employed to allow nonlinear correlation between molar volume, pressure and temperature. It should be noted that a major disadvantage of the PR equation of state is its inability to accurately describe the observed singularities in variation of the second order derivatives including sound velocity.

Specifically, the PR equation of state was found to under-estimate the speed of sound in hydrocarbon liquids [135]. Solutions to this problem suggested by Salimi *et al*. [135] include developing new equations of state making use of the measured sound velocities and developing a molecular model explaining the molecular speed of sound. The application of the former to general diesel fuels is extremely limited due to the significant variation in fluid thermo-physical properties across a range of diesel fuels [136]. The latter solution may substantially increase the complexity of the implementation. Further, the addition of a molecular model may result in decreased computational efficiency and unknown numerical stability, which is beyond the scope of this study. However, the current implementation of the PR equation of state is sufficient for the demonstration of shockwave production associated with cavitation, of which detailed analysis is provided in section 4.5. Following this cubic equation of state, static pressure of the gas phases can be expressed in terms of gas constant R and molar volume v_m as:

$$\left.\begin{aligned} p &= \frac{RT}{v_m} - \frac{a}{v_m\left(v_m+b\right)+b\left(v_m-b\right)}, \\ a &= a_c\alpha, \\ \alpha &= \left[1+\kappa\left(1-\sqrt{T_r}\right)\right]^2, \\ \kappa &= 0.37464+1.54226\omega-0.26992\omega^2, \\ a_c &= 0.45724\frac{R^2T_c^{\,2}}{p_c}, \\ b &= 0.07780\frac{RT_c}{p_c} \end{aligned}\right\} \tag{4-19}$$

The PR equation of state can also be reformulated to become a polynomial function of compressibility factor Z as:

$$Z^3-\left(1-\frac{bp}{RT}\right)Z^2+\left(\frac{a_c\alpha p}{R^2T^2}-\frac{2bp}{RT}-3\left(\frac{bp}{RT}\right)^2\right)Z-\left(\frac{a_c\alpha bp^2}{R^3T^3}-\left(\frac{bp}{RT}\right)^2-\left(\frac{bp}{RT}\right)^3\right)=0 \tag{4-20}$$

Being a cubic form of the PR equation of state, Eqn (4-20) can be solved analytically to give either one (supercritical conditions) or three (subcritical conditions) real roots depending on the temperature and pressure conditions. At subcritical conditions, the largest root corresponds to the compressibility factor of the vapour, while the smallest positive root corresponds to that of the liquid. The third root does not have physical meaning for pure substance since the transition from the gaseous phase to the liquid phase is abrupt and discontinuous in reality [137]. For the gas phases, the maximum real root $Z_{\max}$ is taken as the compressibility factor to calculate density following:

$$\left.\begin{aligned} \rho_i &= \frac{p}{\psi_i} \\ \psi_i &= Z_{\max}RT \end{aligned}\right\} \tag{4-21}$$

The solution of Eqn (4-20) is again used to construct the departure function from ideal gas sensible specific enthalpy as presented in Kyle's work [138]:

$$h_{T,p}^{real} = h_{T,p}^{ideal} + RT_c\left[T_r\left(Z-1\right) - 2.078\left(1+\kappa\right)\sqrt{\alpha}\ln\left(\frac{Z+2.414B}{Z-2.414B}\right)\right] \qquad (4\text{-}22)$$

in which T_r and p_r are the reduced temperature and pressure respectively, and B is given as $0.07780\frac{p_r}{T_r}$. Calculating the second term on the RHS of Eqn (4-22) gives solution to enthalpy departure H_i' for the vapour and gas phases. According to the derivation of Passut and Danner [139], the evaluated enthalpy departure H_i' can be used to obtain the real constant pressure heat capacity C_{pi}^{real} following:

$$C_{pi}^{real} = C_{pi}^{ideal} + \left(\frac{\partial H_i'}{\partial T}\right)_p \qquad (4\text{-}23)$$

The calculated enthalpy departure H_i' and constant pressure heat capacities C_{pi}^{real} for the vapour and gas phases are then substituted into the multi-phase energy equation Eqn (4-18) to iteratively solve for the temperature field.

The use of PR gas equation of state only requires the specification of critical temperature T_c, critical pressure p_c and acentric factor ω for a pure substance. For the vapour and air phases considered in this study, values for these three parameters are specified in *Table 4-1*.

Table 4-1: Critical parameters and acentric factors for air and diesel vapour taken from Lapuerta *et al*. [140].

	$T_c\left(K\right)$	$p_c\left(bar\right)$	ω
Air	132.16	36.8	0.036
Diesel vapour	700.23	22.56	0.53

The dynamic viscosity μ and thermal conductivity λ of air are modelled using a Sutherland equation [141] and a modified Euken Model [142]:

$$\mu = \frac{C_1 T^{3/2}}{T+T_s}, \quad \frac{\lambda}{\mu\left(C_p-R\right)} = 1.32 + \frac{1.77R}{\left(C_p-R\right)} \qquad (4\text{-}24)$$

in which the Sutherland temperature T_s and the constant C_1 are defined as 110.4 K and $1.458\times10^{-6}\ \frac{kg}{ms\sqrt{K}}$ respectively.

On the other hand, the equation of state for the liquid diesel phase is derived from curve fitting the experimental data presented by Payri *et al*. [143] using a polynomial function. This function consists of a non-linear term approximating density according to pressure and a polynomial temperature correction term. It is obtained as:

$$\rho_l\left(p,T\right) = \underbrace{0.001884p^2 - 0.43p + 1036}_{\rho_l(p)} \underbrace{-\left(8\times10^{-6}p^2 - 0.0029p + 0.6706\right)T}_{\rho_l(p,T)} \qquad (4\text{-}25)$$

where p and T have a unit of MPa and K respectively.

The accuracy of the curve fitting is demonstrated in *Figure 4-1* with a maximum deviation between estimations and measurements being less than 0.5%. This indicates

that the proposed equation of state can predict density variation of the considered liquid diesel based on changes in pressure and temperature with a high level of confidence. However, application of the derived equation of state to general diesel fuels is restricted due to significant variation in thermo-physical properties across a range of diesel fuels [136].

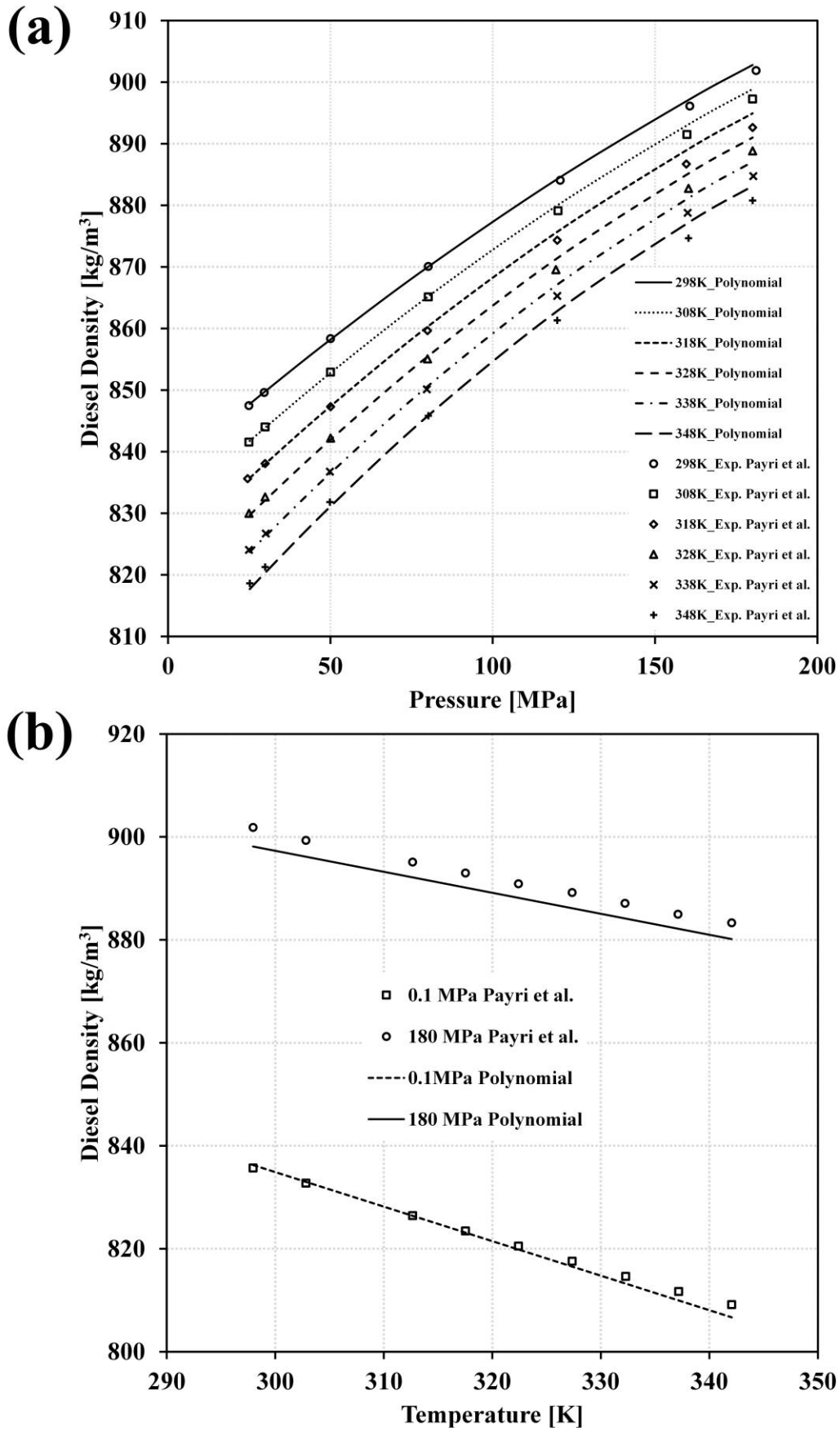

Figure 4-1: Comparison of estimated and measured liquid diesel densities at various pressure (a) and temperature (b) conditions.

With the density being directly related to pressure and temperature, the compressibility (ψ_l) of the diesel fuel is evaluated from $\psi_l = \frac{\rho_l}{p}$.

To evaluate the enthalpy departure H_l' for the liquid phase, a polynomial function relating pressure and enthalpy departure proposed by Kolev [136] is employed:

$$H_l' = -142.3652 + 0.00142p - 3.46467\times10^{-12}p^2 + 8.27876\times10^{21}p^3 \quad (4\text{-}26)$$

Instead of differentiating Eqn (4-26) with respect to temperature at constant pressure, the heat capacity at constant pressure C_{pl}^{real} for the liquid diesel is obtained from curve fitting the experimental date presented by Kolev [136]:

$$\begin{aligned} C_{pl}^{real} &= 1828.5 - 0.0134(T-273)^2 + 6.4806(T-273) \\ &-7.817\times10^{-9}p^3 + 3.794\times10^{-5}p^2 - 0.0364p \end{aligned} \quad (4\text{-}27)$$

The accuracy of the curve fitting is depicted in *Figure 4-2* with a maximum deviation from experiments being less than 0.1%. In addition, the specific enthalpy of phase change (ΔH) for diesel fuel is set to 270 kJ/kg [136, 144].

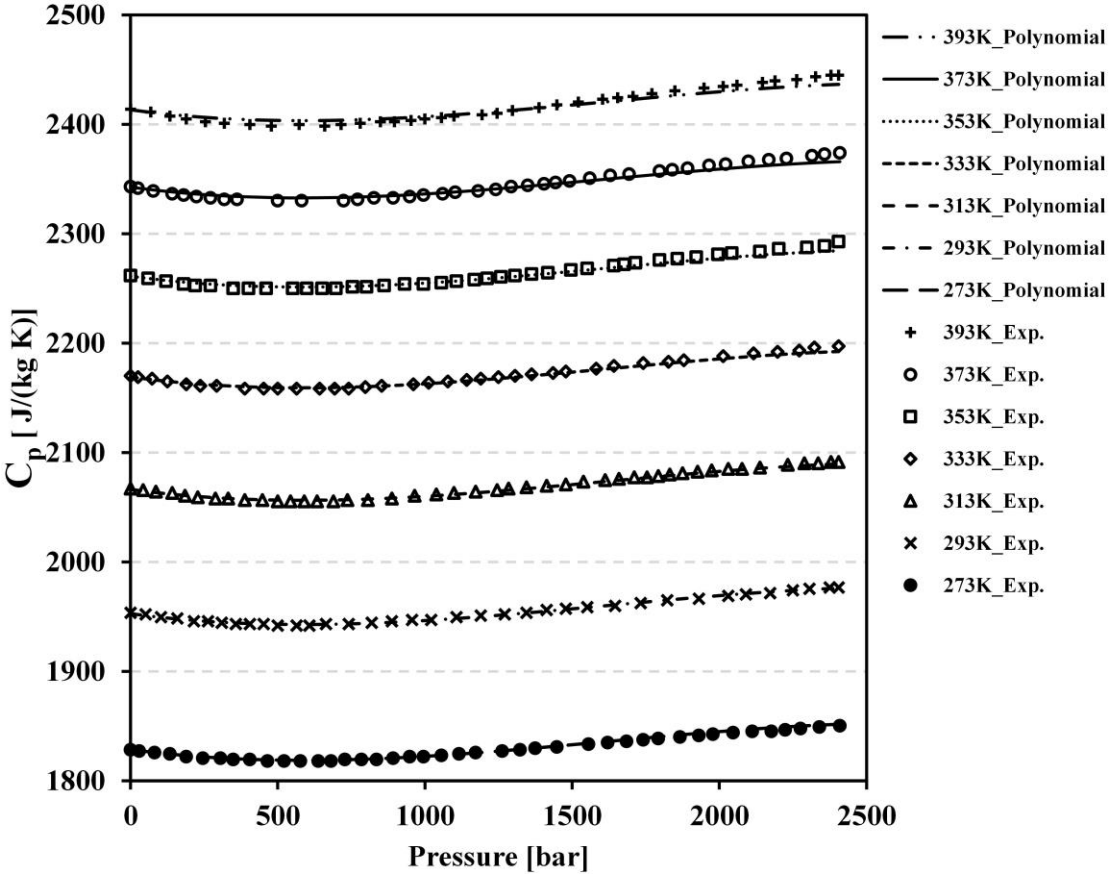

Figure 4-2: Comparison of estimated and measured liquid diesel constant pressure heat capacities at various pressure and temperature conditions.

Due to the lack of a comprehensive thermodynamic library for diesel vapour, its dynamic viscosity is kept constant at 5.953×10^{-6} N s/m^2 for a reference temperature and pressure of 303 K and 1 bar [143] respectively. The thermal conductivity for diesel vapour at the corresponding temperature and pressure is then obtained as 0.00759 W/(mK) [136]. Following this assumption, dynamic viscosity and thermal conductivity

of the liquid diesel are specified as 0.00367 N s/m^2 [143] and 0.1157 W/(mK) [136] respectively at 303 K and 1 bar.

4.5 Single orifice injector simulation

In this section, the capability of the PISOCavitatingInterFoam solver to simulate high pressure diesel injections is demonstrated using a single-hole injector injecting diesel into an air filled constant volume chamber. Experiments were conducted by Salvador *et al.* [89, 145] using three levels of injection pressures (30, 70 and 110 MPa). Simulations replicating these experiments are performed to establish the ability of the code in conditions similar to modern diesel injection systems. Modelling of high injection pressures up to 110 MPa can still be considered a challenging task and has yet to be reported for the evaluation of a multi-phase compressible cavitating code.

4.5.1 Numerical configuration

The geometry reproducing the real nozzle whose internal geometrical characteristics were determined by Salvador *et al*. [89] using a silicon mould technique is depicted in *Figure 4-3*. The computational domain consists of a needle fixed at 250 µm lift, a sac, a convergent-divergent-convergent nozzle hole with a rounded entrance and a portion of the chamber comprising the primary breakup region. Fuel inlet is set at the left end of the geometry with a pre-defined pressure ramp similar to that of Ghiji *et al.* [57]. In the absence of direct measurement, pressure at the inlet is assumed to increase linearly from chamber pressure (4 MPa) to 70% of the maximum injection pressure after 50 µs. Maximum injection pressure is reached after a further 25 µs and then remains constant till the end of simulation (100 µs). This assumption is to some extent arbitrary but is made based on published data that the sac pressure increases rapidly during needle opening [63-65]. For instance, Moon *et al.* [63] found that the quasi-steady state jet velocity was reached when the needle was only elevated to 17% of the maximum lift. The ramp is chosen to give an approximate estimation of pressure variation due to needle dynamics. The passage between the needle and seat is included in the computational domain to allow for any flow disturbance occurring in the passage. Finally, a non-reflective pressure outlet is applied to all ambient boundaries. The remaining face patches are configured to be no-slip and adiabatic walls with a zero-gradient boundary condition for all hydrodynamic variables.

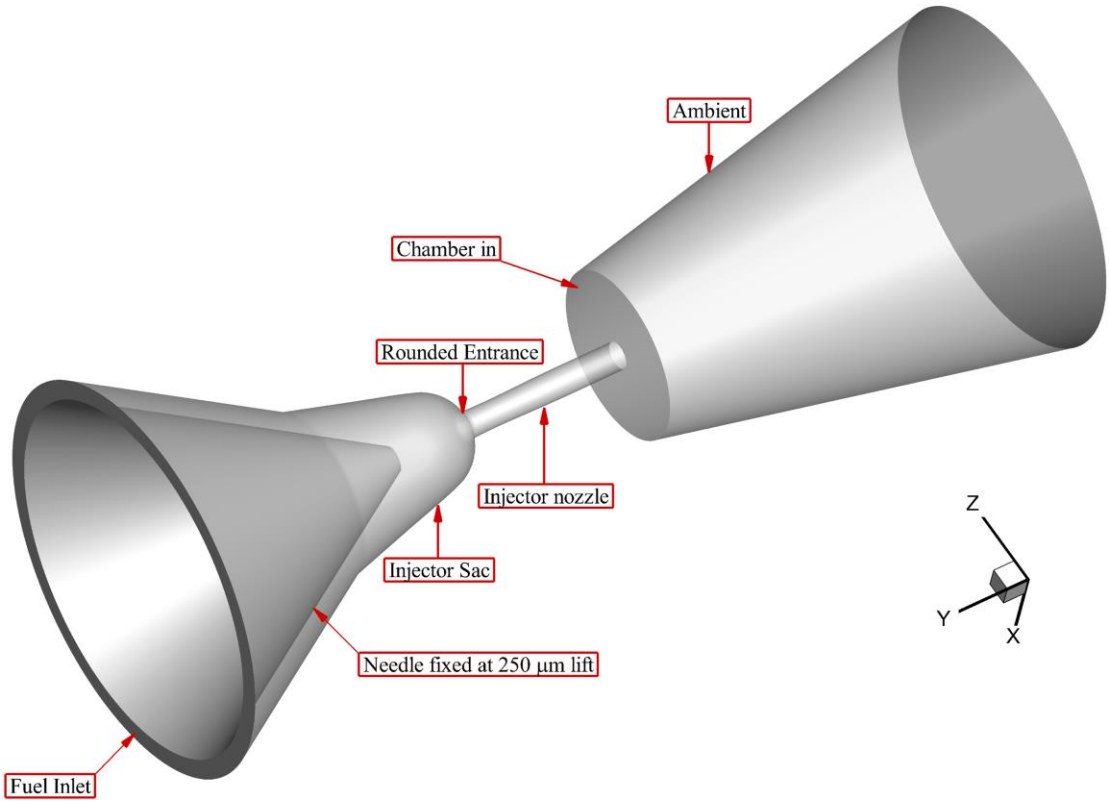

Figure 4-3: Geometry of the single-hole fuel injector.

As shown in *Figure 4-4*, the nozzle hole has an inlet diameter of 155 µm, an outlet diameter (D) of 162 µm and a maximum diameter of 165 µm in the middle section, forming a convergent-divergent-convergent structure which has a length of 1 mm.

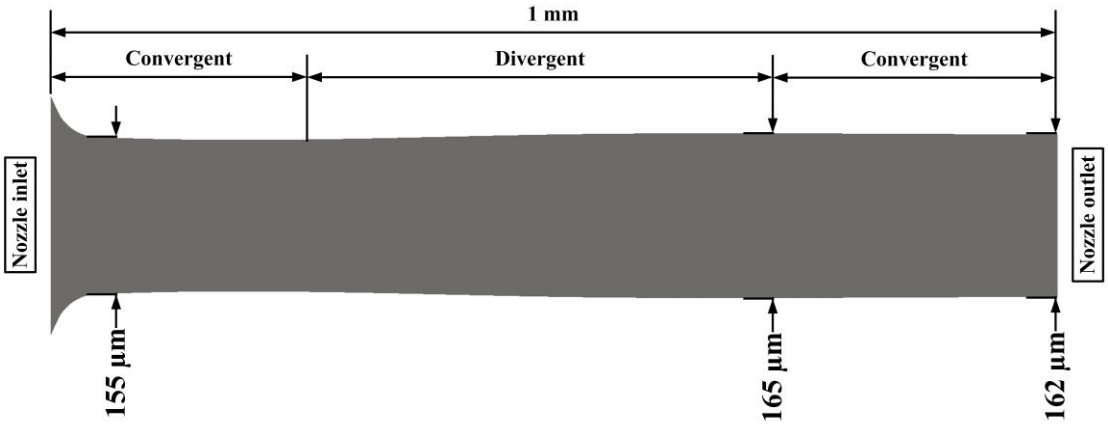

Figure 4-4: Geometrical characteristics of the convergent-divergent-convergent nozzle.

The boundary conditions for the simulations duplicating the experimental configurations [89, 145] are summarised in *Table 4-2*. The properties of the diesel fuel were experimentally characterised by Payri *et al.* [143].

Table 4-2: Fuel properties and boundary conditions based on experimental setup [89, 143, 145].

Parameter	Value
Injection pressures	30, 70 & 110 MPa
Injection Temperature	303 K
Fuel	Diesel fuel
Fuel density (0.1 MPa)	830 kg/m^3
Fuel dynamic viscosity (0.1 MPa)	0.00367 N s/m^2
Surface tension	0.03 N/m
Vapour density (5400 Pa)	0.1361 kg/m^3
Vapour pressure	5400 Pa
Vapour dynamic viscosity	5.953×10^{-6} N s/m^2
Gas Temperature	303 K
Ambient pressure	4 MPa
Ambient gas	Compressed air
Cavitation number	6.504-26.52
Enthalpy of phase change	270 kJ/kg
Max effective velocity (110 MPa)	400 m/s
Max Fuel Reynolds Number (110 MPa)	16490

Fuel properties and Reynolds Number given in *Table 4-2* can be used to evaluate the Kolmogorov scale for the liquid phase, which determines the smallest grid size for constructing the computational domain. The Kolmogorov scale for the diesel fuel injected at 110 MPa is calculated to be 0.11 μm from the following equation:

$$\eta = \frac{W}{(\mathrm{Re})^{3/4}} \tag{4-28}$$

in which the characteristic length W is same as the outlet diameter of the nozzle.

As depicted in *Figure 4-5*, hexahedral elements with a minimum size of 0.08 μm are distributed along the needle and injector walls to capture the effects of wall shear on the flow. A growth rate of 1.01 is applied to construct the grid in the remaining parts of the computational domain, resulting in the use of 22 million elements for the simulation of spray breakup coupled with inner injector flow. These criteria for constructing a structured grid in diesel injectors were demonstrated to be valid for high resolution LES simulations in the work of Yu *et al.* [59, 124] and Ghiji *et al.* [57].

To ensure low numerical dissipation, the minimum orthogonal quality of the grid is kept at 0.8 throughout the computational domain. A fully orthogonal grid has a quality of 1. A bounded Crank-Nicolson scheme is utilised to discretise the temporal terms. A bounded Gamma differencing scheme [60] with a blending factor of 0.2 is applied to the convection terms. A Gauss linear corrected scheme is adopted for the gradient and Laplacian terms to eliminate the effects of mesh non-orthogonality. A conservative interface compression scheme (CICSAM) [47] is used for the evaluation of the artificial compression terms to obtain a sharp liquid-gas interface. However, diffusive liquid-vapour and vapour-gas interfaces due to phase change and gas mixing processes are allowed by setting the compression factor in the CICSAM scheme to 0 at these interfaces. Ideally, improved modelling of liquid-vapour diffusion and vapour-gas diffusion can be achieved by adding a diffusion term in the corresponding volume

fraction transport equations. This will be considered in future work. Finally, a Gauss linear corrected scheme is adopted for the gradient and Laplacian terms to eliminate the effects of mesh non-orthogonality. The simulations are initialised with diesel fuel filling up the injector and therefore the start of penetration occurs immediately after the start of simulation. Simulations with 30, 70 and 110 MPa injection pressures were performed using 400 CPUs and 400 GB of physical memory. The max Courant number was set to 0.3 ensuring high resolution temporal integration with an average time step size of 0.8 ns. The wall clock time for each simulation was around 300 hours. All field results are recorded after start of injection (ASOI) with an interval of 1 μs.

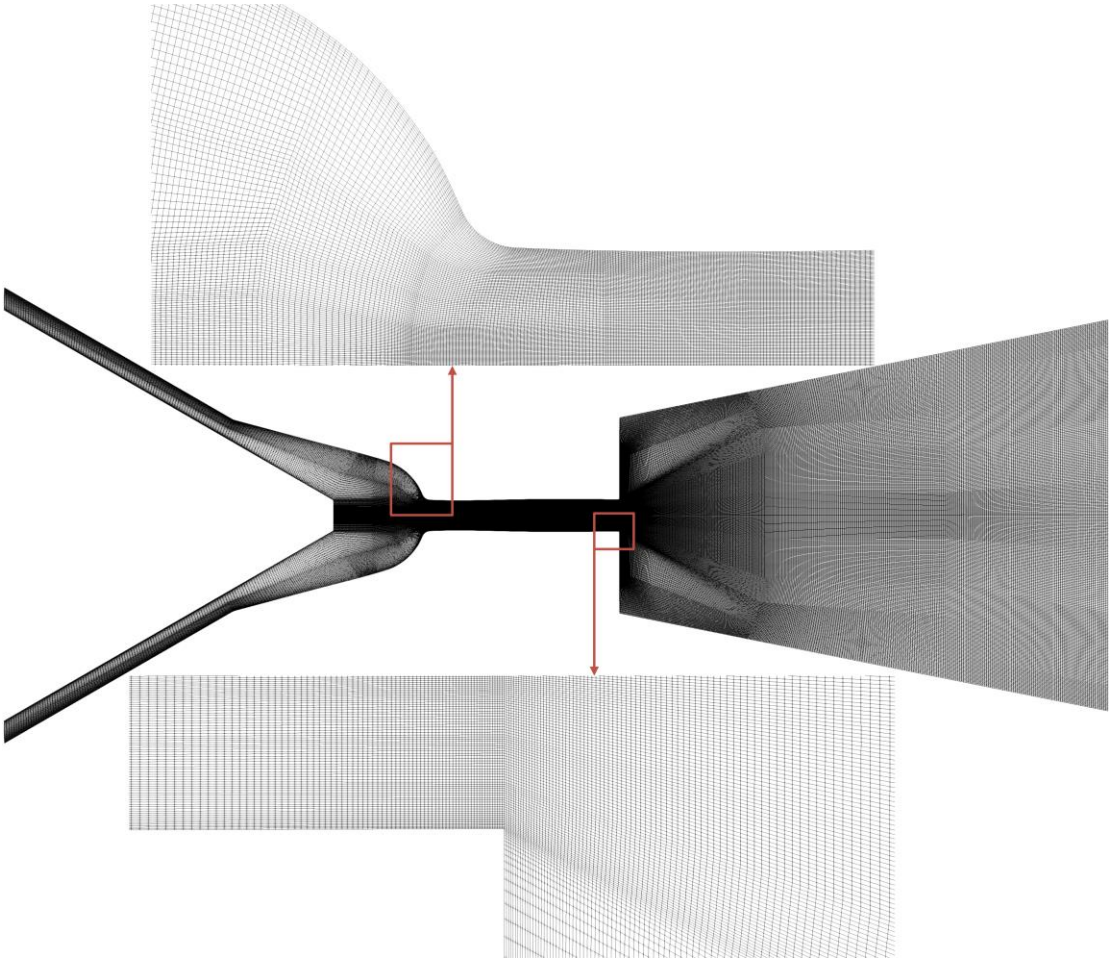

Figure 4-5: Computational domain for the single-hole diesel injector. Minimum mesh size of 0.08 μm is used to form the boundary layer near the wall. The mesh distribution is shown at the centre plane ($x = 0$). Detailed meshing topology around the nozzle inlet and outlet is depicted in the enlarged views. Layers of mesh elements are constructed from the boundary layer with a growth rate of 1.01. In total 22 million mesh elements are used to discretise the computational domain.

4.5.2 Quality of the LES simulation

A mesh sensitivity analysis has been considered not necessary because for VOF-LES methods, increasing grid refinement always leads to the capturing of a sharper interface. Unlike the Reynolds averaged models, such a trend persists until the mesh is fine enough for a DNS simulation. On the other hand, the quality of the LES simulation can be assessed by evaluating the resolved kinetic energy as a fraction of the estimated total

kinetic energy in the computational domain. The resolved kinetic energy is obtained from the Root Mean Square of the velocity components and time averaged over the simulation. This value is then divided by the time averaged total kinetic energy (resolved + modelled) to quantify how much kinetic energy is resolved by the grid. In this study, the quality assessment is only performed on the simulation with an injection pressure of 110 MPa and a maximum Fuel Reynolds Number of 16490. Achieving a high quality LES at these conditions ensures all important flow physics are sufficiently resolved by the grid and therefore better resolution in simulations with lower injection pressures (e.g. 30 & 70 MPa). As depicted in *Figure 4-6*, the flow is well resolved in the inner nozzle boundary layer and around the liquid-gas interface since the resolved kinetic energy in these regions is more than 82% of the total kinetic energy [67]. This indicates that the effects of in-nozzle phenomena are well reflected on the early spray breakup and LES is valid for all concerned regions in all simulations.

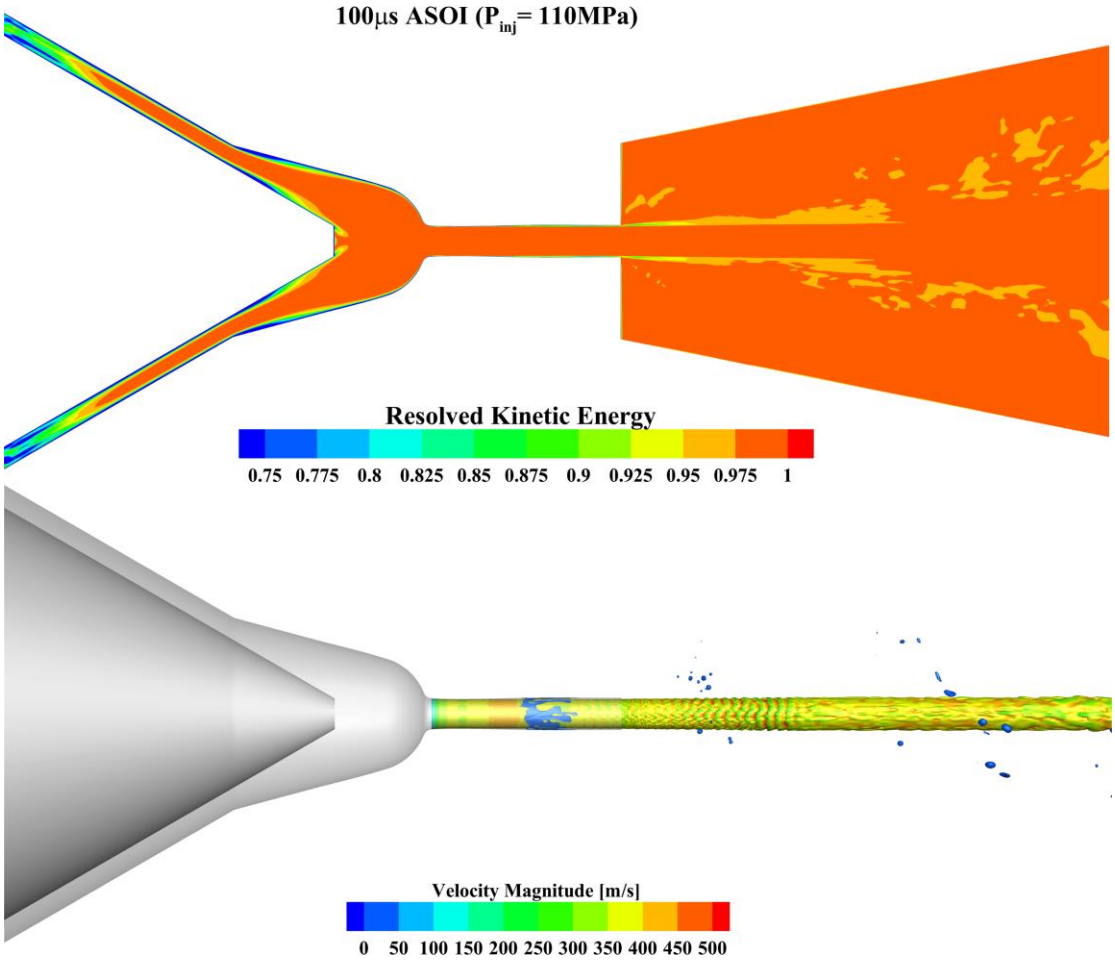

Figure 4-6: Contour plot of resolved kinetic energy as a fraction of total kinetic energy displayed at the $x = 0$ plane (top) and penetrating spray represented by a liquid volume isosurface ($\alpha = 0.1$) coloured by velocity magnitude (bottom).

4.5.3 Validation

Extensive validation is performed by comparing simulated mass flow rates, momentum fluxes, effective injection velocities and discharge coefficients with Salvador *et al.*'s measurements [89, 145]. The momentum flux, apart from being the most important parameter governing the air-fuel mixing process in the chamber [146, 147], provides

mass flow rate and basic information such as effective injection velocity and discharge coefficient. This allows the injector flow to be investigated in a non-intrusive way. All simulations were run until the pressure in the injection sac upstream of the nozzle inlet stabilised at 30, 70 and 110 MPa for the corresponding injection pressure (quasi-steady state). The mass flow rate $\dot{m}_f$, momentum flux $\dot{M}_f$, effective injection velocity u_{eff} and discharge coefficient C_d are sampled at the nozzle exit using the following equations:

$$\dot{m}_f = \int_{A_o} u \rho dA \tag{4-29}$$

$$\dot{M}_f = \int_{A_o} u^2 \rho dA \tag{4-30}$$

$$u_{eff} = \frac{\dot{M}_f}{\dot{m}_f} \tag{4-31}$$

$$C_d = \frac{\dot{m}_f}{A_o \sqrt{2 \rho_l \Delta p}} \tag{4-32}$$

where A_o is the nozzle exit cross-sectional area. The discharge coefficient is derived using Bernoulli's equation between the inlet and the outlet. It represents the measured mass flow rate as a fraction of the theoretical mass flow. The surface integration is performed at the nozzle outlet cross-section. Simulation results are time averaged over 15 µs after the pressure in the sac has stabilised. The comparisons between numerical predictions and experimental measurements are shown in *Figure 4-7*. The results of simulations by Salvador *et al.* [89] using a two-phase Homogeneous Equilibrium Model (also known as cavitatingFoam in OpenFOAM) are also shown.

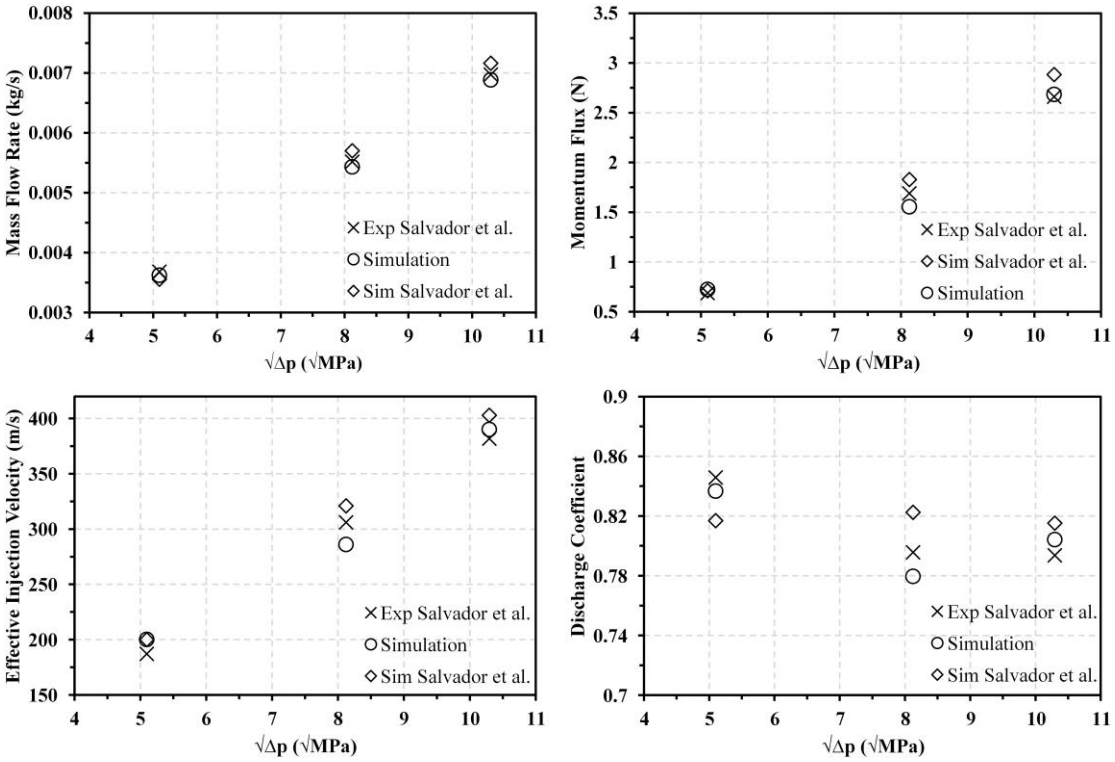

Figure 4-7: Comparison of simulated and measured mass flow rates (a), momentum fluxes (b), effective injection velocities (c) and discharge coefficients (d) which are sampled at the nozzle exit. Numerical data are obtained by averaging the flow field over

15 µs after the pressure in the sac has stabilised. These mean values are plotted as a function of the square root of the pressure drop across the nozzle.

Both experiments and CFD calculations show that mass flow rate, momentum flux and effective injection velocity increase with the injection pressure. The discharge coefficient, however, gives an opposite trend especially at higher injection pressures. This can be attributed to the reduced effective area of the flow at the nozzle exit after the onset of cavitation induced hydraulic flip. As depicted in *Figure 4-8*, the onset of hydraulic flip allows ambient gas to be drawn into the nozzle hole, forming a gas layer that separates the liquid jet from the wall. This agrees with the observation of Soteriou *et al*. [119] for single orifice nozzles. As a result, the effective flow area of the liquid in the hole is reduced and the spray atomisation is suppressed. This aspect is discussed further in the next section.

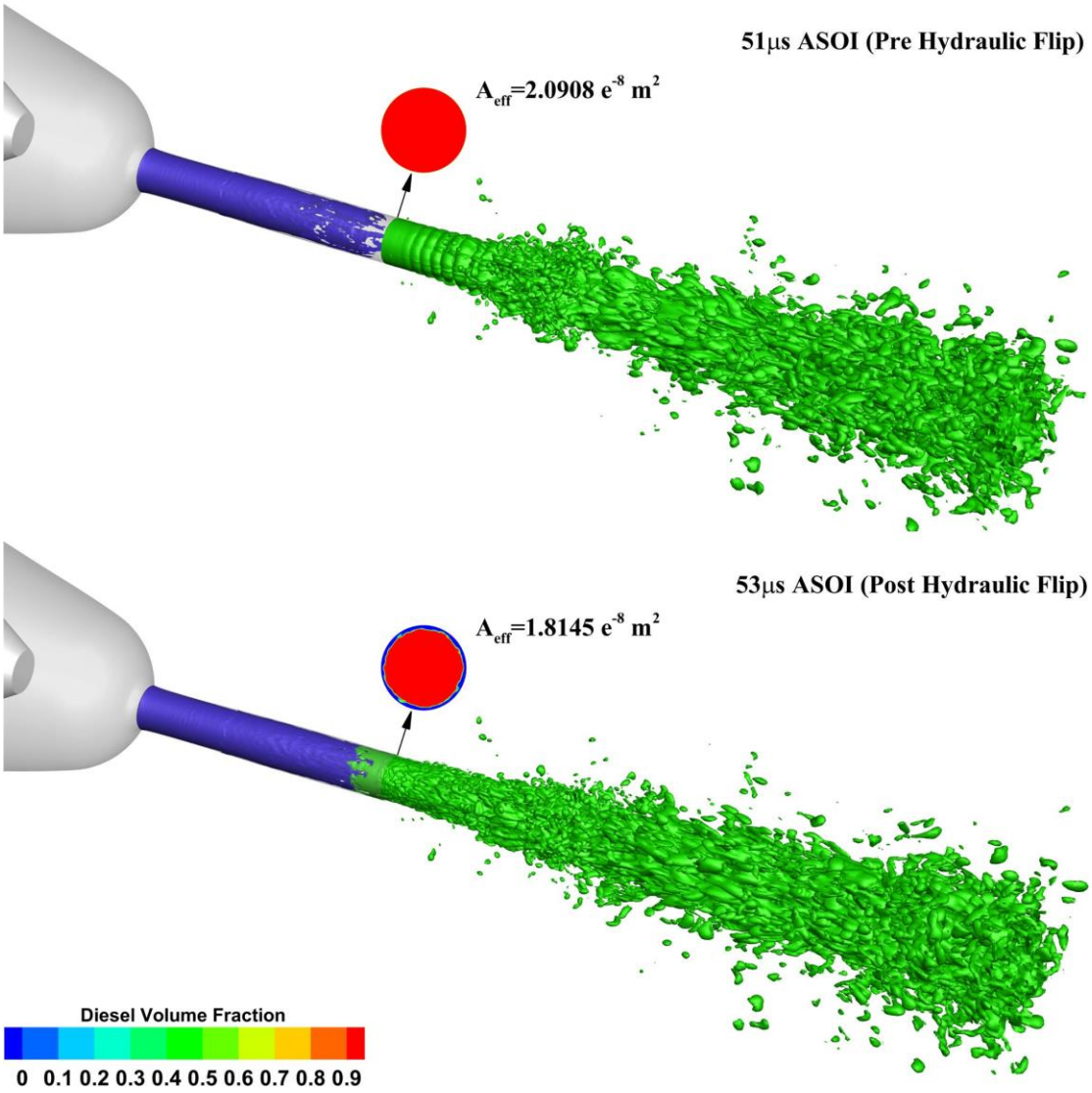

Figure 4-8: Penetrating spray ($p_{inj} = 110$ MPa) represented by a liquid volume isosurface ($\alpha = 0.2$) for two instants (pre- and post-hydraulic flip). The liquid-gas and liquid-vapour interfaces are coloured in green and blue respectively. Cross sections at the nozzle exit are coloured by liquid fraction (red: liquid, blue: gas) and labelled with corresponding effective flow areas.

The PISOCavitatingInterFoam solver provides accurate predictions of the experimental mass flow rate while increasing deviation from measured momentum flux, effective injection velocity and discharge coefficient is observed at intermediate injection pressure ($\sqrt{\Delta p} = 8.124\sqrt{MPa}$). Deviation between predictions and measurements is attributable to the unknown experimental uncertainties and under-estimation of wall shear due to omission of surface roughness in numerical simulations. Nevertheless, the maximum deviation of the predictions from the experimental data is only 6.6%. In addition, the comparison with Salvador *et al.*'s simulations results [89] demonstrates that PISOCavitatingInterFoam has a comparable capability to predict overall flow parameters. In general, PISOCavitatingInterFoam is able to calculate variables as important as the mass flow rate, momentum flux, effective injection velocity and discharge coefficient with a high level of confidence.

For simplicity, evolution of the spray from inner nozzle flow to primary atomisation, including the transient stages while the injection pressure is ramping up to its full value (at 75 us), is discussed in the next section only using the 110 MPa case. Relevant comparisons with sprays injected at lower pressures (30 & 70 MPa) are presented in Section 5.5 at the quasi-steady stage specifically to demonstrate the effects of wall shear on the spray morphology.

4.5.4 Inner nozzle flow and spray structure

The transient process from non-cavitating flow to hydraulic flip in the injector nozzle is illustrated in *Figure 4-9*. At 40 μs ASOI, high flow inertia, flow contraction and adverse pressure gradient create a recirculation region just downstream of the orifice entrance, leading to pressure reduction that initiates cavitation. Further downstream, the static pressure recovers above vapour pressure due to increase in effective flow area at the divergent section of the nozzle. As injection pressure increases, the low pressure region extends further into the orifice and there is a visible vapour cavity starting to grow along the wall. At 52 μs ASOI, the growth of this cavity extends up to the nozzle exit, which results in complete detachment of liquid flow from the wall (53 μs ASOI). At 53 μs ASOI, after the onset of hydraulic flip, the pressure gradient at the nozzle exit causes ambient gas to be drawn into the orifice, which also leads to pressure increase in the second half of the nozzle. The flow then reaches quasi-steady state at 90 μs ASOI. The lengths of the vapour and air cavities remain relatively constant in the nozzle after the flow has reached the quasi-steady state (100 μs ASOI).

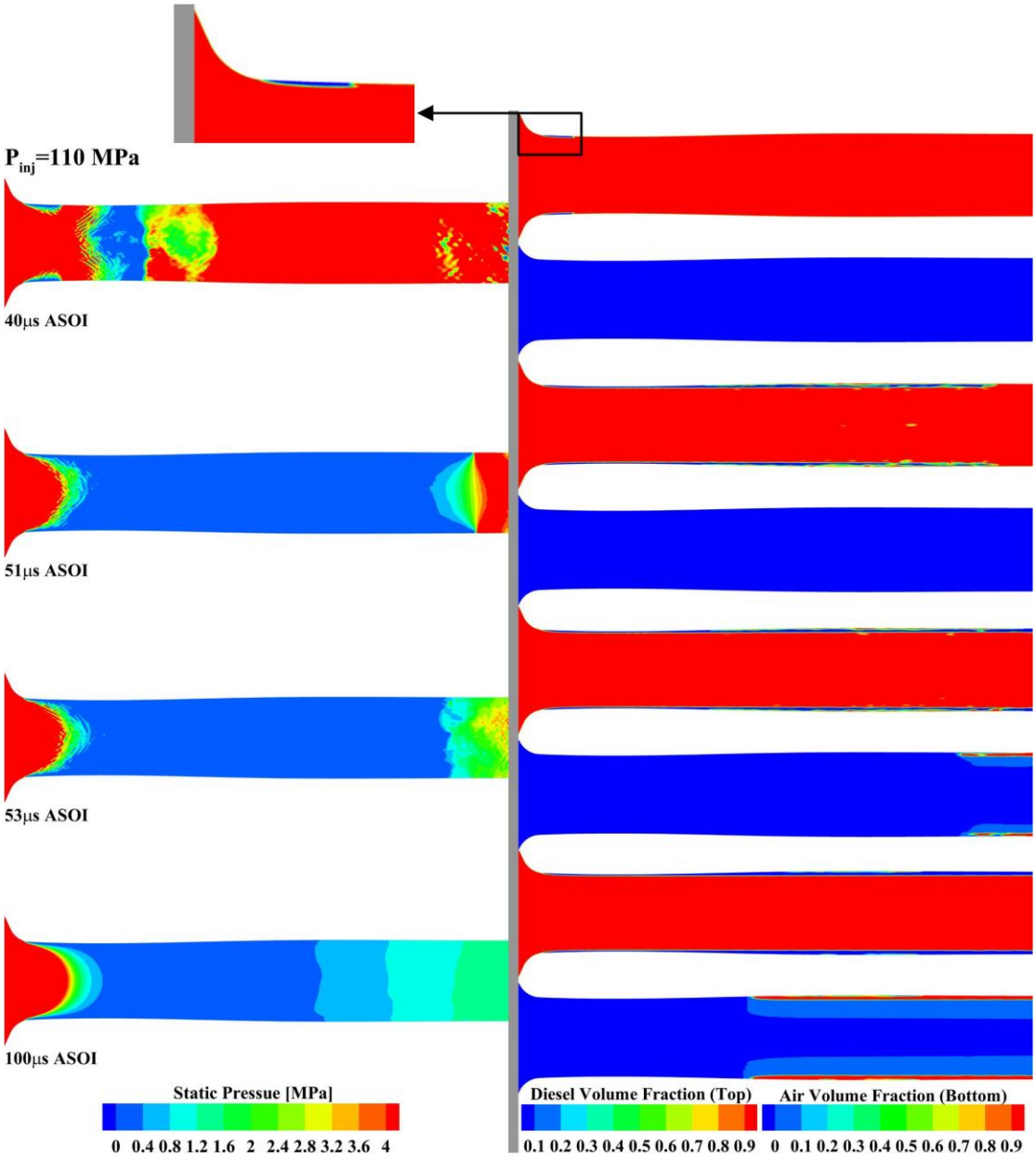

Figure 4-9: Contour plots of static pressure (left column), liquid volume fraction (right column top) and air volume fraction (right column bottom) at various time steps. A cavitation pocket forms in the low pressure region downstream of the orifice entrance and extends to the nozzle exit as upstream pressure increases. At 53 μs ASOI, after the onset of cavitation induced hydraulic flip, ingestion of air into the orifice causes pressure increase in the second half of the nozzle.

With the implementation of a modified multi-phase mixture energy equation and realistic equations of state for all phases, temperature and density variations of the flow in the nozzle can be investigated numerically. As shown in *Figure 4-10(a)* at 52 μs ASOI, just after the onset of hydraulic flip, a slight temperature decrease (2 K) across the nozzle entrance due to flow acceleration and pressure reduction can be observed. Decrease in pressure also causes significant reduction in flow density in the same region as depicted in *Figure 4-10(b)*. Such trends continue until the divergent section of the nozzle where pressure recovery causes temperature and density to increase again with the former then decreasing slightly (less than 1 K) as a result of hydraulic flip induced flow acceleration in the second half of the nozzle. At 1D downstream of the nozzle exit,

sudden increase in injection velocity due to complete flow detachment from the nozzle wall leads to abrupt change in flow properties. This is manifested by fluctuations in both flow temperature and flow density just downstream of the nozzle exit. This aspect will be further analysed in the next section.

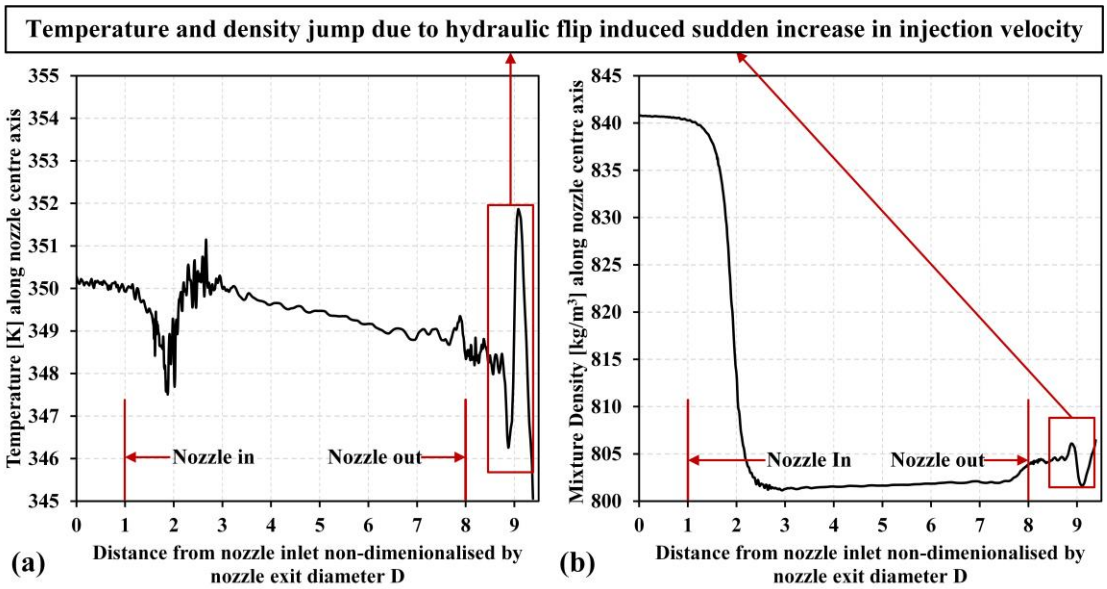

Figure 4-10: Instantaneous variation of flow temperature (a) and flow density (b) along the nozzle centre axis at 52 µs ASOI. Temperature and density jump due to hydraulic flip induced sudden increase in injection velocity is shown in a red rectangle.

Furthermore, the thermal effects of in-nozzle cavitation and the collapse of vapour cavities downstream of the nozzle exit are revealed in *Figure 4-11*. In the first half of the nozzle, increase in sensible enthalpy caused by wall shear on the flow leads to formation of high temperature pockets near the wall. However, a decrease in temperature as a result of high vaporisation rate in the near wall region is observed to correlate spatially with the accumulation of liquid residue (due to turbulent mixing in the boundary layer [148]) in the second half of the nozzle. From a thermodynamic standpoint, vaporisation takes energy from the liquid in the form of enthalpy of vaporisation and the reverse process occurs when there is condensation of vapour. Thus, increase in surface temperature of the exiting liquid jet can be observed where pressure recovery results in high rates of condensation at nozzle exit. Collapse of vapour cavities near the nozzle exit also causes pressure peaks at various locations on the nozzle wall. In real diesel injection process, however, dissolved gases within the liquid can diffuse into vapour cavities due to concentration gradients and the incondensable gases present in the cavities could decrease the condensation rate, which may lead to smaller temperature increase and smaller local pressure maxima. Modelling this phenomenon requires the addition of diffusion terms in the volume fraction transport equations, which will be considered in future study.

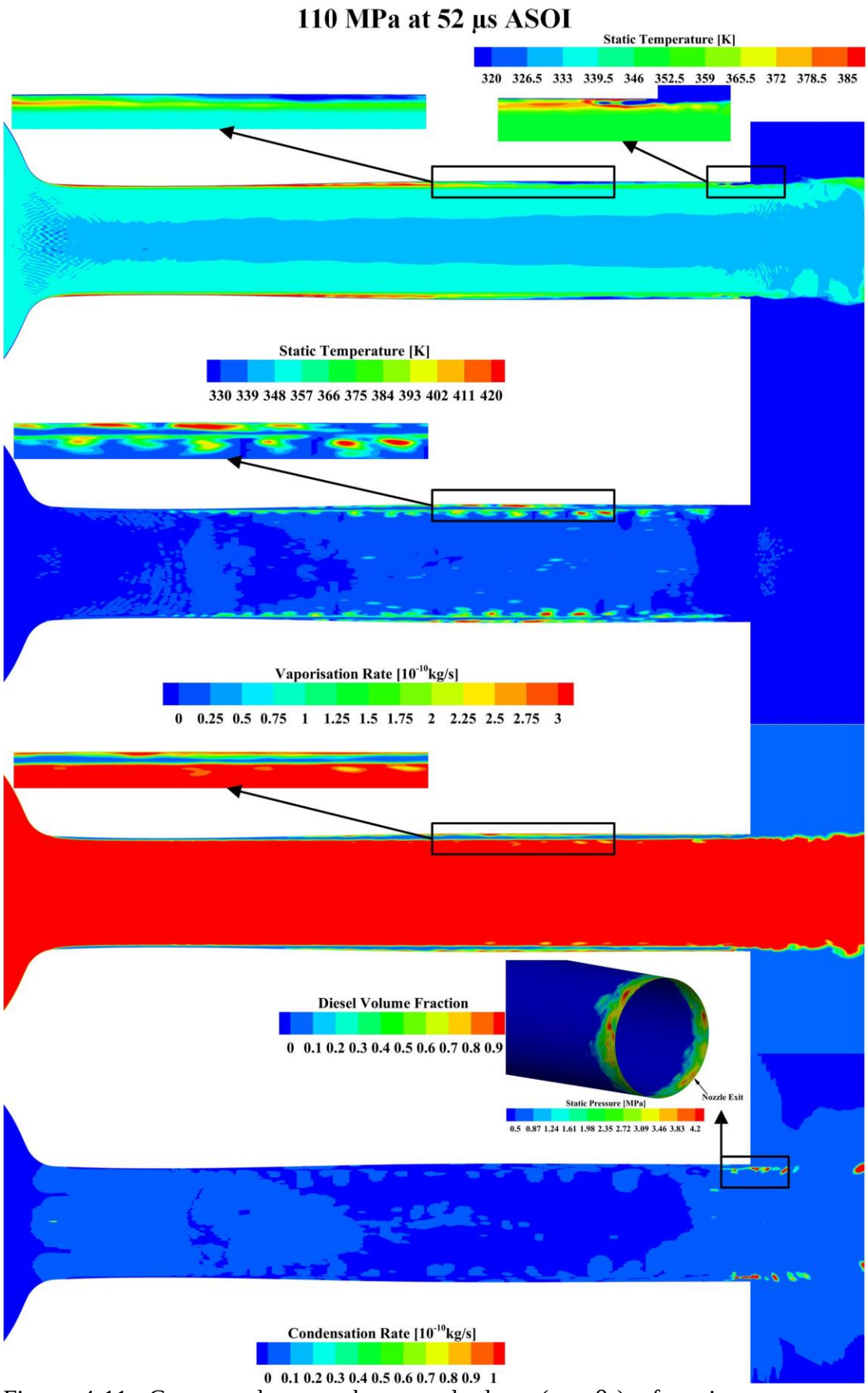

Figure 4-11: Contour plots on the central plane ($x = 0$) of static temperature, vaporisation rate, diesel volume fraction and condensation rate at 52 µs ASOI. Depicted

in enlarged views are spatially correlated temperature variation, diesel volume fraction and vaporisation rate near the wall in the second half section of the nozzle. A separate contour plot of pressure variation is employed to correlate collapse of vapour cavities with local pressure peaks on the nozzle wall near the nozzle exit.

The computed spray structures at different times are illustrated in *Figure 4-12*. The inner nozzle flow is represented using a Q-criterion isosurface (2×10^9) coloured by vorticity magnitude while the emerging spray is depicted using a liquid volume isosurface ($\alpha_l = 0.1$) coloured by resolved turbulent kinetic energy. The choice of a large positive value for Q isosurfaces isolates areas where the strength of rotation overcomes the strain, thus making those surfaces eligible as vortex envelopes [149]. Since vorticity (rotational strength of flow) should increase as the centre of the vortex is approached, Q can be expected to remain positive in the core of the vortex. Therefore colouring positive Q isosurfaces with vorticity magnitude ensures a good estimation of the intensity of local flow rotation. At 30 μs ASOI, flow inertia, geometry change and pressure gradient induced moderate flow separation at the first convergent section (nozzle entrance) and second convergent section of the nozzle (nozzle exit) generates large vortical structures that span across the separation region. At the start and the end of these separation regions, production of small scale vortical structures due to local flow rotation is observed. However, small quantities of in-nozzle turbulent structures and their low vorticity magnitude (vorticity < 2×10^7) lead to the generation of weak surface instabilities that do not result in observable waves on the liquid-gas interface in the vicinity of the nozzle exit. On the other hand, aerodynamic forces on the tip of the liquid jet creates a stagnation zone around which air flow interacts with the edge of the penetrating tip. This interaction results in the formation of a mushroom structure due to vortex roll-up which also initiates Kelvin-Helmholtz instabilities. Such flow instabilities create visible irregularities at the edge of the mushroom structure and also on the trailing liquid-gas interface. By 40 μs ASOI surface instabilities start to strip a considerable amount of liquid ligaments and droplets from the liquid-gas interface further downstream. In addition, two toroidal vortices (vorticity magnitude > 4×10^7) appear at the nozzle entrance due to cavitation initiation as a result of intensifying flow separation and recirculation. Vortex rings near the nozzle wall are also observed to increase at the second convergent section of the nozzle because of the increasing wall shear on the accelerating flow. These turbulent structures only affect the spray once they have been transported the length of the nozzle. At around 3D from the nozzle exit, toroidal span-wise waves are visible on the liquid-gas interface. These span-wise waves are most probably generated due to either Kelvin-Helmholtz instability (velocity shear) or 2D Tollmien-Schlichting instability as recently reported by Shinjo and Umenura [62]. From 40 μs to 52 μs ASOI, as the length of the inlet vapour cavity continues to grow, the velocity shear and difference in viscosity between liquid and vapour together with wall shear strengthen local flow rotation on the liquid-vapour interface. This causes an increase in the number of vortical structures and their vorticity magnitude with cavity growth the growth along the wall. Once the cavitation enhanced in-nozzle turbulence has travelled beyond the nozzle exit (53 μs ASOI), the amplitude of transverse waves on the liquid-gas interface is observed to increase. After 53 μs ASOI, complete separation of liquid jet from the wall significantly diminishes the wall shear induced surface disturbances. The spray angle gradually becomes smaller and the atomisation is suppressed as compared to previous time steps. At the last stage of the simulation (100 μs ASOI), turbulence levels in the second half of the nozzle are again increased due to stronger convection between the penetrating liquid jet and the refluxing ambient

gas. However, the increased turbulence level does not contribute to the generation of irregularities on the liquid-gas interface. This indicates that wall shear is one of the main factors contributing to the generation of surface disturbances that lead to the primary spray breakup. This aspect is discussed in the next section.

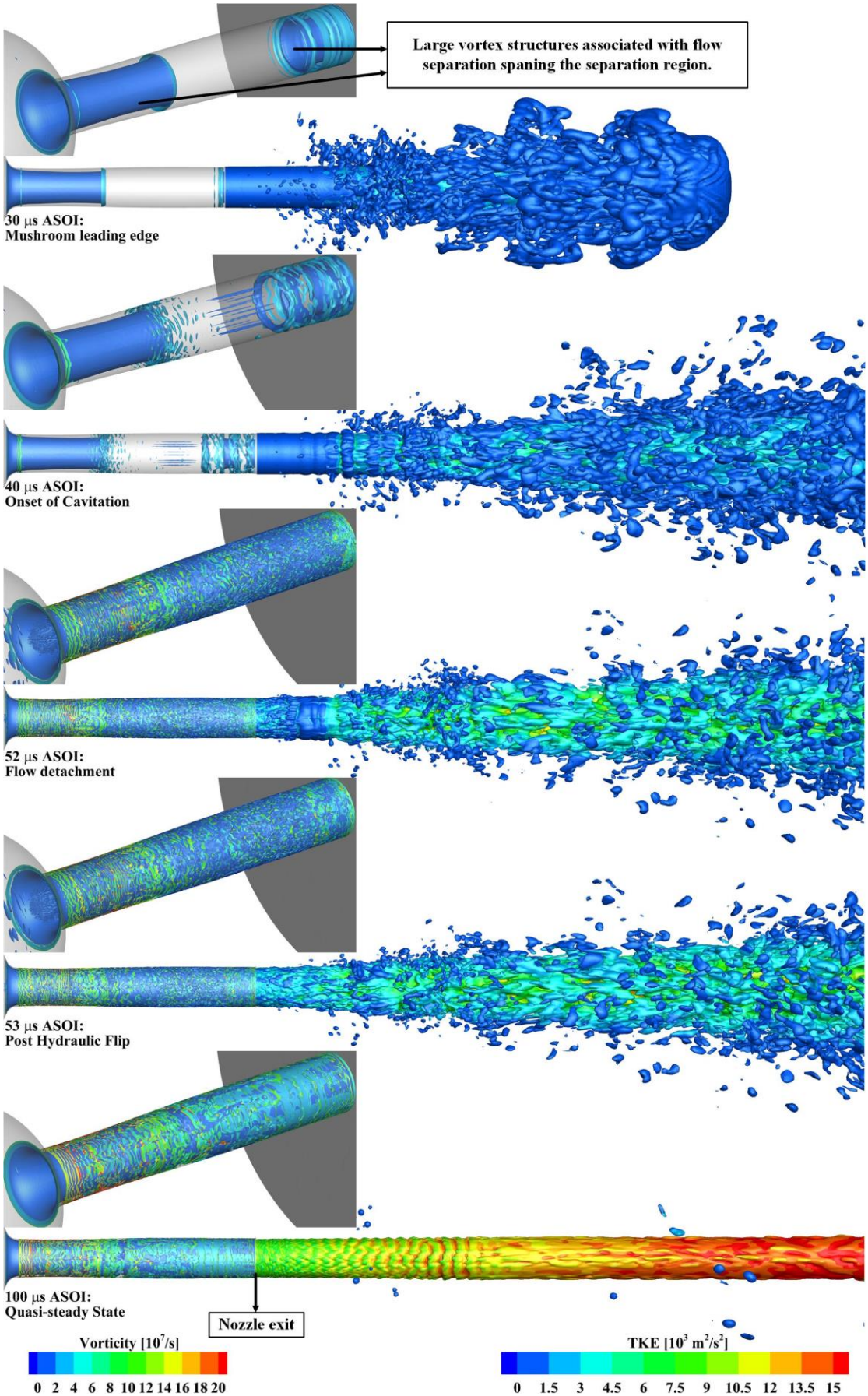

Figure 4-12: Inner nozzle flow and penetrating spray represented by a Q-criterion isosurface of 2×10^9 and a liquid volume isosurface of $\alpha = 0.1$ respectively. The Q

isosurface in the nozzle is coloured using vorticity magnitude while the liquid isosurface of the emerging jet is coloured by resolved Turbulent Kinetic Energy. Enlarged 3D visualisations of the in-nozzle turbulent structures are utilised for a better clarity.

4.5.5 Effects of wall shear and hydraulic flip

The importance of wall shear to liquid jet disintegration is demonstrated by comparing quasi-steady spray structures at different injection pressures. In *Figure 4-13(a)*, quasi-steady spray structures at 100 µs ASOI are represented using Q-criterion (2×10^9) and liquid volume fraction ($\alpha = 0.1$) isosurfaces coloured by vorticity magnitude and resolved turbulent kinetic energy respectively. No cavitation is observed in the 30 MPa case. Only moderate generation of in-nozzle turbulence can be seen in the 30 MPa case due to relatively low flow rates and absence of cavitation. However, growth of span-wise toroidal waves due to Kelvin-Helmholtz or Tollmein Schlichting instability can be observed at around 3D from the nozzle exit. Further downstream, three-dimensional instabilities continue to form on the jet surface, which ultimately breakup the jet into ligaments and droplets.

At this quasi-steady stage, ambient gas ingestion (associated with hydraulic flip) up to 345 µm and 556 µm into the orifice can be observed in the 70 MPa and the 110 MPa cases respectively. Enlarged views of the nozzle region in *Figure 4-13(a)* show the liquid-gas interface coloured in red and the liquid-vapour interface coloured in blue. The transition from red to blue in the middle nozzle section represents the gas-vapour mixing process. The conventional understanding of hydraulic flip is that with vapour cavitation extending from nozzle entrance to nozzle exit the cavity surrounding the free jet is fully ventilated with ambient gas. However these results show that vapour production at nozzle entrance remains which fills the surrounding cavity for several diameters downstream limiting the extent of air influx. As compared to the 70 MPa case, ambient gas extends further into the orifice in the 110 MPa case due to the existence of a larger high pressure region extending into the nozzle as shown in *Figure 4-13(b)*. Thus, stronger shear between the liquid and the ambient gas causes noticeably higher local flow rotation (quantified by vorticity magnitude) in the second half of the nozzle in the 110 MPa case. However, quasi-steady structures of the emerging spray are more stable for the 110 MPa case than for the 70 MPa case although the turbulent kinetic energy of the spray is considerably higher with a 110 MPa injection pressure. A possible explanation for this could be high flow inertia resulting in insufficient relaxation time for surface instabilities to produce visible irregularities on the liquid-gas interface. Comparison of these three cases reveals that the absence of wall shear due to hydraulic flip substantially limits the development of instabilities on the jet surface, which results in diminished fragmentation and therefore significantly smaller early spray angle. Furthermore, the appearance of the ambient gas cavity is completely stable in both the 70 MPa and 110 MPa cases with negligible time-dependent variations during the quasi-steady state.

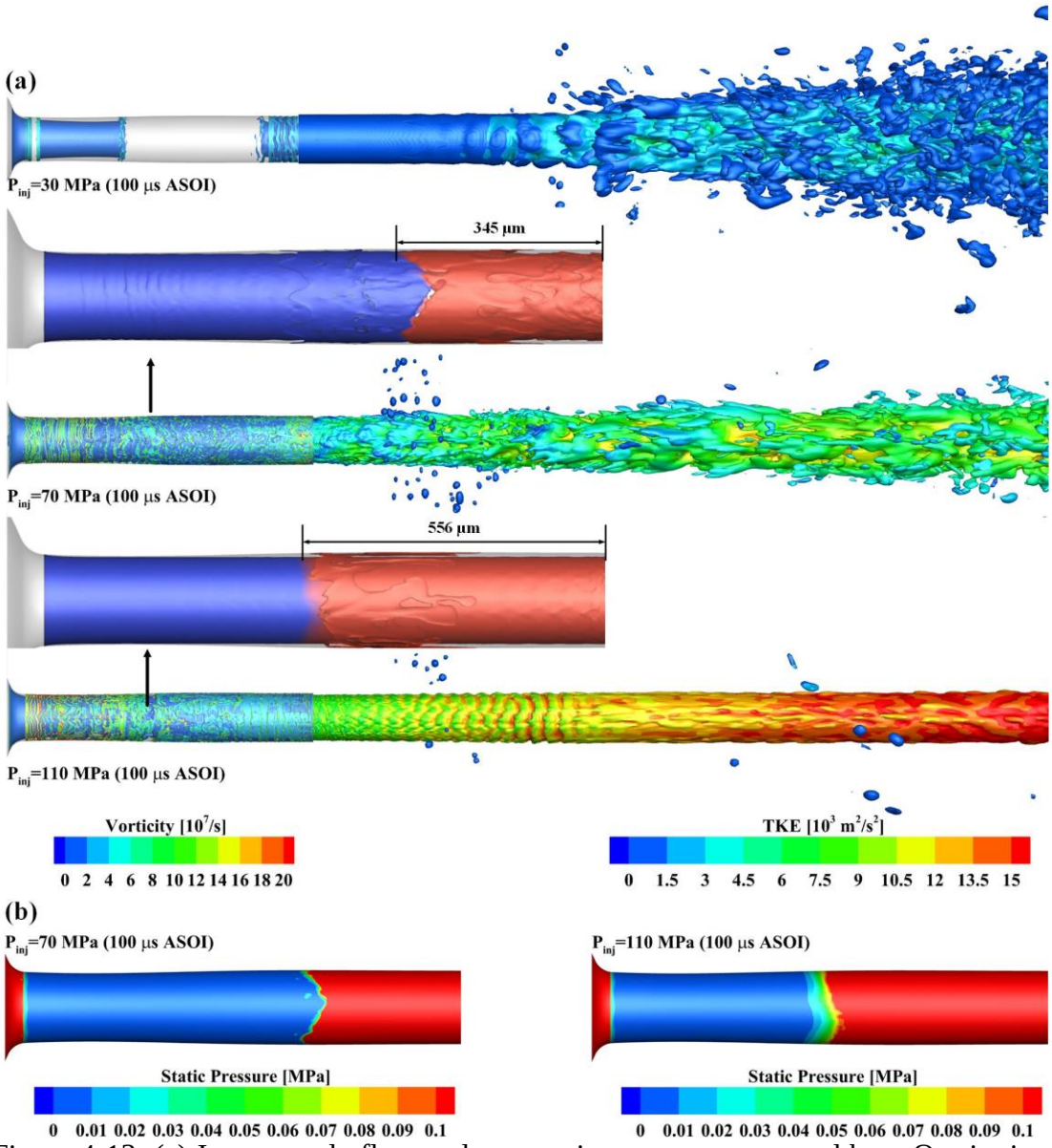

Figure 4-13: (a) Inner nozzle flow and penetrating spray represented by a Q-criterion isosurface of 2×10^9 and a liquid volume isosurface of $\alpha = 0.1$ respectively. The Q isosurface is coloured using vorticity magnitude while the liquid volume isosurface is coloured by resolved turbulent kinetic energy. For the 70 MPa and 110 MPa cases, enlarged views are shown for the ambient gas ingestion process which is described using a liquid volume isosurface of $\alpha = 0.1$. The liquid-vapour interface is coloured in blue while the liquid-gas interface is coloured in red. Air-vapour mixing process in the middle nozzle section is illustrated by the red-blue transition. (b) Contour plots of static pressure for the inner nozzle flow at 70 MPa (left) and 110 MPa (right) injection pressure cases.

Averaged span-wise density and velocity profiles at the middle and end sections of the nozzle are given in *Figure 4-14*.

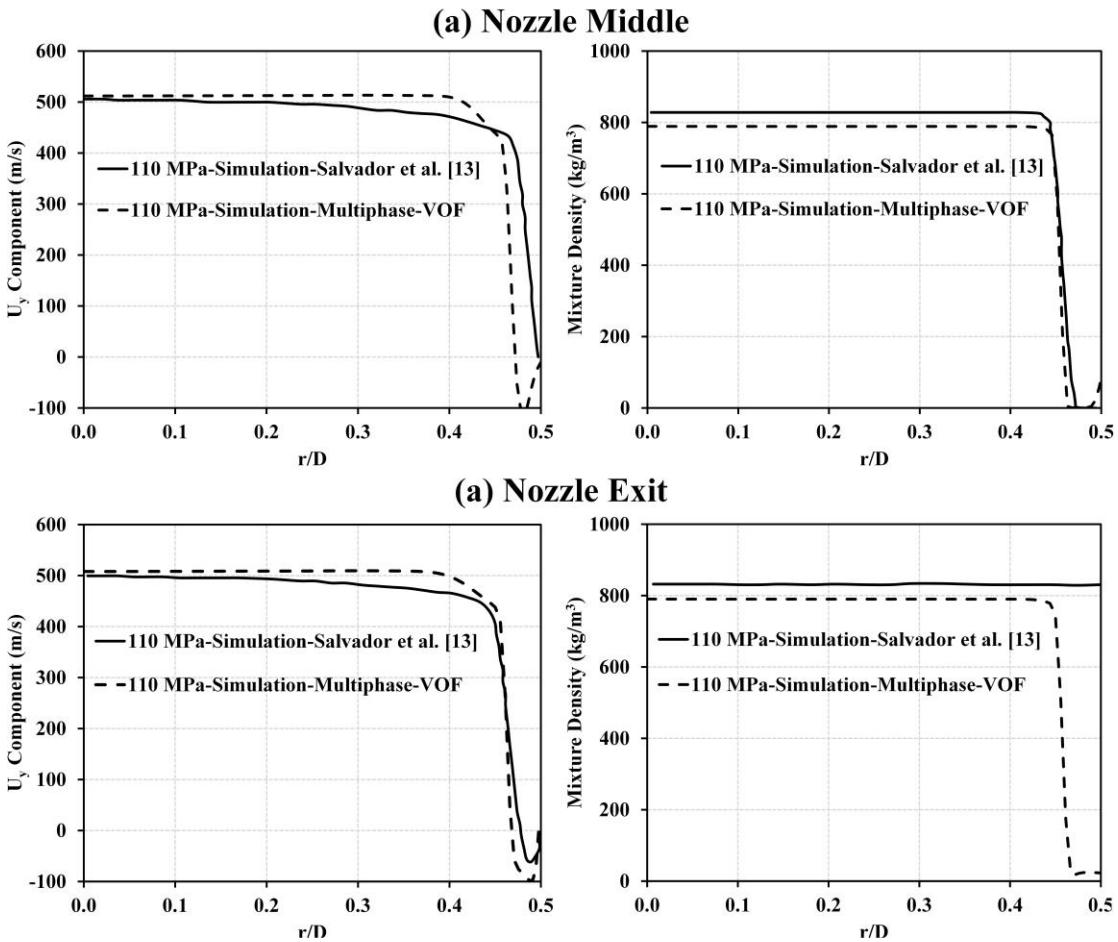

Figure 4-14: Averaged span-wise density and velocity profiles obtained at the middle and the end sections of the nozzle. The comparison is made between the predictions from the PISOCavitatingInterFoam solver (Multi-phase-VOF) and a two-phase homogeneous equilibrium model employed by Salvador et al. [89, 145].

As shown in *Figure 4-14*, stable in-nozzle liquid and gas distributions result in the development of smooth span-wise density and velocity profiles at the middle and end sections of the nozzle. In the near wall region, PISOCavitatingInterFoam (Multi-phase-VOF) predicts a marginally lower injection velocity at both sections as compared to the predictions of the homogeneous two-phase model employed by Salvador *et al*. [89, 145]. This can be partly attributed to different near wall mesh resolution between two simulations (0.8 µm for the homogeneous model and 0.08 µm for PISOCavitatingInterFoam). Another possible reason for this deviation could be the ability of PISOCavitatingInterFoam to model ambient gas ingestion that causes moderate reduction in injection velocity near the wall. Ambient gas ingestion also leads to significant reduction in flow density near the wall at the nozzle exit as simulated by PISOCavitatingInterFoam. In addition, the use of a non-linear equation of state for the liquid phase in the VOF simulation leads to prediction of a lower liquid density in the central nozzle region as compared to that of the homogeneous model. Apart from these deviations, the density profiles near the wall at half nozzle length obtained from PISOCavitatingInterFoam and the two-phase code show only small differences. This indicates that the two compressible codes have comparable capability in predicting density of compressible diesel vapour.

The occurrence of shockwaves in the chamber is illustrated in *Figure 4-15*. Correlating *Figure 4-15* and *Figure 4-12* reveals that shockwaves originate from the liquid-gas interface where the interfacial velocity approaches the speed of sound in the chamber gas. Another notable aspect is that the appearance of a near nozzle shockwave is concurrent with the onset of hydraulic flip in both the 70 MPa (67 μs ASOI) and the 110 MPa (52 μs ASOI) cases, as shown in the contour plots of *Figure 4-15*. Such a phenomenon is clearly illustrated by the plot of instantaneous variation in the interfacial Mach number (extracted from the 0.9 liquid volume isosurface) before and after the onset of hydraulic flip using the 110 MPa case. This is possibly attributable to the sudden reduction in the effective flow area due to the onset of hydraulic flip which is also concurrent with the increased nozzle exit velocity as the result of wall shear reduction and increase in upstream pressure. Also, shockwaves in the 110 MPa simulation are more oblique as compared to the results of the 70 MPa simulation, indicating a higher spray penetration velocity. The 30 MPa injection pressure case, on the other hand, only produces a subsonic quasi-steady spray in the chamber as indicated by the comparison of interfacial Mach numbers in *Figure 4-16*. Since there is no cavitation in the 30 MPa case, the liquid jet remains attached to the zero-slip nozzle wall, which causes the jet to have a zero interfacial velocity at the point of exit from the nozzle.

After 1D from the nozzle exit, pressure variation on the interface is observed to be mainly governed by the relative motion between liquid and ambient gas as depicted in *Figure 4-17*. Regions of high pressure appear just upstream of the shockwave front. This complies with the variation of static pressure across an oblique shock wave reported by Courant *et al*. [150]. Regions of low static pressure, on the other hand, correspond to the locations of the shockwave roots where convex surface protrusions are also observed to occur.

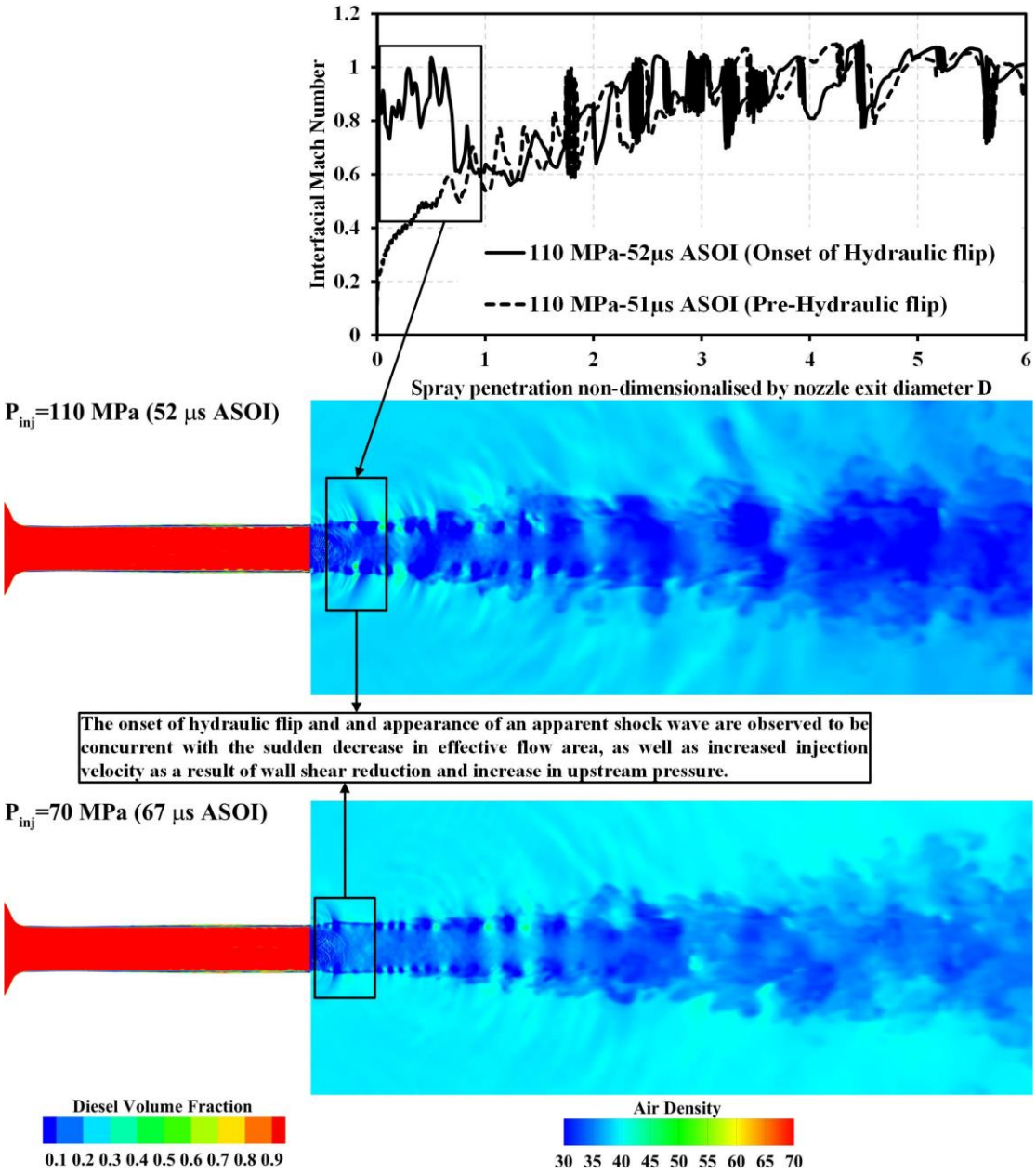

Figure 4-15: Contour plots of diesel volume fraction in the nozzle and span-wise shockwaves represented by air density in the spray chamber. The central plane ($x = 0$) contour plots are captured at 52 μs ASOI for the 110 MPa case and at 67 μs ASOI for the 70 MPa case. These two instants also correspond to the onset of hydraulic flip. The appearance of a shockwave just downstream of the nozzle exit is shown in a black rectangle. This phenomenon is clearly illustrated by the plot of instantaneous variation in the interfacial Mach number (extracted from the 0.9 liquid volume isosurface) before and after the onset of hydraulic flip for the 110 MPa case.

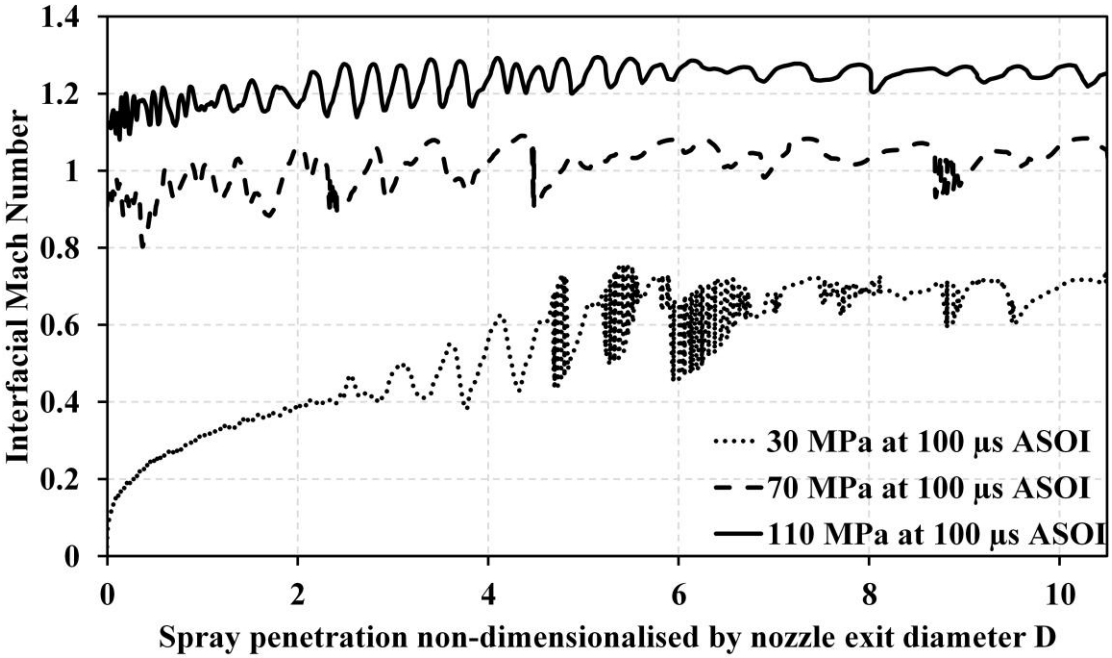

Figure 4-16: Instantaneous variation of interfacial Mach numbers of the penetrating spray extracted from a quasi-steady interface represented by a 0.9 liquid isosurface. The jet has reached quasi-steady velocity for all three injection pressure cases.

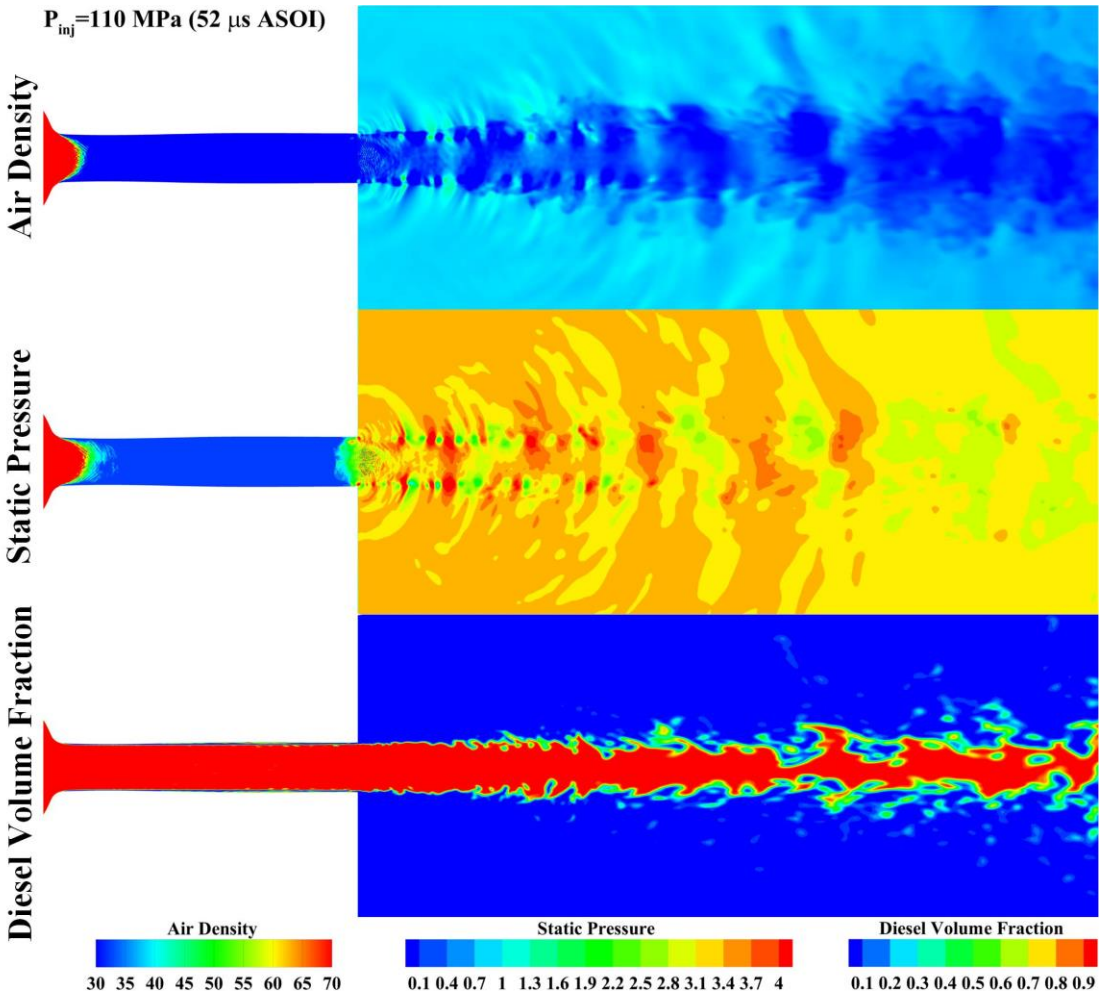

Figure 4-17: Contour plots of air density, static pressure and diesel volume fraction displayed at $x = 0$ plane for the 110 MPa case at 52 µs ASOI (onset of hydraulic flip).

4.6 Conclusions

A modified mixture energy equation based on enthalpy and including enthalpy of phase change source terms due to cavitation is implemented in a previously developed compressible multi-phase VOF-LES code. Simulation of high pressure diesel injection process is enabled by the use of non-linear equations of state as well as pressure and temperature dependent properties for the liquid and gas phases. These new implementations provide the new cavitation solver (PISOCavitatingInterFoam) with the ability to model thermo-physics of cavitating diesel sprays at higher injection pressures with improved fidelity. The solver has been first validated against published experimental data including mass flow rates, momentum fluxes, effective injection velocities and discharge coefficients obtained using a convergent-divergent-convergent single orifice diesel injector. It has been demonstrated that the developed model can predict these important hydrodynamic parameters with high levels of confidence. However, slight over-prediction of effective injection velocity is found, which can be attributed to the omission of surface roughness on the injector walls and unknown experimental uncertainties. Further calculation of in-nozzle flow and primary atomisation using the same injector has revealed:

- Cavitation initiates just downstream of the nozzle entrance where high flow inertia and flow contraction causes flow rotation and reduction of pressure to, or below, vapour pressure.
- Small-scale vortical structures generated in-nozzle correlate spatially with the presence of both cavitation and liquid-wall shear.
- Flow acceleration, pressure reduction and cavitation lead to decrease in flow temperature in the injector nozzle. However, increase in sensible enthalpy due to condensation of vapour at the nozzle exit as a result of pressure recovery increases the surface temperature of the exiting jet.
- The present work shows that with the onset of hydraulic flip vapour production remains at nozzle entrance, which fills the surrounding cavity for several diameters downstream limiting the extent of ambient gas influx. The extent of the vapour filled length reduces with increasing injection pressure.
- The onset of hydraulic flip minimises the effects of wall shear on the jet, which reduces production of surface instabilities. It also occurs simultaneously with significant increase in injection velocity and the sudden reduction in effective flow area. A shockwave is generated just downstream of the nozzle exit which is simultaneous with the initiation of hydraulic flip.
- Localised low pressure regions, convex surface protrusions, and the roots of shockwaves are observed to correlate spatially in the chamber.

5 Adaption of fractional step method and central-upwind flux scheme for compressible multi-phase flows: Application to cavitating high-pressure diesel sprays

Abstract

In this study, a new finite volume solver for all Mach number multi-phase flows suitable for high fidelity simulation of high-pressure cavitating diesel sprays is presented. This solver is developed by replacing the PISO algorithm in a previously developed compressible multi-phase VOF-LES solver (PISOCavitatingInterFoam) with an efficient and low dissipative all Mach number compressible fraction step method. Improved numerical resolution is achieved with the implementation of the Kurganov-Noelle-Petrova numerical scheme for the formulation of non-oscillating convective fluxes. The performance of the compressible fractional step method is first established by considering single-phase supersonic flows in a convergent-divergent nozzle and over a forward-facing step. This is followed by detailed mathematical derivations that extend this single-phase all Mach number solver to multi-phase flows. The superiority of the new all Mach number multi-phase solver in numerical resolution and computing speed is demonstrated by comparing it with the PISOCavitatingInterFoam solver described in Chapter 4. The comparison is performed for the atomisation of a cavitating diesel spray from a single-hole injector with a sharp edged orifice. Due to the addition of a pressure dissipation term in the evaluation of numeric flux for preventing pressure-velocity decoupling, the new multi-phase solver is found to be slightly more diffusive than PISOCavitatingInterFoam at the low Mach number limit. However, as flow Mach number increases, the new multi-phase solver is able to resolve small-scale turbulence with a better resolution and increasingly higher efficiency compared to the predictions of PISOCavitatingInterFoam. Extended validations will be conducted in future work to provide a comprehensive and detailed assessment of the developed all Mach number multi-phase solver.

Key words: All Mach number Multi-phase flow; Volume of Fluid; Large Eddy Simulation; Cavitation; Primary atomisation

5.1 Introduction

Numerical investigation of high pressure diesel injection processes requires modelling of turbulent multi-phase flows over a wide range of Mach numbers. A common problem associated with the simulation of all Mach number flows is the large time scale disparity between the acoustic waves and the waves convected at fluid speed. This disparity contributes to numerical stiffness at the low Mach number limit if no eigenvalue scaling is used [151]. Increasing numerical stiffness occurs at the incompressible flow limit because the time step required for stable computations is mainly dominated by acoustic time scales. Due to the extremely small acoustic time scale in low Mach number flows, employing compressible flow solvers for viscous flow simulations with low Mach numbers (<0.3) is extremely inefficient. A solution to this problem is associated with the use of time preconditioning techniques [152, 153]. These techniques scale the eigenvalues of the system of compressible flow equations to diminish the disparity in wave speeds. However, removal of most of the numerical stiffness due to multiple time scales through time preconditioning comes at the cost of significantly decreased computational efficiency as a result of iterative time stepping [152].

On the other hand, compressible solvers adopting semi-implicit methods such as PISO, SIMPLE and their combinations have been successfully employed for solving subsonic problems [154]. When applying these models to compute supersonic flows, a major disadvantage is related to numerical oscillations in regions of flow discontinuities. The remedy can be found in a hybrid scheme developed by Kraposhin et al. [155]. This scheme combines PISO/SIMPLE algorithms for implicit discretisation of the conservation equations and the Kurganov-Noelle-Petrova (KNP) numerical scheme [156] for the formulation of non-oscillating convective fluxes. The limitation that the stability of the KNP scheme is ensured by maintaining the acoustic Courant-Friedrichs-Lewy (CFL) number less than 0.5 in low Mach number limit is removed by using a switcher function. This function switches between high Mach number (KNP) and low Mach number (PISO/SIMPLE) regimes of this hybrid scheme based on local Mach and CFL numbers. Thus, simulation of flows over a wide range of Mach numbers would be possible with an acoustic CFL number far exceeding 1. Nevertheless, the use of PISO/SIMPLE algorithms needs additional sub-iterations in solving the pressure equation within each time step in order to ensure strict mass conservation [157]. This potentially reduces the computational efficiency of the PISO/SIMPLE-KNP hybrid scheme.

Alternatively, extension of primitive variable fractional step methods [158, 159] to all Mach number flows has been first realised by Shi et al. [157]. A new central flux scheme is proposed to remove the checkerboard instability in the lower Mach number limit by re-introducing coupling between velocity and pressure fields. Numerical stability at high Mach numbers is then achieved using a new formulation of the compressible pressure equation containing a pressure Laplacian term pre-multiplied by the time step size. Since the Laplacian operator is acting directly on the pressure field, the coarse levels for this operator need to be formed only once and they remain constant during the time evolution of the pressure field. This leads to significant computational benefits as compared to PISO/SIMPLE algorithms. However, the use of the central flux scheme, to some extent, lacks robustness in capturing sharp shockwaves due to high numerical dissipation. This problem can be overcome by replacing the central flux scheme with the KNP scheme since it has very high resolution due to the smaller

amount of numerical dissipation as compared to the central schemes [156]. Therefore, the main objective of this study is to first improve the resolution of the all Mach number fractional step method by replacing the central flux scheme with the KNP scheme. Extension of the improved all Mach number method, which is termed as compressible fractional step method (cFSM), to multi-phase flows is achieved by replacing the PISO based multi-phase mixture pressure equation in PISOCavitatingInterFoam [160] with the cFSM based compressible multi-phase mixture equation. Since the new all Mach number multiphase solver is based on replacing the PISO algorithm with the cFSM algorithm, it is given the name cFSMCavitatingInterFoam.

The present chapter is divided into 5 sections. In section 2, a description of the all Mach number fractional step method is provided together with the modifications to include the KNP scheme. Two test cases are employed in section 3 to demonstrate the performance of the new all Mach number solver (cFSM) for single-phase flows. This is followed by detailed description of the procedures extending this solver to multi-phase flows in section 4. In section 5, the advantages of the new all Mach number multi-phase solver (cFSMCavitatingInterFoam) in numerical resolution and computing speed are demonstrated by comparing it with PISOCavitatingInterFoam described in Chapter 4. Finally, the main conclusions of the development are drawn in section 6.

5.2 Description of the all Mach number fractional step method

The initial formulation that extends Chorin's [159] incompressible fractional step method (FSM) to all Mach number flows is first reported by Shi et al. [157]. This formulation involves separating mass flux into potential and convective parts, which is a generalisation of the Helmholtz-Hodge decomposition method to define the projection step of FSM. The derivation of the all Mach number fractional step method starts with a predictor step which employs a discrete form of the momentum equation:

$$\frac{\rho^* U^* - \rho^n U^n}{\Delta t} = -\nabla \cdot \left(\rho^* U^* U^* - \tau^* \right) - \nabla p^n \tag{5-1}$$

in which only the gradient pressure term is kept explicit and the intermediate density field ρ^* is obtained from solving the continuity equation:

$$\frac{\partial \rho}{\partial t} + \nabla \cdot \left(\rho U \right) = 0 \tag{5-2}$$

Subsequently, the predicted intermediate density ρ^* and velocity U^* are used to solve the energy equation (here we use sensible specific enthalpy h instead of sensible specific internal energy e in the original derivation [157]):

$$\frac{\partial \rho^* h}{\partial t} + \nabla \cdot \left(\rho^* U^* h \right) + \frac{\partial \rho K}{\partial t} + \nabla \cdot \left(\rho U K \right) - \frac{\partial p}{\partial t} = \lambda \left(\nabla^2 T \right) + \nabla \cdot \left(\tau \cdot U \right) \tag{5-3}$$

At this step, the temperature field T is evaluated using the calculated enthalpy h and constant pressure heat capacity C_p through a Newton iterative approach. The temperature field is then used to update flow compressibility $\psi = \frac{1}{RT}$ which relates density and pressure as:

$$\rho = \psi p \tag{5-4}$$

This density-pressure relation can be integrated into the continuity equation Eqn (5-2) to obtain a new compressible pressure equation in the form of:

$$\frac{p^{n+1}\psi^{n+1} - p^{n}\psi^{n}}{\Delta t} + \nabla \cdot \left(\left(\tilde{\rho}\tilde{U} \right)_f \right) - \Delta t \nabla^2 p^{n+1} = 0 \tag{5-5}$$

It is noted that the Laplacian operator ∇^2 in the new pressure formulation above is applied directly to the pressure field. Thus, the discretisation coefficients of this operator will only depend on geometric quantities. When using algebraic multi-grid (AMG) methods to accelerate convergence, the coarse levels for the Laplacian operator need to be formed only once and they remain constant during the time evolution of the pressure field. This significantly improves computational efficiency especially for large simulations such as LES and DNS since the pressure equation only needs to be solved once within each time step. Additionally, the new compressible pressure equation is important in removing the acoustic time step size limitation in low Mach number limit. This can be seen by dividing Eqn (5-5) with time step Δt:

$$\frac{p^{n+1}\psi^{n+1} - p^{n}\psi^{n}}{\Delta t^2} + \frac{\nabla \cdot \left(\left(\tilde{\rho}\tilde{U} \right)_f \right)}{\Delta t} - \nabla^2 p^{n+1} = 0 \tag{5-6}$$

In case of large time steps, it is evident from Eqn (5-6) that the incompressible potential pressure equation can be recovered:

$$\frac{\nabla \cdot \left(\left(\tilde{\rho}\tilde{U} \right)_f \right)}{\Delta t} - \nabla^2 p^{n+1} = 0 \tag{5-7}$$

Thus, no time preconditioning is required for computing low Mach number flows as the limitation associated with acoustic time scale is naturally removed.

To prevent pressure-velocity decoupling at the low Mach number limit, the numeric flux term $\left(\tilde{\rho}\tilde{U} \right)_f$ in Eqn (5-5) can be expressed as the addition of a predicted mass flux and a pressure dissipation term:

$$\left(\tilde{\rho}\tilde{U} \right)_f = \left(\rho^* U^* \right)_f + \frac{\Delta t \left(p_{right} - p_{left} \right)}{\Delta s} l \tag{5-8}$$

where the pressure dissipation term is constructed as the pressure gradient across an arbitrary mesh face along the direction l connecting centres of two neighbouring cells. Therefore, the pressure-velocity decoupling is removed by re-introducing coupling of velocity and pressure in the evaluation of the numeric flux. In the original formulation, the predicted mass flux term is computed using a central scheme that averages the mass fluxes on the left and right finite volumes of an arbitrary face:

$$\left(\rho^* U^* \right)_f = \frac{1}{2} \left(\left(\rho^*_{left} U^*_{left} \right)_f + \left(\rho^*_{right} U^*_{right} \right)_f \right) \tag{5-9}$$

In this work, the numerical resolution of the all Mach number fractional step method is improved by replacing the central scheme above with a Kurganov-Noelle-Petrova (KNP) scheme [155, 156]. By utilising the KNP scheme, the predicted mass flux can be represented as a weighted sum of mass fluxes on the left (P) and right (N) volumes of mesh faces (detailed derivation can be found in Kraposhin et al.'s work [155]):

$$\left(\rho^* U^* \right)_f = \rho_f^P \left(a_f^P U_f^P + a_f^P a_f^{\min} \right) + \rho_f^N \left(a_f^N U_f^N - a_f^N a_f^{\min} \right) \tag{5-10}$$

where a_f^P and a_f^N are calculated using following expressions:

$$\left.\begin{aligned} a_f^P &= \frac{a_f^{\max}}{a_f^{\max} + a_f^{\min}}, a_f^N = \frac{a_f^{\min}}{a_f^{\max} + a_f^{\min}} \\ a_f^{\max} &= \max\left(c_f^P \left|\overrightarrow{S_f}\right| + U_f^P, c_f^N \left|\overrightarrow{S_f}\right| + U_f^N\right) \\ a_f^{\min} &= -\min\left(-c_f^P \left|\overrightarrow{S_f}\right| + U_f^P, -c_f^N \left|\overrightarrow{S_f}\right| + U_f^N\right) \\ c_f^P &= \sqrt{\gamma_f^P R T_f^P}, c_f^N = \sqrt{\gamma_f^N R T_f^N} \end{aligned}\right\} \quad (5\text{-}11)$$

Finally, new pressure field obtained as the solution of Eqn (5-5) is substituted back to momentum equation to correct the velocity field following:

$$\frac{\rho^{n+1}U^{n+1} - \rho^* U^*}{\Delta t} = \nabla p^n - \nabla p^{n+1} \quad (5\text{-}12)$$

The modifications described above lead to the development of a new compressible fractional step method (cFSM) of which the performance is demonstrated in the next section.

5.3 Test cases

The developed compressible fractional step method (cFSM) is tested using two cases for flows with Mach numbers from 0 to 3. The performance of cFSM, in terms of resolution and efficiency, is demonstrated by comparing it with an all Mach number solver PISOCentralFoam developed by Kraposhin et al. [155] and adopting the hybrid PISO/KNP scheme.

All numerical simulations employ a bounded second order Crank-Nicolson scheme for the discretisation of temporal terms. A second order vanLeer scheme is applied to all convective terms. A Gauss linear corrected scheme is adopted for the surface normal gradient and Laplacian terms to eliminate the effects of mesh non-orthogonality. For the calculation of face fluxes in the positive (P) and negative (N) directions, the vanLeer interpolation scheme with a second order accuracy is used. To ensure high temporal resolution, the max flow CFL number is kept at 0.1.

5.3.1 A normal shock in a supersonic convergent-divergent nozzle

The production of a normal shockwave in a convergent-divergent nozzle is investigated. This nozzle comprises a pair of symmetric truncated cones as depicted in *Figure 5-1*.

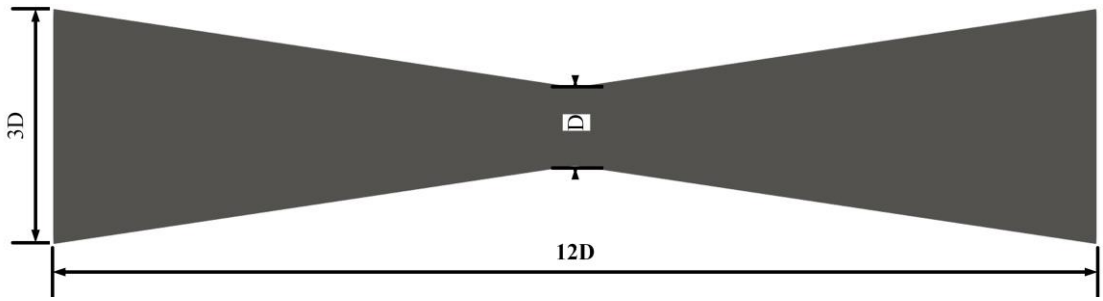

Figure 5-1: Geometry of the 2D convergent-divergent nozzle.

The boundary conditions for initialising the simulations are taken from ANSYS Verification Manual, which are summarised in *Table 5-1*.

Table 5-1: Boundary conditions for the supersonic nozzle problem

Parameter	Value
Inlet absolute pressure	300 kPa
Outlet absolute pressure	175 kPa
Inlet total temperature	500 K
Gas	ideal air
Gas dynamic viscosity	1.831×10^{-5} kg/ms

In *Figure 5-2(a)*, distributions of flow Mach number across the nozzle throat predicted by cFSM and PISOCentralFoam show negligible difference. However, variation of flow Mach number along the nozzle centre axis, as shown in *Figure 5-2(b)*, is slightly better approximated by PISOCentralFoam in the transonic and supersonic regions. The over-prediction of cFSM could be attributed to the added pressure dissipation term for preventing pressure-velocity decoupling. Nevertheless, the error for both codes are smaller than 6% and cFSM is 12% faster than PISOCentralFoam using 1 CPU towards the end of simulation as shown in *Figure 5-2(c)*.

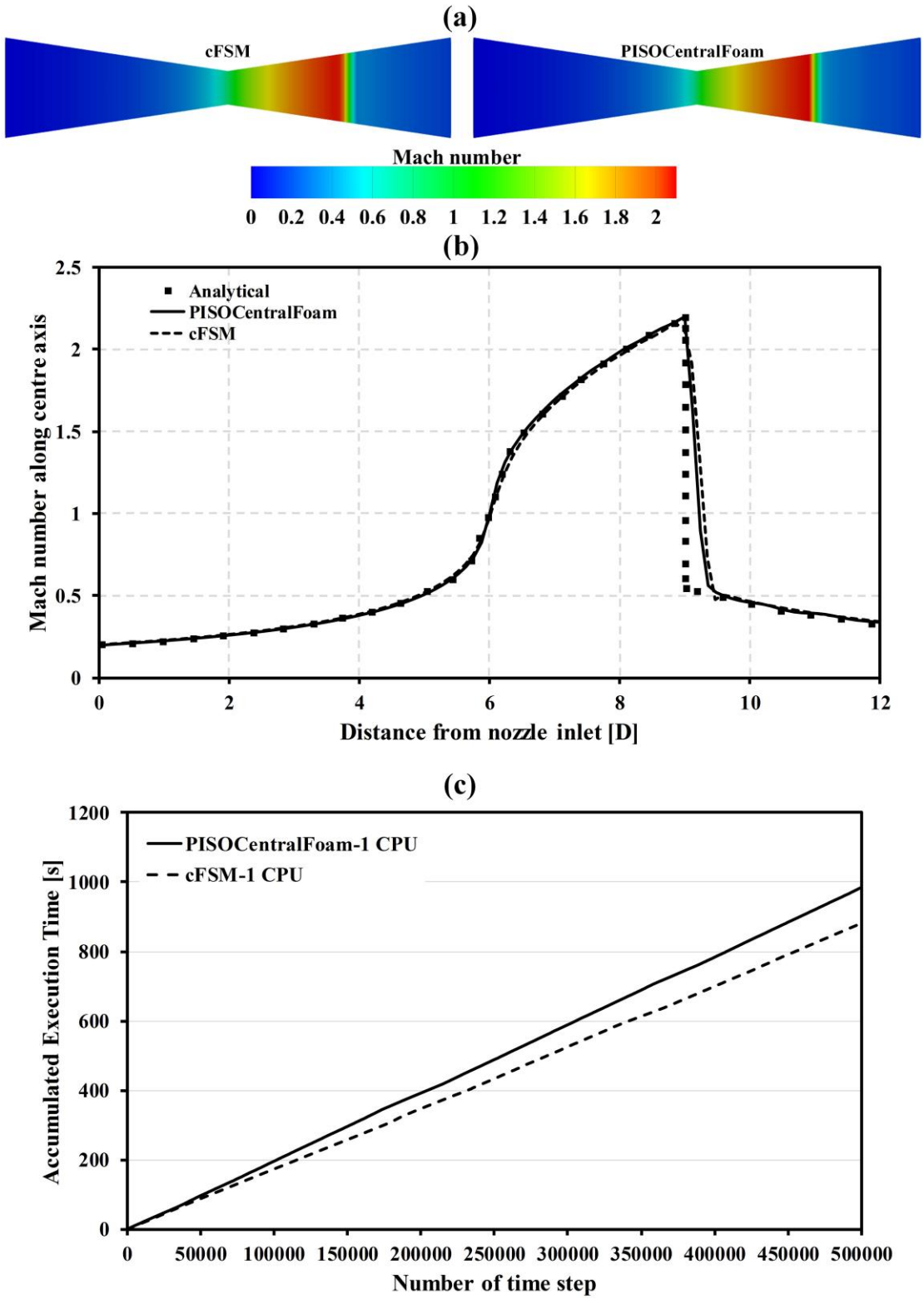

Figure 5-2: Comparison of (a) flow Mach number distribution, (b) variation of Mach number along nozzle centre axis and (c) computing speed between cFSM and PISOCentralFoam for supersonic flow in a convergent-divergent nozzle. In image (b), the analytical solution is calculated based on the laws of isotropic flow and the theory of normal shockwaves [161].

5.3.2 Forward facing step problem with supersonic flow

This problem was extensively studied by Cockburn and Shu [162, 163] to investigate the occurrence of a singularity in pressure and velocity derivatives around a corner point. The setup of the forward facing step is illustrated in *Figure 5-3*. An inviscid uniform flow enters at the left end of the geometry with a speed of Mach 3. After travelling 0.6 unit in length, the flow then interacts with a step that is 0.2 unit high. This interaction results in a singularity that generates a shockwave which bounces off the lower and upper reflective walls. These shock-wall as well as shock-shock interactions are shown in Figure *5-4* which also compares the simulation results of the cFSM solver and the PISOCentralFoam solver with that of a 3rd order Runge-Kutta Discontinuous Galerkin method (RKDG) [162] at $t = 4s$. In Figure *5-4*, the results are presented in order from most to least diffusive.

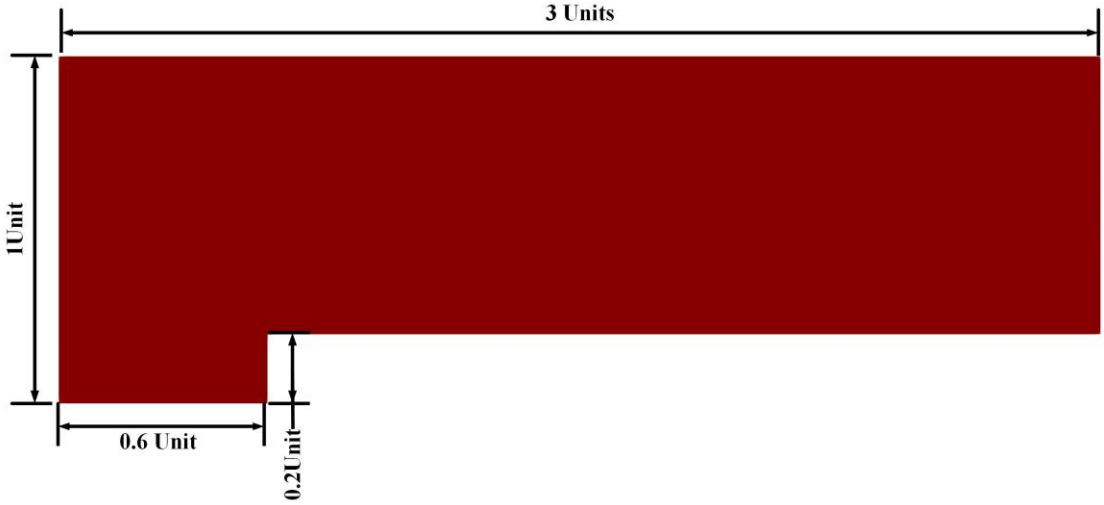

Figure 5-3: Geometry of the 2D forward facing step.

Unlike in Woodward and Colella's work [164], the numerical scheme near the corner is not modified in any way. This causes an erroneous entropy layer as well as a spurious Mach stem (shown in the red rectangle) at the bottom wall. This artefact is most prominent in the simulation with PISOCentralFoam where the stem of the shock detaches from the bottom wall. Another notable aspect is that the 2nd order finite volume cFSM is slightly less diffusive than the 3rd order finite element RKDG with a grid resolution of 1/160. This is manifested by the observation that more Kelvin-Helmholtz instabilities due to shock-shock interaction near the upper wall are captured in the simulation with cFSM code than that with RKDG at this grid resolution. On the other hand, PISOCentralFoam only predicts a laminar like flow after the point of shock-shock interaction. In addition, the iso-density contour lines upstream of the step as well as near the bottom wall downstream are smoother for cFSM simulation than for the other three simulations. These imply that cFSM provides a better numerical resolution than PISOCentralFoam and RKDG for this particular case. In addition, the results in *Figure 5-5* indicate that cFSM is 20.4% faster than PISOCentralFoam with a five-order-of-magnitude lower pressure equation residue towards the end of the simulation using 4 CPUs.

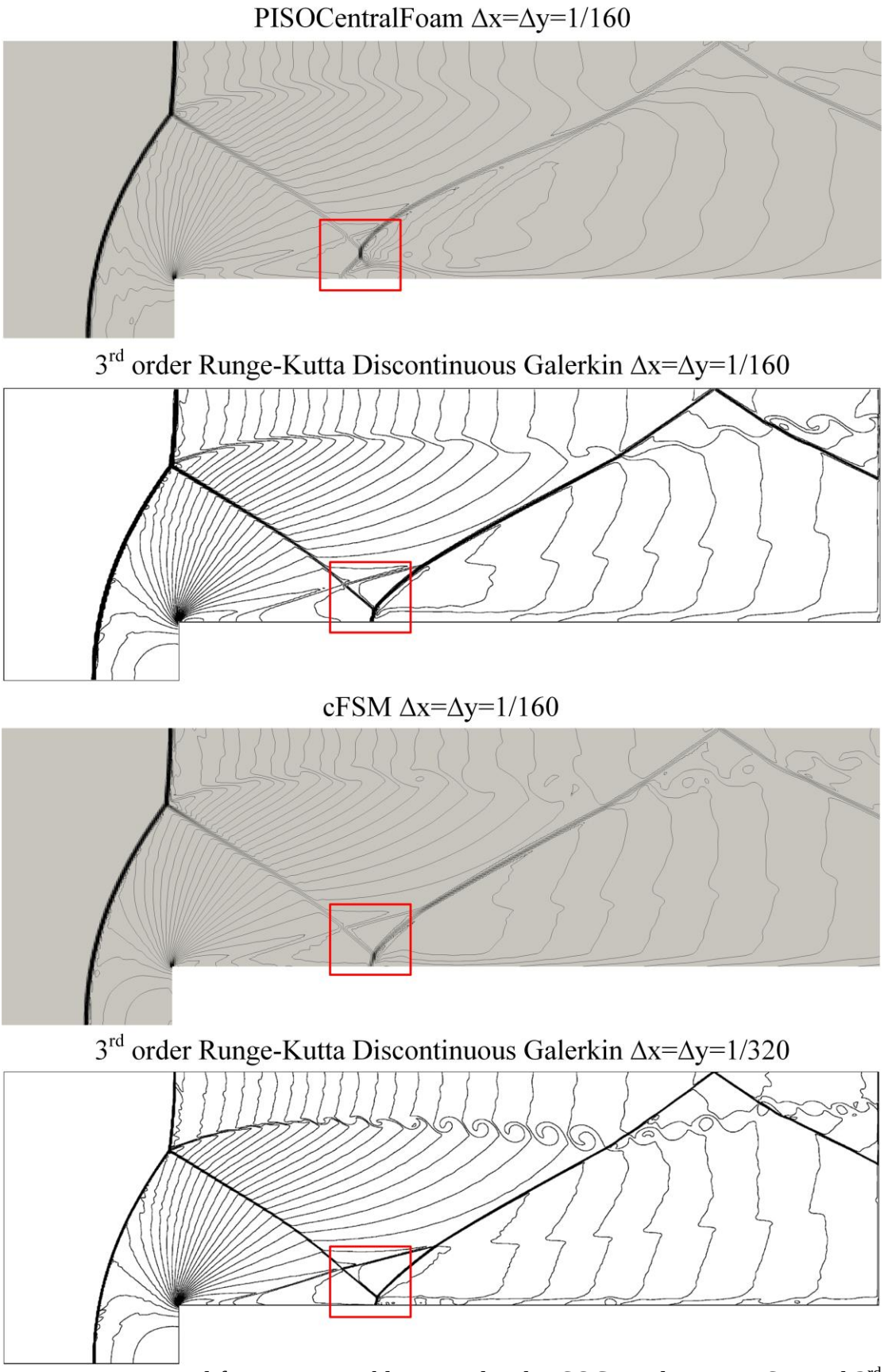

Figure 5-4: Forward facing step problem simulated PISOCentralFoam, cFSM and 3rd order RKDG. The iso-density contour lines are represented using 30 equally spaced

contour lines from $\rho = 0.090338$ to $\rho = 6.2365$. From top to bottom $\Delta x = \Delta y = \frac{1}{160}$, $\frac{1}{160}$, $\frac{1}{160}$, $\frac{1}{320}$. Animation showing the comparison between cFSM and PISOCentralFoam considering the forward-facing problem can be found in [165] (https://www.youtube.com/watch?v=egTq2adnXPY&ab_channel=HongjiangYu).

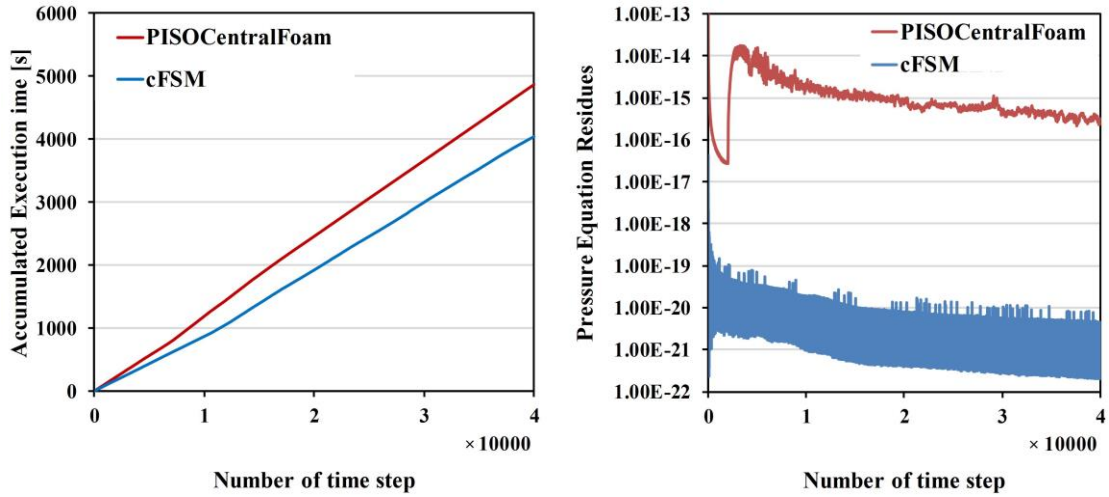

Figure 5-5: Comparison of computational speed (left) and residues of the pressure equation (right) between simulations with cFSM and PISOCentralFoam respectively. Both codes employed 4 CPUs to simulate supersonic flows over a forward facing step. The pressure equation residues from both simulations are plotted against number of time step using a logarithmic scale with a base of 10.

5.4 Extension to multi-phase flows

Mathematically, integration of the compressible fractional step method (cFSM) into the multi-phase VOF code can be based on the PISOCavitatingInterFoam solver recently developed by Yu et al. [59, 160]. Firstly, the mixture density ρ can be related to densities of each phase (ρ_i) and their corresponding volume fractions (α_i) in a finite volume V:

$$\rho = \sum_V \alpha_i \rho_i \tag{5-13}$$

This enables the generalisation of transport equations for phase volume fractions by splitting the generic continuity equation Eqn (5-2) as following (detailed derivation can be found in our previous work [59]):

$$\begin{cases} \dfrac{\partial \alpha_l}{\partial t}+\nabla\cdot\left(\alpha_l U\right)+\nabla\cdot\left(\alpha_l\alpha_v\left(U_l-U_v\right)+\alpha_l\alpha_i\left(U_l-U_i\right)\right)=-\dfrac{\alpha_l}{\rho_l}\left[\dfrac{D\rho_l}{Dt}\right]\left(1-\alpha_l\right)+\alpha_l\left(\nabla\cdot U\right) \\ +\alpha_l\left[\dfrac{\alpha_v}{\rho_v}\dfrac{D\rho_v}{Dt}+\dfrac{\alpha_i}{\rho_i}\dfrac{D\rho_i}{Dt}\right]+\dot{m}\left(\dfrac{1}{\rho_l}-\alpha_l\left(\dfrac{1}{\rho_l}-\dfrac{1}{\rho_v}\right)\right) \\ \dfrac{\partial \alpha_v}{\partial t}+\nabla\cdot\left(\alpha_v U\right)+\nabla\cdot\left(\alpha_v\alpha_l\left(U_v-U_l\right)+\alpha_v\alpha_i\left(U_v-U_i\right)\right)=-\dfrac{\alpha_v}{\rho_v}\left[\dfrac{D\rho_v}{Dt}\right]\left(1-\alpha_v\right)+\alpha_v\left(\nabla\cdot U\right) \\ +\alpha_v\left[\dfrac{\alpha_l}{\rho_l}\dfrac{D\rho_l}{Dt}+\dfrac{\alpha_i}{\rho_i}\dfrac{D\rho_i}{Dt}\right]-\dot{m}\left(\dfrac{1}{\rho_v}+\alpha_v\left(\dfrac{1}{\rho_l}-\dfrac{1}{\rho_v}\right)\right) \\ \dfrac{\partial \alpha_i}{\partial t}+\nabla\cdot\left(\alpha_i U\right)+\nabla\cdot\left(\alpha_i\alpha_l\left(U_i-U_l\right)+\alpha_i\alpha_v\left(U_i-U_v\right)\right)=-\dfrac{\alpha_i}{\rho_i}\left[\dfrac{D\rho_i}{Dt}\right]\left(1-\alpha_i\right)+\alpha_i\left(\nabla\cdot U\right) \\ +\alpha_i\left[\dfrac{\alpha_l}{\rho_l}\dfrac{D\rho_l}{Dt}+\dfrac{\alpha_v}{\rho_v}\dfrac{D\rho_v}{Dt}\right]-\alpha_i\dot{m}\left(\dfrac{1}{\rho_l}-\dfrac{1}{\rho_v}\right) \end{cases} \tag{5-14}$$

In Eqn (5-14), the mass transfer source term $\dot{m}=\dot{m}^{+}+\dot{m}^{-}$ due to cavitation is modelled using a modified Schnerr and Sauer model of which the modifications are detailed in [160]:

$$\dot{m}=\frac{3\rho_l\rho_v}{\rho}\alpha_l\alpha_v\left(rR_b\right)\sqrt{\frac{2\left|p-p_v\right|}{3\rho_l}}\begin{cases} \dot{m}^{+}=\dfrac{3\rho_l\rho_v}{\rho}\alpha_l\alpha_v\left(rR_b\right)\cdot \\ \sqrt{\dfrac{2}{3\rho_l\left(\left|p-p_v\right|+0.001p_v\right)}}\max\left(p-p_v,0\right) \\ \dot{m}^{-}=\dfrac{3\rho_l\rho_v}{\rho}\alpha_l\alpha_v\left(rR_b\right)\cdot \\ \sqrt{\dfrac{2}{3\rho_l\left(\left|p-p_v\right|+0.001p_v\right)}}\min\left(p-p_v,0\right) \end{cases} \tag{5-15}$$

where rR_b is related to α_l, α_v and nuclei density n by:

$$\left.\begin{aligned} rR_b&=\left(\frac{4\pi n\alpha_l}{3\left(\alpha_v+\alpha_{nuc}\right)}\right)^{1/3} \\ \alpha_{nuc}&=\frac{n\pi\left(d_{Nuc}\right)^3}{6+n\pi\left(d_{Nuc}\right)^3} \end{aligned}\right\} \tag{5-16}$$

The updated phase volume fractions are then used to obtain the intermediate mixture density ρ^{*} by solving:

$$\left.\begin{aligned} &\rho=\sum\nolimits_V\alpha_i\rho_i \\ &\frac{\partial\rho^{*}}{\partial t}+\nabla\cdot\left(\rho U\right)=0 \end{aligned}\right\} \tag{5-17}$$

Secondly, the mixture momentum equation which takes into account surface tension source terms is solved to obtain the intermediate velocity field U^* for the mixture:

$$\frac{\partial \rho^* U^*}{\partial t} + \nabla \cdot \left(\rho^* U^* U^* \right) = -\nabla p + \nabla \cdot \tau + \sum \int_{S(t)} \sigma_{i-j} \kappa n \cdot \delta \left(x - x' \right) ds \qquad (5\text{-}18)$$

Here zero surface tension is assumed at the liquid-vapour and vapour-gas interfaces by setting $\sigma_{liquid-vapour} = 0 \,\&\, \sigma_{vapour-gas} = 0$. This permits diffusive liquid-vapour and gas-vapour interfaces due to phase change and gas mixing processes. On the other hand, the surface tension between liquid and gas (which is the main mechanism incurring interfacial instabilities that lead to liquid jet breakup) is evaluated using a continuum surface model developed by Brackbill et al. [45].

Thirdly, the calculated volume fractions α_i for each phase and their respective densities ρ_i together with the intermediate mixture velocity U^* and density ρ^* fields are used to ensure energy conservation by solving a multi-phase mixture energy equation (detailed derivation can be found in [160]):

$$\begin{aligned}
&\left[\frac{\partial \rho^* T}{\partial t} + \nabla \cdot \left(\rho^* T U^* \right) \right] - \left(\frac{\alpha_l \lambda_l}{C_{pl}} + \frac{\alpha_v \lambda_v}{C_{pv}} + \frac{\alpha_g \lambda_g}{C_{pg}} \right) \left(\nabla^2 T \right) \\
&+ \left(\frac{\alpha_l}{C_{pl}} + \frac{\alpha_v}{C_{pv}} + \frac{\alpha_g}{C_{pg}} \right) \left[\frac{\partial \rho K}{\partial t} + \nabla \cdot \left(\rho K U \right) - \frac{\partial p}{\partial t} - \nabla \cdot \left(\tau \cdot \mathrm{U}^* \right) \right] \\
&+ \left(\frac{\alpha_l}{C_{pl}} \right) \left[\frac{\partial \rho^* H_l'}{\partial t} + \nabla \cdot \left(\rho^* H_l' U^* \right) \right] + \left(\frac{\alpha_v}{C_{pv}} \right) \left[\frac{\partial \rho^* H_v'}{\partial t} + \nabla \cdot \left(\rho^* H_v' U^* \right) \right] \\
&+ \left(\frac{\alpha_g}{C_{pg}} \right) \left[\frac{\partial \rho^* H_g'}{\partial t} + \nabla \cdot \left(\rho^* H_g' U^* \right) \right] \\
&= \dot{m} \rho^* \left[\left(\Delta H - K \right) \left(\frac{1}{\rho_l C_{pl}} - \frac{1}{\rho_v C_{pv}} \right) \right]
\end{aligned} \qquad (5\text{-}19)$$

in which the H_i' terms are pressure dependent enthalpy departure from ideal liquid and gas specific sensible enthalpies. The inclusion of these terms allows important pressure related thermal effects such as Joule-Thomson cooling and heating to be modelled.

Similar to the compressible fractional step method, the derivation of the pressure-velocity coupling procedure for the multi-phase VOF approach starts with dismantling individual phase continuity equations. By replacing phase densities with the product of pressure and compressibility and following the mathematical manipulation in [59], the pressure equation for the mixture can be derived:

$$\left.\begin{aligned}&\frac{\alpha_l}{\rho_l}\left[\psi_l\frac{\partial p}{\partial t}+U^*\cdot\nabla(\rho_l)\right]+\frac{\alpha_v}{\rho_v}\left[\psi_v\frac{\partial p}{\partial t}+U^*\cdot\nabla(\rho_v)\right]+\frac{\alpha_i}{\rho_i}\left[\psi_i\frac{\partial p}{\partial t}+U^*\cdot\nabla(\rho_i)\right]:\langle 1\rangle\\&+\\&\nabla\cdot(U_f)-\dot{m}(\frac{1}{\rho_l}-\frac{1}{\rho_v}):\langle 2\rangle\\&=0\end{aligned}\right\}$$

(5-20)

Comparing Eqn (5-20) with Eqn (5-5) reveals that part $\langle 1\rangle$ of Eqn (5-20) corresponds to the temporal term in Eqn (5-5). Applying the Helmholtz-Hodge decomposition to the velocity field in part $\langle 2\rangle$ of Eqn (5-20) leads to a new formulation for the incompressible mass flux:

$$\nabla\cdot\left(\left(U_f\right)\right)=\nabla\cdot\left(\left(\tilde{U}_f\right)\right)-\frac{\Delta t}{\rho_f^*}\nabla^2 p \tag{5-21}$$

It is evident that Eqn (5-21) corresponds to the convection and Laplacian parts of Eqn (5-5). Therefore, the new mixture pressure equation formulated based on the compressible fractional step method can be expressed as:

$$\left.\begin{aligned}&\frac{\alpha_l}{\rho_l}\left[\psi_l\frac{\partial p}{\partial t}+U^*\cdot\nabla(\rho_l)\right]+\frac{\alpha_v}{\rho_v}\left[\psi_v\frac{\partial p}{\partial t}+U^*\cdot\nabla(\rho_v)\right]+\frac{\alpha_i}{\rho_i}\left[\psi_i\frac{\partial p}{\partial t}+U^*\cdot\nabla(\rho_i)\right]:\langle 1\rangle\\&+\\&\nabla\cdot\left(\left(\tilde{U}_f\right)\right)-\frac{\Delta t}{\rho_f^*}\nabla^2 p-\dot{m}(\frac{1}{\rho_l}-\frac{1}{\rho_v}):\langle 2\rangle\\&=0\end{aligned}\right\}$$

(5-22)

Expressing the numeric flux $\tilde{U}_f$ as the addition of a predicted incompressible mass flux U_f^* and a pressure dissipation term $\frac{\Delta t\left(p_{right}-p_{left}\right)}{\rho_f^*\Delta s}l$ leads to:

$$\left.\begin{aligned}&\frac{\alpha_l}{\rho_l}\left[\psi_l\frac{\partial p}{\partial t}+U^*\cdot\nabla(\rho_l)\right]+\frac{\alpha_v}{\rho_v}\left[\psi_v\frac{\partial p}{\partial t}+U^*\cdot\nabla(\rho_v)\right]+\frac{\alpha_i}{\rho_i}\left[\psi_i\frac{\partial p}{\partial t}+U^*\cdot\nabla(\rho_i)\right]:\langle 1\rangle\\&+\\&\nabla\cdot\left(\left(U_f^*\right)\right)+\nabla\cdot\left(\frac{\Delta t\left(p_{right}-p_{left}\right)}{\rho_f^*\Delta d}l_i\right)-\frac{\Delta t}{\rho_f^*}\nabla^2 p-\dot{m}(\frac{1}{\rho_l}-\frac{1}{\rho_v}):\langle 2\rangle\\&=0\end{aligned}\right\}$$

(5-23)

The predicted incompressible mass flux U_f^* can also be calculated using the KNP scheme following:

$$U_f^*=\left(a_f^P U_f^P+a_f^P a_f^{\min}\right)+\left(a_f^N U_f^N-a_f^N a_f^{\min}\right) \tag{5-24}$$

Therefore, the complete solution algorithm consists of solving the phase volume fraction transport equations Eqn (5-14) followed by solving the general mixture continuity Eqn (5-17), momentum equation Eqn (5-18), energy equation Eqn (5-19), pressure equation Eqn (5-23) and momentum corrector equation Eqn (5-11). Since the PISO pressure-velocity coupling algorithm in PISOCavitatingInterFoam is replaced with the cFSM algorithm, the developed new all Mach number multiphase VOF solver is termed as cFSMCavitatingInterFoam.

5.5 Application to high pressure cavitating diesel spray

In this study, the cFSMCavitatingInterFoam solver is employed to investigate the primary atomisation of a high pressure cavitating diesel spray. A custom thermo-physical library developed in our previous work [160] (Chapter 4) for simulating high pressure diesel injection processes is employed to model the thermo-physics of the diesel spray. This library includes non-linear equations of state for the liquid, vapour and gas phases. Specifically, the polynomial function correlating pressure, density and temperature of the liquid diesel is derived from Payri et al.'s [143] comprehensive experimental data. For the gas phases, the Peng-Robinson equation of state is applied with model constants taken from Lapuerta et al.'s work [140]. In addition, pressure and temperature dependent fluid properties (e.g. constant pressure heat capacity, enthalpy departure, latent heat and dynamic viscosity) are obtained from various sources [136, 141-144]. Since diesel injection processes involve the transition of the flow from subsonic to supersonic as pressure in the injector sac increases, the choice of this case study allows the performance and capabilities of cFSMCavitatingInterFoam to be established for weakly and highly compressible multi-phase flows. Advantages of cFSMCavitatingInterFoam in numerical resolution and efficiency is demonstrated by making relevant comparisons with PISOCavitatingInterFoam.

5.5.1 Numerical configuration

Experimental conditions given in the work of Ghiji et al. [57], relevant for a non-evaporative spray from a single-hole diesel injector with a sharp edged nozzle entrance are simulated. The geometry reproducing the real injector whose internal geometrical characteristics were determined by X-ray Computer-Aided Tomography analysis is shown in *Figure 5-6*. The computational domain consists of a sac, a straight nozzle and a portion of the chamber comprising the primary atomisation region. Fuel is set to enter at the sac inlet with a pre-defined pressure ramp same as that used by Ghiji et al. [57]. In the absence of direct measurement, pressure at the sac inlet is assumed to increase linearly from chamber pressure (3 MPa) to 85 MPa in 50 μs. Maximum injection pressure of 120 MPa is reached after a further 25 μs and then remains constant. This assumption is to some extent arbitrary but is made based on published data that the quasi-steady state jet velocity was reached when the needle was only elevated to 17% of the maximum lift [63]. The ramp is chosen to give an approximate estimation of pressure variation in the sac due to needle dynamics. The ambient volume is non-reactive and filled with pressurised air at 3 MPa. Finally, a non-reflective pressure outlet is applied to all ambient boundaries. The remaining face patches are configured to be no-slip and adiabatic walls with a zero gradient boundary condition for all hydrodynamic variables. Boundary conditions for numerical simulations are set to match experimental conditions summarised in *Table 5-2*.

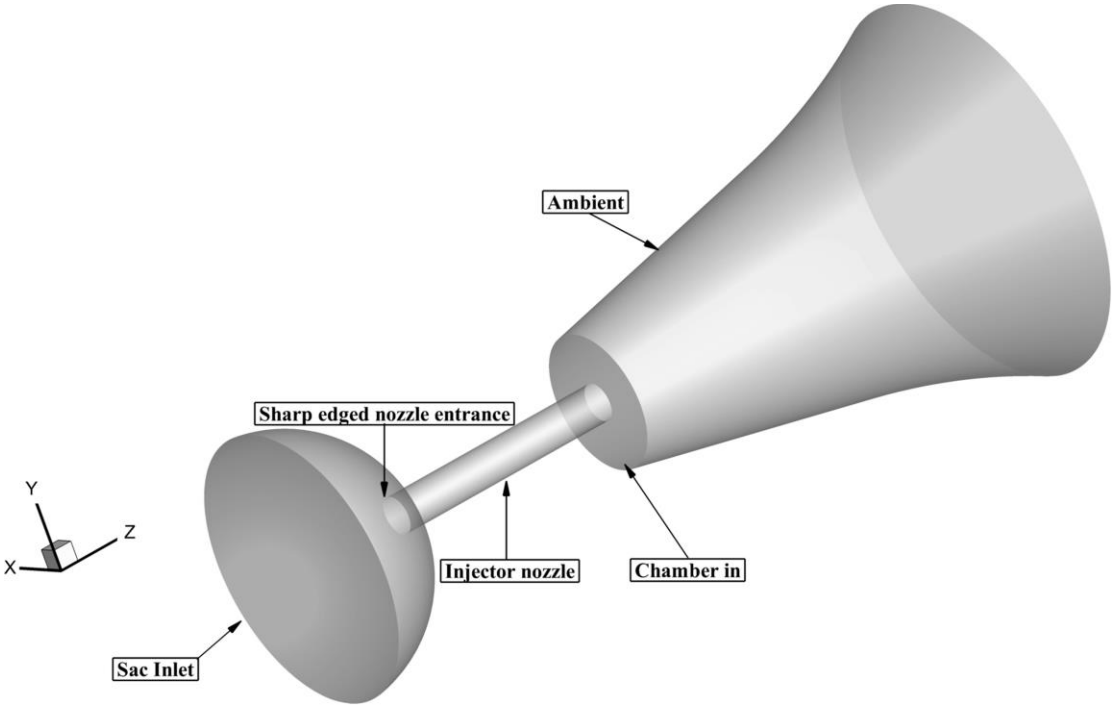

Figure 5-6: Geometry of the single-hole injector with a sharp edged nozzle entrance.

Table 5-2: Fuel properties and boundary conditions based on experimental setup [4, 143].

Parameter	Value
Injection pressures	120 MPa average
Chamber pressure	3 MPa
Nozzle diameter	250 µm
Nozzle length	1600 µm
Nozzle nominal geometry	$K_s = 0$
Nozzle inlet radius	Sharpe edged
Sac volume	0.19371 mm^3
Injector wall temperature	298 K
Fuel	Diesel
Speed of sound in Fuel	1250 m/s
Fuel Temperature	298 K
Fuel density (0.1 MPa)	830 kg/m^3
Fuel dynamic viscosity (0.1 MPa)	0.00367 N s/m^2
Surface tension	0.03 N/m
Gas Temperature	298 K
Ambient pressure	4 MPa
Ambient gas	Compressed air
Enthalpy of phase change	270 kJ/kg
Max injection velocity (120 MPa)	367 m/s
Max Fuel Reynolds Number (120 MPa)	46000

Fuel properties and Reynolds number given in *Table 5-2* can be used to evaluate the Kolmogorov scale for the liquid phase, which determines the smallest grid size for

constructing the computational domain. The Kolmogorov scale for the diesel fuel injected at 120 MPa is calculated to be 0.08 µm:

$$\eta = \frac{W}{\left(\mathrm{Re}_l\right)^{3/4}} \tag{5-25}$$

in which the characteristic length W is the nozzle diameter.

As depicted in *Figure 5-7*, hexahedral elements with a minimum size of 0.1 µm are distributed in the injector nozzle to sufficiently capture the effects of in-nozzle turbulence and wall shear on the flow. A growth rate of 1.01 is applied to construct structured grid in the remaining parts of the computational domain, resulting in the use of 20 million elements for the simulation of spray atomisation coupled with inner injector flow. This mesh has the same resolution and topology as the finest mesh used in Ghiji et al.'s analysis [57].

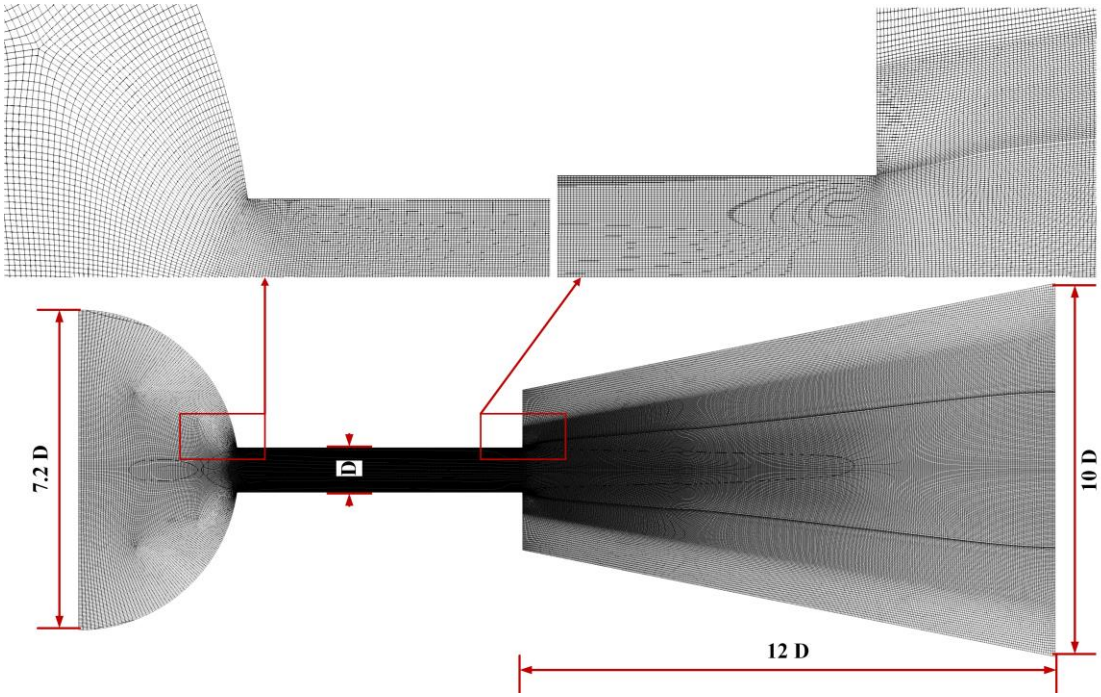

Figure 5-7: Dimensions and mesh topology for the computational domain. Refined hexahedral elements of 0.1 µm are distributed in the injector nozzle. The mesh size increases gradually from the nozzle to the remaining parts of the domain with a growth rate of 1.01. In total, 20 million hexahedral elements are used.

To ensure low numerical dissipation, the minimum orthogonal quality of the grid is kept at 0.9 throughout the computational domain. A fully orthogonal grid has a quality of 1. A bounded second order Crank-Nicolson scheme is utilised to discretise the temporal terms. A bounded second order limitedLinear scheme [166] with a Sweby limiting factor of 0.2 is applied to the convection terms and an interface compression scheme (CICSAM) [47] is used for the evaluation of the artificial compression terms. A Gauss linear corrected scheme is adopted for the gradient and Laplacian terms to eliminate the effects of mesh non-orthogonality. The simulations are initialised with diesel fuel filling 81% of the injector. This is to account for transient physics associated with End of Injection (EOI) process from the previous injection events [57]. Simulations with cFSMCavitatingInterFoam and PISOCavitatingInterFoam are performed using 140 CPUs and 140 GB of physical memory. The max CFL number

was set to 0.2 ensuring high resolution temporal integration with an average time step size of 0.4 ns. The wall clock time for each simulation was around 400 hours. All field results are recorded after start of penetration (ASOP) with an interval of 1 μs.

5.5.2 Comparison of simulation results

In *Figure 5-8*, comparisons between the cFSMCavitatingInterFoam solver and the PISOCavitatingInterFoam solver in terms of simulated spray structures and inner-nozzle flows are shown at four instances from cavitation initiation (10 μs ASOP) to post hydraulic flip (30 μs ASOP). The inner nozzle flow is represented using a Q-criterion isosurface (2.1×10^9) coloured by vorticity magnitude while the emerging spray is depicted using a liquid volume isosurface ($\alpha = 0.5$) coloured by resolved turbulent kinetic energy (TKE).

At 10 μs ASOP, the emerging spray predicted by PISOCavitatingInterFoam appears to be more unstable with a larger number of liquid ligaments shedding from the edge of the mushroom-like spray tip as compared to the cFSMCavitatingInterFoam predictions. This is attributed to the generation of a larger quantity of small scale turbulent structures within 2D upstream of the nozzle exit in the simulation with PISOCavitatingInterFoam than in the simulation with cFSMCavitatingInterFoam. At this instance, the predicted axial velocity near the nozzle exit is approximately 200 m/s in both simulations, which implies a weakly compressible flow regime since the maximum Mach number in the liquid phase is smaller than 0.2. At this low Mach number limit, the pressure dissipation term added to prevent pressure-velocity decoupling in cFSMCavitatingInterFoam results in numerical dissipation that causes under-prediction of turbulence generation in the second half of the nozzle. However, decreasing difference in simulated spray morphology and in-nozzle phenomena between the two simulations is observed as upstream pressure and flow Mach number increase. Another notable aspect is that the turbulence intensity (represented using vorticity magnitude) in the first half of the nozzle is lower than that in the second half of the nozzle at 22 μs ASOP in both simulations. Regions of low turbulence intensity are observed to correlate spatially with the growth of vapour cavities along the wall, which leads to detachment of the liquid jet from the wall. This indicates that the absence of liquid-wall shear could potentially reduce the strength of local flow circulation (vorticity magnitude) despite cavitation generating an increasing number of small-scale turbulent structures on the liquid-vapour interface. This phenomenon is more evident when the liquid jet becomes completely detached from the wall (onset of hydraulic flip) at 27 μs ASOP. At 30 μs ASOP, after the onset of hydraulic flip, the pressure gradient at the nozzle exit causes air to be drawn into the low pressure regions of the nozzle. Air influx leads to intensified liquid-gas convection which slightly strengthens local flow circulation (increase in vorticity) just upstream of the nozzle exit. The onset of hydraulic flip also occurs concurrently with a decrease in the exiting spray width just upstream of a convex structure on the liquid-gas interface. The appearance of this convex structure is associated with the production of a shockwave as a result of a sudden increase in injection velocity caused by significant reduction in liquid-wall shear and effective flow area. This is also demonstrated by comparing interfacial Mach numbers of the emerging spray (a) and the contour plots of the air density (b) before and after the onset of hydraulic flip for both simulations, as depicted in *Figure 5-9*. These observations agree with the simulation results reported by Yu et al. [160].

In *Figure 5-9*, the hydraulic flip induced shockwave downstream of the nozzle exit appears slightly earlier and more oblique in the cFSMCavitatingInterFoam simulation than that in the PISOCavitatingInterFoam simulation. This indicates that cFSMCavitatingInterFoam predicts a higher injection velocity within 1D downstream of the nozzle exit, as also shown in *Figure 5-9(c)* which compares the predicted interfacial Mach number of the emerging jet between two simulations at 27 μs ASOP (onset of hydraulic flip). This could be attributed to cFSMCavitatingInterFoam's higher numerical resolution for high Mach number flows. This aspect is discussed in the next section.

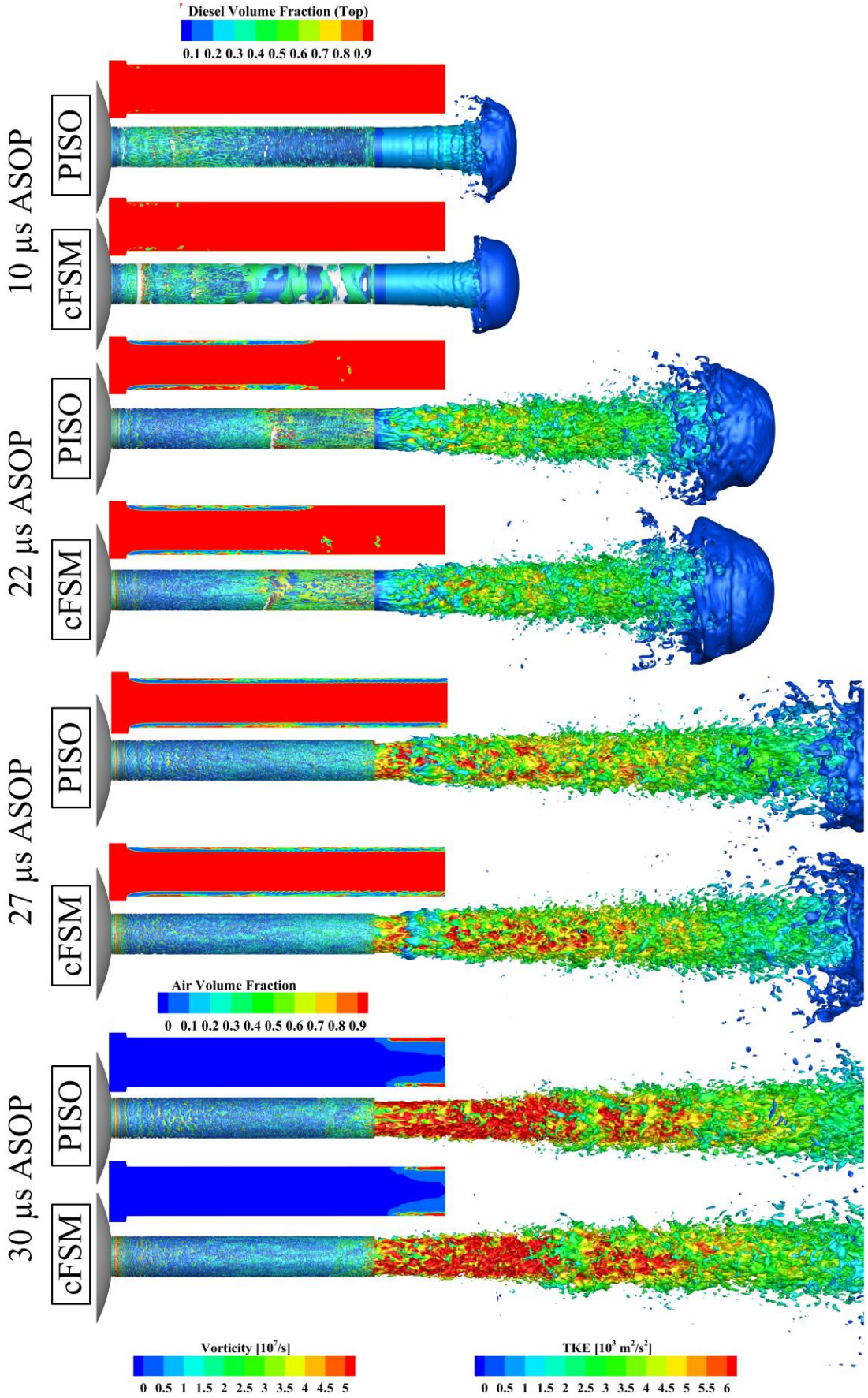

Figure 5-8: Inner nozzle flow and penetrating spray represented by a Q-criterion isosurface of 2.1×10^9 and a liquid volume isosurface of $\alpha = 0.5$ respectively. The Q

isosurface in the nozzle is coloured using vorticity magnitude while the liquid isosurface of the emerging jet is coloured by resolved Turbulent Kinetic Energy (TKE). These plots are taken at 10 µs, 22 µs, 27 µs and 30 µs ASOP corresponding to the transition of flow from cavitating to hydraulic flip with comparisons between cFSMCavitatingInterFoam and PISOCavitatingInterFoam in terms of inner-nozzle flows and emerging spray structures. Enlarged contour plots of liquid volume fraction at the $x = 0$ plane are used to show the transient process from cavitation initiation (10 µs ASOP) to hydraulic flip (27 µs ASOP) in the nozzle. At 30 µs ASOP, after the onset of hydraulic flip, the liquid volume fraction plots are replaced with air volume fraction contour plots to illustrate the hydraulic flip induced air ingestion at the nozzle exit.

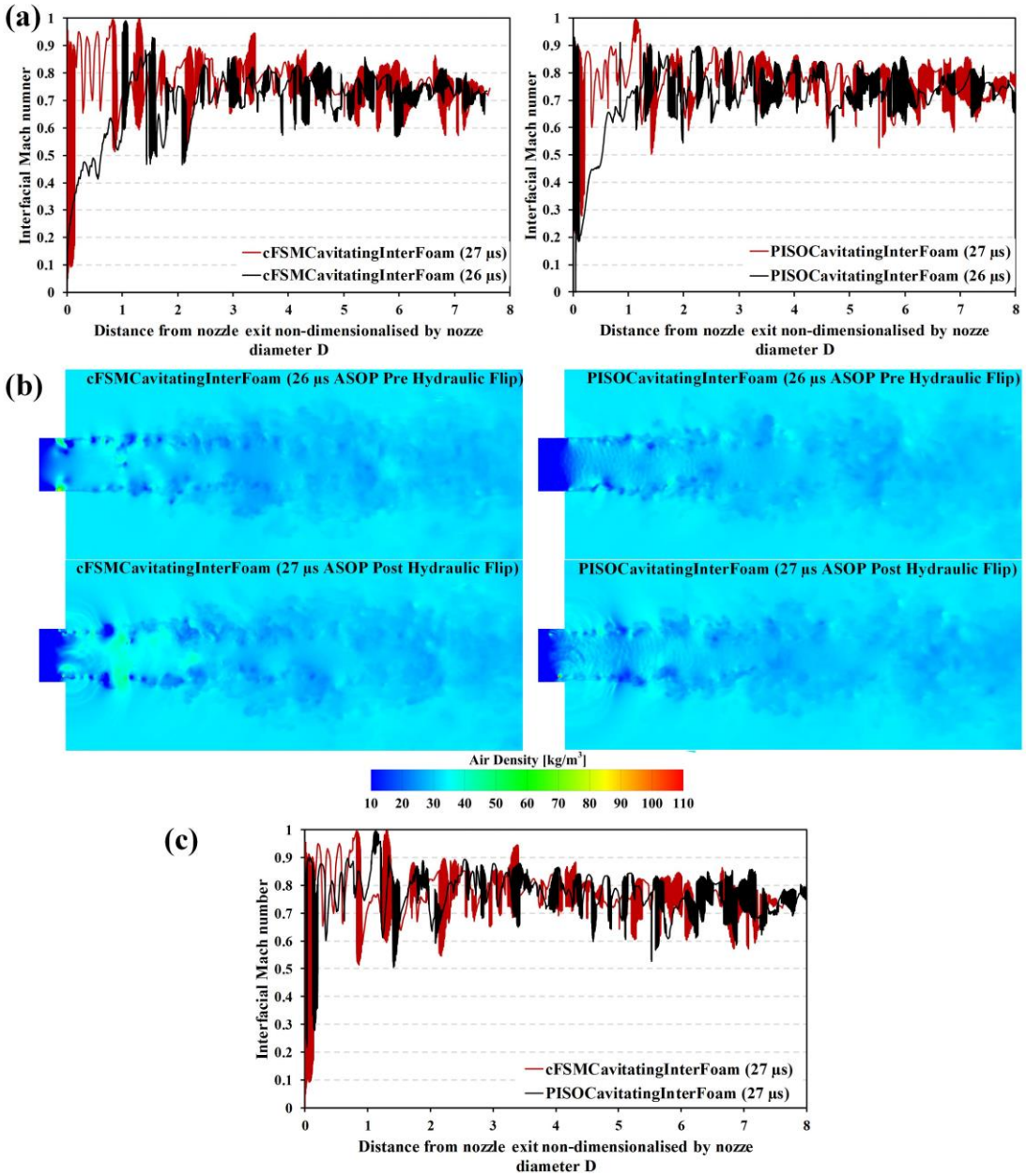

Figure 5-9: Comparison of interfacial Mach numbers (extracted from a $\alpha = 0.9$ liquid volume iso-surface) (a) and air density distributions at the $x = 0$ plane (b) before and after the onset of hydraulic flip. In image (c), comparison of interfacial Mach number of the emerging jet indicates that cFSMCavitatingInterFoam predicts a slightly higher injection velocity within 1D downstream of the nozzle exit.

5.5.3 Comparison of numerical resolution and efficiency

According to Pope [167], a satisfactory LES simulation requires that more than 80% of the turbulent kinetic energy in the flow is resolved. Turbulent kinetic energy resolved can be calculated from the Root Mean Square of the velocity components which are averaged over time. This value is then divided by the time averaged total turbulent kinetic energy (resolved + modelled) to quantify how much turbulent kinetic energy is resolved by the grid. Such assessment is employed in the present study to analyse and compare the numerical resolution of the cFSMCavitatingInterFoam solver and the PISOCavitatingInterFoam solver.

To demonstrate the ability of the cFSMCavitatingInterFoam solver to maintain numerical resolution with increasing flow Mach number, time dependent variations in the resolved turbulent kinetic energy as a fraction of the total turbulent kinetic energy is plotted along the nozzle and at a distance 2 µm from the nozzle wall in *Figure 5-10*. The choice of sampling the resolved turbulent kinetic energy in this region is based on the consideration that flow separation, cavitation and the development of shear layer instabilities occur within 5 µm from the nozzle wall. The capability of this solver in resolving small-scale turbulence can therefore be demonstrated by comparing the amount of turbulent kinetic energy it resolves in this highly turbulent region with that resolved by PISOCavitatingInterFoam. At 10 µs ASOP when cavitation initiates just downstream of the nozzle entrance, both solvers resolve only 30% of the turbulent kinetic energy at the point where flow enters the nozzle and starts to separate. In this region, flow separation and cavitation inception create a highly turbulent regime that significantly reduces the turbulent length scale. The resolution of both solvers in this region, however, increases above 70% when there is a stable vapour cavity developing downstream of the nozzle entrance at later stages. Further downstream, both solvers are able to resolve more than 80% of the turbulent kinetic energy with cFSMCavitatingInterFoam performing slightly better in the first half of the nozzle where the flow Mach number is high and PISOCavitatingInterFoam performing marginally better within 2D of the nozzle exit where the flow Mach number reduces below 0.2. This complies with the observation in *Figure 5-8* that PISOCavitatingInterFoam predicts the generation of a larger amount of small-scale turbulent structures in the second half of the nozzle than the cFSMCavitatingInterFoam prediction at 10 µs ASOP. From 22 µs to 30 µs ASOP, as injection pressure ramps up and flow Mach number increases, cFSMCavitatingInterFoam is able to provide a numerical resolution of at least 78% throughout the nozzle while the PISOCavitatingInterFoam resolution drops to or below 75% at the nozzle entrance. As the flow Mach number increases, the superiority of cFSMCavitatingInterFoam in resolving the turbulence is increasingly evident with numerical resolution being mostly higher than PISOCavitatingInterFoam after 1D from the nozzle entrance. In general, as compared to PISOCavitatingInterFoam, cFSMCavitatingInterFoam yields a more satisfactory LES simulation, in terms of numerical resolution, for the investigation of the primary atomisation of a high-pressure cavitating diesel spray considered in this study.

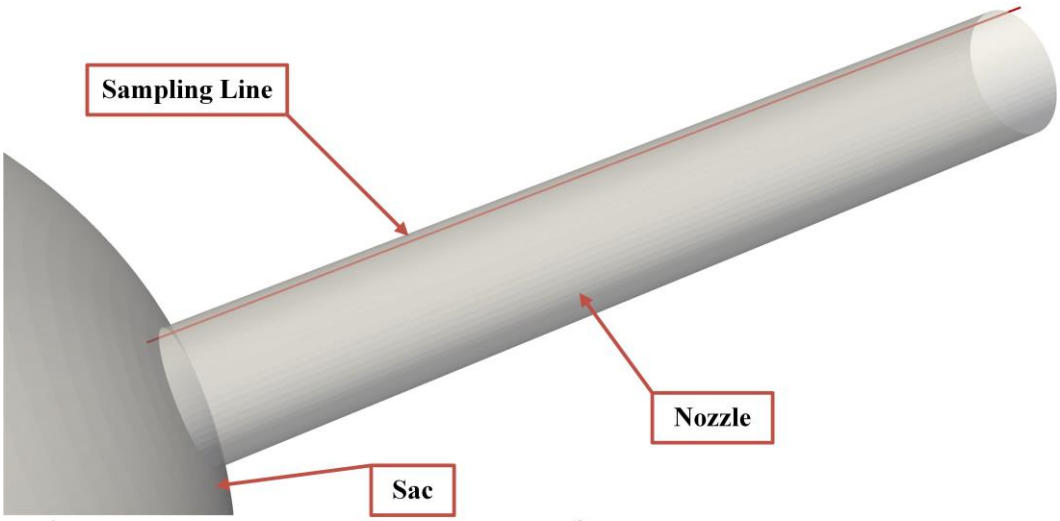
Sampling Line
Nozzle
Sac

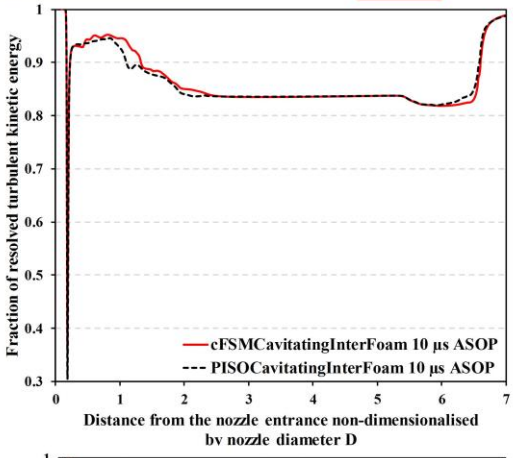
Fraction of resolved turbulent kinetic energy
cFSMCavitatingInterFoam 10 µs ASOP
PISOCavitatingInterFoam 10 µs ASOP
Distance from the nozzle entrance non-dimensionalised by nozzle diameter D

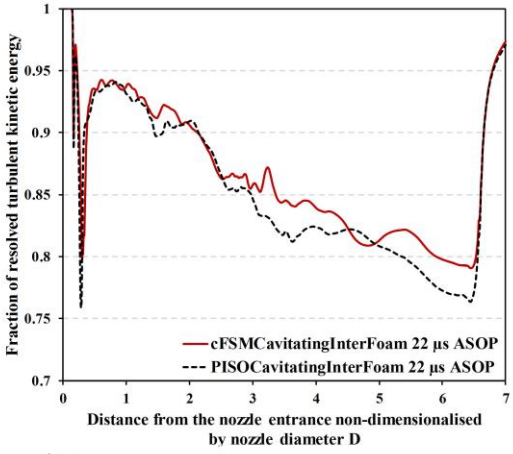
Fraction of resolved turbulent kinetic energy
cFSMCavitatingInterFoam 22 µs ASOP
PISOCavitatingInterFoam 22 µs ASOP
Distance from the nozzle entrance non-dimensionalised by nozzle diameter D

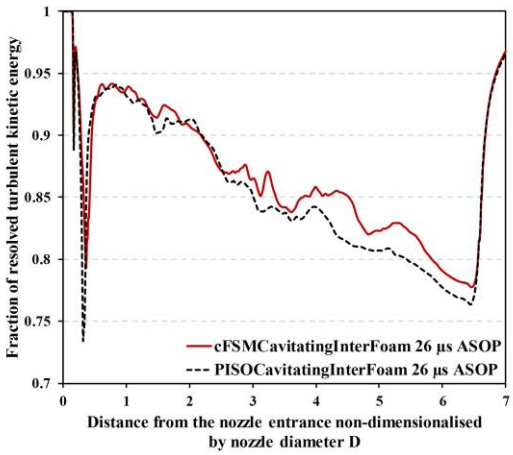
Fraction of resolved turbulent kinetic energy
cFSMCavitatingInterFoam 26 µs ASOP
PISOCavitatingInterFoam 26 µs ASOP
Distance from the nozzle entrance non-dimensionalised by nozzle diameter D

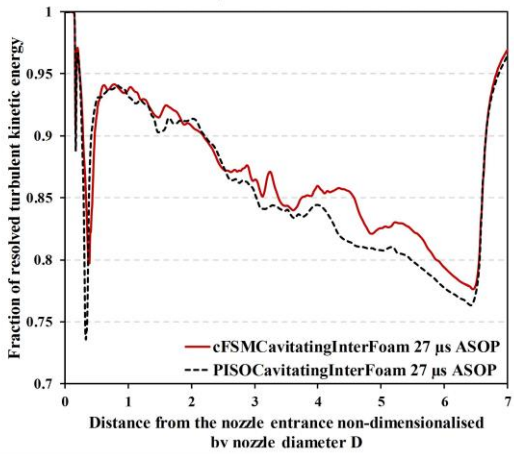
Fraction of resolved turbulent kinetic energy
cFSMCavitatingInterFoam 27 µs ASOP
PISOCavitatingInterFoam 27 µs ASOP
Distance from the nozzle entrance non-dimensionalised by nozzle diameter D

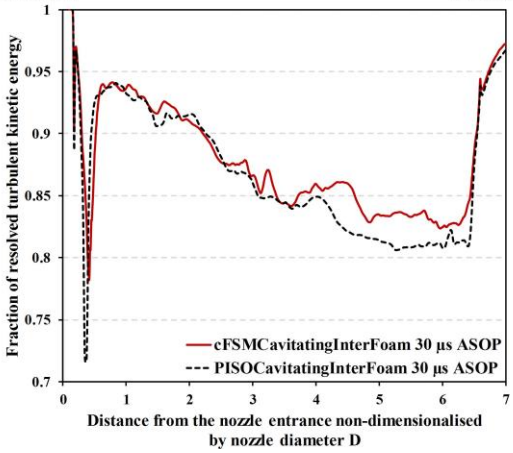
Fraction of resolved turbulent kinetic energy
cFSMCavitatingInterFoam 30 µs ASOP
PISOCavitatingInterFoam 30 µs ASOP
Distance from the nozzle entrance non-dimensionalised by nozzle diameter D

Figure 5-10: Comparison of the resolved turbulent kinetic energy in simulations with cFSMCavitatingInterFoam and PISOCavitatingInterFoam at five instances (10 μs, 22 μs, 26 μs, 27 μs and 30 μs ASOP). The resolved turbulent kinetic energy as a fraction of the total turbulent kinetic energy is sampled in both simulations along a line parallel to the nozzle and is 2 μm from the nozzle wall.

To show the effects of numerical resolution on simulated spray atomisation, the droplet identification algorithm developed by Yu et al. [124] is used to sample the number of small liquid structures shed from the liquid jet. As shown in *Figure 5-11(a)*, a larger quantity of small-scale liquid structures (droplets) generated due to interfacial instabilities is sampled from the simulation with cFSMCavitatingInterFoam than from the simulation with PISOCavitatingInterFoam at 27 μs ASOP. In comparison with the statistics of the PISOCavitatingInterFoam simulation, the PDF of the droplet diameter sampled from the cFSMCavitatingInterFoam simulation also shifts more to the spectrum of larger diameter. Shedding of more and larger liquid structures from the liquid jet indicates a more intensive liquid jet breakup simulated by cFSMCavitatingInterFoam than that simulated by PISOCavitatingInterFoam. These deviations between the two simulations could be attributable to the higher numerical resolution of cFSMCavitatingInterFoam for high Mach number flows, which leads to more turbulent kinetic energy incurring interfacial instabilities to be resolved in the cFSMCavitatingInterFoam simulation than that in the PISOCavitatingInterFoam simulation. In addition, comparison of the accumulated execution time between the two simulations in *Figure 5-11(b)* shows that cFSMCavitatingInterFoam is 40% faster than PISOCavitatingInterFoam in completing the simulation from cavitation initiation (10 μs ASOP) to onset of hydraulic flip (27 μs ASOP). Exponential growth in computational time observed with PISOCavitatingInterFoam makes it increasingly inefficient as compared to cFSMCavitatingInterFoam which displays a more linear increase in accumulated execution time.

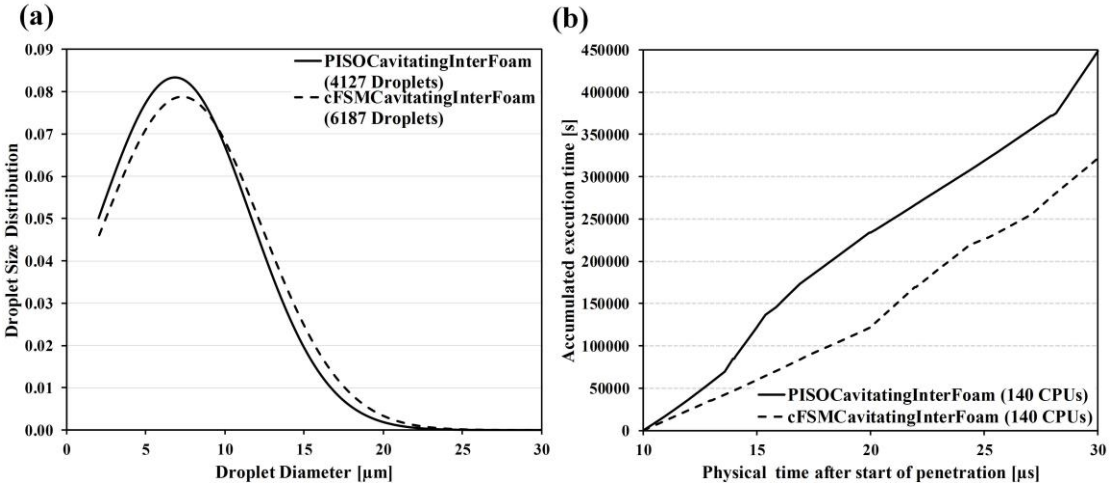

Figure 5-11: (a) Comparison of droplet size PDFs sampled from simulations with PISOCavitatingInterFoam and cFSMCavitatingInterFoam respectively at 27 μs ASOP. (b) Comparison of the time taken for the PISOCavitatingInterFoam solver and the cFSMCavitatingInterFoam solver to complete simulation from cavitation inception (10 μs ASOP) to onset of hydraulic flip (27 μs ASOP).

5.6 Conclusions

A compressible fractional step method (cFSM) is implemented in a previously developed multi-phase VOF-LES code that integrates non-linear equations of state and pressure dependent fluid properties. The detailed derivation of cFSM is first presented for single-phase compressible flows. High numerical resolution is achieved with the use of the Kurganov-Noelle-Petrova (KNP) scheme for the formation of non-oscillating convective fluxes. Application of the cFSM solver to model single-phase supersonic flows shows that this new all Mach number solver has a numerical resolution comparable to that of a 3rd order Runge-Kutta Discontinuous Galerkin method. However, the pressure dissipation term added in the formulation of the numeric flux to prevent decoupling of pressure and velocity makes the cFSM solver slightly more diffusive than the PISOCentralFoam solver adopting a hybrid PISO/KNP scheme at the low Mach number limits. Nevertheless, the cFSM solver has been demonstrated to be more efficient (12% faster with 1 CPU and 20.4% faster with 4 CPUs) than the PISOCentralFoam solver with a significantly lower pressure equation residue. Further, cFSM is extended to multi-phase flows, which leads to the development of an all Mach number multiphase VOF cavitation solver termed as cFSMCavitatingInterFoam. The advantages of cFSMCavitatingInterFoam have been demonstrated by comparing its performance with that of the previously developed PISOCavitatingInterFoam. The comparison between the two multiphase solvers, in terms of numerical resolution and computing speed, is performed considering the atomisation of a high pressure cavitating diesel spray from a single-hole injector with a sharp edged orifice. Calculation of in-nozzle flow and primary atomisation reveals that:

- cFSMCavitatingInterFoam is found to be slightly more diffusive than PISOCavitatingInterFoam in regions where flow Mach number is low (<0.2). This is attributed to the pressure dissipation term added in the formulation of the numeric flux.
- As flow Mach number increases, the use of the non-oscillating low dissipation KNP scheme enables cFSMCavitatingInterFoam to resolve small-scale turbulences with a higher resolution than PISOCavitatingInterFoam.
- cFSMCavitatingInterFoam is 40% faster than PISOCavitatingInterFoam in completing flow simulation from cavitation initiation in the nozzle to the onset of hydraulic flip. The main reason for this improved computational efficiency is the elimination of sub-iteration (mandatory in the PISO algorithm) when solving the pressure equation. This is enabled by the use of the Helmholtz-Hodge decomposition that allows the Laplacian operator to act directly on the pressure field.

6 Closure

This research work has been concerned with the development of advanced CFD methodologies for simulating atomising and compressible multi-phase flows at high Mach numbers and high pressures. In this study, the multi-phase VOF methodology has been further developed, justified and utilised. Several contributions are made towards improved numerical techniques as well as mathematical models of key multi-phase phenomena associated with high-speed liquid jets.

This last chapter concludes the thesis and is divided into two sections. The first section summaries the conclusions drawn from this work and the second one makes recommendations for future work.

6.1 Conclusions

The results of the present study have been extensively assessed and discussed in the previous chapters. In the following paragraphs, the most important conclusions are summarised.

- Simulation of the entire spray evolution from intact liquid jet to dispersed droplets requires a numerical tool that is efficient and capable of handling multi-scale flow physics. The solution is found in a coupled procedure that partially combines high resolution Eulerian interface capturing and efficient Lagrangian parcel tracking. These two simulations are linked with a parallel Eulerian-Lagrangian conversion scheme that transforms insufficiently resolved Eulerian structures to Lagrangian droplet parcels. Computational efficiency and numerical resolution of this coupling procedure, as compared to direct and segregated coupling approaches, is improved by the use of a region coupling method and an additional modelling of secondary breakup. Preservation of the numerical resolution is achieved through interpolating field data at runtime between identical Eulerian and Lagrangian grids in the coupling region.

- The developed mass-conservative-compressible-multi-phase-cavitation code based on the multi-phase VOF formulation and the perfect fluid assumption is suitable for the LES of low pressure cavitating diesel spray. In particular, the findings using this method are:
  - Cavitation initiates in diesel injectors through the combined effects of sudden geometry change, high pressure gradients and flow inertia.
  - Cavitation generates a large quantity of small scale turbulent structures on the liquid-vapour interface, leading to production of inner-nozzle interfacial instabilities.
  - As injection pressure increases, vapour cavities can grow along the nozzle wall to the extent that vapour bubbles collapse at the nozzle exit where static pressure increases above the vapour pressure. This results in enhanced interfacial instabilities.
  - Cavitation induced complete liquid detachment from the wall minimises in-nozzle turbulence production and allows air to be drawn into the nozzle orifice due to the pressure gradient at the nozzle exit.

- Inclusion of cavitation and pressure related thermal effects entails a non-linear EOS for each individual phase and an enthalpy based multi-phase mixture energy equation comprising phase change source terms. The integration of realistic equations of state and pressure dependent fluid properties together with a modified energy equation in the multi-phase VOF cavitation code reveals the following physical phenomena in high pressure cavitating diesel sprays:
  - The presence of cavitation and liquid-wall shear contributes to the generation of small-scale vortical structures in the injector nozzle.
  - High pressure in the injector increases the temperature of the flow (as a result of the increased pressure dependent enthalpy). However, flow acceleration and pressure reduction across the nozzle entrance causes reduction in the flow temperature.
  - Wall shear on the flow causes temperature increase in the near wall boundary layer. Also, enthalpy of condensation can increase the surface temperature of the exiting jet when vapour cavities collapse outside of the nozzle exit.
  - High vaporisation rates correlate spatially with low temperature regions near the wall in the second half of the injector nozzle. This indicates that latent heat of evaporation could counteract the increase in sensible enthalpy due to viscous heating.
  - Collapse of vapour cavities near the nozzle exit correlates spatially with pressure peaks on the nozzle wall. This could be associated with the erosive nature of cavitation and needs more simulations and experimental measurements to confirm.
  - Elimination of wall shear due to cavitation induced hydraulic flip leads to sudden increase in injection velocity, causing immediate production of shockwaves just downstream of the nozzle exit.
  - Fluctuations in temperature and density of the flow are observed to spatially correlate with the production of shockwaves downstream of the nozzle exit.
  - The absence of wall shear reduces the production of interfacial instabilities, leading to reduced spray width.
  - Vapour production at nozzle entrance continues after the onset of hydraulic flip simultaneous with ambient gas injection at nozzle exit. The extent of air ingestion is proportional to maximum injection pressure.

- As compared to PISO based solvers, the all Mach number fractional step method integrated with the KNP central upwind flux scheme has been demonstrated to provide a better numerical resolution for single-phase and multi-phase flows at high Mach numbers. However, the all Mach number algorithm has been shown to be slightly more diffusive than the PISO algorithm in the low Mach number limit. This is attributable to the pressure dissipation term added in the all Mach number algorithm to prevent pressure-velocity decoupling in the low Mach number limit. Comparisons with the PISO algorithm using three test cases highlight the following two major superiorities of the all Mach number algorithm:

- The all Mach number algorithm has a better ability to maintain numerical resolution at high Mach numbers due to the implementation of the non-oscillating KNP flux scheme.
- The all Mach number algorithm becomes increasingly more efficient with higher level of parallelisation. This is attributed to the single pressure equation solve within each time step.

6.2 Suggestions for future work

The results of this study can be improved in several ways, mainly in the areas of validation and methodology improvements. The following recommendations for future work are proposed:

- Comprehensive validation of the parallel VOF-LPT coupling procedure using experimental data such as that provided in Bong's PhD Thesis [33].

- Comprehensive validation of the all Mach number multi-phase cavitation code using experimental data such as that collected by Ghiji *et al.* [57].

- Inclusion of a dynamic mesh capability to allow modelling of injector needle dynamics and its effects on the atomisation processes.

- Integration of the all Mach number multi-phase cavitation code into the VOF-LPT coupling procedure for improved modelling of the complete spray evolution. Comprehensive data sets available on the Engine Combustion Network for cavitating (Spray C) and non-cavitating (Spray A and D) sprays can be employed to validate the numerical model.

- Inclusion of a generic cubic equation of state correlating density, pressure and temperature for the liquid phase. Improved variants of Peng-Robinson EOS can be considered.

The present study should be regarded as a further step towards the realistic simulation of spray atomisation processes. The coupling procedure and multi-phase approaches presented here have not addressed flow phenomena associated with needle dynamics upstream of the injector nozzle. The inclusion of needle dynamics into the frame work of the spray atomisation model is by no means uncharted territory and many researchers have made contributions towards it. However, there still exists a gap in high pressure spray simulations entailing coupled transient solvers correlating needle dynamics, cavitation, thermal effects, interfacial instabilities and multi-scale flow physics. In this respect, it is hoped that the high-resolution numerical models for all Mach number multi-phase high pressure flows developed in this study will serve as a stepping stone for other modellers and engineers in industry who attempt the prediction of such flows.

7 Appendix

Total Enthalpy

$$\frac{\partial(\rho h)}{\partial t}+\nabla\cdot(\rho U h)+\frac{\partial(\rho K)}{\partial t}+\nabla\cdot(\rho U K)-\frac{\partial p}{\partial t}=\nabla\cdot(\tau\cdot U)-\nabla\cdot q \qquad (1)$$

in which heat conduction term $-\nabla\cdot q$ is replaced with $\lambda\left(\nabla^2 T\right)$ according to Fourier's law of heat conduction.

$$\frac{\partial(\rho h)}{\partial t}+\nabla\cdot(\rho U h)+\frac{\partial(\rho K)}{\partial t}+\nabla\cdot(\rho U K)-\frac{\partial p}{\partial t}=\nabla\cdot(\tau\cdot U)+\lambda\nabla^2 T \qquad (2)$$

The energy equations for liquid, vapour and gas phases respectively can be expressed in terms of energy density as follows:

$$\frac{\partial(\alpha_l\rho_l h_l)}{\partial t}+\nabla\cdot(\alpha_l\rho_l h_l U)+\frac{\partial(\alpha_l\rho_l K)}{\partial t}+\nabla\cdot(\alpha_l\rho_l U K)-\frac{\alpha_l\rho_l}{\rho}\left[\frac{\partial p}{\partial t}+\nabla\cdot(\tau\cdot\mathrm{U})\right] \qquad (3)$$
$$=\frac{\alpha_l\rho_l\lambda_l}{\rho}\left(\nabla^2 T\right)$$

$$\frac{\partial(\alpha_v\rho_v h_v)}{\partial t}+\nabla\cdot(\alpha_v\rho_v h_v U)+\frac{\partial(\alpha_v\rho_v K)}{\partial t}+\nabla\cdot(\alpha_v\rho_v K U)-\frac{\alpha_v\rho_v}{\rho}\left[\frac{\partial p}{\partial t}+\nabla\cdot(\tau\cdot\mathrm{U})\right] \qquad (4)$$
$$=\frac{\alpha_v\rho_v\lambda_v}{\rho}\left(\nabla^2 T\right)$$

$$\frac{\partial(\alpha_g\rho_g h_g)}{\partial t}+\nabla\cdot(\alpha_g\rho_g h_g U)+\frac{\partial(\alpha_g\rho_g K)}{\partial t}+\nabla\cdot(\alpha_g\rho_g K U)-\frac{\alpha_g\rho_g}{\rho}\left[\frac{\partial p}{\partial t}+\nabla\cdot(\tau\cdot\mathrm{U})\right] \qquad (5)$$
$$=\frac{\alpha_g\rho_g\lambda_g}{\rho}\left(\nabla^2 T\right)$$

With the inclusion of mass transfer $\dot{m}$ and enthalpy of phase change ΔH source terms due to cavitation, the energy equation for each individual phase can be rewritten as:

Liquid phase

$$\frac{\partial(\alpha_l\rho_l h_l)}{\partial t}+\nabla\cdot(\alpha_l\rho_l h_l U)+\frac{\partial(\alpha_l\rho_l K)}{\partial t}+\nabla\cdot(\alpha_l\rho_l K U)-\frac{\alpha_l\rho_l}{\rho}\left[\frac{\partial p}{\partial t}+\nabla\cdot(\tau\cdot\mathrm{U})\right] \qquad (6)$$
$$=\frac{\alpha_l\rho_l\lambda_l}{\rho}\left(\nabla^2 T\right)+\dot{m}\left(h_l+\Delta H\right)$$

Vapour phase

$$\frac{\partial(\alpha_v\rho_v h_v)}{\partial t}+\nabla\cdot(\alpha_v\rho_v h_v U)+\frac{\partial(\alpha_v\rho_v K)}{\partial t}+\nabla\cdot(\alpha_v\rho_v U K)-\frac{\alpha_v\rho_v}{\rho}\left[\frac{\partial p}{\partial t}+\nabla\cdot(\tau\cdot\mathrm{U})\right] \qquad (7)$$
$$=\frac{\alpha_v\rho_v\lambda_v}{\rho}\left(\nabla^2 T\right)-\dot{m}\left(h_v+\Delta H\right)$$

Gas phases

$$\frac{\partial\left(\alpha_g\rho_g h_g\right)}{\partial t}+\nabla\cdot\left(\alpha_g\rho_g h_g U\right)+\frac{\partial\left(\alpha_g\rho_g K\right)}{\partial t}+\nabla\cdot\left(\alpha_g\rho_g UK\right)-\frac{\alpha_g\rho_g}{\rho}\left[\frac{\partial p}{\partial t}+\nabla\cdot\left(\tau\cdot\mathrm{U}\right)\right] \quad (8)$$
$$=\frac{\alpha_g\rho_g\lambda_g}{\rho}\left(\nabla^2 T\right)$$

Partial differentiation of the specific enthalpy is a function of pressure and temperature expressed as $\partial h=C_p\partial T+\left(\frac{\partial h}{\partial p}\right)_T\partial p$ in which the pressure dependent term $\left(\frac{\partial h}{\partial p}\right)_T\partial p$ is replaced with $\partial H'$ for simplicity. Substituting ∂h and multiplying $\frac{1}{\rho_i C_{pi}}$ to the above equations, we obtain:

$$\frac{1}{\rho_l}\left[\frac{\partial\left(\alpha_l\rho_l T\right)}{\partial t}+\nabla\cdot\left(\alpha_l\rho_l UT\right)\right]+\frac{1}{\rho_l C_{pl}}\left[\frac{\partial\left(\alpha_l\rho_l H_l'\right)}{\partial t}+\nabla\cdot\left(\alpha_l\rho_l UH_l'\right)\right]$$
$$+\frac{1}{\rho_l C_{pl}}\left[\frac{\partial\left(\alpha_l\rho_l K\right)}{\partial t}+\nabla\cdot\left(\alpha_l\rho_l UK\right)\right]-\frac{\alpha_l}{\rho C_{pl}}\left[\frac{\partial p}{\partial t}+\nabla\cdot\left(\tau\cdot\mathrm{U}\right)\right] \quad (9)$$
$$=\frac{\alpha_l\lambda_l}{\rho C_{pl}}\left(\nabla^2 T\right)+\frac{\dot{m}}{\rho_l}\left(T+\frac{\Delta H}{C_{pl}}+\frac{H_l'}{C_{pl}}\right)$$
$$\frac{1}{\rho_v}\left[\frac{\partial\left(\alpha_v\rho_v T\right)}{\partial t}+\nabla\cdot\left(\alpha_v\rho_v UT\right)\right]+\frac{1}{\rho_v C_{pv}}\left[\frac{\partial\left(\alpha_v\rho_v H_v'\right)}{\partial t}+\nabla\cdot\left(\alpha_v\rho_v H_v' U\right)\right]$$
$$+\frac{1}{\rho_v C_{pv}}\left[\frac{\partial\left(\alpha_v\rho_v K\right)}{\partial t}+\nabla\cdot\left(\alpha_v\rho_v UK\right)\right]-\frac{\alpha_v}{\rho C_{pv}}\left[\frac{\partial p}{\partial t}+\nabla\cdot\left(\tau\cdot\mathrm{U}\right)\right] \quad (10)$$
$$=\frac{\alpha_v\lambda_v}{\rho C_{pv}}\left(\nabla^2 T\right)-\frac{\dot{m}}{\rho_v}\left(T+\frac{\Delta H}{C_{pv}}+\frac{H_v'}{C_{pv}}\right)$$
$$\frac{1}{\rho_g}\left[\frac{\partial\left(\alpha_g\rho_g T\right)}{\partial t}+\nabla\cdot\left(\alpha_g\rho_g UT\right)\right]+\frac{1}{\rho_g C_{pg}}\left[\frac{\partial\left(\alpha_g\rho_g H_g'\right)}{\partial t}+\nabla\cdot\left(\alpha_g\rho_g UH_g'\right)\right]$$
$$+\frac{1}{\rho_g C_{pg}}\left[\frac{\partial\left(\alpha_g\rho_g K\right)}{\partial t}+\nabla\cdot\left(\alpha_g\rho_g UK\right)\right]-\frac{\alpha_g}{\rho C_{pg}}\left[\frac{\partial p}{\partial t}+\nabla\cdot\left(\tau\cdot\mathrm{U}\right)\right] \quad (11)$$
$$=\frac{\alpha_g\lambda_g}{\rho C_{pg}}\left(\nabla^2 T\right)$$

Applying expansion of the temporal derivatives and convection terms to Eqn (9 -11) and using conservation of phase mass:

$$\frac{\partial\left(\alpha_l\rho_l\right)}{\partial t}+\nabla\cdot\left(\alpha_l\rho_l U\right)=\dot{m} \quad (12)$$
$$\frac{\partial\left(\alpha_v\rho_v\right)}{\partial t}+\nabla\cdot\left(\alpha_v\rho_v U\right)=-\dot{m} \quad (13)$$

$$\frac{\partial\left(\alpha_g \rho_g\right)}{\partial t}+\nabla\cdot\left(\alpha_g \rho_g U\right)=0 \tag{14}$$

The energy conservation equation for each phase can be expressed as:

$$\begin{aligned}&\frac{1}{\rho_l}\left[\dot{m}T+\alpha_l\rho_l\left(\frac{\partial T}{\partial t}+U\cdot\nabla T\right)\right]+\frac{1}{\rho_l C_{pl}}\left[\dot{m}H_l'+\alpha_l\rho_l\left(\frac{\partial H_l'}{\partial t}+U\cdot\nabla H_l'\right)\right]\\&+\frac{1}{\rho_l C_{pl}}\left[\dot{m}K+\alpha_l\rho_l\left(\frac{\partial K}{\partial t}+U\cdot\nabla K\right)\right]-\frac{\alpha_l}{\rho C_{pl}}\left[\frac{\partial p}{\partial t}+\nabla\cdot\left(\tau\cdot\mathrm{U}\right)\right]\\&=\frac{\alpha_l\lambda_l}{\rho C_{pl}}\left(\nabla^2 T\right)+\frac{\dot{m}}{\rho_l}\left(T+\frac{\Delta H}{C_{pl}}+\frac{H_l'}{C_{pl}}\right)\end{aligned} \tag{15}$$

$$\begin{aligned}&\frac{1}{\rho_v}\left[-\dot{m}T+\alpha_v\rho_v\left(\frac{\partial T}{\partial t}+U\cdot\nabla T\right)\right]+\frac{1}{\rho_v C_{pv}}\left[-\dot{m}H_v'+\alpha_v\rho_v\left(\frac{\partial H_v'}{\partial t}+U\cdot\nabla H_v'\right)\right]\\&+\frac{1}{\rho_v C_{pv}}\left[-\dot{m}K+\alpha_v\rho_v\left(\frac{\partial K}{\partial t}+U\cdot\nabla K\right)\right]-\frac{\alpha_v}{\rho C_{pv}}\left[\frac{\partial p}{\partial t}+\nabla\cdot\left(\tau\cdot\mathrm{U}\right)\right]\\&=\frac{\alpha_v\lambda_v}{\rho C_{pv}}\left(\nabla^2 T\right)-\frac{\dot{m}}{\rho_v}\left(T+\frac{\Delta H}{C_{pv}}+\frac{H_v'}{C_{pv}}\right)\end{aligned} \tag{16}$$

$$\begin{aligned}&\frac{1}{\rho_g}\left[\alpha_g\rho_g\left(\frac{\partial T}{\partial t}+U\cdot\nabla T\right)\right]+\frac{1}{\rho_g C_{pg}}\left[\alpha_g\rho_g\left(\frac{\partial H_g'}{\partial t}+U\cdot\nabla H_g'\right)\right]\\&+\frac{1}{\rho_g C_{pg}}\left[\alpha_g\rho_g\left(\frac{\partial K}{\partial t}+U\cdot\nabla K\right)\right]-\frac{\alpha_g}{\rho C_{pg}}\left[\frac{\partial p}{\partial t}+\nabla\cdot\left(\tau\cdot\mathrm{U}\right)\right]\\&=\frac{\alpha_g\lambda_g}{\rho C_{pg}}\left(\nabla^2 T\right)\end{aligned} \tag{17}$$

Merging energy equations for all phases, the energy equation for mixture can be expressed as:

$$\begin{aligned}&\left[\frac{\partial T}{\partial t}+U\cdot\nabla T\right]+\left(\frac{\alpha_l}{C_{pl}}\right)\left[\frac{\partial H_l'}{\partial t}+U\cdot\nabla H_l'\right]+\left(\frac{\alpha_v}{C_{pv}}\right)\left[\frac{\partial H_v'}{\partial t}+U\cdot\nabla H_v'\right]\\&+\left(\frac{\alpha_g}{C_{pg}}\right)\left[\frac{\partial H_g'}{\partial t}+U\cdot\nabla H_g'\right]+\left(\frac{\alpha_l}{C_{pl}}+\frac{\alpha_v}{C_{pv}}+\frac{\alpha_g}{C_{pg}}\right)\left[\frac{\partial K}{\partial t}+U\cdot\nabla K\right]\\&-\left(\frac{\alpha_l}{\rho C_{pl}}+\frac{\alpha_v}{\rho C_{pv}}+\frac{\alpha_g}{\rho C_{pg}}\right)\left[\frac{\partial p}{\partial t}+\nabla\cdot\left(\tau\cdot\mathrm{U}\right)\right]\\&=\left(\frac{\alpha_l\lambda_l}{\rho C_{pl}}+\frac{\alpha_v\lambda_v}{\rho C_{pv}}+\frac{\alpha_g\lambda_g}{\rho C_{pg}}\right)\left(\nabla^2 T\right)+\dot{m}\left(\Delta H-K\right)\left(\frac{1}{\rho_l C_{pl}}-\frac{1}{\rho_v C_{pv}}\right)\end{aligned} \tag{18}$$

By multiplying mixture density to the above equation and utilising continuity equation, the final form of the energy equation for the mixture can be written as:

$$
\begin{aligned}
&\left[\frac{\partial \rho T}{\partial t}+\nabla\cdot\left(\rho TU\right)\right]+\left(\frac{\alpha_l}{C_{pl}}\right)\left[\frac{\partial \rho H_l'}{\partial t}+\nabla\cdot\left(\rho H_l'U\right)\right]+\left(\frac{\alpha_v}{C_{pv}}\right)\left[\frac{\partial \rho H_v'}{\partial t}+\nabla\cdot\left(\rho H_v'U\right)\right]\\
&+\left(\frac{\alpha_g}{C_{pg}}\right)\left[\frac{\partial \rho H_g'}{\partial t}+\nabla\cdot\left(\rho H_g'U\right)\right]+\left(\frac{\alpha_l}{C_{pl}}+\frac{\alpha_v}{C_{pv}}+\frac{\alpha_g}{C_{pg}}\right)\left[\frac{\partial \rho K}{\partial t}+\nabla\cdot\left(\rho KU\right)\right]\\
&-\left(\frac{\alpha_l}{C_{pl}}+\frac{\alpha_v}{C_{pv}}+\frac{\alpha_g}{C_{pv}}\right)\left[\frac{\partial p}{\partial t}+\nabla\cdot\left(\tau\cdot\mathrm{U}\right)\right]-\left(\frac{\alpha_l\lambda_l}{C_{pl}}+\frac{\alpha_v\lambda_v}{C_{pv}}+\frac{\alpha_g\lambda_g}{C_{pg}}\right)\left(\nabla^2 T\right)\\
&=\dot{m}\rho\left[\left(\Delta H-K\right)\left(\frac{1}{\rho_l C_{pl}}-\frac{1}{\rho_v C_{pv}}\right)\right]
\end{aligned}
\tag{19}
$$

Rearranging Eqn (19) leads to the final formation of the multi-phase mixture energy equation implemented in OpenFOAM as:

$$
\begin{aligned}
&\left[\frac{\partial \rho T}{\partial t}+\nabla\cdot\left(\rho TU\right)\right]-\left(\frac{\alpha_l\lambda_l}{C_{pl}}+\frac{\alpha_v\lambda_v}{C_{pv}}+\frac{\alpha_g\lambda_g}{C_{pg}}\right)\left(\nabla^2 T\right)\\
&+\left(\frac{\alpha_l}{C_{pl}}+\frac{\alpha_v}{C_{pv}}+\frac{\alpha_g}{C_{pg}}\right)\left[\frac{\partial \rho K}{\partial t}+\nabla\cdot\left(\rho KU\right)-\frac{\partial p}{\partial t}-\nabla\cdot\left(\tau\cdot\mathrm{U}\right)\right]\\
&+\left(\frac{\alpha_l}{C_{pl}}\right)\left[\frac{\partial \rho H_l'}{\partial t}+\nabla\cdot\left(\rho H_l'U\right)\right]+\left(\frac{\alpha_v}{C_{pv}}\right)\left[\frac{\partial \rho H_v'}{\partial t}+\nabla\cdot\left(\rho H_v'U\right)\right]\\
&+\left(\frac{\alpha_g}{C_{pg}}\right)\left[\frac{\partial \rho H_g'}{\partial t}+\nabla\cdot\left(\rho H_g'U\right)\right]\\
&=\dot{m}\rho\left[\left(\Delta H-K\right)\left(\frac{1}{\rho_l C_{pl}}-\frac{1}{\rho_v C_{pv}}\right)\right]
\end{aligned}
\tag{20}
$$

8 References

[1] Gorokhovski M, Herrmann M. Modeling primary atomization. Annu Rev Fluid Mech 2008;40:343-66.

[2] Fath A, Fettes C, Leipertz A. Investigation of the diesel spray break-up close to the nozzle at different injection conditions. *Fourth International Symposium on Diagnostics and Modeling of Combustion in Internal Combustion Engines, Kyoto, Japan, JSME.* 1998:429-34.

[3] Goldsworthy L, Ashraf N, Brandner P. Development of a high pressure chamber for research into diesel spray dynamics. Australian Journal of Mechanical Engineering 2009;7(2):15-34.

[4] Goldsworthy L, Bong C, Brandner P. Measurements of diesel spray dynamics and the influence of fuel viscosity using PIV and shadowgraphy. Atomization and Sprays 2011;21(2).

[5] Kastengren AL, Tilocco FZ, Duke DJ, Powell CF, Zhang X, Moon S. Time-resolved X-ray radiography of sprays from engine combustion network spray a diesel injectors. Atomization and Sprays 2014;24(3).

[6] Sharma P, Fang T. Spray and atomization of a common rail fuel injector with non-circular orifices. Fuel 2015;153:416-30.

[7] Xue Q, Battistoni M, Som S, Quan S, Senecal P, Pomraning E, et al. Eulerian CFD Modeling of Coupled Nozzle Flow and Spray with Validation Against X-Ray Radiography Data. SAE International Journal of Engines 2014;7(2014-01-1425):1061-72.

[8] Bianchi GM, Pelloni P, Toninel S, Scardovelli R, Leboissetier A, Zaleski S. Improving the knowledge of high-speed liquid jets atomization by using quasi-direct 3d simulation. SAE Technical Paper; 2005.

[9] Grosshans H, Movaghar A, Cao L, Oevermann M, Szász R-Z, Fuchs L. Sensitivity of VOF simulations of the liquid jet breakup to physical and numerical parameters. Computers & Fluids 2016;136:312-23.

[10] Herrmann M. A dual scale volume-of-fluid approach for modeling turbulent phase interface dynamics. *Proceedings of the Summer Program.* 2014:69.

[11] Hirt CW, Nichols BD. Volume of fluid (VOF) method for the dynamics of free boundaries. Journal of computational physics 1981;39(1):201-25.

[12] Löhner R, Yang C, Oñate E. On the simulation of flows with violent free surface motion. Computer Methods in Applied Mechanics and Engineering 2006;195(41):5597-620.

[13] Reddy R, Banerjee R. GPU accelerated VOF based multiphase flow solver and its application to sprays. Computers & Fluids 2015;117:287-303.

[14] Villiers Ed, Gosman D, Weller H. Detailed investigation of diesel spray atomisation using quasi-direct CFD simulation(Spray Technologies, Atomization). The Proceedings of the International symposium on diagnostics and modeling of combustion in internal combustion engines 2004;2004.6:295-302.

[15] Sussman M, Smereka P, Osher S. A level set approach for computing solutions to incompressible two-phase flow. Journal of Computational physics 1994;114(1):146-59.

[16] Herrmann M. A balanced force refined level set grid method for two-phase flows on unstructured flow solver grids. Journal of Computational Physics 2008;227(4):2674-706.
[17] Sussman M, Puckett EG. A coupled level set and volume-of-fluid method for computing 3D and axisymmetric incompressible two-phase flows. Journal of Computational Physics 2000;162(2):301-37.
[18] Ménard T, Tanguy S, Berlemont A. Coupling level set/VOF/ghost fluid methods: Validation and application to 3D simulation of the primary break-up of a liquid jet. International Journal of Multiphase Flow 2007;33(5):510-24.
[19] Arlov D, Revstedt J, Fuchs L. A different approach for handling large bubbles in a square cross-sectioned bubble column combining Large Eddy Simulation with Lagrangian Particle Tracking. *6th International Conference on Multiphase Flow*. 2007.
[20] Vallier A, Revstedt J, Nilsson H. Procedure for the break-up of cavitation sheet. *4-th International Meeting on Cavitation and Dynamic Problems in Hydraulic Machinery and Systems, October, 26-28, 2011, Belgrade, Serbia.* 2011:77-85.
[21] Vuorinen VA, Hillamo H, Kaario O, Nuutinen M, Larmi M, Fuchs L. Effect of droplet size and atomization on spray formation: A priori study using large-eddy simulation. Flow, turbulence and combustion 2011;86(3-4):533-61.
[22] Vreman B, Geurts BJ, Deen N, Kuipers J, Kuerten J. Two-and four-way coupled Euler–Lagrangian large-eddy simulation of turbulent particle-laden channel flow. Flow, turbulence and combustion 2009;82(1):47-71.
[23] Reitz RD. Modeling atomization processes in high-pressure vaporizing sprays. Atomisation Spray Technology 1987;3:309-37.
[24] O'Rourke PJ, Amsden AA. The TAB method for numerical calculation of spray droplet breakup. SAE Technical Paper; 1987.
[25] Oefelein JC, Sankaran V, Drozda TG. Large eddy simulation of swirling particle-laden flow in a model axisymmetric combustor. Proceedings of the Combustion Institute 2007;31(2):2291-9.
[26] Jangi M, Solsjo R, Johansson B, Bai X-S. On large eddy simulation of diesel spray for internal combustion engines. International Journal of Heat and Fluid Flow 2015;53:68-80.
[27] Elghobashi S. On predicting particle-laden turbulent flows. Applied Scientific Research 1994;52(4):309-29.
[28] Apte S, Mahesh K, Lundgren T. A Eulerian-Lagrangian model to simulate two-phase/particulate flows. Annual Research Briefs 2003:161-71.
[29] Apte S, Gorokhovski M, Moin P. LES of atomizing spray with stochastic modeling of secondary breakup. International Journal of Multiphase Flow 2003;29(9):1503-22.
[30] Li Y, Kong S-C. Integration of parallel computation and dynamic mesh refinement for transient spray simulation. Computer Methods in Applied Mechanics and Engineering 2009;198(17):1596-608.
[31] Reitz RD, Diwakar R. Structure of high-pressure fuel sprays. SAE Technical Paper; 1987.
[32] Baumgarten C, Lettmann H, Merker G. Modelling of primary and secondary break-up processes in high pressure diesel sprays. *CIMAC Congress*. 2004.
[33] Bong CH. Numerical and experimental analysis of diesel spray dynamics including the effects of fuel viscosity. University of Tasmania; 2010.

[34] Amsden A, O'Rourke P, Butler T, II K. A computer program for chemically reactive flows with sprays, Los Alamos National Laboratory Rep. LA-11560-MS; 1989.
[35] Lefebvre A. Atomization and sprays. CRC press; 1988.
[36] Herrmann M. A parallel Eulerian interface tracking/Lagrangian point particle multi-scale coupling procedure. Journal of Computational Physics 2010;229(3):745-59.
[37] Tomar G, Fuster D, Zaleski S, Popinet S. Multiscale simulations of primary atomization. Computers & Fluids 2010;39(10):1864-74.
[38] Burluka A, Borghi R. Development of a Eulerian model for the "atomization" of a liquid jet. Atomization and sprays 2001;11(6).
[39] Desportes A. A combined Eulerian Lagrangian spray amortization (ELSA) in DI Diesel combustion: Fully coupled Euelrian/Lagrangian spray with ECFM-CLEH Combustion model.
[40] Grosshans H, Szász RZ, Fuchs L. Development of an efficient statistical volumes of fluid–Lagrangian particle tracking coupling method. International Journal for Numerical Methods in Fluids 2014;74(12):898-918.
[41] Befrui B, D'Onofrio M, Markle LE, Spiekermann P. Coupled LES Jet Primary Breakup-Lagrangian Spray Simulation of a GDi Multi-Hole Fuel Injector. SAE International Journal of Fuels and Lubricants 2015;8(2015-01-0943):179-89.
[42] Musculus MP, Kattke K. Entrainment waves in diesel jets. SAE International Journal of Engines 2009;2(2009-01-1355):1170-93.
[43] Open C. OpenFOAM user guide. OpenFOAM Foundation 2011;2(1).
[44] De Villiers E, Gosman A, Weller H. Large eddy simulation of primary diesel spray atomization. SAE Technical Paper; 2004.
[45] Brackbill J, Kothe DB, Zemach C. A continuum method for modeling surface tension. Journal of computational physics 1992;100(2):335-54.
[46] Mencinger J, Žun I. A PLIC–VOF method suited for adaptive moving grids. Journal of Computational Physics 2011;230(3):644-63.
[47] Ubbink O. Numerical prediction of two fluid systems with sharp interfaces. University of London UK; 1997.
[48] Ghiji M, Goldsworthy L, Garaniya V, Brandner P, Hield P. CFD Modelling of Primary Atomisation of Diesel Spray. *19th Australasian Fluid Mechanics Conference.* 2014:1-4.
[49] Yoshizawa A, Horiuti K. A statistically-derived subgrid-scale kinetic energy model for the large-eddy simulation of turbulent flows. Journal of the Physical Society of Japan 1985;54(8):2834-9.
[50] O'Rourke PJ. Statistical properties and numerical implementation of a model for droplet dispersion in a turbulent gas. Journal of Computational Physics 1989;83(2):345-60.
[51] Solsjö R, Bai X-S. Injection of Fuel at High Pressure Conditions: LES Study. SAE Technical Paper; 2011.
[52] Kitaguchi K, Hatori S, Hori T, Senda J. Optimization of breakup model using LES of diesel spray. Atomization and Sprays 2012;22(1).
[53] Nordin P. Complex chemistry modeling of diesel spray combustion. Chalmers University of Technology; 2001.
[54] O'Rourke PJ. Collective drop effects on vaporizing liquid sprays. Los Alamos National Lab., NM (USA); 1981.
[55] Rusche H. Computational fluid dynamics of dispersed two-phase flows at high phase fractions. Imperial College London (University of London); 2003.

[56] Ghiji M, Goldsworthy L, Brandner P, Garaniya V, Hield P. Numerical and experimental investigation of early stage diesel sprays. Fuel 2016;175:274-86.
[57] Ghiji M, Goldsworthy L, Brandner P, Garaniya V, Hield P. Analysis of diesel spray dynamics using a compressible Eulerian/VOF/LES model and microscopic shadowgraphy. Fuel 2017;188:352-66.
[58] Jasak H. Error analysis and estimation for finite volume method with applications to fluid flow. 1996.
[59] Yu H, Goldsworthy L, Brandner P, Garaniya V. Development of a compressible multiphase cavitation approach for diesel spray modelling. Applied Mathematical Modelling 2017;45:705-27.
[60] Jasak H, Weller H, Gosman A. High resolution NVD differencing scheme for arbitrarily unstructured meshes. International journal for numerical methods in fluids 1999;31(2):431-49.
[61] Maidi M, Lesieur M, Métais O. Vortex control in large-eddy simulations of compressible round jets. Journal of Turbulence 2006(7):N49.
[62] Shinjo J, Umemura A. Surface instability and primary atomization characteristics of straight liquid jet sprays. International Journal of Multiphase Flow 2011;37(10):1294-304.
[63] Moon S, Gao Y, Park S, Wang J, Kurimoto N, Nishijima Y. Effect of the number and position of nozzle holes on in-and near-nozzle dynamic characteristics of diesel injection. Fuel 2015;150:112-22.
[64] Papadopoulos N, Aleiferis P. Numerical modelling of the in-nozzle flow of a diesel injector with moving needle during and after the end of a full injection event. SAE International Journal of Engines 2015;8(2015-24-2472):2285-302.
[65] Battistoni M, Poggiani C, Som S. Prediction of the nozzle flow and jet characteristics at start and end of injection: transient behaviors. SAE International Journal of Engines 2015;9(2015-01-1850):84-97.
[66] Yu H. Animated diesel spray atomisation simulated using two-phase compressible Volume of Fluid Method. YouTube; 2017, Retrieved from: https://www.youtube.com/watch?v=pZlppXNau-g&ab_channel=HongjiangYu.
[67] Pope SB. Ten questions concerning the large-eddy simulation of turbulent flows. New journal of Physics 2004;6(1):35.
[68] Yu H. Simultaneous simulation of primary and secondary spray atomisation using a coupled VOF-LPT approach. YouTube; 2017, Retrieved from: https://www.youtube.com/watch?v=hajIFoEr4D4&ab_channel=HongjiangYu.
[69] Agarwal AK, Som S, Shukla PC, Goyal H, Longman D. In-nozzle flow and spray characteristics for mineral diesel, Karanja, and Jatropha biodiesels. Applied Energy 2015;156:138-48.
[70] Chaves H, Knapp M, Kubitzek A, Obermeier F, Schneider T. Experimental study of cavitation in the nozzle hole of diesel injectors using transparent nozzles. SAE technical paper; 1995.
[71] Reitz R, Bracco F. Mechanism of atomization of a liquid jet. Physics of Fluids (1958-1988) 1982;25(10):1730-42.
[72] Tamaki N, Nishida K, Hiroyasu H, Shimizu M. Effects of the internal flow in a nozzle hole on the breakup processes of a liquid jet. International Journal of Fluid Mechanics Research 1997;24(4-6).
[73] Afzal H, Arcoumanis C, Gavaises M, Kampanis N. Internal flow in diesel injector nozzles: modelling and experiments. IMechE Paper S 1999;492:25-44.
[74] Andriotis A, Gavaises M. Influence of vortex flow and cavitation on near-nozzle diesel spray dispersion angle. Atomization and Sprays 2009;19(3).

[75] Gavaises M, Andriotis A. Cavitation inside multi-hole injectors for large diesel engines and its effect on the near-nozzle spray structure. SAE Technical Paper; 2006.

[76] Gavaises M, Papoulias D, Gianadakkis E, Andriotis A, Mitroglou N, Theodorakakos A. Comparison of cavitation formation and development in Diesel VCO nozzles with cylindrical and converging tapered holes. *THIESEL 2008 Conference on Thermo-and fluid dynamics processes in Diesel Engines, Valencia, Spain.* 2008.

[77] Kim J-H, Nishida K, Yoshizaki T, Hiroyasu H. Characterization of flows in the sac chamber and the discharge hole of a DI Diesel injection nozzle by using a transparent model nozzle. SAE Technical Paper; 1997.

[78] Mitroglou N, McLorn M, Gavaises M, Soteriou C, Winterbourne M. Instantaneous and ensemble average cavitation structures in Diesel micro-channel flow orifices. Fuel 2014;116:736-42.

[79] Payri F, Bermudez V, Payri R, Salvador F. The influence of cavitation on the internal flow and the spray characteristics in diesel injection nozzles. Fuel 2004;83(4):419-31.

[80] Schmidt DP, Corradini M. The internal flow of diesel fuel injector nozzles: a review. International Journal of Engine Research 2001;2(1):1-22.

[81] Westlye FR, Battistoni M, Skeen S, Manin J, Pickett LM, Ivarsson A. Penetration and Combustion Characterization of Cavitating and Non-Cavitating Fuel Injectors. SAE Technical Paper; 2016.

[82] Befrui B, Corbinelli G, Hoffmann G, Andrews R, Sankhalpara S. Cavitation and Hydraulic Flip in the Outward-Opening GDi Injector Valve-Group. SAE Technical Paper 2009(2009-01):1483.

[83] Soteriou C, Andrews R, Smith M. Direct injection diesel sprays and the effect of cavitation and hydraulic flip on atomization. SAE technical paper; 1995.

[84] Desantes JM, Payri R, Pastor JM, Gimeno J. Experimental characterization of internal nozzle flow and diesel spray behavior. Part I: nonevaporative conditions. Atomization and sprays 2005;15(5).

[85] Paciaroni M, Hall T, Delplanque J-P, Parker T. Single-shot two-dimensional ballistic imaging of the liquid core in an atomizing spray. Atomization and sprays 2006;16(1).

[86] Yue Y, Powell CF, Poola R, Wang J, Schaller JK. Quantitative measurements of diesel fuel spray characteristics in the near-nozzle region using X-ray absorption. Atomization and sprays 2001;11(4).

[87] Giannadakis E, Papoulias D, Gavaises M, Arcoumanis C, Soteriou C, Tang W. Evaluation of the predictive capability of diesel nozzle cavitation models. SAE Technical Paper; 2007.

[88] Kubota A, Kato H, Yamaguchi H. A new modelling of cavitating flows: A numerical study of unsteady cavitation on a hydrofoil section. Journal of fluid Mechanics 1992;240(1):59-96.

[89] Salvador F, Romero J-V, Roselló M-D, Martínez-López J. Validation of a code for modeling cavitation phenomena in Diesel injector nozzles. Mathematical and Computer Modelling 2010;52(7):1123-32.

[90] Schmidt DP, Rutland CJ, Corradini M. A numerical study of cavitating flow through various nozzle shapes. SAE Technical Paper; 1997.

[91] Singhal AK, Athavale MM, Li H, Jiang Y. Mathematical basis and validation of the full cavitation model. Journal of fluids engineering 2002;124(3):617-24.

[92] Salvador F, Martínez-López J, Romero J-V, Roselló M-D. Computational study of the cavitation phenomenon and its interaction with the turbulence developed in diesel injector nozzles by large eddy simulation (les). Mathematical and Computer Modelling 2013;57(7):1656-62.

[93] Som S, Aggarwal S, El-Hannouny E, Longman D. Investigation of nozzle flow and cavitation characteristics in a diesel injector. Journal of Engineering for Gas Turbines and Power 2010;132(4):042802.

[94] Alajbegovic A, Grogger H, Philipp H. Calculation of transient cavitation in nozzle using the two-fluid model. *12th Annual Conf. on Liquid Atomization and Spray Systems, May.* 1999:16-9.

[95] Battistoni M, Grimaldi CN. Numerical analysis of injector flow and spray characteristics from diesel injectors using fossil and biodiesel fuels. Applied Energy 2012;97:656-66.

[96] Grogger H, Alajbegovic A. Calculation of the cavitating flow in venturi geometries using two fluid model. ASME Paper FEDSM 1998;5295.

[97] Greif D, Strucl J. Numerical Study of Transient Multi Component Fuel Injection. SAE Technical Paper 2013:01-2550.

[98] Giannadakis E, Gavaises M, Roth H, Arcoumanis C. Cavitation modelling in single-hole Diesel injector based on eulerian-lagrangian approach. *Proc. THIESEL International Conference on Thermo-and Fluid Dynamic Processes in Diesel Engines. Valencia, Spain.* 2004.

[99] Mohan B, Yang W, Yu W, Tay KL. Numerical analysis of spray characteristics of dimethyl ether and diethyl ether fuel. Applied Energy 2016.

[100] Roth H, Giannadakis E, Gavaises M, Arcoumanis C, Omae K, Sakata I, et al. Effect of multi-injection strategy on cavitation development in diesel injector nozzle holes. SAE Technical Paper; 2005.

[101] Sou A, Biçer B, Tomiyama A. Numerical simulation of incipient cavitation flow in a nozzle of fuel injector. Computers & Fluids 2014;103:42-8.

[102] De Villiers E, Gosman A, Weller H. Large eddy simulation of primary diesel spray atomization. SAE transactions 2004;113(3):193-206.

[103] Marcer R, Le Cottier P, Chaves H, Argueyrolles B, Habchi C, Barbeau B. A validated numerical simulation of diesel injector flow using a VOF method. SAE Technical Paper; 2000.

[104] Biçer B, Sou A. Application of the improved cavitation model to turbulent cavitating flow in fuel injector nozzle. Applied Mathematical Modelling 2015.

[105] Kunz RF, Boger DA, Stinebring DR, Chyczewski TS, Lindau JW, Gibeling HJ, et al. A preconditioned Navier–Stokes method for two-phase flows with application to cavitation prediction. Computers & Fluids 2000;29(8):849-75.

[106] Schnerr GH, Sauer J. Physical and numerical modeling of unsteady cavitation dynamics. *Fourth international conference on multiphase flow, New Orleans, USA.* 1. 2001.

[107] Weller H. A new approach to VOF-based interface capturing methods for incompressible and compressible flow. OpenCFD Ltd, Report TR/HGW/04 2008.

[108] Harvie DJ, Davidson M, Rudman M. An analysis of parasitic current generation in volume of fluid simulations. Applied Mathematical Modelling 2006;30(10):1056-66.

[109] Jasak H. Error Analysis and Estimation for the Finite Volume Method with Applications to Fluid Flows, 1996. Ph. D. Thesis, University of London Imperial College; 1996.

[110] Demirdžić I, Lilek Ž, Perić M. A collocated finite volume method for predicting flows at all speeds. International Journal for Numerical Methods in Fluids 1993;16(12):1029-50.
[111] Winklhofer E, Kull E, Kelz E, Morozov A. Comprehensive hydraulic and flow field documentation in model throttle experiments under cavitation conditions. *Proceedings of the ILASS-Europe conference, Zurich.* 2001:574-9.
[112] Karrholm FP, Weller H, Nordin N. Modelling injector flow including cavitation effects for diesel applications. *ASME/JSME 2007 5th joint fluids engineering conference.* American Society of Mechanical Engineers; 2007:465-74.
[113] Payri R, Salvador F, Gimeno J, Venegas O. Study of cavitation phenomenon using different fuels in a transparent nozzle by hydraulic characterization and visualization. Experimental Thermal and Fluid Science 2013;44:235-44.
[114] Hunt JC, Wray AA, Moin P. Eddies, streams, and convergence zones in turbulent flows. 1988.
[115] Kolář V. Vortex identification: New requirements and limitations. International journal of heat and fluid flow 2007;28(4):638-52.
[116] Payri F, Payri R, Salvador F, Martínez-López J. A contribution to the understanding of cavitation effects in Diesel injector nozzles through a combined experimental and computational investigation. Computers & Fluids 2012;58:88-101.
[117] Leboissetier A, Zaleski S. Direct numerical simulation of the atomization of liquid jet. *Proceeding of the ILASS-Europe.* 2001:2-6.
[118] Schnerr GH, Schmidt SJ, Sezal IH, Thalhamer M. Shock and wave dynamics of compressible liquid flows with special emphasis on unsteady load on hydrofoils and on cavitation in injection nozzles. *Proceedings of 6th International Symposium on Cavitation, Wageningen, The Netherlands.* 2006.
[119] Soteriou C, Andrews R, Smith M. Further studies of cavitation and atomization in diesel injection. SAE Technical Paper; 1999.
[120] Greif D, Morozov A, Winklhofer E, Tatschl R. Experimental and numerical investigation of erosive effects due to cavitation within injection equipment. *Proc. of 4th International Conference on Computational Heat and Mass Transfer.* 2005.
[121] Salvador F, Jaramillo D, Romero J-V, Roselló M-D. Using a homogeneous equilibrium model for the study of the inner nozzle flow and cavitation pattern in convergent–divergent nozzles of diesel injectors. Journal of Computational and Applied Mathematics 2016.
[122] Mishra C, Peles Y. Size scale effects on cavitating flows through microorifices entrenched in rectangular microchannels. Journal of microelectromechanical systems 2005;14(5):987-99.
[123] Koukouvinis P, Gavaises M, Li J, Wang L. Large Eddy Simulation of Diesel injector including cavitation effects and correlation to erosion damage. Fuel 2016;175:26-39.
[124] Yu H, Goldsworthy L, Ghiji M, Brandner P, Garaniya V. A parallel volume of fluid-Lagrangian Parcel Tracking coupling procedure for diesel spray modelling. Computers & Fluids 2017;150:46-65.
[125] Salvador F, Martinez-Lopez J, Romero J-V, Roselló M-D. Computational study of the cavitation phenomenon and its interaction with the turbulence developed in diesel injector nozzles by Large Eddy Simulation (LES). Mathematical and Computer Modelling 2013;57(7):1656-62.

[126] Cailloux M, Helie J, Reveillon J, Demoulin F. Large Eddy Simulation of a Cavitating Multiphase Flow for Liquid Injection. *Journal of Physics: Conference Series.* 656. IOP Publishing; 2015:012081.
[127] Yu H, Goldsworthy L, Brandner P, Garaniya V. Modelling of In-Nozzle Cavitation and Early Spray Breakup Using a Multiphase Volume of Fluid Method. *20th Australasian Fluid Mechanics Conference* Perth; 2016.
[128] Schnerr G, Sauer J. Physical and numerical modeling of unsteady cavitation dynamics. 4th Int. *Conf. on Multiphase Flow.* Orleans, USA; 2001.
[129] Niedźwiedzka A, Lipiński S, Kornet S. Verification of CFD tool for simulation of cavitating flows in hydraulic systems. Journal of Hydroinformatics 2017.
[130] Damián SM. An extended mixture model for the simultaneous treatment of short and long scale interfaces. Dissertationsschrift, Universidad Nacional del Litoral, Argentinien Krepper, E, Lucas, D, Frank, T, Prasser, H-M, & Zwart, PJ (2008) The inhomogeneous MUSIG model for the simulation of polydispersed flows Nuclear Engineering and Design 2013;238(7):1690-702.
[131] Ghiaasiaan SM. Convective heat and mass transfer. Cambridge University Press; 2011.
[132] Haider J. Numerical Modelling of Evaporation and Condensation Phenomena-Numerische Modellierung von Verdampfungs-und Kondensationsph änomenen. Universität Stuttgart; 2013.
[133] Matheis J, Hickel S. Multi-component vapor-liquid equilibrium model for LES of high-pressure fuel injection and application to ECN Spray A. International Journal of Multiphase Flow 2017.
[134] Lopez-Echeverry JS, Reif-Acherman S, Araujo-Lopez E. Peng-Robinson equation of state: 40 years through cubics. Fluid Phase Equilibria 2017;447:39-71.
[135] Salimi M, Bahramian A. The prediction of the speed of sound in hydrocarbon liquids and gases: the Peng-Robinson equation of state versus SAFT-BACK. Petroleum Science and Technology 2014;32(4):409-17.
[136] Kolev NI. Thermodynamic and transport properties of diesel fuel. Multiphase Flow Dynamics 4. Springer; 2011, p. 293-327.
[137] Ahmed T. Reservoir engineering handbook. Gulf Professional Publishing; 2006.
[138] Kyle BG. Chemical and process thermodynamics. 1984.
[139] Passut CA, Danner RP. Correlation of ideal gas enthalpy, heat capacity and entropy. Industrial & Engineering Chemistry Process Design and Development 1972;11(4):543-6.
[140] Lapuerta M, Ballesteros R, Agudelo JR. Effect of the gas state equation on the thermodynamic diagnostic of diesel combustion. Applied Thermal Engineering 2006;26(14):1492-9.
[141] Sutherland W. LII. The viscosity of gases and molecular force. The London, Edinburgh, and Dublin Philosophical Magazine and Journal of Science 1893;36(223):507-31.
[142] Poling BE, Prausnitz JM, O'connell JP. The properties of gases and liquids. Mcgraw-hill New York; 2001.
[143] Payri R, Salvador F, Gimeno J, Bracho G. The effect of temperature and pressure on thermodynamic properties of diesel and biodiesel fuels. Fuel 2011;90(3):1172-80.
[144] Heywood J. Internal combustion engine fundamentals. McGraw-Hill Education; 1988.

[145] Salvador F, Hoyas S, Novella R, Martinez-Lopez J. Numerical simulation and extended validation of two-phase compressible flow in diesel injector nozzles. Proceedings of the Institution of Mechanical Engineers, Part D: Journal of Automobile Engineering 2011;225(4):545-63.
[146] Desantes J, Payri R, Garcia J, Salvador F. A contribution to the understanding of isothermal diesel spray dynamics. Fuel 2007;86(7):1093-101.
[147] Desantes J, Salvador F, López J, De la Morena J. Study of mass and momentum transfer in diesel sprays based on X-ray mass distribution measurements and on a theoretical derivation. Experiments in fluids 2011;50(2):233-46.
[148] Campbell I, Turner J. Turbulent mixing between fluids with different viscosities. Nature 1985;313(5997):39-42.
[149] Dubief Y, Delcayre F. On coherent-vortex identification in turbulence. Journal of turbulence 2000;1(1):011-.
[150] Courant R, Friedrichs KO. Supersonic flow and shock waves. Springer Science & Business Media; 1999.
[151] Turkel E, Vasta V, Radespiel R. Preconditioning Methods for Low-Speed Flows. INSTITUTE FOR COMPUTER APPLICATIONS IN SCIENCE AND ENGINEERING HAMPTON VA; 1996.
[152] Weiss JM, Smith WA. Preconditioning applied to variable and constant density flows. AIAA journal 1995;33(11):2050-7.
[153] Zori L, Rajagopalan G, Zori L, Rajagopalan G. The development of an Euler/Navier-Stokes flow solver for all speeds on 2D unstructured meshes. *35th Aerospace Sciences Meeting and Exhibit.* 1997:332.
[154] Ferziger JH, Peric M. Computational methods for fluid dynamics. Springer Science & Business Media; 2012.
[155] Kraposhin M, Bovtrikova A, Strijhak S. Adaptation of Kurganov-Tadmor numerical scheme for applying in combination with the PISO method in numerical simulation of flows in a wide range of Mach numbers. Procedia Computer Science 2015;66:43-52.
[156] Kurganov A, Noelle S, Petrova G. Semidiscrete central-upwind schemes for hyperbolic conservation laws and Hamilton--Jacobi equations. SIAM Journal on Scientific Computing 2001;23(3):707-40.
[157] Shi K, Morris S, Jemcov A. A Primitive Variable Central Flux Scheme for All Mach Number Flows. *53rd AIAA Aerospace Sciences Meeting.* 2015:5-9.
[158] Kim J, Moin P. Application of a fractional-step method to incompressible Navier-Stokes equations. Journal of computational physics 1985;59(2):308-23.
[159] Chorin AJ. Numerical solution of the Navier-Stokes equations. Mathematics of computation 1968;22(104):745-62.
[160] Yu H, Goldsworthy L, Brandner P, Garaniya V, Li J. Modelling thermal effects in cavitating high-pressure diesel sprays using an improved compressible multiphase approach. Fuel 2017;under review.
[161] White FM. Fluid Mechanics. 3rd ed. New York, NY: McGraw-Hill Book Co.; 1994.
[162] Cockburn B, Shu C-W. The Runge–Kutta discontinuous Galerkin method for conservation laws V: multidimensional systems. Journal of Computational Physics 1998;141(2):199-224.
[163] Cockburn B, Shu C-W. Runge–Kutta discontinuous Galerkin methods for convection-dominated problems. Journal of scientific computing 2001;16(3):173-261.

[164] Woodward P, Colella P. The numerical simulation of two-dimensional fluid flow with strong shocks. Journal of computational physics 1984;54(1):115-73.
[165] Yu H. Supersonic flow over a forward-facing step. YouTube; 2017, Retrieved from: https://www.youtube.com/watch?v=egTq2adnXPY&ab_channel=HongjiangYu.
[166] Sweby PK. High resolution schemes using flux limiters for hyperbolic conservation laws. SIAM journal on numerical analysis 1984;21(5):995-1011.
[167] Pope SB. Turbulent flows. IOP Publishing; 2001.